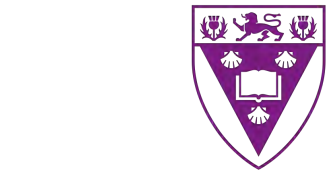

RHODES UNIVERSITY

Where leaders learn

MeerKAT: A journey from commissioning to science

Dissertation submitted in partial fulfillment of the requirements of the degree of
Doctorate of Philosophy
Radio Astronomy Techniques and Technologies division
Department of Physics and Electronics
Rhodes University South Africa

Author:
Benjamin HUGO
NRF South African Radio Astronomy Observatory

Supervisors:
Oleg SMIRNOV
Department of Physics and Electronics, Rhodes University
NRF South African Radio Astronomy Observatory
Gianni BERNARDI
INAF Bolognia Italy
Department of Physics and Electronics, Rhodes University

September, 2024

The circle of life: This overlay shows a portion of the Milky Way (G330+0). In purple is a 6 pointing mosaic synthesized from one of the first observations with the full-polarization correlator and 61 antenna MeerKAT array for the array inauguration in 2018. Several supernovae shells are visible to the middle left and are all that remains of 3 red giants. Next to that to the middle right are a series of brightly lit stellar nurseries where young stars are ionizing the local hydrogen content. The red overlay shows the corresponding patches of heated dust surrounding these stellar nurseries, as captured by the NASA Spitzer Space Telescope (archive). **Image credit:** B. Hugo & S. Goedhart (2018). SARAO (obs. 1524852817) / NASA archives

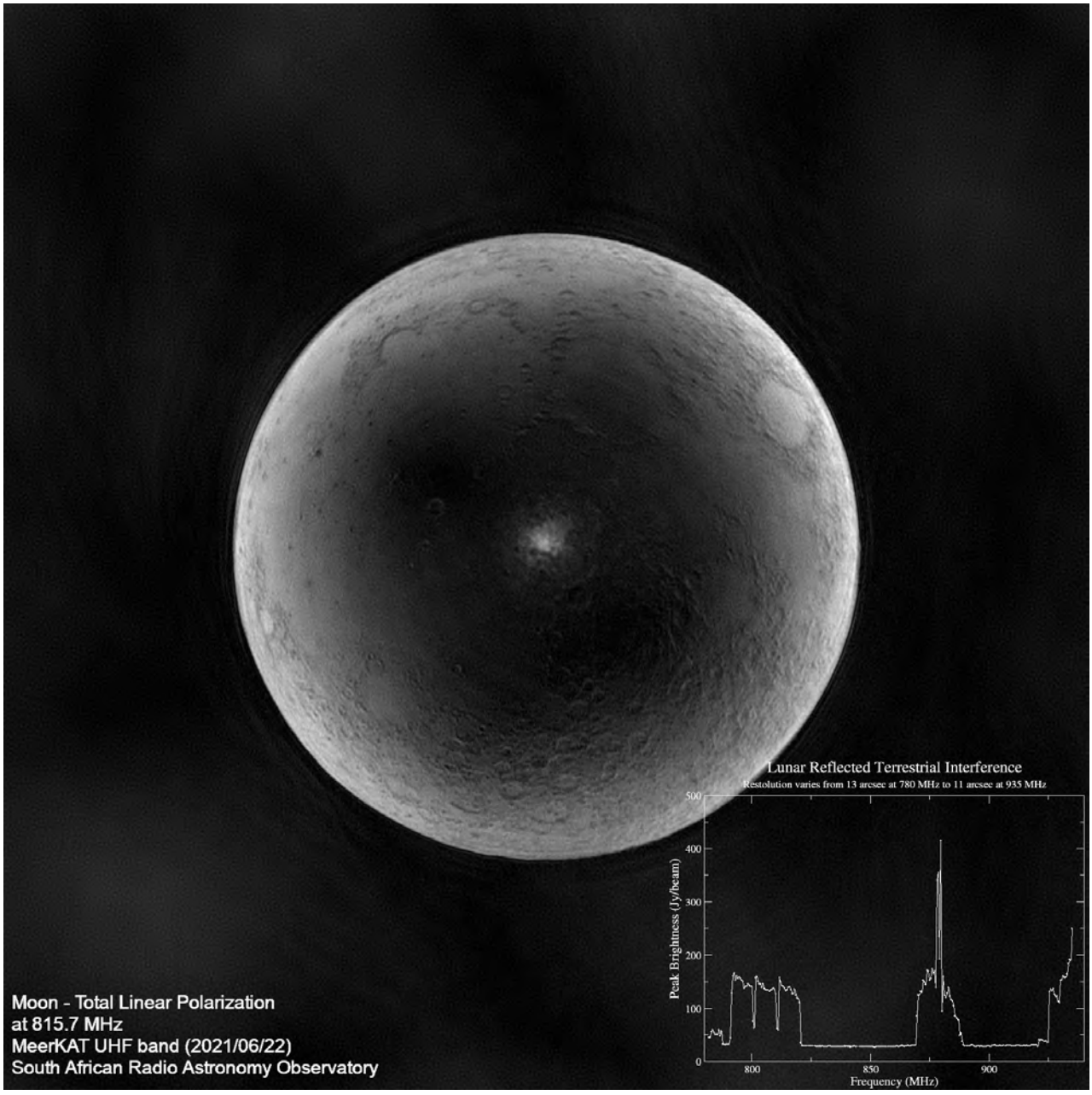

Refraction of sub-surface thermal radiation through Lunar regolith. At centimeter wavelengths the observed emission from the Moon is dominated by thermal radiation, originating a few wavelengths underneath the Lunar surface. As a result it is (approximately) always fullmoon at centimeter wavelengths. The thermal emission is refracted through the powdery surface rock of the Moon. At the boundary between the regolith and free space the radial component of the emission dominates, causing the light to become strongly linearly polarized. The degree of the polarization depends only on the incidence angle and maximizes at the Lunar limb. This large-scale brightening is seen in this total linear polarization map of the Moon, observed with MeerKAT in the UHF band. In this image – easily mistaken for an optical image – differences in regolith structure in the Lunar craters are detected thanks to the remarkable low surface brightness sensitivity of the MeerKAT interferometer. Towards the center of the Lunar disk terrestrial radio interference is reflected. The peak emission at the center of the Lunar disk is plotted as a function of frequency in the overlayed plot to the right. **Image credit:** B. Hugo & R. Perley (2022). SARAO (obs. 1624381270)

Abstract

This dissertation presents a collection of work completed for the South African Radio Astronomy Observatory in characterizing calibrator fields PKS B1934-638, PKS B0407-65 and 3C286, the development of a facet-based multi-direction peeling scheme for the CUBICAL calibration framework and incorporation into an end-to-end containerized data reduction framework, a study of a transitional millisecond pulsar candidate, and characterization of baseline dependent archiving tooling for MeerKAT.

Our long term studies of PKS B1934-638, PKS B0407-65 indicate that these bandpass and flux calibrators are stable over multiple years. We also find that, especially at low frequencies in the UHF band, the population of sources surrounding these stellar Gigahertz Peaked Sources (GPS) can contribute to errors two to three orders of magnitude above desired bandpass calibration solution stability, if left unmodeled. We derive new new full sky models of these fields, currently in use by the MeerKAT Science Data Processor.

We characterize the MeerKAT feed alignment using the refraction-driven linearly polarized thermal light from the Moon in order to derive a new model for the linear polarization of the stable quasar 3C286 down to 544 MHz. Part of this work includes characterization of ionospheric corrections using the International Global Navigation Satelite System Service and direct measurement of total electron content above the MeerKAT site using interchange data from the South African TrigNET service. We find that current commonly-employed techniques achieve corrections to ionospheric Faraday rotation no better than 1 rad m^{-2}. This is the main limitation on the accuracy of polarimetric observation using the MeerKAT array. We find that 3C286 intrinsically depolarizes at frequencies below 1 GHz, with an associated non-linear increase in the intrinsic source rotation measure.

We present an improvement to workflows using the CUBICAL calibration framework, developed at Rhodes University. Modern radio interferometers presents a significant challenge to calibrate, often necessitating memory and compute-intensive direction-dependent calibration towards many directions in order to improve the fidelity of radio images in order to meet scientific goals. We developed a framework to simplify the model prediction aspect of these direction-dependent calibration workflows using targeted faceting. Using our scheme users use models derived from the DDFACET imaging package and only need to provide lattices to mark regions of sky to which direction-dependent calibration solutions need to be solved for. This simplifies a laborious multi-step process in traditional calibration packages that need to be executed per direction. The approach is compared to an image-space corrective regime and incorporated into the VERMEERKAT end-to-end calibration framework for MeerKAT data.

The improved direction-dependent calibration techniques were then applied in an analysis of the transitional millisecond pulsar candidate CXOU J110926.4-650224. The link between accreting binary systems (where emission is dominated by the synchrotron emission of relativistic jets from thermo-nuclear reaction onto the Neutron Star surface by the infalling matter) and binary radio pulsars is currently elusive. This is due to the lack of a large population of such transitional systems — only three confirmed transitional systems are known at the time of writing. It is thought that infalling matter effectively quenches the radio pulsar mechanism. Our candidate was found to be variable in the optical and the X-ray,

with transitions between low, high and flaring states lasting anywhere from a tens of seconds to tens of minutes, seen in archival observations spanning nearly three decades. For the first time we detect low level synchrotron emission (~ 50 μJy beam^{-1}) coincident with this system using MeerKAT, including a flare within minutes of a flare detected in X-ray using the XMM-Newton observatory. Our analysis indicate that there is no clear anti-correlated behaviour between radio and X-ray state transitions in this system, unlike other candidate systems — indicating that such transitional systems may not exhibit homogenous behaviour. This suggests that the processes driving the X-ray mode-switching in this system are not directly linked to the processes responsible for emitting radio synchrotron radiation.

Finally, we consider the problem of MeerKAT data archiving. We present a qualification analysis, using MeerKAT data, of the Rhodes University baseline-dependent archiving package XOVA, which can be used to compress and archive MeerKAT data in interchange standard-compliant format. The data rates from interferometric array radio telescopes, such as MeerKAT, grow as the square of the number of antennas in such an array. For the sake of reproducibility and future re-analysis it is important to archive calibrated visibility products. The degree to which calibrated visibility products can be compressed, by averaging, depends on the amount of smearing that can be tolerated at a fixed distance from the center of the images synthesized from these visibility products. This is, traditionally, set by the longest spacing in the interferometric array, with all other spacings averaged to the same integration and channelization as the longest spacing. We find that, using baseline-dependent averaging techniques – where averaging intervals are set per interferometric spacing – we can achieve space savings an order of magnitude better than traditional averaging approaches, with no appreciable loss of image fidelity when compared to traditional averaging approaches.

Publication Declaration

This thesis is submitted in partial fulfillment of the requirements of this degree. The remainder of the requirements of the degree is fulfilled through first author peer-reviewed publication of a study of the merging cluster system Abell 781, using the Westerbork Synthesis Radio Telescope, in the Monthly Notices of The Royal Astronomical Society. The publication can be accessed here: `https://doi.org/10.1093/mnras/stad2873`

The content of Chapters 1 and 2 have been published in various memos, reformatted and reprinted here with permission from my employer.

The comparitive analysis of the simultaneous facet-based peeling presented in Chapter 3.4 I have implemented in the Cubical package [87] has been taken from published co-authored work published in MDPI Galaxy: `https://doi.org/10.3390/galaxies9040090`.

The content of Chapter 4 has been drawn from a publication in Astronomy & Astrophysics on a transitional millisecond pulsar candidate, CXOU J110926.4-650224, in which I lead the MeerKAT data analysis: `https://doi.org/10.1051/0004-6361/202141431`.

A full list of publications to which I contributed over the course of my employment can be found in Appendix A.

Acknowledgements

I thank the National Research Foundation of the Republic of South Africa, firstly, for the part-time funding support provided towards this research and, secondly, for the use of telescope time on the MeerKAT radio interferometer. I also thank my line manager, Prof. Oleg Smirnov at SARAO for the time allocated to enable the completion of this work.

I want to thank my supervisors, Profs. Smirnov and Bernardi for many insightful discussions on instrumentation, calibration, and galaxy cluster science topics, without which this work would not have been possible. I also want to thank my colleagues and friends, although they are too numerous to name here, at partner institutions around the world for discussions and technical support over the many years I have been at SARAO.

Plagiarism

I acknowledge that plagiarism is wrong and hereby declare that the work contained in this document and in the supporting software is my own, save for that which is properly acknowledged.

Benjamin Vorster Hugo

Contents

List of Figures

List of Tables

Preface

Dear reader

This thesis is a collection of work, on diverse topics, completed for the South African Radio Astronomy Observatory (previously SKA-SA) for the period spanning 2016 to 2023. A series of topics are presented to highlight the importance of characterizing and understanding instrumentation, as well as advanced techniques in radio interferometric data reduction that can be used to correct for calibration error to enable science.

This work was originally conceived to be fairly "modest" in scope – a WSRT and MeerKAT study of a selection of galaxy clusters. However, life intervened: on the one hand, MeerKAT was commissioned and inaugurated during the course of this thesis, and on the other hand, our team found itself involved in some very important software projects, notably the DDFACET [152] imager, the CUBICAL [87] / QUARTICAL [88] calibration packages, the STIMELA [100] pipelining framework, and others. My journey took me into all aspects of observational radio interferometry, from 1^{st} Generation Calibration and fundamental calibrator characterization, to polarization calibration, to direction-dependent effects treatment, to data archiving. In order to structure this thesis into a coherent narrative, I have chosen a chapter to represent each stage of this process, and have reluctantly left some other work out of the picture entirely (prominent examples being the Westerbork Synthesis Radio Telescope cluster work, published separately [71], and my contributions to early telescope characterization). Due to the diversity of topics covered, I do not provide an overall background chapter. Rather, each chapter provides its own background, and is structured as a more or less self-contained discussion. You may therefore choose to read the work in order of preference. It is hoped that you will find the work insightful and that the software contributed here will help you in your own endeavours.

Chapter 1 covers the modeling of bandpass and flux calibrators PKS B1934-638 and PKS B0407-65 during a long-term study. We show the effect of neglecting field structure on bandpass solution stability on a sensitive modern instrument such as MeerKAT. It is found that unmodelled field contributions can cause variations between two and three orders of magnitude above the desired system bandpass gain stability specification.

Chapter 2 deals with characterizing the source linear polarization angle for quasar field 3C286 using measurements of the Moon, Venus and Mars with MeerKAT and the Jansky Very Large Array, for frequencies ranging from 544 MHz to 12 GHz. As part of the study we characterize off-axis leakage effects and the variability of the Ionosphere using differential measurements of Ionospheric Total Electron Content using the International Global Navigation Satellite System Service and data from the TrigNET service, operated by the South African Government. We find that 3C286 depolarizes below L-band, with an intrinsic complex increase in its Rotation Measure and associated change in its linear polarization vector angle. Using Lunar observations we place an upper bound to intrinsic circular polarization on the level of ~ -30 dB. We also find that the ionosphere is the predominant driver of error on measurement of linear polarization angle below the S-band.

Chapter 3 deals with the development of a multi-direction simultaneous peeling solution using on-the-fly targeted faceting for modeling portions of fields requiring direction-dependent gains. We show a co-authored comparative study of this

work against image-space calibration solutions provided by the KILLMS package. Lastly we discuss VERMEERKAT — an end-to-end reduction framework for transfer, direction-independent and direction-dependent calibration of MeerKAT continuum data based on the direction-dependent calibration capability developed in this chapter.

Chapter 4 discusses the detection of a transitional millisecond pulsar candidate CXOUJ110926.4-650224 in co-temporal MeerKAT XMM-Newton X-ray and optical data. We find, for the first time, evidence of centimeter radio emission and flaring of this candidate, which is thought to originate from compact jet and ejection processes close to the neutron star in this, currently, accreting system. The data analysis done here makes use of the direction-dependent calibration techniques developed in Chapter 3.

Lastly, Chapter 5 deals with improving tooling for archiving large interferometric datasets. Large modern radio interferometers, such as MeerKAT, readily produce observations with storage requirements in the hundreds of gigabytes to tens of terabytes range. As calibration is a moderately complex activity, it is desirable to store calibrated data products to improve future re-imaging and extended analysis. We show how the XOVA [8] averaging software developed in the group can reduce storage requirements of such datasets by an order of magnitude, without compromizing image reconstruction fidelity, through Baseline Dependent Averaging.

Chapter 1

MeerKAT commissioning: stability and long term monitoring and modeling of calibrator fields

The MeerKAT array consists of 64 $\sim$ 13.5m offset-Gregorian dishes, with a maximum separation of 7697m. Roughly three quarters of the array are randomly distributed within a 1km core region. Each antenna has a "feed indexer" turn table on which a maximum of 4 receivers can be mounted and repositioned in the secondary focus position. At the time of writing, the array has array-wide L-band (effective bandwidth 900 - 1650 MHz) receivers, UHF (effective bandwidth 580 - 1015 MHz) and S-band (digitized bandwidth 1.75 - 3.5 GHz) receivers. This digitized signal is transmitted via fibre to the channelizers and correlators housed in the Karoo Array Processing Building. A detailed system design overview is given in [80].

In this section I discuss the MeerKAT L-band calibrator characterization undertaken during the period spanning 2017-2019. Some of this period predates the current public-facing archive, and the data may not be available through the public-facing archive as a result. Calibrated products are available on request. I also detail the derivation of calibrator models to include the field structure surrounding the two main primary MeerKAT flux and passband calibrators PKS B0407-65 and PKS B1934-638. These models have been in use in the MeerKAT Science Data Processor since 2020. The SDP pipeline is responsible for calibrating the phase and passband response of the system prior to tied-array (coherent) beamforming, and to form quick look images available through the MeerKAT data archive.

With permission from my employer, this work is drawn from memoranda, notably M2600-0000-029 and M2600-0000-043, as well as supporting earlier documents. The catalogs derived here are stored in electronic form on the MeerKAT Archive at the following DOI:

- PKS B1934-638 — `https://doi.org/10.48479/hhhy-4r55`
- PKS B0407-65 — `https://doi.org/10.48479/ez63-vx81`

1.1 Motivation

Flux calibration of radio interferometers requires the observation of strong compact reference sources with well-known spectra. The calibration procedure, transferred onto a science target, solves the time variability and the frequency response

of the telescope receiver system, in what is known as 1^{st} Generation Calibration. Further refinement of (predominantly) the system phase is possible through a process termed self-calibration. More on that in Chapter 3. However, self-calibration depends, heavily, on the stability of transfer-derived calibration solutions to establish an initial model of the target field for further refinement of the system gains. The telescope receiver systems are designed to ensure stability of the analog electronic receiver components, such that systemic frequency and temporal variability effects can be decoupled. Further to this the stability of the frequency-dependent solutions are important for successful subtraction of continuum emission in spectral line studies. The channel-to-channel variation target is set as -43dB over the span of 8 hours in memo M0000-0000V1-11 TM.

The time variable gains of, primarily, the analog components are typically solved for using compact sources of moderate power (usually in the few Jansky range) and can usually be accomplished without a calibrator model through reference flux scaling with respect to the flux calibrator. On the other hand, a per-channel correction to the passband requires a bright source in order to meet signal-to-noise requirements. Such sources need to have flux densities in the tens of Jansky range for calibration of high spectral cadence correlator modes.

Ideal flux calibrators can be described as having relatively flat-spectrum, unresolved compact emission (in other words observed as a constant power on all uv-spacings), which is several orders (typically at least 20-30 dB) brighter than any other emission in their vicinity. Only a handful of southern fields meet such stringent requirements. PKS B1934-638 (L-band spectrum turnover), 3C286, 3C138, PKS B0407-65 and J0825-5010 (L-band spectrum turnover) are a few examples that come closest to meeting these requirements, at least for MeerKAT. Due to their very high declinations 3C286 and 3C138 cannot readily be observed and are known to be highly polarized sources [127] which significantly complicates calibration procedures for linear feed systems — see Chapter 2 for a detailed discussion on polarimetry. MeerKAT typically uses either PKS B1934-638 – same as the Australia Telescope Compact Array (ATCA) – or PKS B0407-65 as bandpass and flux scale calibrators. J0825-5010 is a fainter Gigahertz-Peaked Source (hereafter "GPS") (about 5.8 Jy at its peak in L-band — this is described in MeerKAT memo M2600-0000-028) that is only used for telescope phase and passband calibration for the coherent beamforming modes. As primary calibrators for imaging, the field modeling of PKS B1934-638 and PKS B0407-65 are discussed here.

PKS B0407-65 is classified as a compact GPS associated with an optical galaxy by [110]. Spectroscopic measurements by [94] using the VLT confirms the optical host of PKS B0407-65 (CDS position J2000 04h08m20.37884s -65d45m 09.0806s) as a galaxy at redshift z=0.962, with an R-band magnitude of ~ 20. Data from NED [65] indicates no peak within the usable UHF or L-band bandwidth of MeerKAT. This is confirmed from spectra taken from [93, and references therein].

PKS B1934-638 (CDS position J2000 19h39m25.025s -63d42m45.64s) is a compact GPS source co-inciding with an 18.9 magnitude galaxy [85] (within 0.1" [77] from deep CCD images) at z=0.183 [125]. Long-term Very Long Baseline Interferometry ("VLBI") observations [59, 158, 159, 113, 89, 160] show the source to be a very stable compact double lobe galaxy with a lobe separation of roughly 41-43 mas (depending on observing frequency) with no detectable core and no significant expansion between the lobes [160]. [21] found the source to have a curved integrated spectrum peaking at 15.6 Jy at 1.19 GHz, with a steep spectral index thereafter of -1.2 found by [85]. Throughout we rely on the spectral curvature model of the source provided by [Reynolds 134] to calibrate the flux scale of our centimeter-wavelength observations. [139] provides an updated flux scale between 10 and 24 GHz using co-observations of Mars, while [122] provides a comparison between ground and space-based Planck observations up to Q-band (48.87 GHz). The source is known to be unpolarized (with an upper limit given as 0.1%) [159].

The achievable stability in the derived calibration solutions, as it turns out, is interdependent with the accuracy of modeling the sky emission, especially at low frequencies due to the wide area covered by the instrument primary beam and the instantaneous sensitivity of modern interferometers, such as MeerKAT. Initial investigations of the stability of the

bandpass of the ROACH II 16-antenna and full 64-antenna full polarization SKARAB correlator (dating back to system commissioning prior to inauguration) shows that systematics introduced by classical calibration methodology were well above the design limits set. Unmodelled field sources surrounding the calibrator PKS B1934-638, for instance, introduce structure in the frequency dependent bandpass solutions at the -20 dB level in L-band and an order of magnitude worse at UHF frequencies.

To understand the problem we start by discussing the general procedure for calibrating an interferometer in Section 1.2 next. We show the effect of neglecting the surrounding field sources on the solutions describing the frequency response of a sensitive wideband interferometer such as MeerKAT in Section 1.3. Section 1.4 discusses the observations used in this study. Section 1.5 discusses the new spatio-spectral models of PKS B1934-638 and PKS B0407-65 derived from long-term commissioning observations, spanning the three years. We also determine the suitability of the sources for calibration of on-axis leakages between horizontal and vertical feeds.

1.2 Procedural review

Following [146] the response of a 2 element interferometer consisting of alt-az mounted antennas can be described by a chain of 2x2 complex Jones [82] matrices, assuming that the sky is primarily modulated by only the far field antenna response:

$$V(t,\nu) = \mathbf{G}_p(\sum_{l,m} \mathbf{P}_p\mathbf{A}_p\mathbf{K}_p\mathbf{S}\mathbf{K}_q^H\mathbf{A}_q^H\mathbf{P}_q^H)\mathbf{G}_q^H$$

Here p and q are antennas, l,m are direction cosines, $\mathbf{G}$ matrices are complex 2x2 voltage gains that depend on time and frequency, $\mathbf{P}$ is the time-variable parallactic angle (difference between Zenith and North Celestial Pole) matrix which rotates the sky around the third antenna axis. The $\mathbf{P}$ matrices are real-valued Euclidean rotation matrices for a linear feed system, which may be offset by an additional feed mount angle. $\mathbf{A}$ is the directional far field response of the individual antennas, $\mathbf{K}$ are, diagonal, geometric delay matrices which relate the sky to its spatial frequency for a particular hour angle and channel. $\mathbf{S}$ is the power coherency matrix consisting of the parallel hand and cross hand correlation products between voltages from horizontal and vertical dipoles on antennas p and q.

Under the assumption that the field is dominated by on-axis emission the equations simplify to become independent of direction:

$$V(t,\nu) = \mathbf{G}_p\mathbf{P}_p\mathbf{S}\mathbf{P}_q^H\mathbf{G}_q^H$$

The complex 2x2 $\mathbf{G}$ matrices can be further simplified[1] and linearized under assumptions of stability [62]. On-axis the system response is primarily dominated by the diagonal of the $\mathbf{G}$ matrices. The diagonal matrix for antenna p (and analogously the Hermitian transpose for antenna q) is further assumed to be frequency stable and can be separated into multiple terms, iteratively solvable on a mix of calibrator sources,

$$\mathbf{G} = \bar{\mathbf{K}}_p(\nu)\bar{\mathbf{G}}_p(t)\bar{\mathbf{B}}_p(\nu))\bar{\mathbf{D}}_p(\nu)\bar{\mathbf{K}}\mathbf{Cross}_p(\nu))\bar{\mathbf{X}}_p(t))$$

where,

$$\mathrm{diag}(\bar{\mathbf{G}}_p(t)) = [g_{p_x(t)}, g_{p_y(t)}],$$

[1]The linearization presented neglects several terms — notably it assumes radio sources are weakly linearly polarized, that the cirular polarization component is small enough for leakages not to affect the diagonal terms and that the source flux is at moderate levels where the squared leakage terms (e.g. $I(1+d_{p_x}d_{q_x}^*)$ on the V_{XX} correlation is at noise-like levels). These we refer to as second-order leakage effects.

a slow varying frequency slope (delay) with diagonal:

$$\text{diag}(\bar{\mathbf{K}}_p(\nu)) = [e^{j\tau_{px}\nu}, e^{j\tau_{py}\nu}],$$

a complex frequency-variable diagonal matrix:

$$\text{diag}(\bar{\mathbf{B}}_p(\nu)) = [b_{p_x(\nu)}, b_{p_y(\nu)}],$$

a complex frequency-variable (ambiguous) crosshand delay diagonal matrix:

$$\text{diag}(\bar{\mathbf{K}}\mathbf{Cross}_p(\nu)) = [e^{j(\tau_{x-y}\nu)}, 0] = [e^{j/2(\tau_{x-y}\nu)}, -e^{j/2(\tau_{x-y}\nu)}],$$

a complex time-variable (ambiguous) crosshand phase diagonal matrix:

$$\text{diag}(\bar{\mathbf{X}}_p(t)) = [e^{j\phi_{x-y}(t)}, 0] = [e^{j/2\phi_{x-y}(t)}, -e^{j/2\phi_{x-y}(t)}],$$

a (presumed time-stable) leakage matrix of the form:

$$\bar{\mathbf{D}}_p(\nu) = \begin{bmatrix} 1 & d_{p_x} \\ d_{p_y} & 1 \end{bmatrix}$$

This leakage and ambiguous crosshand phase matrix describes two effects:

1. The signal chain delay between the streams from the orthogonal dipoles (here referred to as τ_{x-y}). This delay has a slope ($\bar{\mathbf{K}}\mathbf{Cross}$) and (roughly) frequency-constant phase offset ($\bar{\mathbf{X}}$) time-variable phase per antenna. We give the alternate (equivalent) Jones formalism as well. This term only has an effect on the off-diagonal ("cross-hand") terms of the coherency matrix,

2. Off-diagonal (complex) d_{p_x} and d_{p_y} describes the mutual coupling between the orthogonal feeds. The real part, predominantly describes the relative feed angle offset per receiver (more on absolute calibration of these terms in Chapter 2).

Following [62] this equation can be linearized for a linear feed system as follows (absorbing any cable delays into the frequency dependent complex diagonal $\bar{\mathbf{B}}$ matrices):

$$\begin{aligned}
V_{XX} &\approx g_{p_x(t)} g^*_{q_x(t)} b_{p_x(\nu)} b^*_{q_x(\nu)} [(I + Q_\Phi) + U_\Phi (d_{p_x} + d^*_{q_x})] \\
V_{XY} &\approx g_{p_x(t)} g^*_{q_y(t)} b_{p_x(\nu)} b^*_{q_y(\nu)} [(U_\Phi + jV) + I(d_{p_x} + d^*_{q_y}) - Q_\Phi (d_{p_x} - d^*_{q_y})] \\
&\quad e^{j(\tau_{x-y}\nu + \phi_{x-y})} \\
V_{YX} &\approx g_{p_y(t)} g^*_{q_x(t)} b_{p_y(\nu)} b^*_{q_x(\nu)} [(U_\Phi - jV) + I(d_{p_y} + d^*_{q_x}) + Q_\Phi (d_{p_y} - d^*_{q_x})] \\
&\quad e^{-j(\tau_{x-y}\nu + \phi_{x-y})} \\
V_{YY} &\approx g_{p_y(t)} g^*_{q_y(t)} b_{p_y(\nu)} b^*_{q_y(\nu)} [(I - Q_\Phi) + U_\Phi (d_{p_y} + d^*_{q_y})]
\end{aligned} \tag{1.1}$$

The parallactic angle (Φ) is a rotation matrix (in linear bases) which rotates plane-polarized linear emission to feed-relative frame. It is dependent on the hour angle to the source (H) and the array latitude L_a. For a relatively compact array such as MeerKAT we assume that the array latitude is approximately the same between antennas (giving rise to the factor of 2

in the visibilities here):

$$Q_\Phi := U\cos(2\Phi) - Q\sin(2\Phi)$$
$$U_\Phi := Q\cos(2\Phi) + U\sin(2\Phi)$$
$$\tan\Phi := \frac{\sin H}{\cos\delta\tan L_a - \sin\delta\cos H}$$

These parameterized equations describe the various systemic problems introduced in the MeerKAT signal chain as illustrated in Fig. 1.1. The equations can be solved by using a series of calibrator sources with known polarimetric properties. First the dominant diagonal ("parallel" hands XX, YY) have to be corrected using a unpolarized calibrator, this removes any leakage contribution from the crosshands into the parallel hands, by setting the power on the crosshands equal to 0.

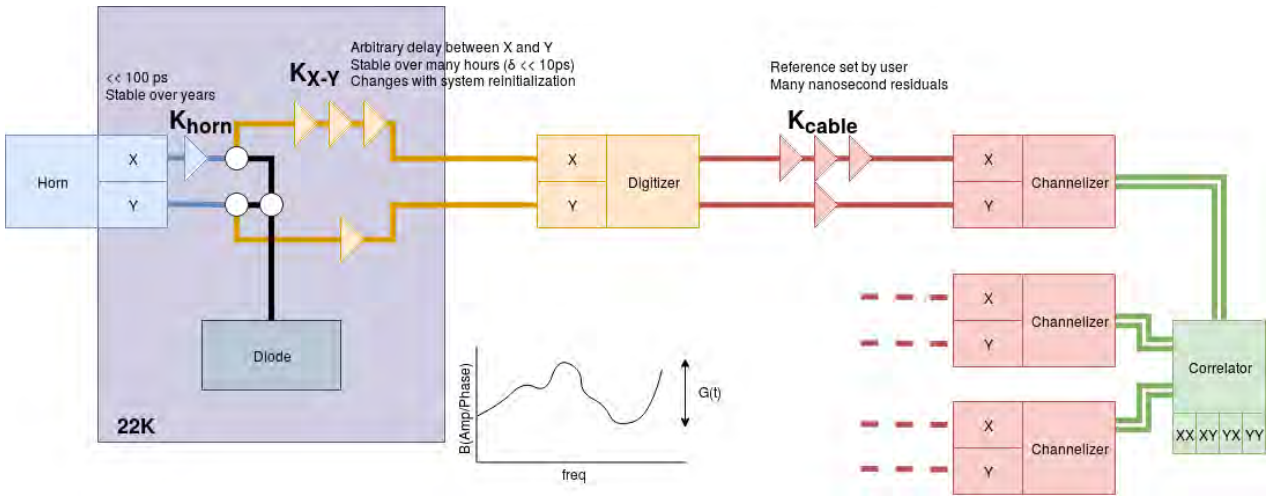

Figure 1.1: Simplified block diagram indicating MeerKAT signal chain for its L-band receiver system. Various calibration errors within the chain are illustrated: the crosshand (x-y) phase difference is primarily caused by a signal chain delay between the two digitized streams, with a minor contribution from the optical path in the horn. The path length between the receiver and digitizer is designed to be as short as possible to reduce the effect of standing waves on the bandpass, thus the digitizers are located right behind each of the receiver systems. Each receiver contains a noise source that is contained within the temperature stabilized receiver enclosure. It is coupled in to the signal path by quarterwave coupler behind the ortho-mode transducer.

The "x-y" phase difference between the orthogonal feeds are then removed using a calibrator with enough power on the off-diagonal ("crosshands" XY, YX) to solve for a slope and offset in phase. One way of achieving this (as implemented in CASA [104]) is by phase referencing the solutions of all antennas to an observer-chosen reference antenna. The normal cable delays and phase offsets brings the horizontal and vertical phases of the orthogonal feeds into alignment across the entire array with a global offset between X and Y. The residual "x-y" phase difference on the reference antenna must then be solved for using a source which illuminates the orthogonal dipoles with apriori-known fractional power. Here a highly polarized source such as 3C286 or 3C138 is used. It is noted that this does not set the absolute angle on linear system, which is still subject to receiver/dipole rotation, antenna tilt and ionospheric offsets. We will deal with polarimetry and absolute on-sky alignment of the MeerKAT feeds more thoroughly in Chapter 2.

Finally, the leakages are removed by again observing an unpolarized source. In both the cases of the diagonal and off-diagonal terms we solve for time variable solutions with the available bandwidth at 30s intervals before solving for frequency dependent solutions over the entire observation.

The calibration routine is implemented using primarily CASA [104] v.4.7 and the SARAO in-house TRICOLOUR [72]

[2] RFI flagging software. The routine is pipelined using our in-house STIMELA [100] [3] containerization framework. We perform two rounds of diagonal calibration and flagging before polarimetric calibration solutions are derived. The approach here is implemented in the VERMEERKAT reduction framework, see Chapter 3.

1.3 Field distribution modeling error effects on transfer calibration error

It is common practice to assume a single compact component with known flux to model both primary and secondary calibrator fields. However, in practice MeerKAT is sensitive enough to detect emission below the 1% flux level of a standard 10-20 Jy primary calibrator in under 10 minutes at 26 kHz spectral resolution [4]. These are fairly typical primary calibration scan lengths for the telescope.

Most of the primary calibrator fields have neighbouring sources well within the FWHM of the far field response at these levels. Depending on averaging time and array layout the error introduced by this lack of modeling accuracy can lead to noticeable ripples on the bandpass solutions. This effect is illustrated using a simple example.

Consider the analytical expression of the Fourier transform of two unresolved point sources. One source is at phase center, the other at some coordinate $(x_1, 0)$ on the celestial sphere, but well-within the primary beam of the antennas. The two sources have modulated flux densities S_0 and S_1 Jy respectively:

$$
\begin{aligned}
V(u(t,\nu),v(t,\nu)) &= S_0 + S_1 e^{-2\pi j(ux_1)} \\
&\Longrightarrow \\
|V(u(t,\nu),v(t,\nu))|^2 &= S_0^2 + S_1^2 + 2S_0^2 S_1^2 \cos(2\pi x_1 u(t,\nu)) \\
\arg(V(u(t,\nu),v(t,\nu))) &\approx \tan^{-1}\left(\frac{S_1 \sin(-2\pi x_1 u(t,\nu))}{S_0}\right) \\
&(S_0 \gg S_1)
\end{aligned}
$$

This periodic variation ("ripple") is hour angle and frequency dependent. It has a period that increases with increasing baseline length and the source distance from phase center. The frequency structure of the ripple is thus very sensitive to the sky projection onto the array spacings, and hence elevation dependent. A full discussion can be found in co-authored paper [67]. At UHF frequencies we find fractional off-axis contributions at levels between $\sim 20-50\%$ for the first half of the bandwidth, of which the first $\sim$ 100 MHz is substantially affected. We construct a model of the AGN population by Cleanmasking and deconvolving deeply the field surrounding PKS B1934-638 (after careful self-calibration). We simulate the visibilities correspond to the field down to 10s of mJy without noise to illustrate the effect of these projection-dependent ripples on visibility phases and amplitudes for various baseline lengths. The x-axis is coarsely channelized to the full 544 MHz fractional bandwidth. See Fig. 1.2. We also verified that the ripples in frequency and time illustrated here correspond, to a high degree, to the ripple structure seen from real UHF observation using a selection of baselines.

The (noiseless) simulated data was then calibrated against the [Reynolds 134] model without the field structure included as per the standard point source calibration assumption of the CASA [104] `setjy` and `bandpass` combination regularly employed in calibration pipelines. We varied the solution interval and imposed baseline length cuts, as indicated in the legend, and found that only the large-scale ripple structure noticeably washed out to any extent, with the high frequency

[2] Available at `https://github.com/ratt-ru/tricolour.git`
[3] Available at `https://github.com/ratt-ru/stimela.git`
[4] Assuming a SEFD of 425 Jy employing both orthogonal feeds

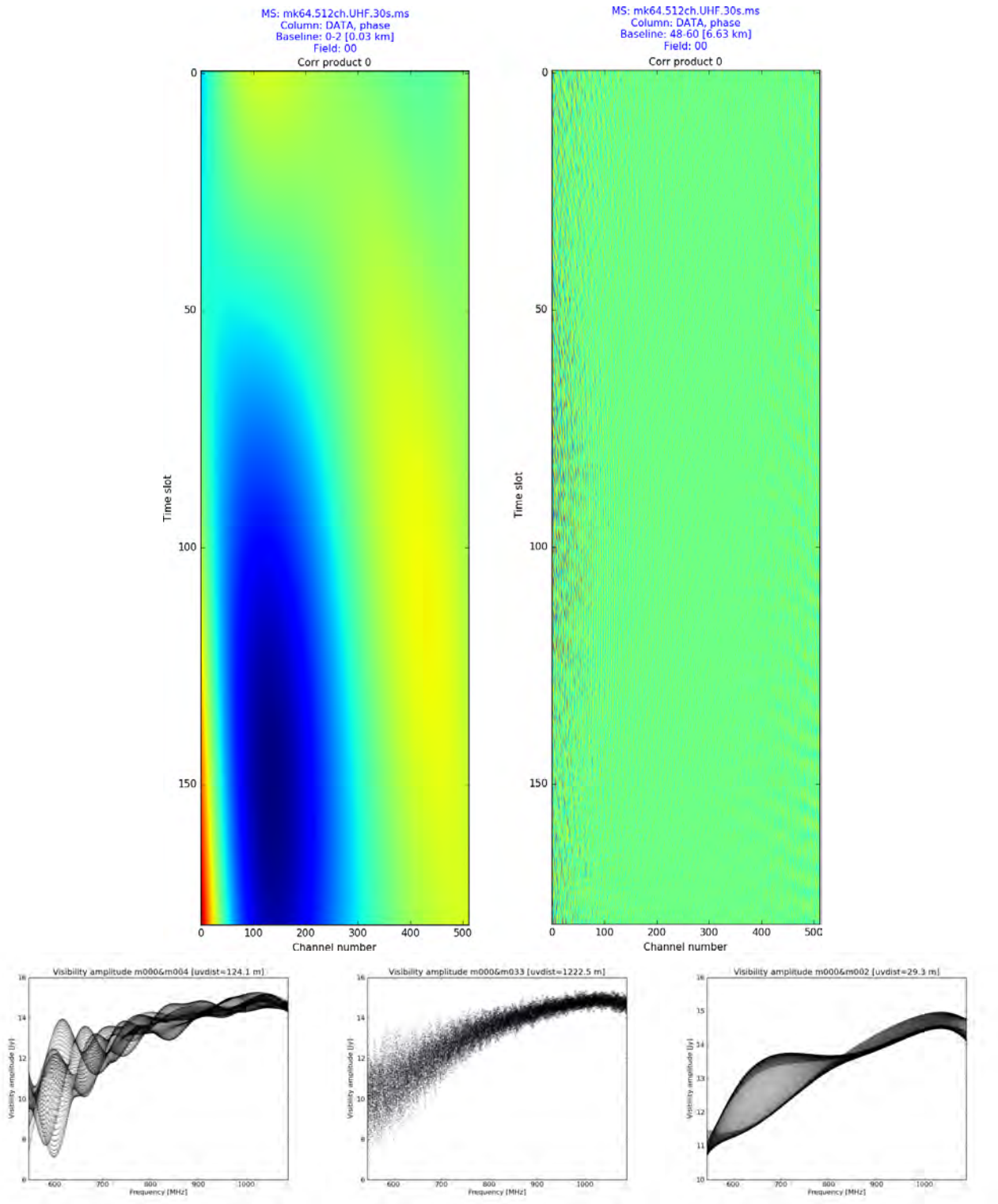

Figure 1.2: Top: Effects of off-axis sources on visibility phases on 0.03 km (left) and 6.63 km (right) baselines. Due to the GPS turnover of B1934-638 substantial phase variations are noticed on the lower frequencies of the band. The effects are most pronounced on short spacings indicating that the phase is dually contributed by well-resolved sources and the lack of fringe washing on these spacings. Blue to red scale corresponding to the range [-180, +180) degrees in visibility phase. Bottom: Effects of off-axis sources on visibility amplitudes as a function of baseline length from 0.124, 1.22, 0.029 km left to right respectively. Multiple time slots are overplotted to illustrate the time-variability of the visibility ripples.

ripples remaining at similar scales. We plot the channel-normalized bandpass solution to emphasize the relative scale of the induced ripple error. This is shown in Fig. 1.3.

For a compact core array such as MeerKAT this ripple does not diminish significantly with longer solution integration times for sources that are in close vicinity (few arcminutes) to the calibrator source.

Similarly, to show the full effect of neglecting a full sky model in the calibration of PKS B0407-65 on finely channelized MeerKAT data, we simulate a beam-attenuated source catalog without noise into a 26 kHz channelized 1.5 hour measurement set of PKS B0407-65 near transit using SIMMS[5] and MEQTREES [109]. The simulated data is then calibrated with a model that lacks the neighbouring sources of PKS B0407-65, at intervals of increasing length with the standard CASA [104] `bandpass` task. The resulting ripples for the H feed of antenna M032 are shown in Fig. 1.4.

At 26kHz 20 hours on a local target results in a core tapered channel RMS sensitivity of 63 μJy beam^{-1} when imaged. The induced subtraction error on the the relatively ubiquitous ~ 100 mJy beam^{-1}[6] L-band AGN population [e.g. 32] could be mistaken for real line emission when considering performing subband targetted searches for line emission: as shown, the induced ripples have scales comparable to the HI line widths of low-inclination slightly resolved galaxies.

Luckily the solution to this problem is relatively straightforward: including a full model of the sky distribution around the primary calibrator during calibration of the system bandpass will largely eliminate this source of error.

1.4 Observation and method

Observation information on the target calibrator field is summarized in Table 1.1. Each of the L-band observations contain at least a single scan PKS B1934-638, 3C286 and PKS B0407-65. These measurements were taken during construction of the telescope, where technical issues were still present. As such the number of antennas available for measurement varies from as little as 4 to the full 64 complement and the flag percentages are typically higher than what is generally achievable in current observations. We have indicated the antenna hours on target for reference.

As these observations were taken during early commissioning stages, we very conservatively flagged the calibrator scans to ensure corrected data phases less than 20 degrees across the band on both orthogonal modes on all fields. This often necessitated excision of one or more antennas due to significant baseline calibration errors at the time the data was taken. We also flagged all cases where one or more antennas stopped tracking or there were drops in measured power for other instrumental reasons. This is reflected in the substantial flagging percentages indicated in Table 1.1. The contribution from RFI to the indicated percentages is typically dominated by Global Navigation Satellite Systems ("GNSS") bands in L-Band, and the 870-890 Global System for Mobile communication ("GSM") downlink band affecting the lower and upper ends of L-Band and UHF bands respectively. We completely excised these bands from our polarimetric measurements.

The alt-azimuth mounted MeerKAT antennas add the additional complexity that the crosshand correlation products of a linearly polarized source does not always contain enough power to calibrate for the crosshand phase terms in Eqn. 1.1. Most observations listed in Table 1.1 had multiple scans where the parallactic angle-rotated U_Φ was close to 0. These scans were excised by inspection prior to calibration.

The Gigahertz-Peaked source PKS B1934-638, is co-observed for every dataset selected for this study. The source spectum inverts within the MeerKAT L-Band (Fig. 1.5) and covers the effective bandwidths of all three MeerKAT receiver systems at adequate flux density: the source has been stable in past observations [134].

[5] Available from `https://github.com/SpheMakh/simms`

[6] Assuming a wide range of possible MeerKAT synthesized beam widths ranging from a few arcseconds to several arcminutes depending on common choice of weighting and tapering

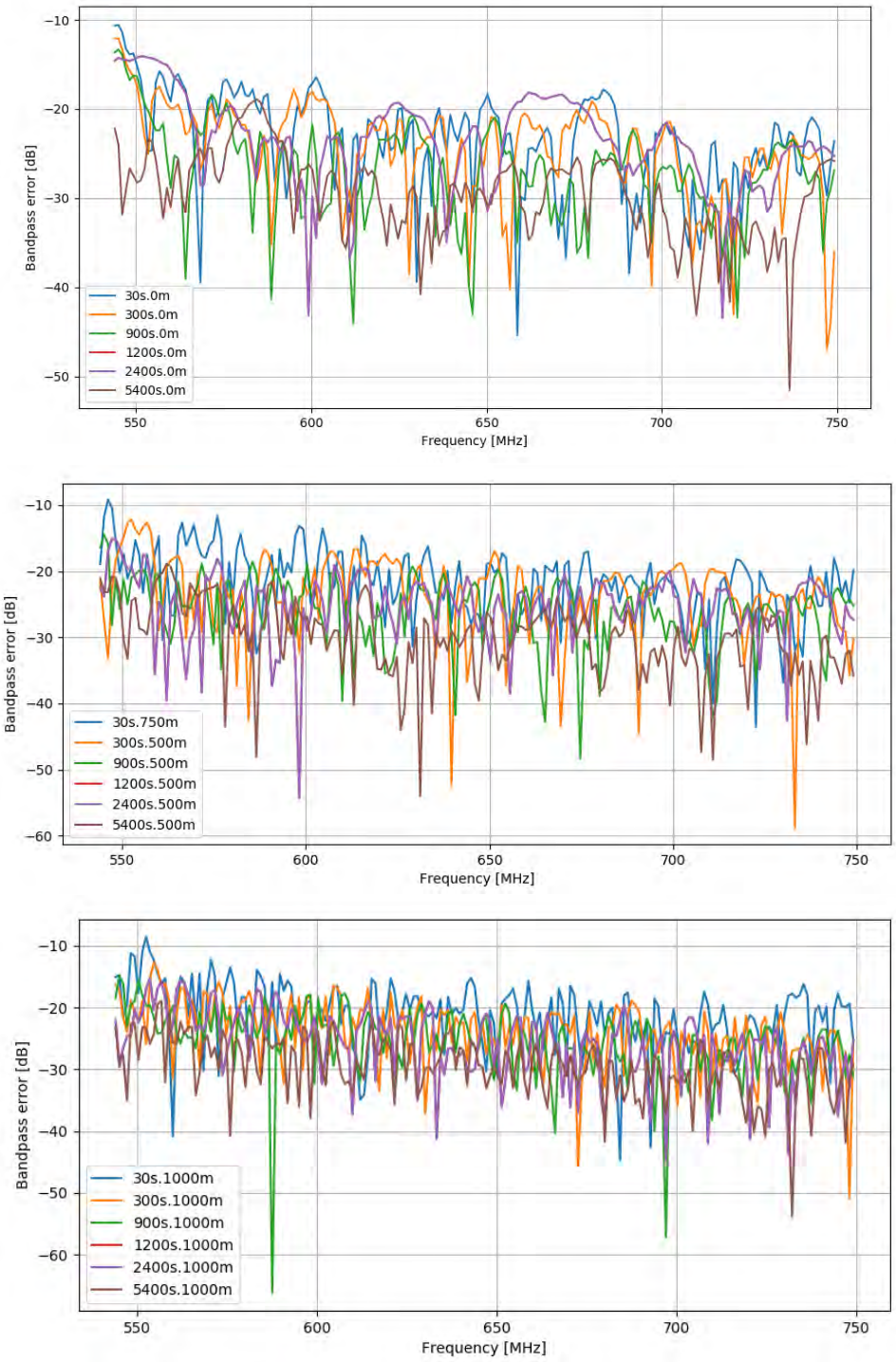

Figure 1.3: Amplitude gain absorbed ripples as a function of frequency for various baseline length cuts and solution intervals, for an arbitrarily chosen antenna. Neither longer solution intervals, nor stringent uv cutoffs have any noticeable effects on the peak error, aside from changing the length scales of the absorbed ripples.

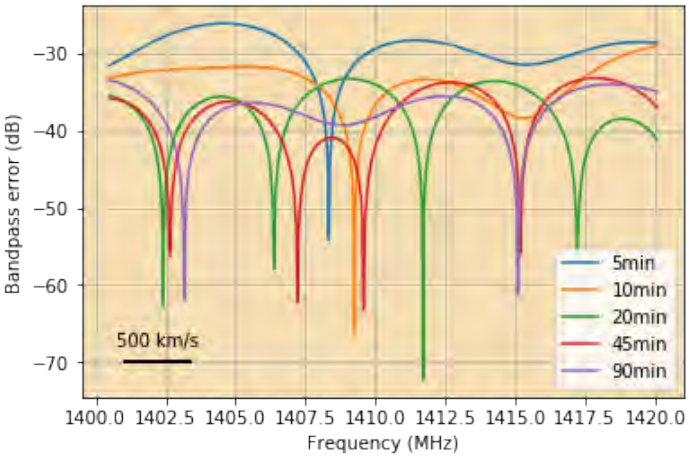

Figure 1.4: Induced bandpass errors resulting from a lack of accounting for neighbouring sources in PKS B0407-65. Solution intervals of increasing intervals are shown. As expected calibration error diminishes slightly with longer solution intervals due to fringe washing on the longer spacings. The error for a short interval is comparable to the level of the unmodelled field sources. A scalebar indicating maximum reasonable line widths for low inclination galaxies is shown for reference. Due to the proximity of the brightest off-axis source the error diminishes very slowly with integration time.

Table 1.1: Target observation information for calibrator field PKS B0407-65. Where applicable, multiple consecutive observations were combined.

	Observation information					
Epoch	obs. id(s)	Elevation	Antenna hours	Wall time	flag %	Band
2017/04/13	1492094204	20 – 53°	92:04:04	5:45:15	82.942	L
2017/04/21	1492794322	21 – 38°	44:01:01	2:45:04	86.876	L
2017/05/01	1493665209	20 – 23°	2:37:48	0:09:52	86.105	L
2017/06/23	1498145355	20 – 43°	17:30:45	1:56:45	97.928	L
2017/07/23	1500817620	21 – 21°	0:52:47	0:04:48	93.678	L
2017/07/25	1501002360	20 – 45°	17:42:13	1:46:13	89.612	L
2017/09/08	1504941644	17 – 42°	47:52:23	2:59:31	63.477	L
2017/09/24	1506241357	16 – 29°	17:16:22	1:04:46	73.441	L
2017/09/26	1506418083	17 – 22°	5:22:00	0:20:07	50.527	L
2017/10/26	1509002001	18 – 23°	4:36:09	0:19:43	67.549	L
2017/11/18	1511048006	18 – 54°	99:56:24	6:14:46	67.062	L
2017/12/29	1514570504, 1514902845	37 – 54°	52:57:19	3:18:35	81.761	L
2018/03/04	1520185226	16 – 52°	41:15:45	5:09:28	94.05	L
2018/04/07	1523128805, 1523101227, 1523102687	21 – 55°	226:41:03	4:55:40	77.798	L
2018/05/29	1527617191	16 – 17°	5:16:40	0:11:44	93.318	L
2018/05/30	1527694287	16 – 32°	44:02:05	1:34:22	87.961	L
2018/09/04	1536060219	16 – 22°	11:50:06	0:14:48	97.669	L
2019/03/02	1551564570	21 – 27°	54:07:34	0:55:03	80.023	L
2019/09/22	1569150359	20 – 55°	184:25:36	7:01:54	62.100	UHF

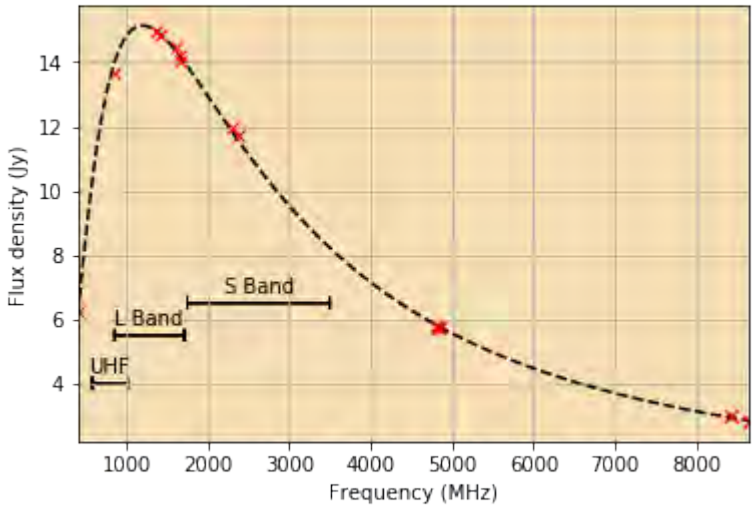

Figure 1.5: [Reynolds 134] spectral model of PKS B1934-638. The effective bandwidths of the 3 MeerKAT receivers are plotted in scalebars. The various ATCA, Parkes, Molonglo and MOST observations for this fit are shown with red crosses.

1.5 Results and discussion

Our campaign aims to establish both the long term stability of the calibrator source, a spectral model for the calibrator, a model of the surrounding field sources to reduce their impact on calibration (as discussed in Section 1.3) and the polarimetric properties of the calibrator itself. We will deal with each of these in turn.

1.5.1 Derivation of sky models

The derivation of the sky models at L-band is not excessively complicated, due to the off-axis sources contributing at maximum 5% of the total field flux within this band at the top end of the band. We followed the standard self-calibration procedure — a model is constructed within an automask that masks out residual calibration correlation with the PSF that primarily affects the calibrator itself. The phase is then adjusted through delay and phase solutions until a final bandpass correction can be applied on a deeply cleaned model to minimize systemically biasing the flux scale. All imaging is performed in the apparent scale with WSCLEAN [112].

At UHF the situation is more complicated — here the off-axis emission is much more pronounced, see Table 1.2. As already alluded to the off-axis flux density contributions to the average field flux are not hour angle-dependent and by bootstrapping the initial flux scale from a point source [Reynolds 134] model the flux scale of all the sources, on and off-axis, is already biased. We provide a smooth fit to the spectrum of PKS B1934-638 itself from long tracks at L and UHF bands and compare this to the [Reynolds 134] coefficients in Fig 1.6.

After self-calibration to include the additional components and adjustment we have no significant relative departure in scale of the flux of the calibrator itself — as defined by [Reynolds 134]. However, as far as we know the absolute error of the [Reynolds 134] scale is not well quantified in the literature at these low frequencies. This makes a comparison to observations calibrated to the scale of [Perley & Butler 130] hard because the absolute flux scale errors are unknown. We used this opportunity to quantify the error in absolute flux scale by solution transfer onto J1331+3030 (3C286) and comparison to the flux scale quoted in [Perley & Butler 130]. The absolute error in the flux scale is roughly 3% at the highest frequencies and up to 7% at the lowest frequencies of the UHF band. The difference between the scales at 1.4GHz in L-band is about 2.2%, as taken from our long-term co-observation of the sources.

If we augment the observations taken here with those taken for our characterization of 3C286 in Chapter 2 (see Table 2.1),

Table 1.2: The contribution of field sources to the total visibility flux for frequencies spanning UHF to L-band, within a 6 sigma mask.

PKS B1934-638 field sources contribution

Frequency	Calibrator Peak	RMS noise	Field sources contribution to total field flux
MHz	Jy	mJy / beam	%
569	10.33	0.061	52.7
618	10.97	0.058	46.9
668	11.73	0.046	40.0
717	12.34	0.062	34.3
766	12.87	0.057	28.9
816	13.32	0.052	24.4
865	13.61	0.055	20.5
915	13.80	0.090	17.1
964	14.10	0.057	14.4
973	14.75	0.013	15.1
1050	14.97	0.012	13.4
1128	15.09	0.013	11.4
1206	15.13	0.043	9.2
1283	15.08	0.021	7.9
1361	14.98	0.009	7.2
1439	14.83	0.009	6.6
1517	14.65	0.014	6.1
1594	14.45	0.023	5.8
1673	14.25	0.018	5.4

then the error between the two scales remains comparable at this level, with gain variations at 2-3% level across most observations. The analysis also extends to the S-band (up to 3.5 GHz). There are indications that the curvature terms on the [Reynolds 134] scale are slightly wrong at frequencies below 1 GHz and above 2.25 GHz (to 7-8% level). See Fig. 1.7.

PKS B1934-638 is unresolved by MeerKAT and is an ideal flux density calibrator. After deriving a full model of this source we perform a bandpass calibration which sets the effective flux density of the target field PKS B0407-65. The accuracy of the latter is, therefore, tied to the accuracy of the [Reynolds 134] model.

Both catalogs have fitted components of the following polynomial spectral index convention[7]:

$$I(\nu) = I(\nu_0) + \sum_{i \geq 0} c_i (\nu/\nu_0 - 1)^{i+1}$$

where the flux at the specified reference frequency $I(\nu_0)$ and polynomial coefficients c_i are stored. We choose not to fit a logarithmic polynomial here, because the fluxes of the off-axis components are left attenuated by the primary beam and show strong frequency-dependent curvature effects as a result — in practice these are best modelled with a standard polynomial. It also means that these models should only be used with the homogeneous 13.5 m dish interferometer layout and will need to be rederived for the planned MeerKAT extension project.

The component list for PKS B1934-638 contains over 7000 delta scale components at robust factor -2 (approx. uniform weighted). The synthesized beam is $5.81'' \times 5.38''$. The model has been derived to a detection limit of 7 sigma level (RMS noise 25 μJy beam^{-1}) at the highest available spatial resolution to CLEAN. This is a Multi-Frequency Synthesis peak-to-noise ratio of about $\sim 5 \times 10^5$. We do note that the noise immediately next to the calibrator itself is much higher than the noise floor used for the signal-to-noise ratio. These are similar to errors seen in L-band, those stemming mostly from second order leakage effects, as we will show later. It may also be contributed to by source smearing due to Ionospheric path delays between the antennas in the case of UHF. The L-band image was synthesized using observations 1523128805,

[7]Data format is documented here: `https://sourceforge.net/p/wsclean/wiki/ComponentList/`

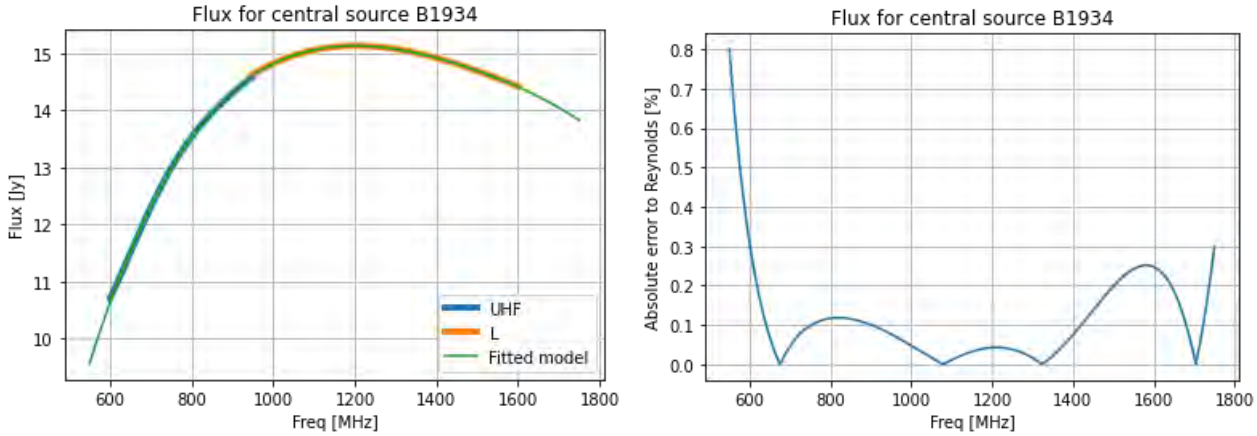

Figure 1.6: Model of the central component of UHF and L band all-sky models (without the contribution of off-axis sources) to compare the flux accuracy of the all-sky model to the original model used to calibrate the data. We note that the flux error is lower than 0.2% across most of the usable band.

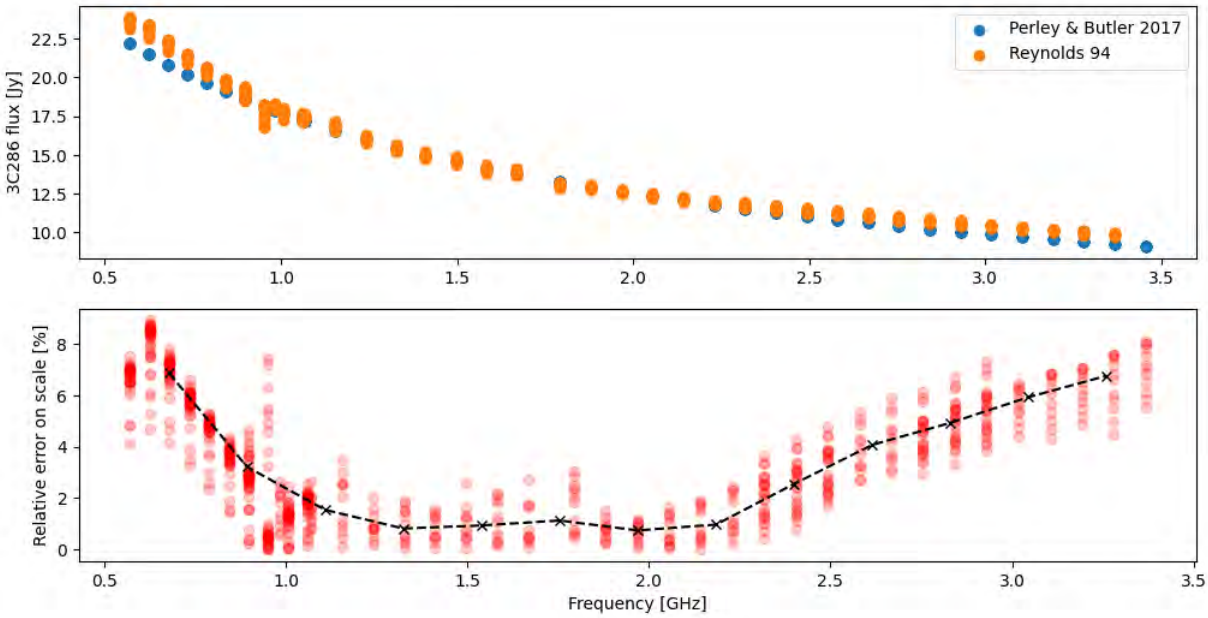

Figure 1.7: Absolute error between the scales of [Perley & Butler 130] of Northern hemisphere calibrator sources and [Reynolds 134] for the scale used at AT Compact Array and MeerKAT. We transfer calibrate the stable quasar 3C286 using the GPS source PKS B1934-638 and compare the measured flux scale to that presented in [Perley & Butler 130]. This complements the flux scale error analysis of [122] at higher frequencies. We plot the median-filtered error as a dashed black line.

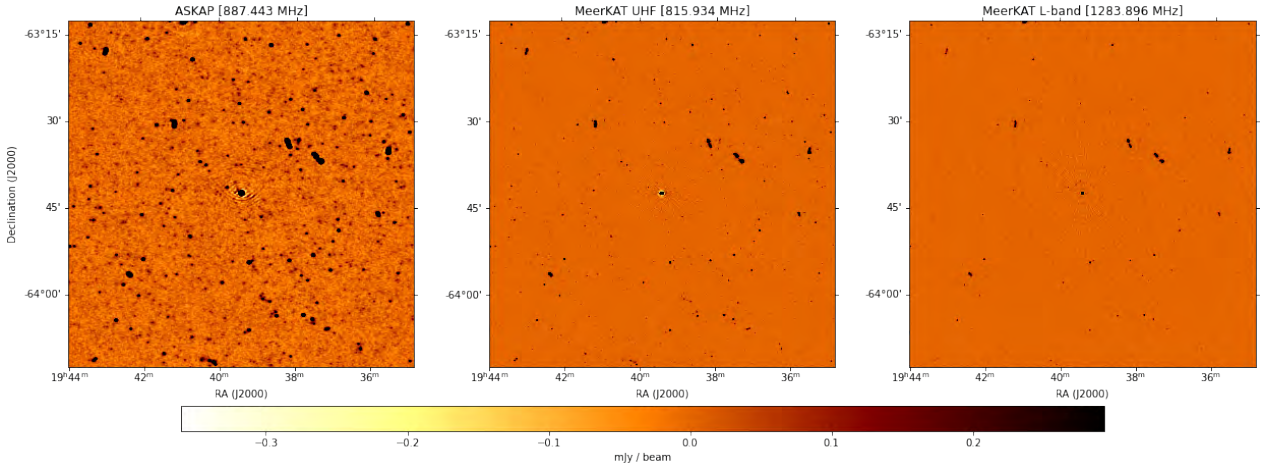

Figure 1.8: Three way comparison between ASKAP 887 MHz (left), MeerKAT UHF Band 816 MHz (middle) and MeerKAT L-Band 1284 MHz (right). Images locked to the same minima and maxima for comparison. The slight extension seen in MeerKAT UHF band is likely Ionospheric smearing or an imaging artefact. Overall the morphologies and astrometry are well matched.

1523101227, 1523102687 (2018/04/07). The extracted model was again constructed down to a local noise detection threshold of 7 sigma (RMS noise 22.5 μJy beam^{-1}). The synthesized beam is $4.068'' \times 3.34''$ at robust -2 weighting. The peak to noise ratio of this map 0.66m:1. The apparent scale MeerKAT images are compared to the central region of an ASKAP apparent scale image[8], with a resolution of $17.7'' \times 14.5''$ and RMS noise of 24 μJy beam^{-1}, in Fig. 1.8.

Using PYBDSF [107] ASKAP and MeerKAT sources positions are fitted and then crossmatched. We find a systematic offset in the UHF positions of about $2''$ at the 25% percentile. The median is plotted in dashed lines. This is indicated in Fig. 1.9 and seems to indicate a systematic error. The final UHF catalog is corrected by the offset from the MeerKAT L-band catalog, as the MeerKAT L-band and ASKAP catalogs are closely matched in astrometry.

It is stressed that, at present, no definitive root cause for the astrometrical error has been established. As this astrometrical error seems to be frequency dependent we strongly suspect that it could be smearing due to differential ionospheric effects (inversely proportional to frequency squared, ν^2). We computed the absolute Total Electron Content (TEC) for the duration of the observation using `ALBUS` which shows strong diurnal variation between 2.3 to 19.5 TECU towards PKS B1934-638. The delay, in meters, induced by a screen of electrons, in the first order, is given as

$$\tau_{\text{iono}} \approx \frac{40.3 \times 10^{16} \Delta\text{STEC}}{\nu^2} \tag{1.3}$$

As interferometer phases (and the positions derived from them) are sensitive to the path length difference of the radiation propagation, the effect on the astrometry of the system stems not from the absolute total electron content, but from the differential electron content seen between different stations / antennas in the array. This is in contrast to the Faraday Rotation induced by the ionosphere, more fully discussed in Chapter 2. It is not uncommon for these differential TEC to be on the order of 0.3 TECU[9] between stations separated up to 50 km [44]. At UHF frequencies, for an array with baselines up to 7.6 km, astrometric errors of $2''$ is plausible at a centre frequency of $\sim$ 816 MHz. At L-band frequencies this effect is sub-arcsecond.

We find most of the calibration error at L-band stems from second order leakage effects — this is in contrast to our suspicions noted in the reduction process of "Modelling of primary calibrator J0825-5010 and incorporation into telescope phase-up" (MeerKAT memo M2600-0000-028). We have applied second order leakage corrections through CUBICAL

[8] Contributed by Emil Lenc, CSIRO
[9] 1 TECU = 10^{16} el.m^{-2}

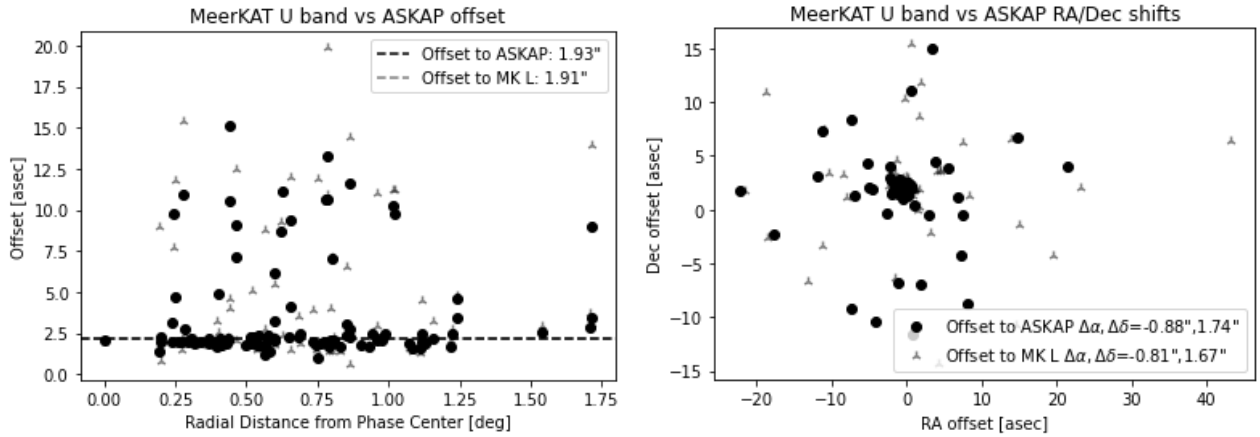

Figure 1.9: ASKAP and MeerKAT nearest neighbour positional crossmatch using positions fitted with PYBDSF [107]. The negatives of the indicated offsets are added to the final catalog to correct for the apparent shift in astrometry in the UHF band

[87] 2x2 Jones solutions per channel, at the same sub-minute solution interval cadences as with CASA, and obtained dynamic ranges of 0.5m:1 in L-band immediately next to the calibrator itself. This shows that HDR calibration and imaging cannot viably be achieved using CASA [104] at the same model fidelity at the time of writing, as the linearized equations implemented in it do not account for second order leakages (see [62] for the linearized equations without second order effects). The differences in CASA self-calibration compared to self-calibration using CUBICAL 2x2 solutions are shown in Fig. 1.10 on the same scales. This has significant implications for e.g. cluster sciences where high dynamic range imaging is important to overcome sidelobe contamination from cluster AGN on surrounding diffuse emission.

We then used the derived full model for PKS B1934-638 to calibrate the transferred bandpass applied to the co-observed PKS B0407-65, while refining the phase using the known position of the latter. We repeated careful self-calibration of the latter to make models at L-band and UHF frequencies. The imaging, both in UHF and L-band, required several rounds of phase and delay calibration with CUBICAL [87], clean masking with CLEANMASK[10] and Multi-Frequency Synthesis imaging using WSCLEAN [112]. We include components in our catalogues above 7 and 8 sigma[11] for L and UHF bands respectively. From visual inspection the masking was found to be adequate to exclude residual calibration-error sidelobes from the calibrator source itself. As the UHF band calibration showed offsets with respect to both MeerKAT and ASKAP L-band images for PKS B1934-638 we also crossmatched the positions of the catalogs of PKS B0407-65. The offsets between the two bands were about 2 arcseconds and we adjusted the UHF positions to the higher resolution positions of the L-band observation. Our catalogues span radii of $1^\circ 49'$ and $2^\circ 20'$ in L and UHF bands respectively. We used uniform weighting to derive field models for both bands, achieving resolutions of $4.15'' \times 3.8''$ and $7.0'' \times 6.5''$ for L and UHF bands respectively.

For the higher Dynamic Range map shown in Fig. 1.11 we additionally applied per channel 2x2 solutions with CUBICAL [87] at high temporal cadence (12s) after averaging to a coarse 531.25kHz channel resolution — this removes second order leakages and residual temporal variability in the bandpass. After subtracting off the calibrator itself with a DFT we achieve a Dynamic Range (peak-to-noise) of 0.6m:1 immediately next to the calibrator and a DR from global noise of 4.2m:1. We indicate the fractional contribution of the field sources as a function of frequency in Table 1.3. It is noted that, since PKS B0407-65 is a steep spectrum source in our bands, it is not subject to as high a field flux contribution as PKS B1934-638 in UHF band. However, the contribution is still substantial enough to warrant inclusion of the off-axis sources to limit bandpass rippling at lower frequencies. **It is, therefore, recommended that the model in Eqn. 1.5 not**

[10] Available from `https://github.com/SpheMakh/cleanmask`

[11] Although we indicate sigma here the automasking tool splits the map into boxes to measure local RMS which, in this case, is highly dependent on distance from the calibrator source. The global RMS, as measured in the far-field sidelobes, is 35 μJy and 33 μJy for L and UHF bands respectively.

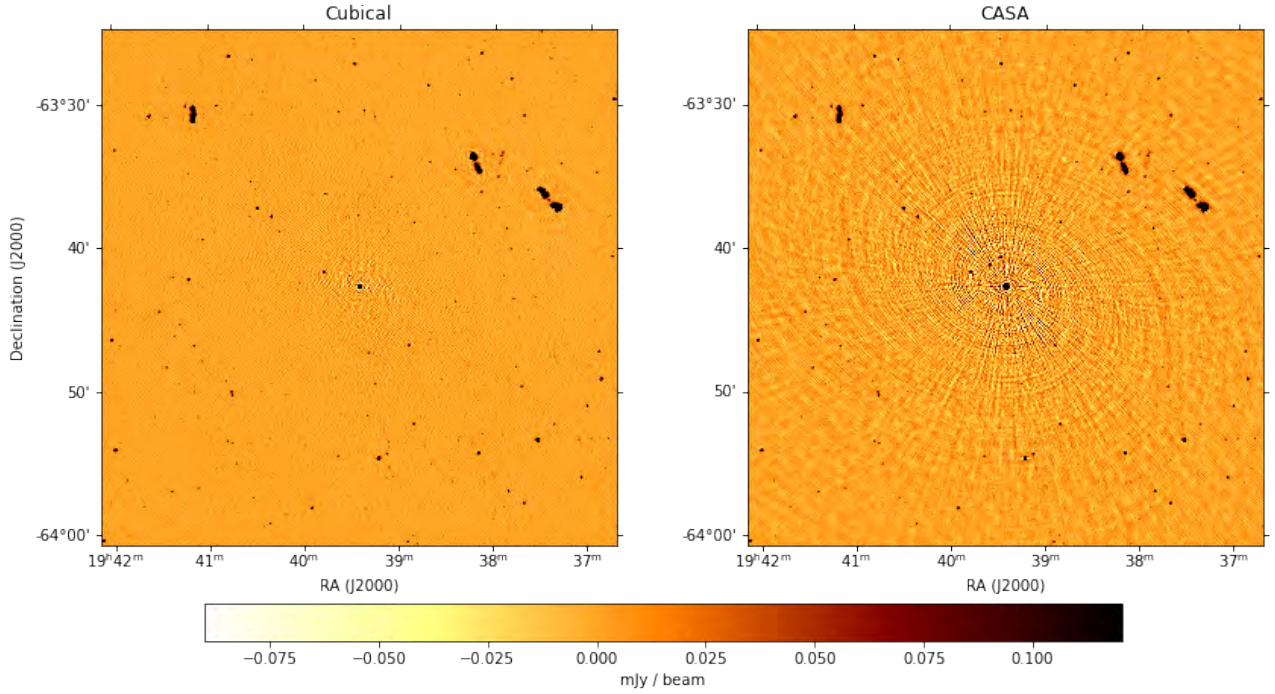

Figure 1.10: HDR image obtained by solving and applying 2x2 Jones solutions on this unpolarized field using CUBICAL [87] (left) after going as far as delay and amplitude self calibration using CASA [104] (right). Images locked to the same minima and maxima for comparison. The improvement is substantial compared to using the linearized form of the RIME implemented in CASA.

be used by itself in a standard single source model-setting step, especially at UHF frequencies. The component models accompanying this document can be predicted via DFT[12] prior to calibration.

In terms of the variability in these models it is important to note that the percentages quoted in Tables 1.2 and 1.3 are cumulative flux contributions from surrounding field sources. However, the strongest individual field source adjacent to the calibrators does not exceed $\sim 3\%$ (in the beam-attenuated apparent scale of the models). As a result we do not expect significant variability in their contribution to the flux scale.

1.5.2 Adaptation for the MeerKAT Science Data Processor

The MeerKAT Science Data Processor (hereafter "SDP") is responsible for ingesting data from the correlator, generation of first look calibration and continuum and line imaging products, intended for quality assurance by the MeerKAT operations team, and storage of the collated data and first look products into the MeerKAT archive. The Science Data Processor is also responsible for initial delay and phase (or "phase-up") calibration. The former is executed for both imaging (product-correlated visibilities) and tied-array coherent beamforming, while the latter is only done when beamforming ("bc" correlator modes in the Operation Planning Tool). The latter also calibrates the bandpass response of the system.

This part of the calibration is done by special observations executed just after array resource (antennas, ingest machines, diagnostic machines, channelizer and correlator field programmable array boards, etc.) acquisition by the MeerKAT Control and Monitoring system. These observations consist of an initial short scan of a calibrator field, after which the system needs to RFI flag and derive reliable calibration solutions, which are applied to a second scan on the calibrator immediately after aquiring the first scan. The delay, phase and bandpass solutions are applied by the channelizer (refer back to Fig. 1.1) to subsequent-observed data, implying the second scan on the calibrator is a transfer-corrected

[12]Using Dask-based Crystalball package `https://github.com/caracal-pipeline/crystalball`

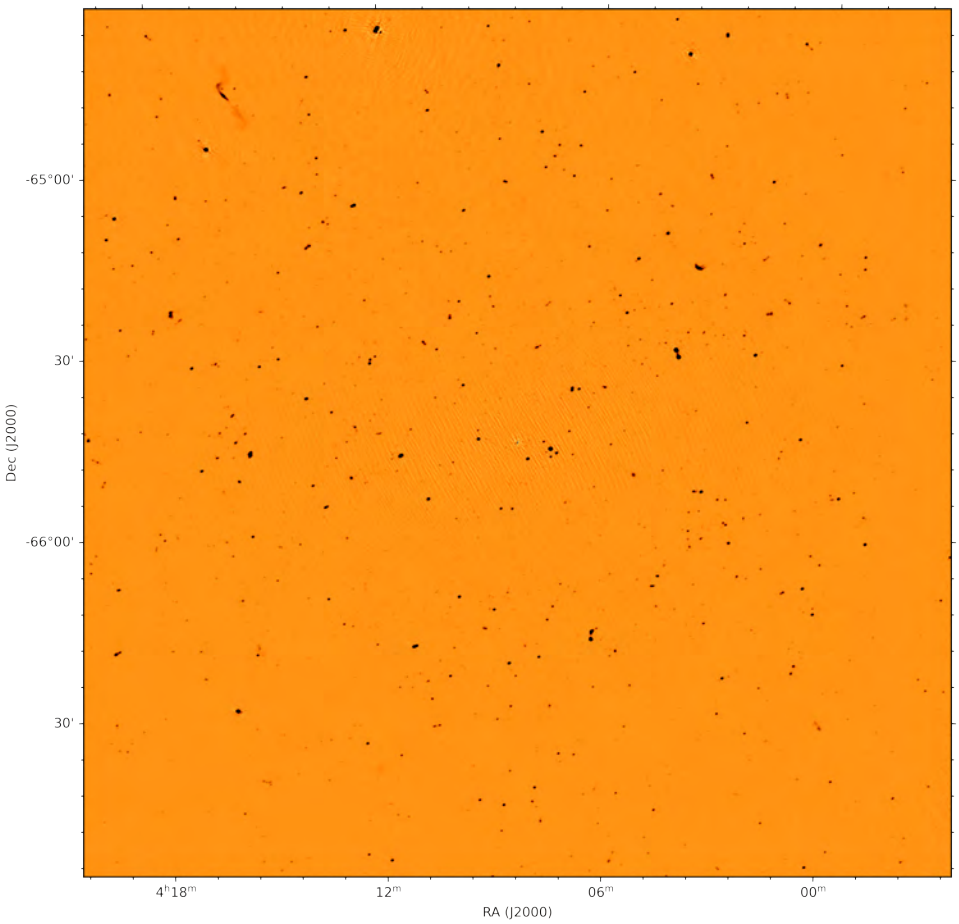

Figure 1.11: Field surrounding PKS B0407-65 as seen in UHF (not corrected for antenna far field attenuation). Here a resolution of $16.2'' \times 12.4''$ (robust 0) is achieved with a global RMS of 6.9 μJy beam^{-1} and RMS of 0.5 mJy beam^{-1} immediately next to the calibrator. Strong sources are visible to the north of the calibrator. The calibrator here is subtracted through a DFT.

Table 1.3: The contribution of field sources to the total visibility flux for frequencies spanning UHF to L-band, within an 8 sigma and 7 sigma mask respectively.

PKS B0407-65 field sources contribution

Frequency	Calibrator Peak	RMS noise	Field sources contribution to total field flux
MHz	Jy	mJy / beam	%
557	39.54	1.500	22.9
585	37.46	1.900	22.6
612	36.50	0.117	21.5
639	34.85	0.650	21.2
666	33.41	0.530	20.6
693	32.03	0.118	19.9
721	30.69	0.640	19.1
748	29.19	0.137	18.4
775	28.40	0.478	17.3
802	27.12	0.112	16.5
829	26.04	0.102	15.7
857	25.02	0.842	14.9
884	24.29	0.125	14.3
911	21.33	0.294	13.4
965	21.30	0.128	17.3
993	21.33	0.082	12.7
1020	20.69	0.220	12.4
1050	20.35	0.161	10.0
1128	18.88	0.100	8.9
1206	17.34	0.216	8.4
1284	16.19	0.136	8.1
1362	15.07	0.070	7.8
1439	14.20	0.065	7.4
1517	13.53	0.097	7.1
1595	12.51	0.131	6.8
1673	12.11	0.096	6.4

observation. The calibrator used is either PKS B1934-638, PKS B0407-65 or J0825-5010 (we discuss this in MeerKAT memo M2600-0000-028), depending on the LST range of the observation.

The phasing of the system is a very important step in the coherent tied-array beamforming mode, because the primary product (the tied-array filterbank), is a squared sum over all calibrated antenna voltages, and effectively discards the phase information. The initial SDP calibration, and (especially) phase stability, is therefore very important.[13]

$$p(t,\nu) = \left[\sum_{i \in \{\text{ant}\}} \bar{\mathbf{G}}_i(t,\nu) \left\langle \mathbf{G}_i(t,\nu)\mathbf{A}_i(l,m,\nu,t)V_i(t,\nu) \exp\left(-2j\pi \frac{w_i(n-1)}{\lambda}\right) \right\rangle \right]^2$$
$$\approx \left[\sum_{i \in \{\text{ant}\}} \bar{\mathbf{G}}_i(t,\nu)\mathbf{G}_i(t,\nu) \left\langle \mathbf{A}_i(l,m,\nu,t)V_i(t,\nu) \exp\left(-2j\pi \frac{w_i(n-1)}{\lambda}\right) \right\rangle \right]^2$$

Here p is the measured output power. The per antenna channelized X and Y feed complex voltage vector is given by V_i. These voltages are phased to a pulsar field of interest by a phasor, where w_i points towards the source and n is the sky-cosine of the field coordinate. This phasor is actively updated by the telescope Control and Monitoring system and smoothly applied in the correlator at sampling cadence. The complex voltage is attenuated by the antenna voltage beam term, $\mathbf{A}_i$. For the tied array beamformer provided by the SDP the pointing center co-incides with the phase stopping center where the coherent beam is formed. For the MeerTRAP [138] User Supplied Equipment multiple coherent beams are formed throughout the antenna main lobe. $\mathbf{G}_i$ represents the product of all time and frequency variable antenna gains, whereas $\bar{\mathbf{G}}_i$ denotes a slowly-variable approximate per-antenna corrective Jones matrix, solved for by the SDP. $<>$ denotes a time and frequency averaging interval. We again assume that the collated per antenna gain term $\mathbf{G}_i$ does not vary quicker than the integration interval. It is not possible to calibrate for per-antenna terms after this initial delay and phase calibration.

From a telescope operations perspective it is equally important that this calibration operation runs quickly, because it has to be launched prior to initiating science observation. Therefore, the SDP uses a truncated version of the models we derived, where the component list is truncated, as we will briefly now discuss. For the purposes of estimating the number of components to include in calibration we can assume that the VV and HH System Equivalent Flux Density is roughly equal. If a fractional wideband channel bandwidth of 132.8 kHz is assumed for UHF this places an effective bound on the calibration noise level of about 1.64 mJy beam^{-1}, 1.16 mJy beam^{-1} and 0.95 mJy beam^{-1} for calibrator scan lengths of 5, 10 and 15 minutes respectively. This assumes no tapering or removal of spacings during calibration. All sources at or above these levels must be accounted for during the bandpass calibration procedure in order not to bias the flux scale of the system – as mentioned before the first order terms are not hour angle dependent and are not washed out by fringe rotation.

The cumulative flux contribution as the number of sources is increased, with priority to brighter emission, is shown in Fig. 1.12. The flux calibration error may be quantified based on the implementation efficiency limitations of the DFT based Science Processor pipeline, currently 90 components for online calibration at the time of writing. Here we show the fractional contribution to the total flux above the estimated noise at the bottom of the band where the combination of steep inverted GPS spectrum of the calibrator and the wide primary beam maximizes off-axis contribution.

The majority of the off-axis apparent flux is dominated by the mJy-level AGN population in the field, as shown in Fig. 1.13 (to 95th percentile). This AGN population (much of which is well-resolved by the telescope) is responsible for the vast number of components needed to account for the cumulative flux shown above. Note that we refer to sources and components interchangeably for the intended purpose of this discussion.

In contrast to the constant average flux contribution of the off-axis sources, the phase spread of the solution-absorbed ripples is strongly dependent on the cumulative superpositions of the field source fringes. These fringes are hour angle dependent and are, therefore, subject to fringe washing. In worst case the fractional error in the argument from all sources

[13]This excludes the dedispersion delay terms added to the signal path to account for the dispersive path delays introduced by the interstellar medium and filterbank folding operations done by the beamforming system.

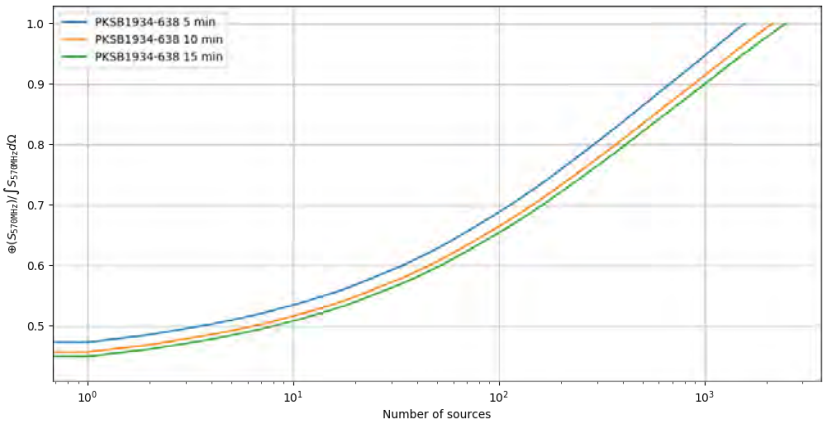

Figure 1.12: Cumulative fractional flux density (in the beam-attenuated / apparent scale) contribution as a function of number of sources at 570 MHz.

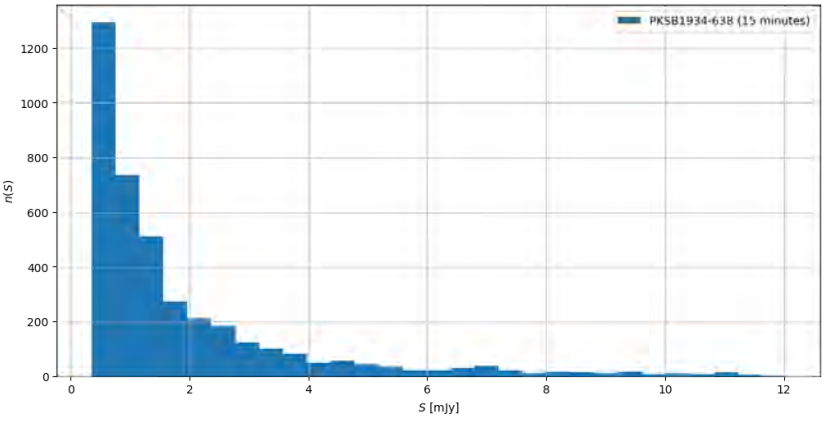

Figure 1.13: Distribution of flux densities of off-axis sources (up to 95th percentile) in the field of PKS B1934-638 at the UHF band. Many of the sources are resolved.

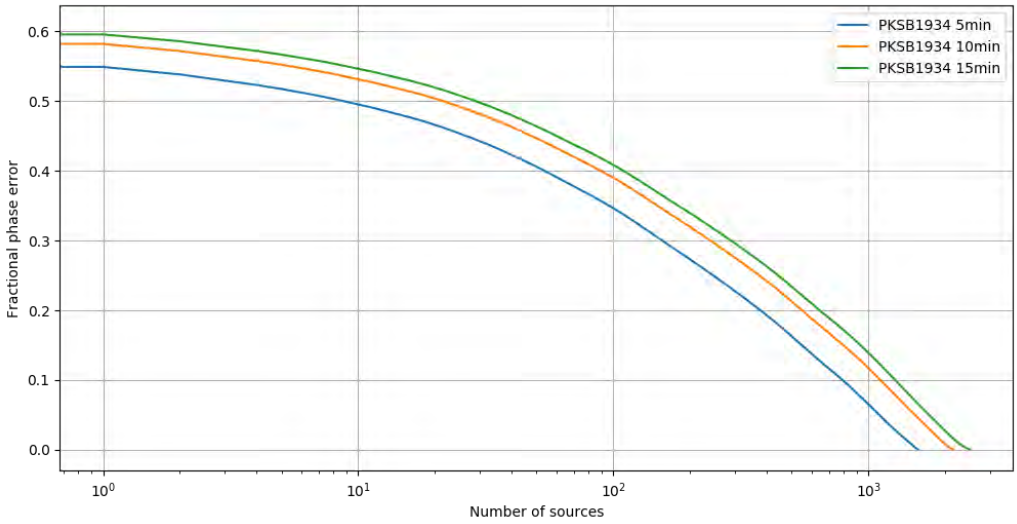

Figure 1.14: Fractional residual phase error as a function of number of included components in the PKS B1934-638 field at UHF frequencies.

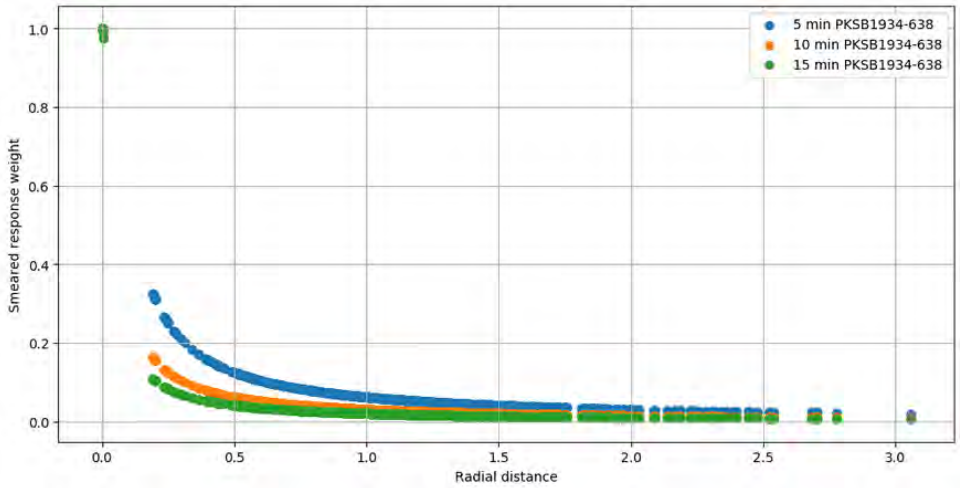

Figure 1.15: Estimated source smearing due to temporal fringe washing as a function of radius. 1.0 represents un-smeared sources.

above SEFD noise can be approximated as, where $\bigoplus$ is the prefix scan (or accumulator) operator:

$$1 - \frac{4}{\pi} \arctan\left(\frac{\bigoplus(S_i w_i)}{\sum_i S_i w_i}\right) \tag{1.4}$$

The w_i terms here are the time-average amplitude response of the source, which scales as the square of the source separation distance from the interferometer phase center. This means that the cumulative residual error is quickest minimized by including distance weighted flux contributions. This is shown in Fig. 1.14 and is computed from the rectangular window approximation to smearing (shown in Fig. 1.15 for the emission in this field) discussed in [154] — θ_b is the instrument resolution, r the separation cosine (approximated as radians in the small-angle approximation) and ω_e the sidereal rotation rate (rad s^{-1}):

$$w_i = 1.0645 \frac{\theta_b}{r\omega_e \Delta t} \text{erf}\left(0.8326 \frac{r\omega_e \Delta t}{\theta_b}\right)$$

The top 90 components contributing to the cumulative phase error, as defined in Eqn. 1.4, plus the calibrator itself are

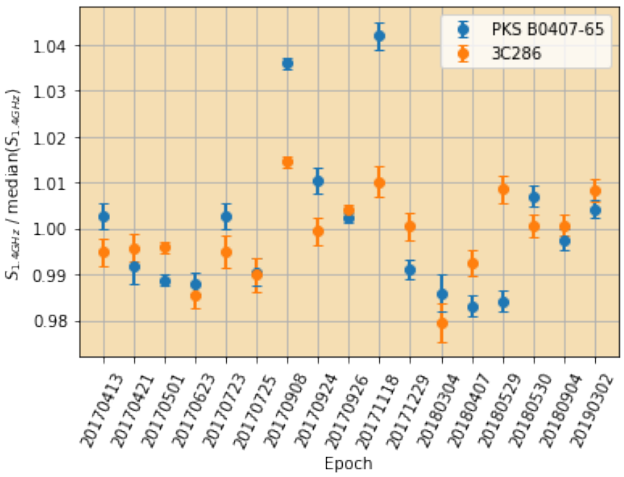

Figure 1.16: Stability of the 1.4GHz flux density of transfer calibrated PKS B0407-65 and 3C286 after derotation to the feed relative frame. Here the absolute deviation from the long term median is cross compared between two independent calibrator fields.

then selected for inclusion in the truncated models in use by the SDP.

1.5.3 Calibrator stability

The long-term stability of the primary calibrator is essential for accurate flux calibration. After excising the GNSS and GSM subbands from the L-band data we fitted a power law spectral index to the flux densities of PKS B0407-65 and 3C286 (after derotating the calibrated data into sky-relative frame). The deviation of the fitted 1.4 GHz Stokes I flux density from the median 1.4 GHz flux measurement is plotted in Fig. 1.16.

The comparison of transferred flux densities (calibrated with and transferred from PKS B1934-638) onto 3C286 and PKS B0407-65 establishes that there are no significant flares on PKS B0407-65 of more than 5% during the campaign. The typical spread is no more than about 3%. We confirmed that there are no definitive trends visible as a function of average elevation. The measured spread also establishes that all 3 calibrator sources are very stable. Furthermore, as we have already established that the absolute scale differences between [Reynolds 134] and [Perley & Butler 130] are on the order of between 3% at the highest frequencies in L-band and up to around 7% at the lowest frequencies in UHF. At 1.4GHz the scale difference is around 2.2%. This is indicated in light red in Fig. 1.17. We indicate the fitted spectra along with their errors from the long term monitoring program on Fig. 1.17. We derive a spectral fit, shown in dashed red line, from long duration observations taken 2018/04/07 (L-band) and 2019/09/22 (UHF band). The best fit (using the polynomial defined for WSClean-based models [112]) is as follows:

$$\begin{aligned} &16.53026775 - 18.45522606\left(\frac{\nu_{\mathrm{GHz}}}{1.2838} - 1\right) \\ &+ 21.4159342\left(\frac{\nu_{\mathrm{GHz}}}{1.2838} - 1\right)^2 - 24.54113514\left(\frac{\nu_{\mathrm{GHz}}}{1.2838} - 1\right)^3 \\ &+ 28.74718038\left(\frac{\nu_{\mathrm{GHz}}}{1.2838} - 1\right)^4 + 28.21201644\left(\frac{\nu_{\mathrm{GHz}}}{1.2838} - 1\right)^5 \end{aligned} \tag{1.5}$$

1.5.4 Polarization limits of PKS B0407-65

Finally, we characterize the calibrator source polarization. With a linear feed receiver system such as the MeerKAT L and UHF band systems it is important to characterize the fractional linear power of the calibrator source as this may influence calibration; per Eqn. 1.1 the parallel hand correlation products are sensitive to fractional linearly-polarized power. The

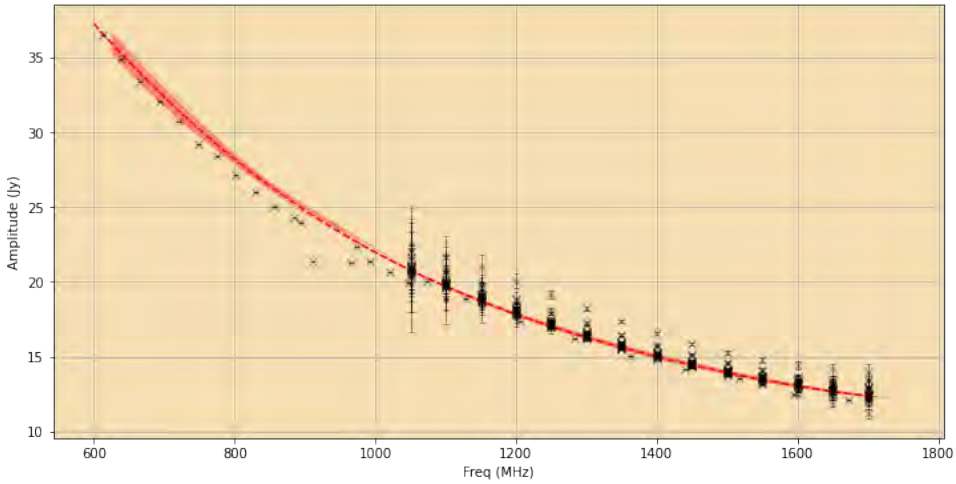

Figure 1.17: Long term flux scale measurements of PKS B0407-65 in, L (primarily) and UHF band. Fitted model for the calibrator is shown in dashed red line. We highlight the absolute transfer error of PKS B1934-638 [Reynolds 134] with respect to 3C286 [Perley & Butler 130] in light red as the scale of the absolute error assumed for this model.

parallel hand flux density of a source with non-zero fractional linear power is, in turn, time dependent due to sky rotation induced by the alt-az mounted antennas. If this fractional polarized power goes unmodelled during flux calibration the target fields have dynamic range limiting gain and polarimetric errors that can be as large as the fractional polarized power of the calibrator.

Throughout this section we adopt the convention for the polarized power of a power-law calibrator in complex form as follows:

$$P_{|} := \sqrt{Q^2 + U^2} e^{2iP_\theta(\lambda)} / I(\lambda) \tag{1.6}$$

where the linear angle is given by,

$$P_\theta := 0.5 \tan^{-1} \left(\frac{U(\lambda)}{Q(\lambda)} \right) \tag{1.7}$$

Similarly the fractional circular power is expressed as,

$$P_\circ := V(\lambda)/I(\lambda) \tag{1.8}$$

The intrinsic fractional linear power of a source is further subject to Faraday Rotation by the free-electron content (n_e) and parallel magnetic field strength ($H_{||}$) along the observer's line of sight to the source through the intergalactic medium according to a ν^{-2} law. Generally, the apparent fractional polarization tends to decrease with increasing wavelength according to the following model [28]:

$$P_{\text{apparent}} = \frac{\int_{\text{source}} P_{|} e^{2i\phi(\vec{s})\lambda^2} d\vec{s} d\Omega}{\int_{\text{source}} I(\lambda) d\vec{s} d\Omega}$$

where the Faraday Depth, ϕ is given as, in c.g.s. units are given as:

$$\phi(\vec{s}) = 2.62 \times 10^{-17} \int_{\text{source}}^{\text{observer}} n_e(\vec{s}) H_{||}(\vec{s}) d\vec{s}$$

These equations describe a depolarizing medium. For a foreground electron screen, and with sufficient spectral and spatial resolution, the intrinsic polarization of source with limited foreground flux along the line of sight can then be recovered

by derotation through Discrete Fourier Transform along the line of sight in λ^2 space [24]. With limited resolution and missing frequency coverage the telescope response to a polarized source at rotation measure $\phi(\vec{s})\lambda^2$ is described by the instrumental Rotation Measure Transfer Function (RMTF). [24] shows that the RMTF is given by a Fourier transform of a channel weight function,

$$R(\phi) = \frac{\int w(\lambda^2) e^{-2i\phi(\vec{s})\lambda^2} d\vec{s}}{\int w(\lambda^2) d\vec{s}} \tag{1.9}$$

For $\Delta\lambda \ll \lambda$ $P_{\text{apparent}} * R(\phi)$ can be approximated by DP^T_{apparent}:

$$(-0.5\phi_{\text{sup}}/\Delta\phi \leq x \leq 0.5\phi_{\text{sup}}/\Delta\phi)$$
$$D := e^{-2i(\Delta\phi x \otimes (\lambda^2)^T)}$$

$\Delta\phi$ is the sampling resolution in Faraday depth space given by Nyquist criterion:

$$\Delta\phi \leq \frac{1}{2\max(\Delta\lambda^2) N_{\text{chan}}}$$

and ϕ_{sup} is approximated as for finely channelized power measurements:

$$\phi_{\text{sup}} \approx \frac{\sqrt{3}}{\min \Delta\lambda^2}$$

Provided a high power SNR measurement can be made of the fractional linear power the polarization angle and fraction is then given by:

$$P_\theta = 0.5(\arg(P_{\text{apparent}}) - 2\lambda^2 \text{argmax}(P_{\text{apparent}} * R(\phi)))$$
$$P | e^{-2iP_\theta} = \max(P_{\text{apparent}} * R(\phi))$$

The measurements here are ultimately bound by residual calibration errors in leakage and crosshand phases, as well as the effects introduced by the ionosphere (discussed in more detail in Chapter 2). For the moment we are only interested in whether PKS B0407-65 is intrinsically polarized. Throughout the non-orthogonality of the horizontal and vertical feeds are calibrated with the unpolarized PKS B1934-638. The instrumental circular polarization (predominantly introduced by the x-y phase offset) is calibrated using 3C286 (a strong linearly polarized calibrator at roughly 9.5% fractional polarization and a polarization angle of $\approx 33^\circ$ if interpolated down from Mars-referenced observations made by [127]). Characterizing the accuracy of the latter at lower frequencies is left to Chapter 2.

Throughout the campaign we find that the off diagonal d terms of 1.2 are as high as -15dB for a significant portion of the array, but that the leakage is relatively stable (within a few dB) over a wide range of elevations during long tracks of PKS B1934-638. After leakage calibration we verify residual leakage by computing P_{quad} on PKS B1934-638 and assure that it is well below -20dB for all observations used in our measurement.

$$P_{\text{quad}} := \frac{Q^2 + U^2 + V^2}{I^2} \tag{1.10}$$

It is further necessary to verify the time stability of the leakage-corrected data and the residual instrumental circular polarization characteristics on a polarized source. We therefore derotate the visibilities into sky-relative frame and compare the cross hand products on 3C286. A well calibrated system (with calibrated data $\bar{V}_{\text{XX}}$, $\bar{V}_{\text{XY}}$, $\bar{V}_{\text{YX}}$ and $\bar{V}_{\text{YY}}$) will measure conjugate products on the two crosshand coherencies. Any potential offsets in these are indicative of crosshand

phase residuals or leakages. The relative error in amplitude between the crosshands gives a good indication of the residual leakage remaining after correction:

$$D_{\text{residual}} := \frac{||\bar{V}_{\text{XY}}| - |\bar{V}_{\text{YX}}||}{|\bar{V}_{\text{XY}}|} \tag{1.11}$$

Similarly, for a strong linearly polarized source the fractional power on the crosshand should be concentrated in the real part of the crosshand. The residual fractional instrumental circular polarization can then be estimated as:

$$\mathscr{V}_{\text{instrumental}} := \frac{|\Im \bar{V}_{\text{XY}}|}{|0.5(\bar{V}_{\text{XX}} + \bar{V}_{\text{YY}})|} \tag{1.12}$$

Ideally both ratios should be stable at levels significantly less than -20dB. The latter two quantities are used to estimate residual instrumental calibration error levels for the polarimetric measurements.

Fig. 1.18 (left) indicates the recovered fractional linear polarization for PKS B0407-65 and 3C286. Since our calibration procedure relies on a transfer flux scale independent of fractional polarization power we can estimate both the rotation measure and total linear power of 3C286. We also measure the circular polarization of PKS B0407-65, as indicated in Fig. 1.18 (right). There is no substantial evidence that this source is linearly or circularly polarized — we can only place upper bounds of $\leq 0.5\%$ linear polarization and $\leq 0.4\%$ circular polarization respectively. The linear polarization bound is marginally higher than derived by [131] and the non-detection of circular polarization is consistent with observations dating back as far as [91].

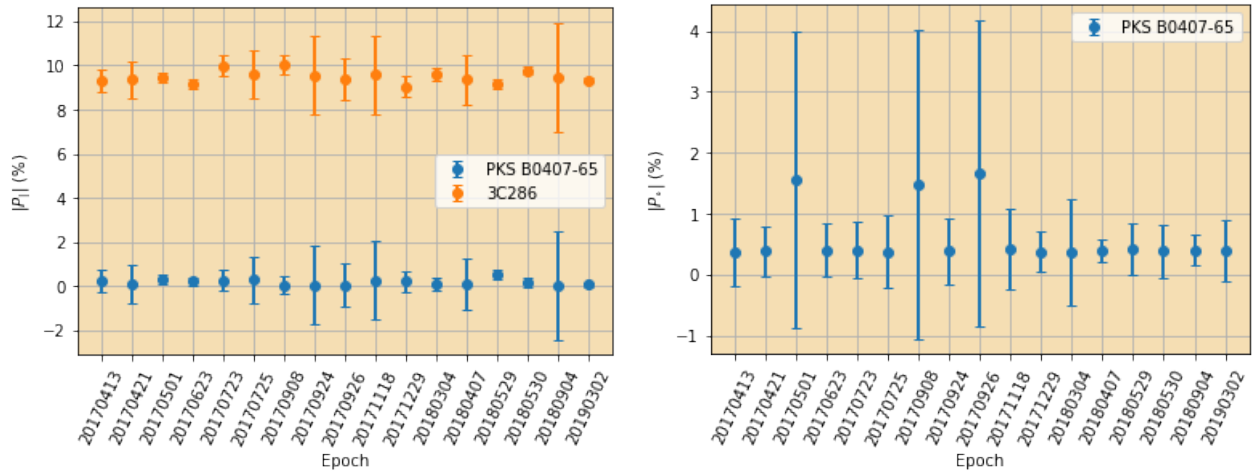

Figure 1.18: Left: Fractional linear polarization power of PKS B0407-65 and 3C286 over the span of the campaign. The error bars here are the first quartile D_{residual} as measured on 3C286. Right: Fractional circular power of PKS B0407-65. The first quartile residual instrumental circular polarization, $V_{\text{instrumental}}$ measured on 3C286, is plotted as error bars.

Ionospheric Faraday Rotation, as monitored on 3C286, was relatively quiescent during the majority of the span of this study, with peak ionospheric RM of -3 rad m^{-2} only in some of the observations.

1.6 Conclusions

In this work we have derived a field model and flux scale for the strong compact calibrator source PKS B0407-65. We also derived a full field model for PKS B1934-638. The field structure around the steep-spectrum PKS B0407-65 is at a level of 20% at UHF frequencies, which necessitates the use of a full field model to reduce bandpass calibration errors. This is even worse for PKS B1934-638: with surrounding field sources contributing up to half the total beam attenuated flux available to calibrate the bandpass at lowest frequencies. PKS B0407-65 is found to be unpolarized, and therefore well-suited to be used as a leakage and flux-scale calibrator for the MeerKAT telescope. We caution the reader that the field models derived in this work are not corrected for the antenna far field response (ie. they are in apparent scale) and should only be used for calibration of the homogeneous $\sim$ 13.5 m 64 dish MeerKAT radio telescope. Deriving high dynamic range intrinsic scale models for the heterogeneous MeerKAT extension and SKA-MID projects will need to be performed in followup work.

Chapter 2

Absolute linear polarization angle calibration using planetary bodies

This chapter deals with, mainly, establishing a full polarimetric model, at centimeter-wavelengths, of 3C286 (J1331+3030). Over the past few years users within the MeerKAT user community indicated that the absolute angle of calibration appeared to be off by many degrees. However, it was unclear whether this was a systematic or an error in the assumption of the Electic Vector Polarization Angle of 3C286 (only well-established at C/X-band and above). Up to this point the various systematic issues introduced by the MeerKAT antennas, as well as ionospheric conditions, were not well-quantified or understood. With this in mind I reached out to Rick Perley of the NRAO in 2021 who subsequently did preliminary work on the much better characterized Jansky Very Large Array system using observations of the radially-polarized limb of the Moon at L-band [126] to characterize the absolute angle of 3C286. This preliminary work suggested that the EVPA was lower than the 33^o extrapolated from a flat intrinsic Rotation Measure of 0 rad m^{-2} down to L-band frequencies, commonly assumed in the literature on polarimetric calibration. However, due to sources of error, notably the ionosphere, a single L-band observation is not enough to firmly establish a new low frequency model. This inspired the more detailed dual observatory study presented here.

In order to present an updated model of 3C286 we necessarily have to dive deeply into the possible systematics at play with the MeerKAT system and the observing environment. We present a detailed study and characterization of the error on polarimetric measurements with the MeerKAT system and site environmental conditions from long term observations, including residual scatter from ionospheric-corrective regimes using Global Navigation Satellite System differential measurements of the Total Electron Content in the ionosphere and plasmasphere. To calibrate the intrinsic angle of 3C286, we observe the Moon, Venus and Mars using MeerKAT and the Jansky Very Large Array in an analysis analogous to the high frequency work presented in [127].

We summarize the main findings in this work here:

- Long term monitoring of 3C286 shows that both global IONEX and GNSS receiver-derived models of the ionospheric electron content induced Faraday Rotation are no better than 1 rad m^{-2} over the MeerKAT site. Although both global and local-derived Total Electron Content (TEC) models effectively track the strong multi-hour diurnal behaviour (many rad m^{-2} on some days), as well as the few tens of minute rapid variation in the ionosphere in the case of the local-derived models, absolute corrections to the Faraday Rotation are limited to the aforementioned accuracy. Indications are that these models are substantially better over the VLA site in New Mexico. This is the main limiting factor to accurate Electric Vector Polarization angle measurements, not systematics induced by

the telescope itself. A discussion showing the differences between products derived from the International Global Navigation Satellite System (GNSS) Service (IGS) and local products derived from the South African TrigNET beacon network are shown in Sections 2.3.3 and 2.3.4. Results from long term monitoring of 3C286 are shown in Section 2.4.4.

- Using extended well-resolved bodies, such as the Moon require that frequency-dependent off-axis leakages (due to optics and, mainly, resonance modes in the receiver waveguides) be well characterized. We use long-duration off-axis measurement of 3C286 to independently verify that frequency-dependent leakages do not significantly affect measurement of the polarization of the Lunar limb when tracking the center of the Moon. We see strong many percent leakages affecting measurement beyond the Full Width at Half Maximum of the antenna primary beam. This analysis is presented in Section 2.4.2.
- Polarization calibration is relative to the dipole alignment for linear feed systems. Absolute alignment of the Electric Vector Polarization Angle is dependent on establishing the absolute alignment. This can be done with absolutely known sources, such as the orthogonally polarized emission from rocky planetary bodies / planetoids. We observe the Moon (L-Band VLA & MeerKAT, UHF and S-band MeerKAT), Venus (S-band VLA) and Mars (C/X-band VLA) for this purpose. We establish that the global alignment of the MeerKAT dipoles are better than 2 degrees across all bands. The scatter (computed by leakage angles) is well within the 5 degree engineering design limits set for the MeerKAT receivers. This is presented in Section 2.4.3.
- After establishing the main drivers of error in our measurement we establish that 3C286 depolarizes at frequencies below 1.0 GHz. This depolarization is not linear and not due to a singular foreground electron screen, but likely due to components with differing spectral indexes within the synthesized beam. Associated with the strong depolarization is a rapid change in the intrinsic Electric Vector Polarization Angle. This model is presented in Section 2.4.4.

For the benefit of the reader we present a thorough revision of the definitions of polarimetric measurement in Section 2.1. We review the origin behind refractive radial linear polarization seen from rocky planatory bodies / planatoids in Section 2.2. We discuss the ionospheric structure and composition of the Earth (as well as the Moon when in the tail of the Earth's magnetosphere), Venus and Mars in Section 2.3.1. An observation schedule of the various observations used to characterize the ionosphere, leakages and absolute angle calibrators (Moon, Venus and Mars) are given in Section 2.4.1.

The work presented here is published in MeerKAT memo SSA-0004E-001 and reproduced with permission from my employer. The work is co-authored by Rick Perley (NRAO), who led the Moon, Mars and Venus observations at the VLA. I initiated the observation program at the South African Radio Astronomy Observatory, and will focus on the MeerKAT part of the analysis work, which spans UHF, L and S-band systems. I want to thank Rick Perley for extensive comment and improvements of this work, as well as providing an independent reduction of the MeerKAT data in AIPS [58] to cross check the results presented here, Tony Willis (NRC/DRAO ret.) for review of these results and assistance with his ALBUS package, Eric Greisen (NRAO) for help with the AIPS[58] TECOR task and extensive work on the linear polarization calibration routines within the package over the past 2-3 years and Maaijke Mevius (ASTRON) for assistance with her RMEXTRACT [106] package.

2.1 Motivation

The calibration of the ambiguous linear Electric Vector Polarization Angle (hereafter "EVPA") in circular feeds, as in-use at the Jansky Very Large Array (hereafter "JVLA"), relies on the use of highly polarized AGN such as 3C286 and 3C138 as reference sources. This requires apriori knowledge of the intrinsic source EVPA. Linear feed systems, as in use at the MeerKAT radio interferometer (as well as the planned ngVLA and SKA-MID), require only the minimization of the fractional elliptical polarization component induced by delay differences between receiver feeds and digitization

systems.

We can easily calibrate for this crosshand phase (inducing system polarization ellipticity in a linear-basis system) and first-order leakage effects using a combination of a strong linearly polarized calibrator (observed at a parallactic angle which will yield polarized power on the XY^* and YX^* hands) and an unpolarized calibrator which will yield the systemic first-order relative leakages. This is implemented in standard transfer routines in both AIPS [58] and CASA [104].

However, for a linear feed system this calibration does not calibrate the absolute angle of the linear EVPA. All angles are calibrated relative to the (mis)alignment of a user-selected reference antenna. For nominally aligned feeds, and in the absence of an ionospheric electron content inducing a Faraday screen, the instrument should measure the correct fractional vertical/horizontal and diagonally linear polarizations after correcting for the (known) time variable parallactic angle. No assumption of the angle is strictly necessary for the linear bases — only that there is enough SNR on the crosshands to measure the ambiguous crosshand phase and that the calibrator has relatively little intrinsic circular polarization. See EVLA memo 219 [128] for full details on calibration of crosshand phases.

Over the past few years there have been various reports from the user community that, primarily in L-band observations, large offsets from the believed polarization angles of our linear calibrators are readily observed. Their origin is not firmly established - it could be intrinsic to the source (ie. the historic model accuracies are in doubt) or be intrinsic to the alignment of the picked receiver on sky or due to the ambiguity that exists in solving for relative leakages on an unpolarized source[1]) or due to time-variable ionospheric Faraday Rotation. Furthermore the accuracy level on GPS-based differential TEC measurements are also not well established at either the MeerKAT or JVLA sites. The induced Faraday Rotation is especially important at the low frequencies of UHF and L-band.

In a linear basis, to first order and assuming the absence of ionospheric electron content and offsets of the feeds from being nominally aligned at the focal point, the interferometer response between antennas p and q is

$$\begin{aligned} X_pX_q^* &= (I + Q_\Psi) \\ X_pY_q^* &= [(U_\Psi + jV)]\, e^{j\rho} \\ Y_pX_q^* &= [(U_\Psi - jV)]\, e^{-j\rho} \\ Y_pY_q^* &= (I - Q_\Psi) \end{aligned}$$

Where +X is aligned nominally north towards the NCP (+Q - vertical polarization) rotating anti-clockwise towards the (+Y) east (in direction of RA) through the +45 diagonal linear polarization mode (+U) according to the IAU convention, as indicated in Fig. 2.1. The parallactic angle, Ψ, is the offset angle between the observer (at latitude L_a) Zenithal direction and NCP and is given as:

$$\tan\Psi = \frac{\sin H}{\cos\delta\tan L_a - \sin\delta\cos H}$$

The parallactic angle rotates the linear polarization vector seen by an Alt-Az mounted instrument north through east. This "feed"-relative linear polarization Q_Ψ and U_Ψ are given as,

$$\begin{aligned} Q_\Psi &:= Q\cos 2\Psi + U\sin 2\Psi \\ U_\Psi &:= U\cos 2\Psi - Q\sin 2\Psi \end{aligned}$$

The crosshand phase, ρ, indicates the system-induced ellipticity between the two orthogonal feeds and serves to split power from intrinsic diagonal linear polarization (Stokes U) into circular (Stokes V) polarization for an observed linearly-

[1]For the linear bases MeerKAT system throughout this document we solve only for relative leakage terms on an unpolarized source, which are degenerate in the sum of leakage pairs which results in induced offsets on the measured angles. See [62]

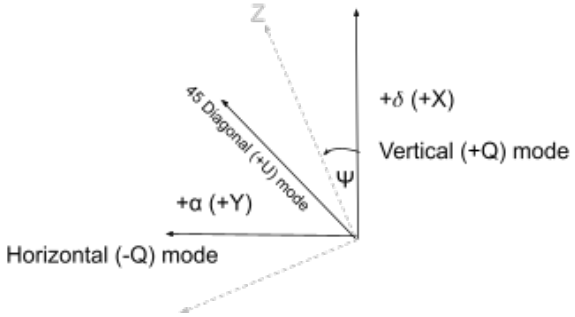

Figure 2.1: IAU convention for linear polarization orientation

polarized source. Without any calibration applied the crosshand phase is by far the dominant source of polarimetric error on the MeerKAT system and can be arbitrarily large depending on the initialization of the digitization streams.

Imperfect receiver feeds and electronics further add sources of error at a lower level than that of the crosshand phase. These imperfections results in cross-polarization mixing. We characterize them as leakage, d, terms in the following more complete expression of the response of the interferometer (after cable delays, bandpasses and remaining time variable frequency constant phases and amplitudes have been calibrated). Following [62],

$$\begin{aligned} X_pX_q^* &= (I+Q_\Psi)+U_\Psi(d_{Xp}+d_{Xq}^*) \\ X_pY_q^* &= \left[(U_\Psi+jV)+I(d_{Xp}+d_{Yq}^*)-Q_\Psi(d_{Xp}-d_{Yq}^*)\right]e^{j\rho} \\ Y_pX_q^* &= \left[(U_\Psi-jV)+I(d_{Yp}+d_{Xq}^*)+Q_\Psi(d_{Yp}-d_{Xq}^*)\right]e^{-j\rho} \\ Y_pY_q^* &= (I-Q_\Psi)+U_\Psi(d_{Yp}-d_{Xq}^*) \end{aligned} \tag{2.1}$$

Leakages in L-band are on the order of 1% in the first order and between 0.1 to 0.01% in further (here neglected) second-order effects on Stokes I. In the S-band this goes up to 5-7% level in the first order. Off-axis multi-modal leakages due to the Ortho Mode Transducer (hereafter "OMT") are frequency-dependent and band-dependent and can be many percent, increasing with offset. This is discussed later in this chapter.

The angle measurement ambiguity is, in some aspects, worse for a system with circular polarizers in the receiver chain (such as the JVLA). If we, for the moment, neglect the leakage terms and any diagonal complex-valued time and frequency variable gains aside from the crosshand phase to simplify the equations for discussion (full linearized terms are discussed in [62]) then the interferometer response to a point source at the phase center for a nominally-aligned receiver becomes

$$\begin{aligned} R_pR_q^* &= (I+V) \\ R_pL_q^* &= \left[(Q+jU)e^{-2j\Psi}\right]e^{j\rho} \\ L_pR_q^* &= \left[(Q-jU)e^{+2j\Psi}\right]e^{-j\rho} \\ L_pL_q^* &= (I-V) \end{aligned}$$

From the expressions for the crosshand terms it is immediately clear that the crosshand phase is an additive term in the ambiguity of the linear angle of response. It can rotate the measured angle to an arbitrary value for the JVLA, and can be

time-variable near Zenith. Establishing an absolute angle model is therefore of paramount importance when calibrating in the circular bases for the JVLA. The calibration procedure for the circular feed VLA data is given in Appendix D.2 of this document.

The low frequency polarization model needed for angle calibration for the quasar source 3C286 dates back to observations taken on the 46m steerable dish of the Algonquin Radio Observatory, Ontario, Canada [16]. They found that the source was exceptionally stable (compared to the other sources observed in their study) and had an angle of 33 and 31 degrees at 4.5 cm and 2.8 cm with an error bar of 1.1 and 2.4 degrees (determined from long term observations) respectively. This stability is later confirmed by [127], where it was found that the fractional linear polarization of the source only increases at a rate of about 0.015% per year with changes in the position angle less than 2 degrees over the past 20 years at frequencies below 50 GHz.

Part of the bootstrapping work done by [16] in determining the angles assumed that the initial ambiguous feed angle could be calibrated by choosing 3C144 as the reference source with an extrapolation of its angle from lower frequencies to the observed bands of the ARO. [127] used resolved observations of the planet Mars to verify the derived model of 3C286 at higher frequencies in D-configuration on the JVLA during a campaign spanning 1995 to 2012. They found the angle increasing from 33 to 35.8 degrees between 5 and 45 GHz. The steady upward trend in the angle is confirmed by IRAM mm observations of the source [2] and increases to 39.2 ± 1 degrees at 225 GHz in CARMA observations of 3C286 and Mars taken by [73].

It is important to note that [127] extrapolates the observed angle of 33 degrees down to L-band in calibrating the ambiguous RL phase for observations of other polarized sources in that study. Other observers using the JVLA, MeerKAT and other observatories at frequencies below C-band have made similar assumptions. **As far as we can tell, little effort has been made to verify the model of this source at lower frequencies.**

The goal of this work is, therefore, to establish and summarize:

- whether our standard angle calibrator 3C286 has an intrinsic degree of rotation measure (or "RM"),
- the degree of ionospheric induced rotation measure,
- the intrinsic EVPA of 3C286,
- errors arising from relative leakages and global feed misalignment, and
- the contribution of off-axis leakages to measurement

For this experiment we assume that the linear calibrator 3C286 is only marginally resolved[2] and we aim to measure the integrated intrinsic EVPA and RM. When processing higher frequency observations in S-band and above UV tapers are used to constrain measurement to core spacings.

We have already established in [128] that the handedness on the MeerKAT visibility products is incorrect — it is defined as +X east and +Y north. This flip in convention flips the signage of Q, U and V depending on the crosshand phase of the system (whether the system reverses its response to RCP and LCP polarized emission). Full details can be found in [128]. It suffices to apply an anti-diagonal matrix to raw visibilities and reset the RECEPTOR feed angle to 0 in Measurement Set v2 [86] visibility products prior to processing [3]. A full flowchart of how the MeerKAT data is calibrated is given in

[2] It is noted that 3C286 consists of a central core of about 80 mas, compact 1" lobe to the east and a 2.5" lobe to the SW. See [127, and references therein].

[3] As it stands, the existing "correction" applied via a simple additional rotation angle assumes the correct phasing in the data. This is, therefore, invalid on reverse-phased systems (such as some of the UHF receivers and the S-band receivers), where the phasing means the handedness go clockwise north through west instead of north through east, looking towards the source. It is also not consistently respected in all software – e.g. `POLAA/POLAB` is not used at all in AIPS and limited to an additional term (based on the first value of the `RECEPTOR_ANGLE` tuple) only in the parallactic angle application in CASA, not the derivation of the phases. From these discussions it has been clarified that the `RECEPTOR_ANGLE` angles are to be interpreted as offsets to the X and Y feeds from their respective nominal definitions in the IAU frame. This means that for S-band systems this should read $[-\pi/2, +\pi]$, however

Appendix D.3 of this document.

After calibration the offset on the EVPA induced by feed rotation, relative leakage effects, as well as ionospheric induced RM can be measured and verified respectively using (well-resolved) blackbody radiation refracted through a surface dielectric medium. We study the quasar 3C286 from MeerKAT UHF through X-band JVLA. We use the Moon, Venus and Mars as absolute angle polarization angle calibrators. More about why we use these bodies next.

2.2 The Moon and planetary bodies as absolute EVPA calibrators

The discussion in this section draws heavily on recent observations of the Moon at L-band using the DRAO [169], and those of Mars in [127].

In rocky planetary (or interchangeably planetoid in this context) bodies the dominant thermal radiation originates in the thermally stable subsurface layer at a depth that depends on observing wavelength (usually a few wavelengths deep) and surface material. In the centimeter-wavelength regime, this thermally-stable subsurface radiation is the dominating source of emission. Upon crossing the surface layer into (almost) free space the radiation is refracted through Snell's Law, subject to the incident angle to the surface normal.

$$\sin\theta_t = \frac{n_i}{n_t}\sin\theta_i$$

Here t and i represents the transmitted and incident radiation. $n = \sqrt{\varepsilon}$ is the the refraction index due to emission passing from a medium with dielectric constant, ε to free space ($n_t \approx 1.0$) at the planetary surface.

With all MeerKAT data taken we use the Moon as the external absolute angle calibrator. The Moon is covered in regolith (powdery dust and loose rock) that covers its bedrock up to 15m deep in the Lunar highlands. This layer is a dielectric medium and, depending on wavelength, thermal radiation from the moon (260+ K in places) is refracted through this medium. This makes the limb of the Moon an excellent source of linear polarized light with a polarization angle depending only on the incident angle of radiation. We also note here that the phases of the Moon have little effect on the observed thermal radiation of the Moon as measured in radio ($\sim 1\%$ at centimeter-wavelengths).

The JVLA can only use the Moon for absolute angle offset calibration at L-band due to the smaller main lobe of its 25 m diameter antennas. The main lobe attenuates the limb emission as a function of frequency — the Moon nearly fills the FWHM at 1.4 GHz, where at 2 GHz the limb is near the first null. Only two VLA observations were taken with the Moon as angle calibrator. To get measurements at higher frequencies we observed Venus at L and S-band, and took new observations of Mars at C and X-band.

Whether it is the Moon, Mars or Venus, the degree of polarization (D) to the relative dielectric constant (ε) and the incident angle θ_i between the incident subsurface light ray to the normal of the surface plane is given as follows,

$$D = \frac{\frac{1}{2}(R_\parallel - R_\perp)}{1 - \frac{1}{2}(R_\perp + R_\parallel)}$$

The incident ray (from beneath the surface boundary) has equal power in the parallel ($R_\parallel$) and orthogonal planes ($R_\perp$). At the boundary both components are refracted by the transmitted angle, however the refracted power differs between the components, with the degree of linear polarization dependent on this difference. If the planetary body is a smooth sphere viewed from afar (ie. a disk) the parallel component is radially oriented along the observable disk and the perpendicular

currently in CASA it is implicitly assumed that the feeds are 90 degrees apart and the second value is not used — and cannot correct handedness and phasing in the data. Eric Greisen, NRAO, and George Moellenbrock, NRAO, priv comm.

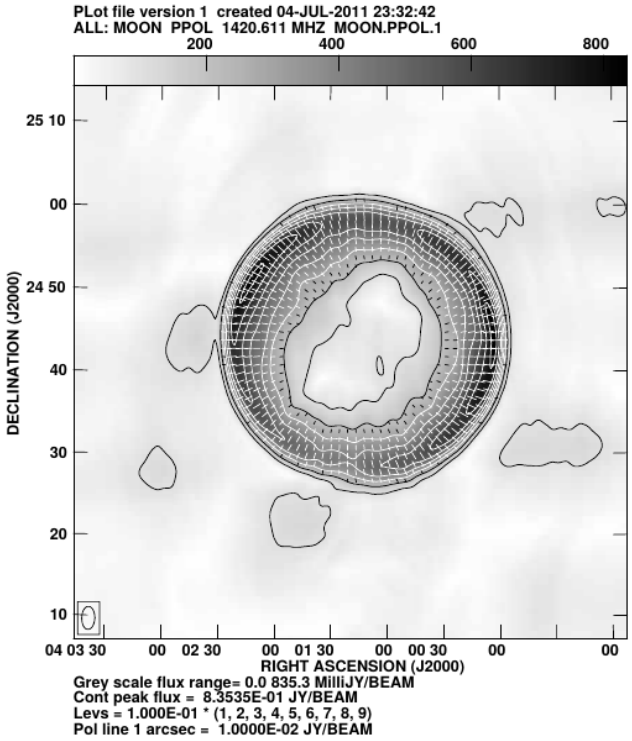

Figure 2.2: Polarization fraction (gray and contours) and E-vector angles measured at 1.4 GHz using the DRAO. Fractional polarization up to 20% is detected at the limb in the DRAO data. Taken from [169].

component is azimuthally orientated. The reflection coefficient of the radial component, $R_{\parallel}$, falls gradually from the disk center outwards to reach a minimum with transmissivity declining rapidly thereafter. The azimuthal component reflection coefficient, $R_{\perp}$, raises steadily with offset. As the transmissivity of the radial component dominates over the azimuthal component we expect linear power at the limb of the planetary body with polarization perfectly perpendicular to the edge of the disk.

$$R_{\perp}(\theta_i) = \left| \frac{\cos\theta_i - \sqrt{\varepsilon - \sin^2\theta_i}}{\cos\theta_i + \sqrt{\varepsilon - \sin^2\theta_i}} \right|^2$$

$$R_{\parallel}(\theta_i) = \left| \frac{\varepsilon\cos\theta_i - \sqrt{\varepsilon - \sin^2\theta_i}}{\varepsilon\cos\theta_i + \sqrt{\varepsilon - \sin^2\theta_i}} \right|^2$$

Under preservation of energy the energy transmission component is given as $T_{\perp} = 1 - R_{\perp}$ and $T_{\parallel} = 1 - R_{\parallel}$.

[169] measure the dielectric constant varying between 2 and 3.2 (with the majority of the disk having a constant of 2.6) and show that the Lunar limb is polarized to fractions up to 20%. This is shown in Fig. 2.2 and is taken directly from their results.

For incident angles beyond the critical angle of reflection, $\theta_c = \arcsin n_t/n_i$, the continuity states between the incident, reflected and transmitted components at the boundary of this non-ferrous material induce a differential phase on the polarization vector of the reflected component. The transmitted component phase remains unchanged throughout. Following

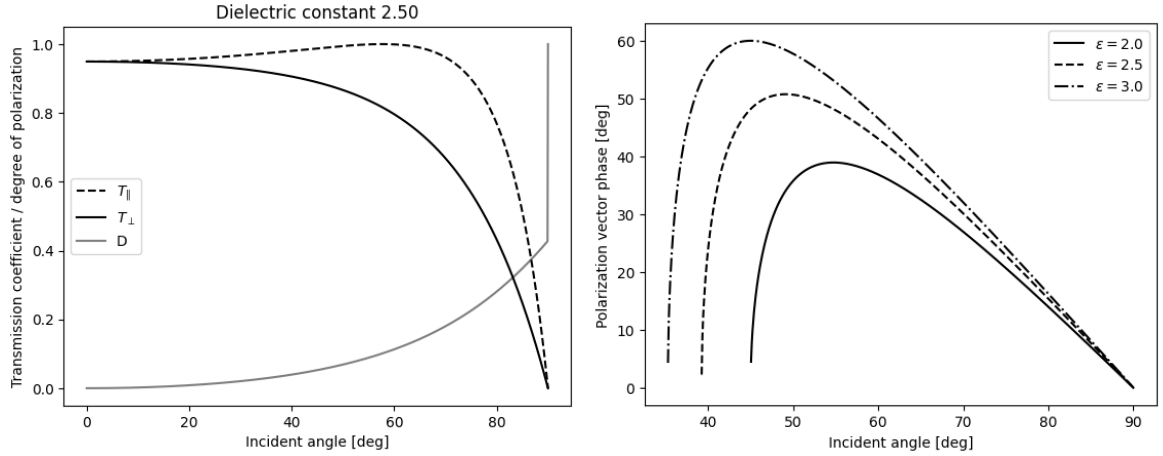

Figure 2.3: (Left) For a dielectric constant of 2.5 for the regolith we show how the radial component (in the plane of the incident and transmitted angles) increases in transmissivity. The degree of observed linear polarization increases towards a maximum at the edge of the observed planetary / planetoid disk. (Right) Ellipticity of the internal reflected component of polarized emission for a range of dielectric constants expected for the Lunar regolith. In all cases there is no induced elliptical polarized light on the transmitted component expected towards the limb, as the broadband thermal emission has equal power in both components.

[15] the differential phase on the reflected component for $\theta_i > \theta_c$ becomes

$$\rho = 2\arctan\left(\frac{\cos\theta_i\sqrt{(\frac{n_i}{n_t})^2\sin^2\theta_i - 1}}{n_i\sin^2\theta_i}\right)$$

This is perhaps conceptualized easiest as a viewgraph, see Fig. 2.3. We expect that the regolith mostly linearly polarizes the blackbody towards the limb with no intrinsic elliptical contribution, save for reflected terrestrial circularly polarized emission towards the center of the disk.

Although we expect the integrated polarization over the entire disk to average out, when the synthesized beam size is substantially smaller than the apparent disk size, the orthogonality of the polarization vectors to the limb can be used to calibrate the absolute angle on sky. For a system with circular polarizers, the calibrated response is set by the assumed model for the angle on calibrator source and for a linearly polarized system is set by the unknown feed orientation on sky[4].

We note this model is independent of observational frequency (for the small bandwidth of our measurements) and therefore can be used to estimate the component of rotation measure that stems from the ionosphere towards the Moon / planet and the constant offset of the receivers to absolute north.

Interferometers are not sensitive to the average temperature of the Moon (due to the lack of single dish measurements covering the spacing up to the shortest baseline in the array). For the purposes of this analysis, we are only concerned with measurement of the Lunar limb and not the average temperature. We therefore do not include single dish spacings[5].

In Section 2.3 we discuss the effect of ionized electron content in the ionosphere and Solar winds on the observed radial component of the linearly polarized light from such rocky bodies. It suffices to summarize that the ionized electron content introduces a wavelength-dependent offset when subjected to the Earth's strong magnetic field. This offset is

[4]It is worth noting here that even with a large sweep of parallactic angle solving for the Stokes parameters and absolute leakage terms on the calibrator field remain degenerate with respect to misaligned feeds on sky. See [62] for a discussion.

[5]Inclusion of single dish data, although available for all MeerKAT antennas and some JVLA antennas for every observation, would require redundant raster scans over the Moon to remove ground spill temperature as a function of elevation and azimuth in order to do accurate polarimetry. These are not included in our interferometric observing plans - the center of the Moon is actively tracked by the MeerKAT and JVLA correlators.

highly spatio-temporally variable.

In the most general form, following [28], the measured polarization state of the electric field, after being subjected to ionized electron content, between the observer and the radiative source, is given as

$$
\begin{aligned}
P(\lambda^2) &= \frac{\iint_{\text{source}} I(\vec{r},\lambda)\, p(\vec{r})\, e^{2i(\text{EVPA}(\vec{r})+F(\vec{r})\lambda^2)}\, dr d\Omega}{\iint_{\text{source}} I(\vec{r},\lambda)\, dr d\Omega} \\
F(\vec{r}) &:= \frac{e^3}{2\pi m_e^2 c^4} \int_{\text{source}}^{\text{observer}} n_e(\vec{r}) B_{|}(\vec{r}) d\vec{r} \\
\text{EVPA}(\vec{r}) &:= 0.5 \arctan\left(\frac{U}{Q}\right), \text{EVPA}(\vec{r}) \in [-90^\circ, 90^\circ)
\end{aligned}
\tag{2.2}
$$

Here light of intensity (I) with fractional polarization (p) emitted by a source offset in line of sight direction $\vec{r}$ has an intrinsic degree of polarization, EVPA($\vec{r}$). The light is subjected to ionized electron content with density n_e and parallel magnetic field, $H_{\|}$, along the line of sight. This induces a counter-clockwise rotation (north through east) in the observed linear angle ($RM\lambda^2$) along the direction of the orthogonal magnetic ($B_{|}$) field, which generally points towards the observer at northern geomagnetic latitudes and away from the observer at southern geomagnetic latitudes. Here m_e is electron mass, c speed of light, e the electron charge and λ the observed wavelength. See further discussions in [51] on accepted convention. We note that if the Faraday Depth is contributed to by a single screen of ionized content, ie. the Rotation Measure equals the Faraday Depth. As the density of the ionospheric contribution is roughly constrained in a dense shell we use these terms interchangeably.

Due to ionospheric gradients across the horizon it is not sufficient to assume that ionospheric-induced angle offsets are the same across the sky for precision polarimetry (ie. observed offsets cannot be transferred from calibrator to target source). Although we can use the wideband measurements of the offsets from the radial linear polarization of e.g. the Moon as a measure of the ionosphere-induced Rotation Measure, it can at best serve as a verification source for the ionospheric RM and a measuring source of frequency-constant feed angle offsets, provided it is of sufficient offset from the Sun to minimize Solar wind contribution. More about this in Section 2.3.

To this end we implemented a special routine to fit for the frequency-dependent and frequency-independent offsets from the expected orthogonal linear polarization based synthesized maps of the Moon for the entire array. We aim to minimize for

$$\theta_{\text{avg}} + \text{RM}\lambda^2,$$

where θ_{avg} is the average on-sky receptor offset angle[6].

The fit is done only on the measured EVPA with the model assumed to be a torus with angle 0 degrees defined north towards NCP and +90 degrees defined east (increasing right ascension) in accordance with IAU convention for linear EVPA. The inner and outer boundaries of the torus are user-adjustable to account for varying SNR between the bands and variation in size due to differing orbital positions. The fit is done by splitting the available bandwidth into subbands through Multi Frequency Synthesis imaging as is implemented in [112]. Only high SNR linear polarization components are selected from the image (with a user adjustable threshold). We expect (roughly[7])

[6] We use the definition of the rotation Jones matrix applied for antennas p and q in RIME onion-formalism [146] in linear bases, where $\mathbf{R}_p = \mathbf{R}_q$ with $\mathbf{X}$ the 2x2 coherency matrix: $\mathbf{R}_p \mathbf{X} \mathbf{R}_q^H$. Using the definition of linear polarization components $Q + iU = p(\vec{r}) e^{2j\text{EVPA}}$ from Eqn. 2.2 it can be shown that the factor of 2 brought about by the 2x2 rotation matrices is cancelled. When measured the perceived array-average feed angle offset on the EVPA from nominal IAU direction can be added to the `::FEED` table of MSv2 [86] datasets. It is noted that AIPS[58] does not take the receptor angle into consideration during calibration (Eric Greisen priv. comm.).

[7] The instrument PSF couples adjacent angle measurements through sidelobes and depolarizes the signal within the main lobe. With sufficient

$$\frac{4\ln 2\Omega_t}{\pi\theta_a\theta_b}$$

independent measurements per frequency band of the angular offsets along the torus, where Ω_t is the total area (in steradians) of the torus after thresholding for linear power SNR. Subscripts a and b are the major and minor axes fitted to the FWHM of the synthesized beam. We expect the distribution of angles to have a Gaussian profile centered at the offset angle as a function of frequency. Subbands yielding significantly non-Gaussian profiles[8] are rejected from the fit.

The frequency-dependent offset component is used to verify external TEC measurement using Global Navigation Satellite Systems (GNSS). The array-average frequency constant offset is assumed to be mainly from dipole misalignment[9]. This is assumed to be temporally stable and transferred to other observations where we do not have the Moon or other planetary body (in the case of the VLA) within the observation.

The relative offsets between the antenna feed angles is captured by the narrow-angle approximated leakages solved for using either CASA [104] or AIPS [58]. As discussed in [128] when the individual dipoles are misorientated by θ_X, θ_Y from their nominal definition, then the off-diagonal leakages are defined[10] as

$$d_X = \theta_X - i\chi_X$$
$$d_Y = \theta_Y - i\chi_Y$$

While electronic contributions may exist, the real component of the leakage encapsulates, primarily, the effects of feed misorientations, while polarization ellipticity manifests in the imaginary part. For relative leakage calibration the leakage on the reference antenna is artificially set to zero. Following along the same line of thought to the discussion presented in [62] the error on the absolute angle resulting from this calibration is then

$$\sigma^2_{\theta_{\rm syst}} \approx [\Re d_{X,\rm ref}]^2 + \sigma^2_{\theta_{\rm avg}} + \sigma^2_d + \sigma^2_{\theta_{\rm ion}}$$

Here the systematic uncertainty on the recovered EVPA angle of the source is the quadrature sum of errors, in order:

- The (artificially) zero'd leakage on the reference antenna
- The uncertainty in the fit for the feed angle using the Moon or other planetary body
- The residual leakage across the array after calibration
- The uncertainty in the ionospheric contribution to the measured EVPA. This term can only be quantified empirically through long term observation and dominates at low frequencies.

We discuss the spatio-temporal-variable ionospheric component next.

2.3 Temporally-variable Faraday Rotation due to the ionosphere

In this Section we cover the necessary theory behind ionospheric composition and Total Electron Content measurement through Global Navigation Satellite System (GNSS) observation. In Sub-section 2.3.1 we discuss the composition of the

resolution compared to the area of the body, the latter is not a significant issue.

[8] Measured in their tailedness and Fisher kurtosis

[9] Which can be up to 5 degrees according to receiver specification for all MeerKAT bands, Adriaan Peens-Hough priv. comm.

[10] Modulo a sign convention difference to [154]

ionospheres of Earth (and its effect on the Moon when the Moon is in the tail of the Earth's magnetic field), Mars and Venus. From the available literature we confirm that there is no appreciable intrinsic ionospheric Faraday Rotation for the Moon, Venus and Mars, compared to the ionospheric variability induced by the Earth's ionosphere on our measured data. In Sub-sections 2.3.2 and 2.3.3 we discuss measurement of the TEC using globally distributed models from the International GNSS Service (IGS) and direct measurement through the TrigNET beacon network operating in South Africa. Although both the international models and the locally derived models describe the ionospheric TEC-induced Faraday Rotation well in terms of short term and diurnal variability, there are large discrepencies between the absolute scale in the predicted ionospheric Rotation Measure between various IGS-derived products, as well as a comparison between the IGS and local direct measurement using the beacon network. We are confident that this does not stem from a specific software (e.g. AIPS [58] `TECOR` vs. RMEXTRACT [106] nor differences in Earth magnetic field models between the software, discussed in Sub-section 2.3.4). The differences stem directly from the IGS-distributed models. The accuracy of these corrections can only be determined from long term monitoring of a celestial source (which should not show intrinsic variability on the scale of decades to centuries). The residuals from long term observation and correction against 3C286 are only discussed later in Sub-section 2.4.4, which shows that the various distributed international models of ionospheric TEC, as well as locally derived products have residual absolute scaling errors of 1 rad m^{-2} at the MeerKAT site, but confirms that the diurnal variability are substantially reduced for all the observations under consideration in this work.

2.3.1 Composition and geometry of the ionospheres of the Earth, Venus, Mars and the Moon

The discussion here is summarized from a review by [92], to which the reader is referred for further details beyond the scope of this work. We thank Bryan Butler (NRAO) for discussions on the composition and characteristics of the ionospheres of Mars, Venus and the Moon — much of which is drawn from here.

The formation and structure of the ionospheres on our sister planets and the Moon have different structure and composition due to the different atmospheric compositions, densities and magnetic field properties of the different bodies. However, they have some similarities in terms of vertical density profiles and their electron content and magnetic field contribute to the total amount of rotation of linearly-polarized radio light as discussed in Section 2.2. We start with the Earth's ionosphere.

Earth's ionosphere is a highly variable region above the stratosphere where the atmospheric gases are photo-ionized by Solar radiation in the higher layers and cosmic background radiation in the lowest part of the ionosphere. Due to the variable densities of atmospheric molecular and atomic gases this ionising radiation causes a peak in electron densities deep inside the ionosphere, with typical electron densities shown in Fig. 2.4.

As shown in Fig. 2.4, the ionosphere can be split into three distinct layers: the D, E and F layers. The D, E and peak of the F layer forms the bottom-side of the ionosphere and the rest forms the top-side. The critical frequencies absorbed by these layers are indicated as f_oD, f_oE, f_oF_1 and f_oF_2 for the various layers and sub layers. Although no firm boundaries can be placed between the different layers of the ionosphere, the layers have very different variability characteristics due to differences in composition, magnetic field structure and ionizing radiation source. The D layer extends from 60-70 to about 90-100 km, the E region upward from there to between 120-150 km and the (highest) F region upwards to beyond 500 km decaying in density to form the plasmasphere (with typical electron densities of 10^{10} el m^{-3}) in the lower part of the magnetosphere. Beyond 30,000 km the plasmasphere decays into the Plasmapause (the boundary between the interplanetary plasma and plasmasphere) where the typical electron densities drop by up to 2 orders of magnitude [18]. Furthermore, the dipole magnetic field strength decays as the inverse cube of radial-altitude.

This ionized plasma is non-homogeneous in density between the various layers and mainly consists of ionized atomic particles (mainly H^+, O^+, He^+, N^+) in the upper regions and heavier gravitationally-bound molecular ionized N_2^+, NO^+

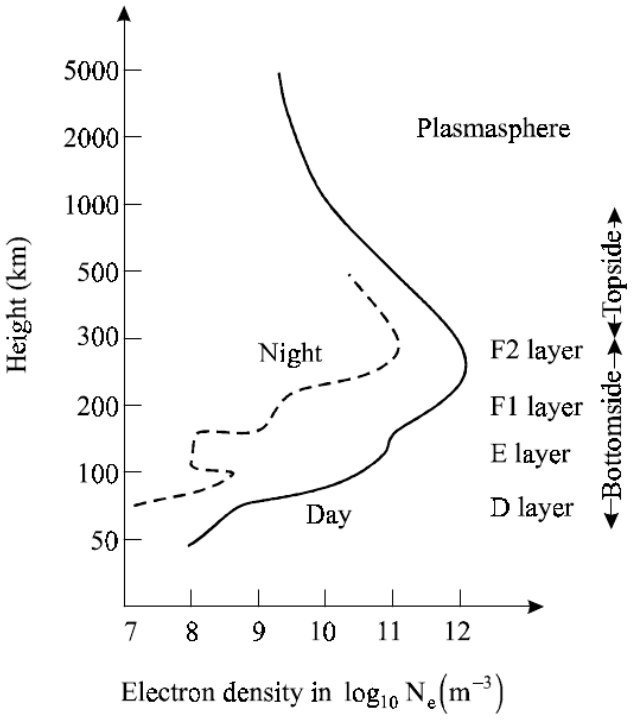

Figure 2.4: Typical day and night-time electron density profiles of the Earth's ionosphere. Taken from [43]. The profile of the ionosphere generally follows what is known as Chapman's Nose Function [30] with the upper part of the D, E and F1 layers highly dependent on X-ray and UV light and only present during daytime.

and O_2^+ at lower altitudes. The free-electron content available to induce the Faraday Rotation on observed polarized light depends on the equilibrium conditions of atomic and molecular re-ionization and photo-ionization in the various layers. Depending on Solar activity and geomagnetic latitude, it has been observed that molecular ionized plasma exists at higher altitudes — as far up as the magnetosphere [97, and references therein]. The F layer carries the bulk of the free-electron content (between 50 and 60% [17] during daytime).

The Earth's ionosphere shows the following variability characteristics, depending on layer and geomagnetic latitude.

- long-term variability during 11yr cycles,
- diurnal variability (due to the relative motion of the Sun on the celestial sphere), and
- periodicities of 27d due to Solar rotations.

We first discuss its dependence on geomagnetic latitude. The conditions of re-ionization in the ionosphere, and therefore its electron content density, are heavily dependent on the magnetic field structure of the planet at the height of the ionosphere, illustrated in Fig. 2.5. At ionospheric height the magnetic field can be broken up into the following major regions: the equatorial, mid-latitude and the high-latitude regions.

At latitudes up to 20 degrees, the electron content spreads and moves horizontally along the magnetic field lines of the planet and causes pronounced amplitude and phase scintillation. Of all the regions, the equatorial region is home to the highest values of peak-electron concentrations — the so-called anomalies. Mostly free from the horizontally spread peak electron concentrations of the equatorial regions, the mid-latitude regions, in contrast, are the most stable regions of the ionosphere, and historically the most well-studied. In the high-latitude region, collisional ionization is pronounced due to near-vertical magnetic field lines, which leads to ionized particles descending into the lower E layer and further ionizing the neutral gasses in this region, enhancing the electron population. This is associated with auroral activity in the

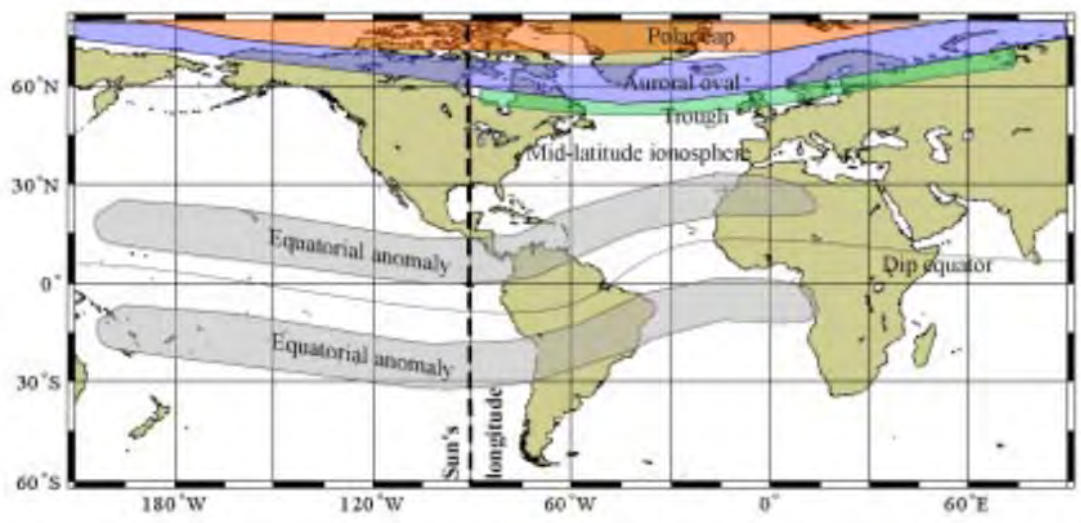

Figure 2.5: Regions of geomagnetic latitude in the ionosphere showing distinct ionization behaviour in the ionosphere, taken from [18].

Auroral Oval latitudes (64 - 70 degrees). The region encircled by the Auroral Oval is known as the polar cap – a region less well-understood – where coronal mass ejections and flares cause increases in D-region electron concentrations. The mid-latitude trough is directly below the auroral ovals. Due to increased recombination as a result of shorter winter days, the local electron content drops by a factor of a few at night-time. Direct interaction between interplanetary and magnetospheric fields causes localized electron density enhancements in the dayside cleft at all altitudes between 78 and 80 degrees latitude [92, and references therein].

Not only does Solar activity directly impact the electron content, but disturbances can also compress the outer-most magnetic field lines of the Magnetopause. The Sun's magnetic field lines stretch into interplanetary space and allow ionized material to travel along field lines. Large flare activity can rapidly change the f_oF_2 critical frequency — therefore affecting the opacity of the ionosphere to radio waves. The magnetic field compression associated with flares, high speed Solar winds and filaments additionally temporarily enhances the magnetic field strength. These enhancements are measured by global stations and the global average is reported as logarithmic "Kp" and linear "Ap" indices. These are directly proportional to the degree of perturbation of the Earth's magnetic field. The highest variation is expected to be 500 nT (or "gammas") for a mid-latitude station and 2000 nT for an equatorial station. In addition to measurements of magnetospheric disturbances, an increase in sunspot numbers and Solar flux, measured by the National Research Council of Canada at the DRAO, correlates with disturbances to the Solar magnetic field [92]. Theoretical parameterized and empirical models both require up-to-date measurements of these values for accurate predictions of ionospheric behaviour. More on this in the next section.

The vertical height-density profile of the ionosphere (with its vertical column component in units of TECU[11]) varies greatly with time of day and Solar activity, and is mainly concentrated in the F layer of the ionosphere. The temporal variability scale can be as short as tens of minutes to hours, with peak height anywhere between 200 and 400 km depending on whether it is day or night respectively. For this reason, the F layer is often split into a lower F1 layer, which only exists during peak UV activity during daytime, and a more stable upper F2 layer with the highest electron density lasting through night time. Combined densities in this layer is about 10^4 el cm^{-3} under typical conditions, but can peak by up to an order of magnitude more during periods of high Solar activity [102].

The lower F1 layer is directly dependent on UV radiation and varies greatly with Solar Zenith angle. It disappears during night-time. The F2 layer is not dependent on Solar Zenith angle on the other hand and its critical frequency and

[11] 1 TECU equals 10^{16} el.m^{-2}

height, h_mF_2, instead depends on Solar activity and geomagnetic latitude. Enhancement in its electron content – and radio opacity – is both diurnal during hemisphere winter months in Mid-Latitudes and varies greatly in the Equatorial regions ($\pm$20 degrees) due to the horizontal anomalies previously discussed.

The high D and E layers are ionized by Solar X-ray emission and therefore effectively disappear during night-time, seen in Fig. 2.4, and are dependent on Solar cycle with seasonal variations. In the E layer, the atmosphere is rare and as a result mostly molecular re-combination dominates. Typical noon Mid-Latitude electron densities are between $1.3 - 1.7 \times 10^{11}$ el m^{-3}. The D layer has two distinct regions. The lower (sometimes referred to as the "C" layer [43]) is dependent on cosmic background radiation and is, therefore, always present. Like the E layer, the top part of the D layer is dependent on Solar X-ray emission and has a strong diurnal presence. At Mid-Latitudes daytime electron concentrations range between $6.1 - 13.1 \times 10^8$ el m^{-3}.

Our primary understanding of variations in the plasmaspheric electron content comes from GPS receivers on board Low Earth Orbit satellites, particularly those in the Constellation Observing System for Meteorology, Ionosphere and Climate (COSMIC) which are able to directly measure electron concentrations above the topside ionosphere [79]. The overall structure of the ionosphere resembles the geomagnetic structure of the ionosphere — with the largest concentrations of electrons located in a belt that spans the -45 to +45 degree region (where the Solar incidence angle maximizes during daytime), with higher latitudes consistently having about half the electron content of low regions. Daytime concentrations are consistently higher than night-time concentrations, particularly in the Equatorial/Low-Latitude region. Furthermore, the plasmasphere is highly affected by Solar activity (and shows very strong correlation with S-band measurements of total Solar flux) and electron concentrations. Equatorial concentrations more than doubles between years of Solar low (2008) and Solar high (2014), with a monthly mean of 14 TECU during the latter observed period [79].

Plasmaspheric contribution to the total integrated TEC can be substantial (more than 60% in the night-time [31, 166]) due to the extent of the region covered by the plasmasphere relative to the ionosphere. That said, the dipole magnetic field strength is expected to decay with the inverse cube of the altitude — being between 2 and 4 orders of magnitude weaker than values expected at typical ionospheric h_mF_2 values. It is therefore expected not to make a substantial contribution to the observed Faraday Rotation.

The ionized plasma in the ionosphere and plasmasphere, coupled with Earth's magnetic field, contributes to the line-of-sight Faraday Depth integral — both spatially and temporally. This contribution to the observed Faraday Depth can be up to 4 rad m^{-2} and can change by as much as 80% during the course of the day [132]. We have observed ionospheric Faraday Depth contributions at this level at both the MeerKAT and JVLA from our historic observations. This is substantial enough to cause offsets of a few degrees at the bottom of MeerKAT and JVLA S-band and 10s of degrees at the bottom of the MeerKAT UHF band.

Ionospheric variability towards other planets and the Moon is expected to be primarily that of the Earth's ionosphere. Contrary to what is seen on Earth, the Moon and Mars lack a strong magnetic field of their own. The Moon is close enough to Earth to fall within its magnetosphere for much of its orbit and is to a large degree shielded from Solar ionization of its, largely, ballistic-driven exosphere. Recent observations by [61] have shown that the Moon has a negligible ionospheric density of ~ 0.2 cm^{-3} (6 - 7 orders of magnitude below that of the Earth) about 50 % of the time while being in the planet's magnetic tail.

Mars has a low-density atmosphere (roughly an order of magnitude less than the Earth at surface level), but has an extensive ionosphere which is subjected to Solar winds due to the lack of a strong magnetic field. The ionosphere is substantially thinner (roughly an order of magnitude compared to the Earth) with peak electron densities about an order of magnitude below that of the Earth (roughly 10^5 cm^{-3}). Its' ionosphere has a similar overall vertical profile shape to Earth's, see Fig. 2.6. The concentration of ions is expected to be diurnal and varying across the disk, depending on observation setup, with peak densities expected to be greatest at observed opposition. The global magnetic field strength of

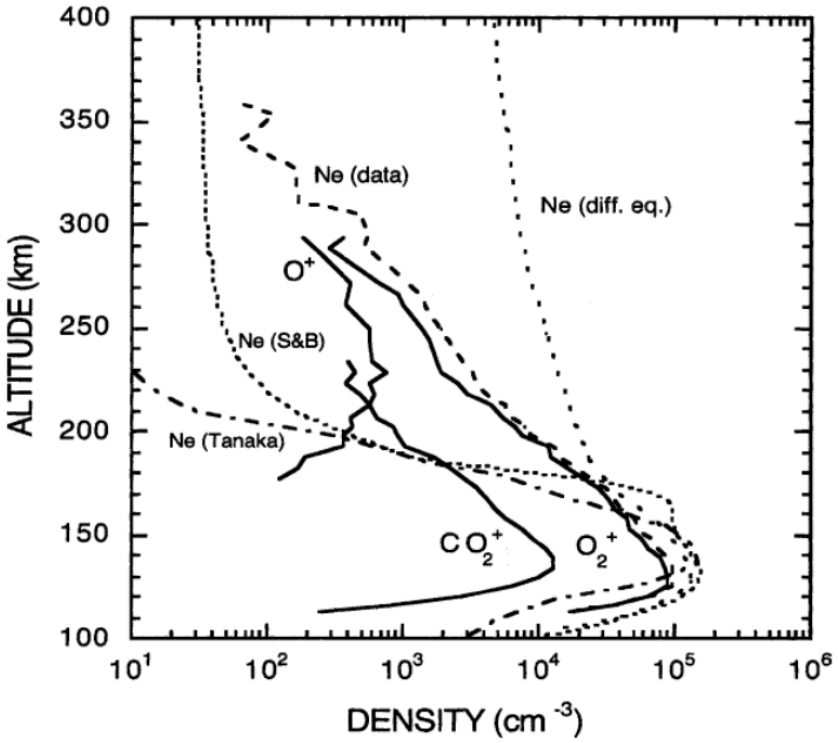

Figure 2.6: Viking 1 measurements of the vertical electron density profile of the ionosphere of Mars. This is taken from [144]

the planet is less than 0.5 nT[1] with internal magnetic fields driven mostly by crustal remanence, peaking at a maximum of 220 nT at altitudes between 370-438 km [34]. Fields as large as 1600 nT are detected at altitudes below the Martian ionosphere, from aerobraking observation by the Mars Global Surveyor [1], and highly dichotomized [34]. The external interplanetary magnetic field was rarely observed to be at levels approaching 100 nT. At peak, the magnetic field strength is 1-2 orders of magnitude below the global dipole magnetic field of Earth. When coupled with the less dense ionosphere it would, therefore, not substantially contribute to observed Rotation Measure towards Mars, when compared to the Earth's own ionosphere in our observation.

Venusian atmospheric density is substantially higher than that of the Earth (roughly 2 orders of magnitude) and there is an extensive ionosphere around the planet, originally measured by the Mariner 5 and 10 missions [52, 53]. Similar to Mars, the lack of a strong intrinsic magnetosphere means that Solar winds impinge directly on the Venusian atmosphere which can lead to orders of magnitude in the variability of the total electron content, as well as high variability in the magnetic fields beyond its ionopause. The Venusian ionosphere is about an order of magnitude thinner than that of the Earth, but the peak densities are similar (10^6 cm^{-3}). Measurements by the VEX [124] and PVO [23] spacecraft show the variability in the shape of the Venusian ionosphere and that the peak of the Venusian ionosphere is at, roughly 140 km (similar to Mars). The effect of Solar minima and maxima on the profile is shown in Fig. 2.7.

Strictly speaking, Venus has a minor variable magnetic field of its own, albeit not strong. Experiments from the Pioneer Venus Orbiter (PVO) down to 150 km from the Venusian surface have shown no significant global magnetic field. There are variable magnetic fields present in the Venus ionosphere, especially in the dayside ionosphere, when the ionopause (driven by high Solar wind pressure against its ionosphere) is at lower altitudes. The magnetic field shows a consistent dichotometry where the magnetic field strength in the dayside rapidly decays to a few 10s of nT at ionospheric levels. In the nightside ionosphere, large-scale structures were detected by the PVO, but were an order of magnitude below that of the dayside structures and located in close vicinity to the Anti-Solar point, particularly for high Solar wind pressures. Venus Express Orbiter (VEX) aerobraking experiments have shown variable magnetic fields up to a few tens of nT at the

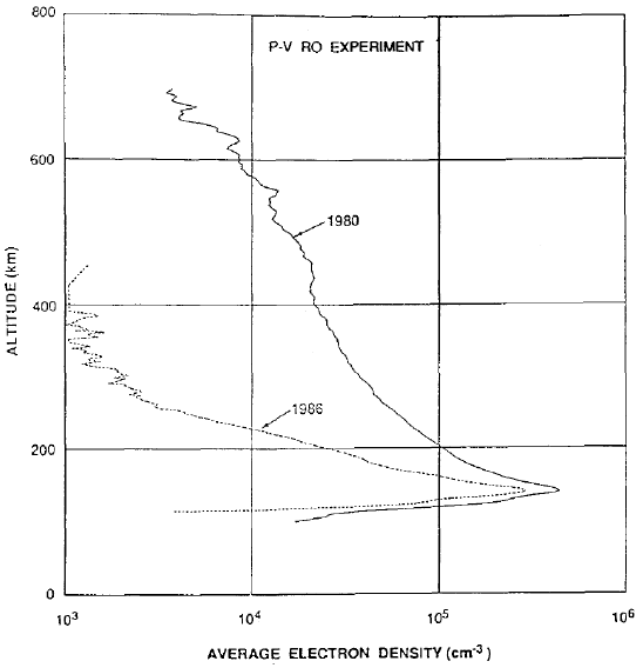

Figure 2.7: Profile of the Venusian vertical electron density, as measured by the PVO spacecraft, for a period of Solar minima (dashed) and maxima (solid). This is taken from [23]

height of the ionosphere and very faint magnetic fields in the atmosphere below ionospheric height [168]. The roughly two-three orders of magnitude weaker magnetic field should preclude significant contribution to the observed RM towards Venus in our measurements.

In order to obtain a temporally stable model of the angle of polarized sources, we need a way to remove the foreground ionospheric contribution of the Earth. There are multiple unknowns and limitations driving measurement error on various places of our model of the Faraday Depth out into the magnetosphere. We discuss each of these in turn.

- The "RM-like" contribution to the Faraday Depth integral is an integral through a medium that is non-homogenous with density and effective depth, varying greatly with time of day and Solar activity due to the variation in, and composition density of, atomic and molecular plasmas in the F and plasmasphere layers. Our understanding of temporal behavior is limited by the physical height limitations of dispersive ground-based ionosondes in determining the composition at various heights and geomagnetic latitudes due to the highest plasma frequency at which ground-based signal is reflected back. Understanding the dynamics in the F2 layer and the plasmasphere is limited to space-based observation [17, 97, 102, and the various references in these].

- In determining total integrated electron content (observed at high cadence by the International GNSS Service (IGS), along with transmitters on the South African TrigNET network), dual-frequency instrumental measurements in the L-band from GPS, Galileo and GLONASS constellations can be used to get measurements at high cadence across the local horizon. However, these are subject to timing and relativistic error at both the transmitter and receiver ends (for instance bias delays on transmitter and receivers and multipath errors), as well as the lack of density of such stations in South Africa.

- The electron content in the ionosphere and plasmasphere is subject to the Earth's Magnetic field. We will discuss this later on, but the most recent model of the International Geomagnetic Reference Field (IGRF version 13) [3] is now available in the AIPS [58] and ALBUS packages. We find the change in magnetic field model has very minimal differences in predicted ionospheric RM at the Socorro and Karoo sites (on the level of a tenth of a radian

per square meter), and can be assumed to be quite stable.

2.3.2 Ionospheric density profiles and TEC measurement using the IGS

Although empirically-driven measurements of the ionospheric profile exist (e.g. the International Reference Ionosphere [17, for a more recent revision]) and can be parameterized, the values are distributed as monthly averages. Work is underway to provide higher cadence updates to this model via the IRI Real-Time Assimilative Modeling (IRTAM) although the authors stress that further comparative measurements are needed to test this new model.

An alternative to this is the Parameterized Ionospheric Model (PIM) originally developed by the United States Air Force which comprises of low, medium and high geomagnetic latitude models of the ionosphere [42]. Instead of cumulative models, such as IRI, PIM is based on theoretical climatology with input of measured Solar and magnetic activity.

The ionization and density characteristics of the plasmasphere (more so than the F layer, although, for example, the ionosphere effective height, $h_m F_2$, is driven by indices derived from Solar flux [17]) requires up to date knowledge of Solar activity. As the atmosphere is, relatively speaking, unheated by Solar activity at cm-frequencies, radio observations of integrated Solar flux are used as a highly correlated measurement of Solar UV output and have been taken in Canada since 1947 in a 100MHz-wide S-band channel centered at 2.8 GHz (or 10.7 cm — henceforth referred to as the $F_{10.7}$ number). When there are rapid changes during Solar high periods, this index can change substantially, and keeping it up to date becomes all the more important. [49] shows that during an extended outage in March 2022 (ie. during the current Solar high period) global ionospheric modeling had induced errors of up to 15 TECU when the value was kept constant at its previously known value.

As the highest density of electron content is situated in the F layer, it is commonplace [see e.g. 132] for ionospheric corrections to assume that the effective F layer can be collapsed into a single thin shell with electron content driven by the vertical column density (in units of TEC) and derive slant TEC measurements from the Zenithal angle. This is illustrated by Fig. 2.8. This is in use by both RMEXTRACT [106] and AIPS [58]. Neither currently directly make use of space weather information[12]. Instead, they rely on globally fitted IONEX[13] maps of the ionospheric content from various providers which is an interpolated value based on a best-effort model of the ionospheric profile and total electron content measurement by the IGS.

Although there are many space weather providers of TEC data in IONEX format, [132] points out that, on average, the UQRG [114] and JPLG [108] databases distributed by the Technical University of Catalonia and NASA CDDIS give the most accurate readings at the individual LOFAR sites in Germany. Our own analysis, and non-peer-reviewed analysis[14] dating to 2012, show that this can be extended to South Africa. We find that CODE [41] databases (Center for Orbit Determination in Europe) consistently give Vertical TEC estimates that overestimate the ionospheric contribution to Faraday Rotation of 3C286 by 10s of degrees at L-band frequencies. Discussions[15] with the authors of RMEXTRACT [106] confirm as much and we note that RMEXTRACT [106] now uses UQRG [114] maps by default.

Work by Rick Perley at the JVLA site in Socorro using Lunar and Venus data at L-band and the lower part of S-band in this study confirms that the JPLG [108] three-layer databases consistently give best results from the options available in AIPS [58], however, the error bars from only a handful observations at the JVLA are not enough to establish error estimates. Long-term analysis, spanning data from the past 30 years, show the accuracy of the JPLG [108] databases to be on the order of 0.2 rad m^{-2} over the Socorro site [129]. This is well below the assumed error bars of about 1 rad m^{-2}

[12] Private comm. Maaijke Mevius and Eric Greisen indicate that this layer is set at an altitude of 450km in both packages, with the latter motivated by JPLG [108] model IONEX file headers. Although there is IRI functionality in RMEXTRACT it is not in widespread use (and not the default).

[13] Standard available here: `https://files.igs.org/pub/data/format/ionex1.pdf`

[14] Available here `https://github.com/twillis449/ALBUS_ionosphere/blob/master/twillis_ALBUS_paper.pdf`

[15] We're immensely grateful to Maaijke Mevius for various discussions on usage of their RMEXTRACT [106] package, its inner workings and experience with various international IONEX database providers.

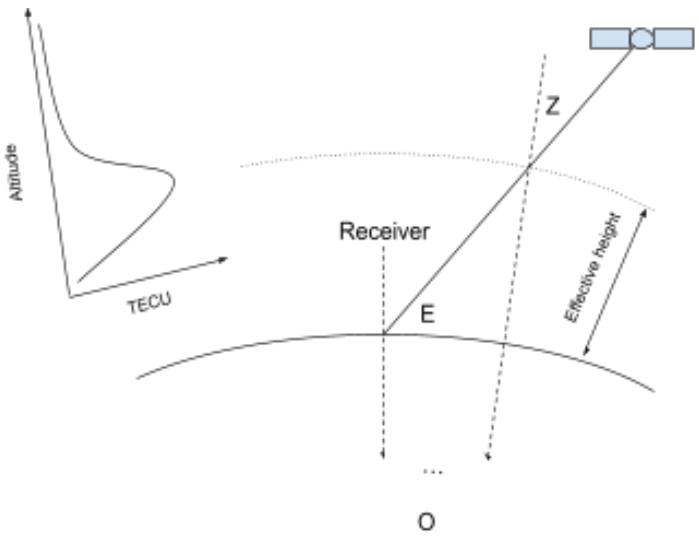

Figure 2.8: Illustration of the thin-shell model. The electron content profile of the ionosphere, with peak density in the F layer, is collapsed into a single thin shell, usually within the range 350-500 km depending on current ionospheric conditions. The vertical component of the electron density in the direction of the satellite, at elevation angle E, through this shell can be related to the zenithal angle at the pierce point through a law of cosines.

as is quoted by [102]. As we will show later, the precision of the JPLG-based [108] corrections over the MeerKAT site is substantially less, but the measurement alignment between the VLA and MeerKAT after correction is a very good fit to well within these error bars.

Contributions to these various models come from the International GNSS Service (most up-to-date list at the time of writing is plotted in Fig. 2.9). It is noteworthy that different providers use different profile and interpolation methods. For instance, the JPLG [108] model assumes a three-shell ionosphere, with slabs centered at heights of 250, 450 and 800 km. Values are aggregated and transmitted at 2-hour cadences. CODE [41] maps use spherical-harmonics with a current transmission cadence of 1 hour.

2.3.3 Direct dual frequency differential measurement using GNSS constellations locally observed

The stations on the IGS are not the only available GNSS stations provided by the international Earth and space sciences communities. As an alternative to relying on IONEX vertical TEC maps from global providers, we can use the IGS and local stations to solve for TEC directly at both JVLA and MeerKAT sites using differential GPS measurement techniques. Due to the sparsity of stations in the geologically stable Southern Africa, we want to verify whether including more local stations will be important for future work in this field. In this work, we compare a third alternative package, the Advanced Long Baseline User Software (ALBUS) to the corrections derived using AIPS [58] and RMEXTRACT [106]. ALBUS uses raw data in Receiver Independent Exchange format (RINEX[16]) from the IGS as well as local providers to estimate integrated vertical TEC using profiles of the ionosphere from either the PIM or IRI[17].

In the case of South Africa, we include various stations from the TrigNET network (`http://www.trignet.co.za/`) operated by the National Geo-Spatial Information (NGI) division of the Department of Agriculture, Land Reform and Rural Development. These stations are plotted in Fig. 2.10 for reference. The network consists of stations separated between 80 and 300 km throughout South Africa. We restrict the contributing stations to 350 km from the MeerKAT core for this work. This typically[18] yields between 8 and 9 local stations on the network. We briefly discuss how differential

[16] Standard specification (v3) available from: `https://files.igs.org/pub/data/format/rinex305.pdf`

[17] At the time of writing the IRI code path is not working as expected. Fixing of this is beyond the scope of the current analysis.

[18] Albertus van der Merwe (priv. comm) at the TrigNET control room indicates that some of the stations on the network have been down since late

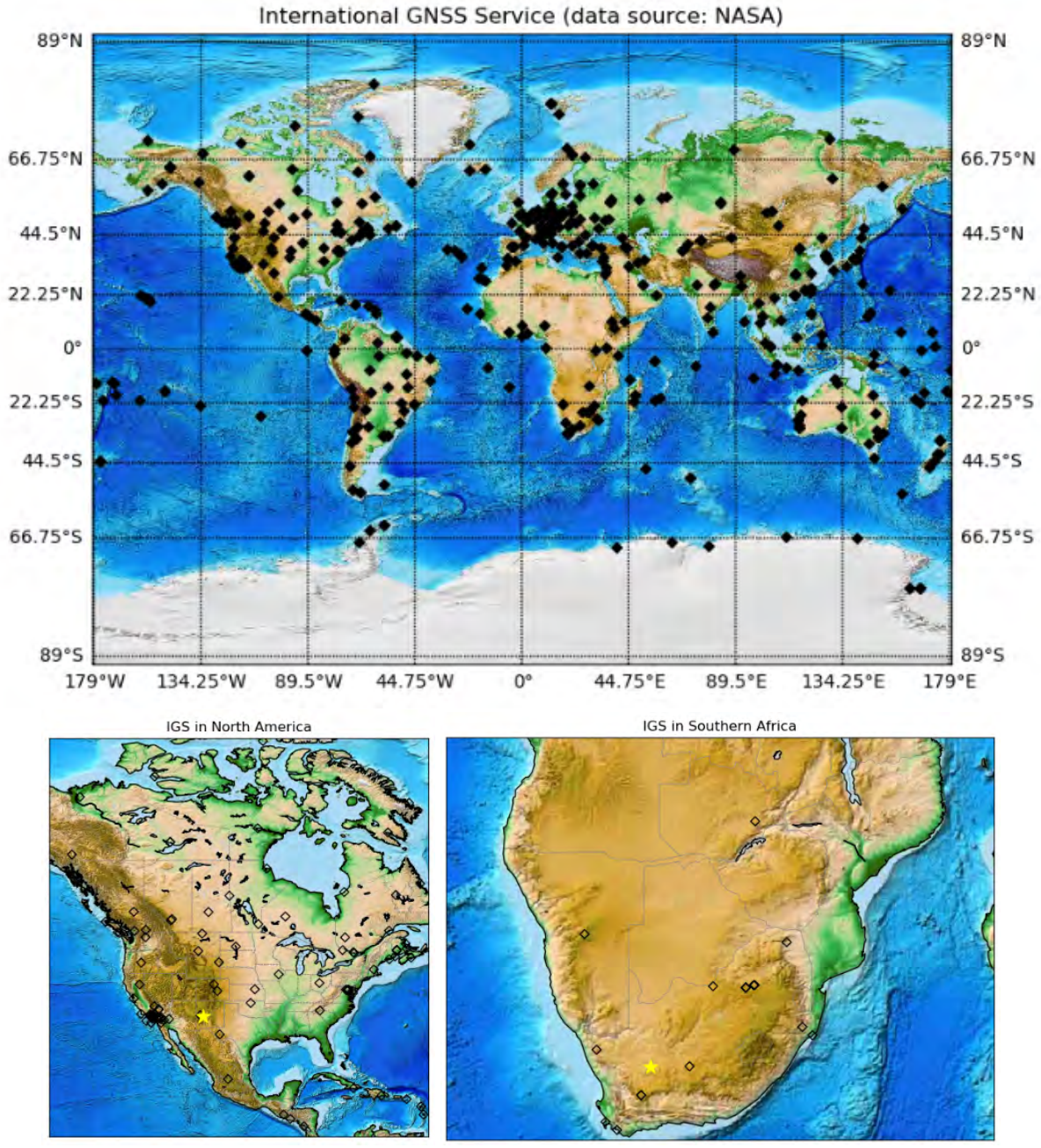

Figure 2.9: International GNSS Service stations worldwide (top), North America (bottom left) and Southern Africa (bottom right). JVLA and MeerKAT site positions are plotted as yellow markers. Data courtesy of NASA's online database (available at `https://network.igs.org/`).

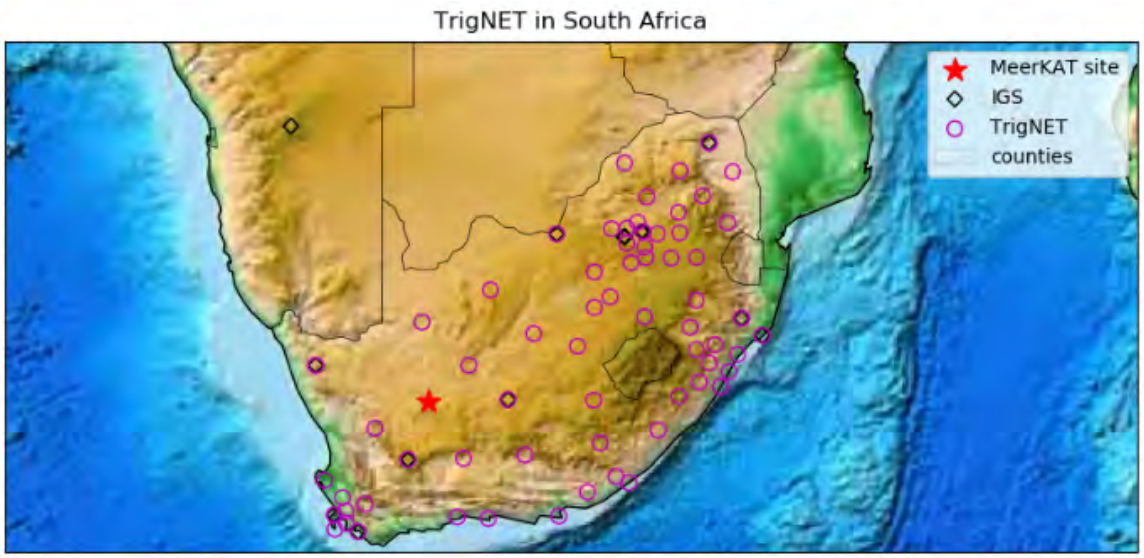

Figure 2.10: All available TrigNET stations in South Africa, as operated by the Department of Agriculture, Land Reform and Rural Development as of 2022.

measurements using these stations are made.

The Global Positioning System [92, and references therein] operates on two primary broadcasting frequencies[19]. These are (primarily) L1 (1575.42 MHz or 19 cm) and L2 (1227.60 MHz or 24 cm). Determination of the range to a satellite depends on measuring the propagation delay for the signal to travel between the satellite and receiver. The GPS satellites operate in circular orbits at an altitude of 22,000 km. Satellite orbital parameters are computed by the Control segment of the service and distributed globally.

Two pseudo-random codes are modulated on the carrier signals. These are the coarse acquisition Civilian Access ("C/A") code on the L1 band and a much longer (37 weeks) high bit-rate Precision ("P") code which is split between satellites in the constellation to prevent spoofing. The codes are used to establish a coarse timing alignment between the receiver and transmitter which gives a coarse pseudo-range between the ground station and each satellite. The (much higher frequency) phase of the carrier is used to increase the precision of the timing on the receiver end.

The ionosphere acts as a smooth-gradient dispersive medium, where the signal path delay[20] can be measured (in meters):

$$\Delta r = 40.3\mathrm{TEC}/\nu^2 \tag{2.3}$$

To give a concrete example, a (slant) column density of 1 TECU towards the satellite results in a path delay of 16.3 cm in the L1 band and 26.7 cm in the L2 band. This yields a pseudo-range difference of 10.4 cm for every 1 TECU of electrons encountered along the line of sight.

Each RINEX-stored measurement contains pseudo-range measurements from code (indicated below as "P") and carrier phase (ϕ) (the beat frequency between the carrier of the satellite signal and receiver-generated reference frequency) on both L1 and L2 bands. Errors exist on both due to internal satellite and receiver oscillator drifts, and external influences such as the ionospheric and Tropospheric-induced delay, multipath (environmental reflections as seen by an omni-directional

2022 due to network issues with the external telecommunications provider. This includes the DEAR station at De Aar, Northern Cape Province.

[19]GLONASS operates on similar G1 and G2 bands, although the frequencies that each satellite operate at are not identical to the American counterpart.

[20]The delay shown here is a truncated version of the Appleton-Hartree magnetoionic dispersion equation. Accurate up to cm-level the formalism discards geo-magnetic contributions three and more orders less than the frequency-dependent term. See [92, and references therein] for a derivation.

antenna) and phase wrapping. Much more detail of this is given in [60, 70, 142, 96, 92]. We draw a discussion on the observables from [92] here for convenience of the reader.

The pseudo-range measurements on the L1 and L2 bands are given as

$$\begin{aligned} P_1 &= r + c.\Delta T + d_{\text{ion}} + d_{\text{trop}} + b_{s_i,L1} + b_{r_j,L1} + m_{P1} + \varepsilon_{P1} \\ P_2 &= r + c.\Delta T + \left(\frac{\nu_{L1}}{\nu_{L2}}\right)^2 d_{\text{ion}} + d_{\text{trop}} + b_{s_i,L2} + b_{r_j,L2} + m_{P2} + \varepsilon_{P2} \\ P_1 - P_2 &\approx \left[1 - \left(\frac{\nu_{L1}}{\nu_{L2}}\right)^2\right] d_{\text{ion}} + \left[b_{s_i,L1} - b_{s_i,L2} + b_{r_j,L1} - b_{r_j,L2}\right] + \dots \end{aligned} \tag{2.4}$$

Here:

- r is the distance between the receiver and transmitting satellite
- ΔT is the absolute time difference between receiver and transmitter clocks
- ν_{L1} and ν_{L2} are the operating frequencies of the bands
- d_{ion} is the ionospheric dispersive delay
- d_{trop} is the Tropospheric delay
- b_{r_j} is the j^{th} receiver instrumental delay per band
- b_{s_i} is the i^{th} satellite instrumental delay per band
- m is the multipath (ground reflection) error near the horizon on the pseudo-range
- ε is the receiver noise on the pseudo-range

The absolute clock offsets between receiver and transmitter is not important in Eqn. 2.4, and when the receiver and transmitter clock delays b_{s_i} and b_{r_j} are accounted for, the measure is an unambiguous insensitive measure of the ranging between satellite and receiver. Multipath effects come into play close to the horizon and we, therefore, specify a cutoff in satellite elevation when computing pseudo-ranges. Combining Eqn. 2.4 and 2.3 we get the following relation between pseudo-range and ionospheric TEC.

$$\text{TEC}_P = 9.52(P_2 - P_1) \tag{2.5}$$

Similarly, the carrier phase measurements between the bands are

$$\begin{aligned} \phi_1 &= r + c.\Delta T + (c/\nu_{L1})N_{L1} - d_{\text{ion}} + d_{\text{trop}} + \Delta\phi_{s_i,L1} + \Delta\phi_{r_j,L1} + m_{\phi 1} + \varepsilon_{\phi 1} \\ \phi_2 &= r + c.\Delta T + (c/\nu_{L2})N_{L2} - \left(\frac{\nu_{L1}}{\nu_{L2}}\right)^2 d_{\text{ion}} + d_{\text{trop}} + \Delta\phi_{s_i,L2} + \Delta\phi_{r_j,L2} + m_{\phi 2} + \varepsilon_{\phi 2} \\ \phi_1 - \phi_2 &\approx (c/\nu_{L1})N_{L1} - (c/\nu_{L2})N_{L2} + \left[\left(\frac{\nu_{L1}}{\nu_{L2}}\right)^2 - 1\right] d_{\text{ion}} + \left[\Delta\phi_{s_i,L1} - \Delta\phi_{s_i,L2} + \Delta\phi_{r_j,L1} - \Delta\phi_{r_j,L2}\right] + \dots \end{aligned} \tag{2.6}$$

Here:

- N_{L1} and N_{L2} are the unknown cycle counts from the reference alignment point in phase
- $\Delta\phi_{s_i}$ and $\Delta\phi_{r_j}$ are the instrumental phase error on the i^{th} satellite and j^{th} receiver
- Phase multipath m per band

- Phase noise ε per band

Notice that the signage between the relations between pseudo-ranges and phases are reversed in relation to ionospheric dispersive delay in Eqns. 2.4 and 2.6. The carrier phase is an ambiguous term for which we indicate an unknown cycle counter N_{L1} and N_{L2}, but is more precise than the pseudo-range. The latter has a bit-rate of 10.23 MHz for the P and C/A codes — two orders of magnitude below the phase cycle rate. Again we can directly relate the differences in phases to TEC, once the phases are locked for receiver/transmitter pairs in Eqn. 2.7.

$$\mathrm{TEC}_{\phi} = 9.52(\phi_1 - \phi_2) \tag{2.7}$$

Corrections for bias induced by the ground stations and satellite delays can be done by assuming receiver and satellite errors are systematically random, spatially uncorrelated and relatively stable. It is further assumed that ionospheric correlations are spatially smooth and have a strong elevation dependence. Corrections for receiver-transmitter delay biases are then solved for on short time scales (default of 5 minutes inside ALBUS). Following [102, 92] the phases can be de-biased / levelled per satellite / receiver pair, on a contiguous (phase-connected) arc (sampled in n intervals along a portion of satellite track for n an even number of samples) as follows:

$$\mathrm{TEC} = \mathrm{TEC}_{\phi i} - \frac{\sum_{j\in[-n/2,n/2]} w_j(\mathrm{TEC}_{\phi j} - \mathrm{TEC}_{Pj})}{\sum_{j\in[-n/2,n/2]} w_j}$$

Here $i \in [1,n]$ starts at the beginning of the arc and p are weights.

ALBUS assumes that satellite clock biases are usually already corrected internally, but that receiver biases (especially those not registered on the IGS) are not yet corrected for reference frequency errors. Such biases are in the range of 10s of TECU and are minimized between available stations, assuming the thin-shell model already discussed. Once biases are corrected the rotation measure is solved for using the IGRFv13 and a PIM 3D model of the ionosphere (mode `RI_G03`) with the current space weather information ($F_{10.7}$ from the DRAO corrected to 1 AU) and Heliospheric model data from NASA[21]. We found significantly less measurement scatter (on the order of 5 degrees at 600 MHz) in assuming a full 3D model of the ionosphere.

We show a comparison between JPLG [108] (downloaded via AIPS [58]) and UQRG [114] databases for the same thin-shell height of 450 km and computed using the World Magnetic Model as predicted through RMEXTRACT[106] [22]. We do not show CODE [41] databases here which we have found give RM significantly larger than both JPLG [108] and UQRG [114] databases and predicted values from direct measurement with ALBUS in Fig. 2.11. There were 9 contributing TrigNET stations for the ALBUS measurements shown for the South African site. There were 9 contributing stations from the IGS and EarchScope Consortium of the United States National Science Foundation. In addition to JPLG [108] predictions via RMEXTRACT[106] we overplot the AIPS [58] prediction of ionospheric changes towards source between distributed measurements for completeness for the same database for the MeerKAT observation. The latter RM is predicted using IGRFv13 as the magnetic field model (same as in use in ALBUS). A long-term comparison between ALBUS, JPLG [108] predictions via AIPS [58] `TECOR` JPLG [108] and UQRG [114] predictions using RMEXTRACT[106] will be discussed in the results section, 2.4.4.

Fig. 2.11, and an analysis of the application of the displayed solutions, shows the following for two observations of 3C286 at the MeerKAT and VLA sites:

[21] We thank Tony Willis for his help in updating these databases, as well as changes necessitated by naming conventions and RINEXv3 support in the software. Up to date space weather can be retrieved from: `ftp://ftp.seismo.nrcan.gc.ca/spaceweather/solar_flux/daily_flux_values/fluxtable.txt` and `http://omniweb.gsfc.nasa.gov/form/dx1.html`

[22] The JPLG [108] database is downloaded through AIPS [58] and manually loaded into RMEXTRACT[106] by manipulating the filename of the cached download in order to use the same magnetic field model for comparison between the databases.

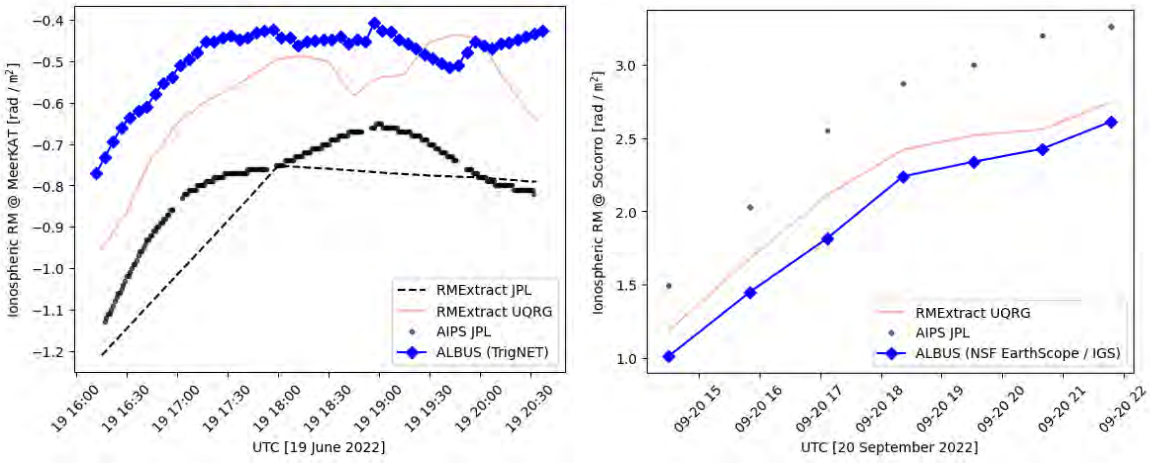

Figure 2.11: Comparison between JPLG [108] and UQRG [114] databases at the MeerKAT site towards 3C286 for a long observation taken 19 June 2022 and direct measurement using ALBUS with the theoretical PIM model of the ionospheric profile (left). Comparison between JPLG [108], UQRG [114] and ALBUS for a long observation on 20 September 2022 on the JVLA using data from NSF EarthScope consortium with the theoretical PIM model of the ionospheric profile (right). Overall we see a slight offset between the two IONEX-databases. Three-layer JPLG [108] databases are aggregated, and distributed (via the CDDIS) at much lower cadences than UQRG [114] databases. ALBUS data is bias-corrected, filtered and computed at 5-minute intervals.

- The internationally distributed (IGS-derived) models, as well as the local direct measurement using the TrigNET and NSF EarthScope beacon networks track diurnal variability in the ionospheric TEC.
- Residuals computed show how many rad m^{-2} variability in the ionosphere is reduced after application of derived solutions. However, it is clear that there is a discrepency between the absolute scales on the induced Rotation Measure even between the various databases, derived from the same IGS stations.
- We plotted the application of JPLG [108] databases using both AIPS [58] and RMEXTRACT [106] packages. AIPS performs an interpolation of the ~ 2 hour cadence JPLG databases, however the RM (computed at an ionospheric height of 450 km) is nearly exactly the same between the two pieces of software at the sampling interval on the same database. This shows that there is a substantial difference between the absolute scales of the UQRG [114] and JPLG fits to the same IGS data products.
- Direct measurements from the local beacon networks in South Africa and the United States on various days show that the absolute scale between locally derived products and various global models do not seem to show a preference to one product — on some days local measurements were closer in absolute scale to JPLG compared to UQRG and on other days this was reversed.

2.3.4 Earth magnetic field models

An analysis of the differences in predicted RM between the different packages (AIPS [58] TECOR[23], RMEXTRACT[106] and ALBUS) is incomplete without a discussion of the differences contributed to by the assumed magnetic field models. The magnetic field is a vector quantity which points towards the observer in the northern hemisphere and points away from the observer in the southern hemisphere. The observed ionospheric contribution should therefore be positive (EVPA increasing counterclockwise with wavelength) in the north and negative in the south.

Fig. 2.12 shows a map of the quadrature magnetic field strength from the IGRF version 13 for an altitude of 450 km

[23]It is noted that prior to version 31DEC2023 AIPS [58] used a simplified dipole model of the magnetic field strength (which markedly excluded the South Atlantic Anomaly) dating back to 1965. We thank Eric Greisen for adapting the TECOR task to provide the IGRFv13 as option (via setting "APARM" as 0 0 1) as of 31DEC2023. An additional AIPS [58] verb, "MFIMG", is now available to plot the magnetic field.

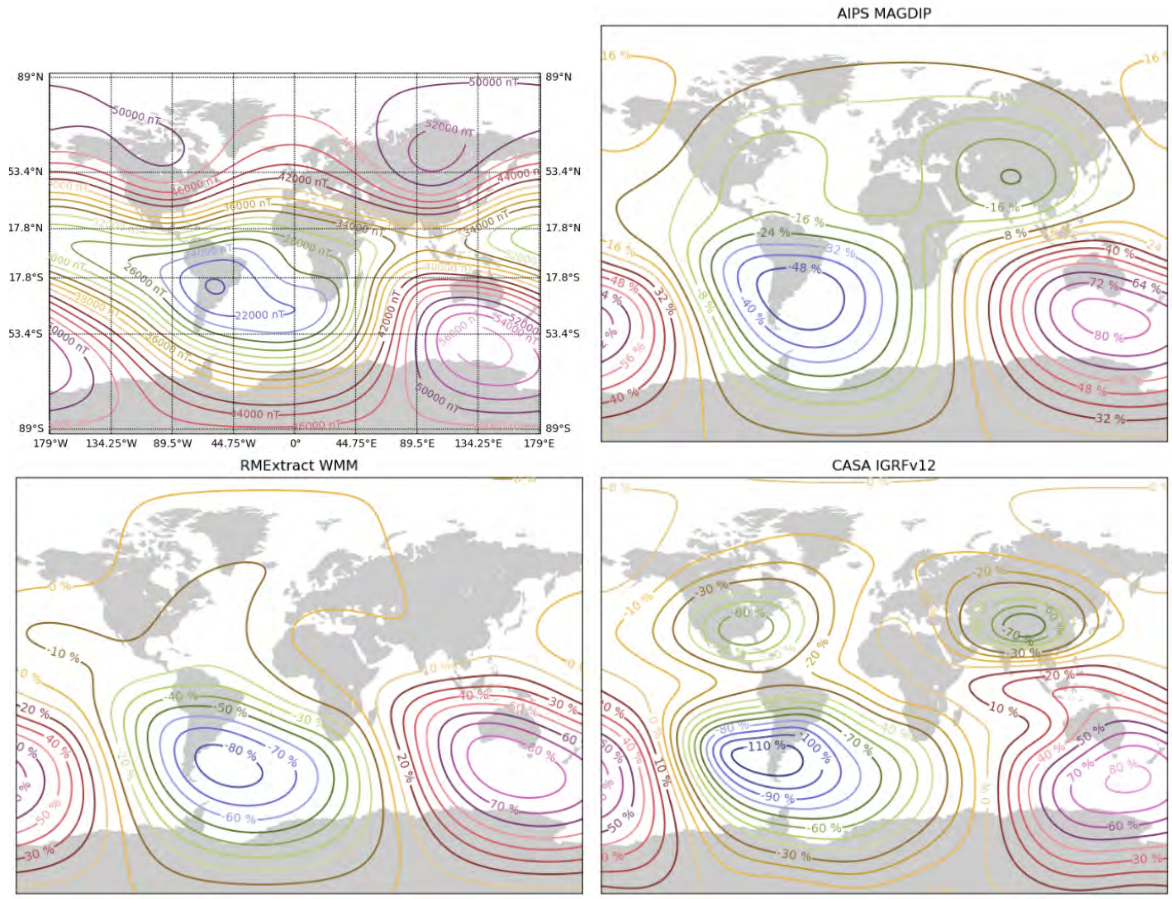

Figure 2.12: (Top-left) Global magnetic field strength as predicted by the IGRF version 13 (as of Dec 2019) includes models for the annual rate of change in field strength, but only needs updating on a many year cadence. This is taken as the reference model for comparison to implementations in CASA [104], AIPS [58] and RMEXTRACT [106] packages, with differences shown in the remaining panels. (Top-right) Difference map for the outdated simplified AIPS [58] dipole model (default). (Bottom-left) World Magnetic field model, as in use by RMEXTRACT[106] (default). (Bottom-right) Difference map for the out of date IGRFv12 model in use in casacore (and CASA [104]). In all cases the percentage difference quoted is the offset with respect to the IGRF version 13 relative to the global magnetic field strength range. In all cases a height of 450 km above mean Earth surface is picked as the evaluation height.

above mean surface height (top-left). Differences between the IGRFv13 and the various magnetic field models within the different pieces of software are shown: the outdated AIPS [58] dipole "MAGDIP" model, outdated casacore (and therefore CASA [104]) IGRFv12 and World Magnetic Model (WMM) in use with RMEXTRACT[106]. The resultant magnetic field errors have very little impact at both the Socorro and Karoo sites. In Fig. 2.13 we show a comparison of ALBUS predicted RM using the AIPS [58] MAGDIP field model[24] and the IGRFv13 using the same RINEX data as input for the Karoo site. In both observations, the impact of the choice of magnetic field model on the predicted Rotation Measure is about an order of magnitude smaller than the variation between TEC models.

2.4 Interferometric measurements of 3C286, Moon, Mars and Venus

In this Section we present the following:

- Sub-section 2.4.1 outlines a schedule of observations used in this study
- Sub-section 2.4.2 establishes an independent measurement of the leakage contribution as a function of radial offset

[24]Compiled to the C language from original AIPS [58] Fortran using the F2C compiler version 20160102 with the convention for the B field bases vectors and quantities changed to match what is required by ALBUS internals in the C++ layer.

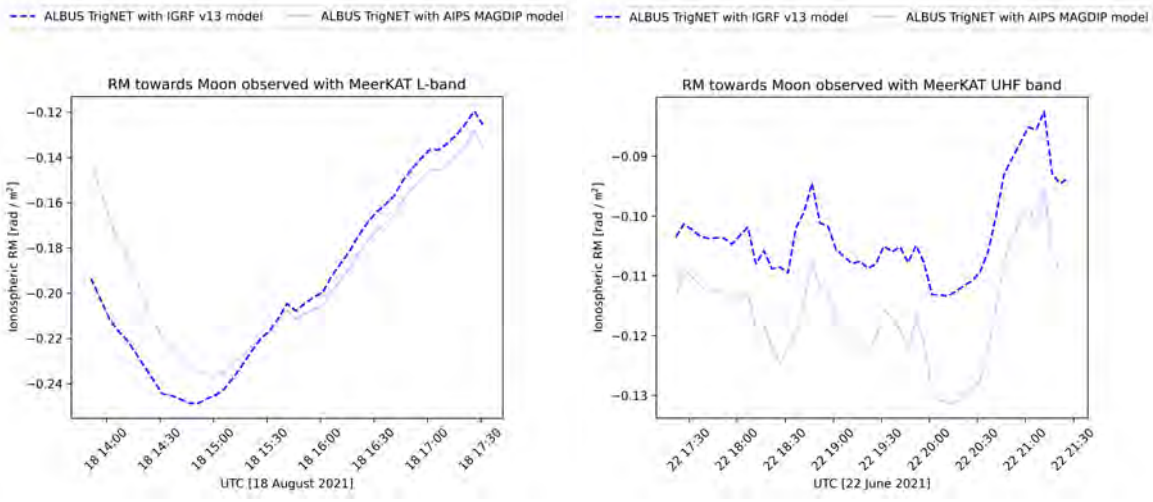

Figure 2.13: Direct comparison of "MAGDIP" simple dipole and IGRFv13 magnetic field models towards the Moon using ALBUS. RINEX data out to 350 km are taken from TrigNET. The magnetic field model makes minimal difference at the South African site.

from the pointing center. This is important to establish since we are measuring the EVPA offset of the polarized Lunar limb out to $\sim 15'$ from the tracking centre.

- Sub-section 2.4.3 presents our fits to the offsets induced by the ionosphere and any misalignment of the MeerKAT feeds from the nominal IAU basis from UHF to S0 bands, as well as the offsets observed using the Moon, Venus and Mars in VLA data. We additionally discuss the differences in calculating these corrections between linear and circular receiver systems.
- Sub-section 2.4.4 presents our final joint VLA/MeerKAT model of 3C286, inclusive of ionospheric corrections (per scan, based on GNSS measurement to capture spatio-temporal variability in the ionosphere) and feed misalignment (fitted from the refraction-polarized radial Lunar emission) in MeerKAT data. We show that residual error from ionospheric corrections are the main limiting factor in accurate measurement of the EVPA.

2.4.1 Observations and calibration

To measure the fractional linear polarization and the EVPA of 3C286 (J1331+3030), as well as qualify the handedness conventions and off-axis leakages, we received substantial engineering observation time on the JVLA and MeerKAT telescopes. In the instances where the Moon, Venus or Mars were observed, we included a nearby compact phase calibrator particular to the observation time[25]. This is important because the visibility transfer function of a pillbox shaped object such as the Moon or planets is a Bessel function, which rapidly decays towards longer spacings. This makes self-calibration of the intermediate spacings practically impossible[26]. The observations are summarized in Table 2.1.

The choice of the observed object and observing time (in the case of Mars and Venus) depends on both the resolution and the extent to which the antenna primary beam attenuates the object. With its 25 m primary reflectors, the JVLA can only effectively observe the Moon in L-band (at S-band and beyond the limb falls too far into the roll-off of the primary lobe). To observe the Moon, the JVLA additionally has to be in D-configuration, due to a lack of core spacings matching

[25] We thank the scheduling and operational teams at both instruments for their assistance in planning and executing these non-regular technically challenging imaging observations.

[26] Although it is possible to adjust flagged solutions on long spacing dominated antennas to unity manually the combined challenge of imaging a flat pillbox through conventional Multiscale Clean and negligible power on the long spacings proved to be tricky (and not strictly necessary) for the purpose of these observations due to the observations not being dynamic range limited. It can be pointed out that a Bessel function may be fitted to the visibilities and subtracted, but implementing this is beyond the scope of this analysis. In all instances we show and measure the linear EVPA off dirty maps of the transfer-calibrated (1GC) Moon.

Table 2.1: Observation schedule for the Lunar, planetary and 3C286 observation program

Observation	Timespan	Phase calibrator	Other calibrators	Bandwidth / Band	Telescope / Config
Lunar*	31 May 2021 08:42 to 15:12	J2131-2036	J1331+3030, J1407+2827, J0521+1638	1-2 GHz	JVLA D
* Note: This L-band observation had the phase calibrator occluded by the Moon for part of the observation due to an issue with the JVLA OPT.					
Lunar	20 September 2022 14:20 to 21:53	J0854+2006	J0521+1638, J1331+3030, J1407+2827	1-2 GHz	JVLA D
Venus	03 March 2022 12:28 to 17:16	J1949-1957	J1331+3030, J1407+2827	1-2 GHz (L) 2-4 GHz (S)	JVLA A
Mars	14 April 2022 11:15 to 17:36	J1528-1501	J1331+3030, J1407+2827	4-8 GHz (C) 8-12 GHz (X)	JVLA A
Lunar	22 May 2021 22:06 to 22:33	None	J1331+3030, J1939-6342	0.86-1.71 GHz (L)	MeerKAT
Lunar	18 August 2021 13:31 to 17:28	J1833-2103	J1331+3030, J1939-6342	0.86-1.71 GHz (L)	MeerKAT
Lunar	22 June 2021 17:01 to 21:23	J1733-1304	J1331+3030, J1939-6342	0.54-1.09 GHz (UHF)	MeerKAT
Lunar**	26 June 2021 19:11 to 23:35	J2052-3640	J1331+3030, J1939-6342	1.75-2.63 GHz(S0)	MeerKAT
** Note: This S0-band partially failed due to being digitally saturated in the correlator's channelizer accumulators. Roughly half the Lunar scans were unusable as a result. The operations team reset the attenuation settings mid-observation. Special care was taken to perform the amplitude scaling on the calibrator scan of 3C286.					
Lunar	4 September 2022 11:56 to 15:58	J1733-1304	J1331+3030, J1939-6342	1.75-2.63 GHz (S0)	MeerKAT
Lunar	2 September 2022 11:55 to 15:57	J1517-2422	J1331+3030, J1939-6342	2.41-3.28 GHz (S3)	MeerKAT
Handedness	19 June 2022 16:17 to 20:31	N / A	J1331+3030, J1939-6342	0.54-1.09 GHz (UHF)	MeerKAT Subarray
Handedness	19 June 2022 16:16 to 20:32	N / A	J1331+3030, J1939-6342	0.86-1.71 GHz (L)	MeerKAT Subarray
Handedness	18 June 2022 16:20 to 20:36	N / A	J1331+3030, J1939-6342	1.75-2.63 GHz (S0)	MeerKAT
Off-axis leakage qualification	31 January 2023 00:37 - 05:43	N / A	J1331+3030, J1939-6342	0.54-1.09 GHz (UHF)	MeerKAT Subarray
Off-axis leakage qualification	14 August 2022 11:43 to 16:55	N / A	J1331+3030, J1939-6342	0.86-1.71 GHz (L)	MeerKAT
Off-axis leakage qualification	31 January 2023 00:37 - 05:46	N / A	J1331+3030, J1939-6342	1.75-2.63 GHz (S0)	MeerKAT Subarray
Off-axis leakage qualification	23 January 2023 01:12 to 06:17	N / A	J1331+3030, J1939-6342	2.19-3.06 GHz (S2)	MeerKAT Subarray
Off-axis leakage qualification	23 January 2023 01:08 to 06:16	N / A	J1331+3030, J1939-6342	2.63-3.5 GHz (S4)	MeerKAT Subarray

the apparent angular scale of the Moon. Both Venus and Mars were observed at A-configuration at a time close enough to orbital perigee in order to limit depolarization by the interferometer synthesized beam (a factor of 10-20 synthesized beams is sufficient for our purposes). It can be noted that for Venus B-configuration data would have been more optimal at S-band in order to optimize the range of spacings available at the desired resolution.

Although the primary reflector is about half the size of that of the VLA (nearly doubling the effective FoV), MeerKAT's limited resolution only enables us to observe the Moon. MeerKAT can only effectively observe the Lunar limb up to the S0[27] band. Although we included an S3-band observation, the Lunar limb was of insufficient SNR due to insufficient UV-coverage at large scales at S3 frequencies.

The observations of the Moon, Venus and Mars followed a semi-standard imaging observation layout where we have a primary, a polarization (HV phase and RL angle for MeerKAT and JVLA respectively) and secondary calibrator along with the observed planetary / planetoid body. The Moon, Venus and Mars were all tracked at the center of the body with the telescope correlator system in the frame of the body's non-celestial ephemeris. These are used to fit for global offsets induced by the feed alignment in the frame of the sky. We point out, however, that the number of scans on 3C286 within these observations are not enough to fully quantify the error in measurement induced by ionospheric correction residuals — a number of the early observations (markedly those in UHF and L-band) only have 2 tracking scans on 3C286.

After measuring the EVPA offsets using the the Moon (results discussed later in Section 2.4.3) and MeerKAT handedness established, as per EVLA memo 219 [128], we use the multi-hour observations marked "Handedness" and "Off-axis leakage qualification" to measure the residual error in the ionospheric-corrections on 3C286. In both observation groups, 3C286 is observed through a wide range of parallactic angles across a transitory arc. In the case of the handedness observations the observation flipped between scans of 3C286 and our flux, bandpass and relative leakage calibrator PKS B1934-638 for the span of the observation. The off-axis leakage observations were set up in such a way that we include scans on PKS B1934-638, 3C286 and 10 offset positions of 3C286 linearly spaced out to 0.5 degrees in declination. The strategy is repeated in round-robin fashion for the span of the observation.

It is important to point out a substantial difference between the designs of the JVLA and MeerKAT: in the case of the JVLA the instrument and correlator design makes sequential multi-band observation possible, with switching taking about 10-20 seconds. This is in contrast to MeerKAT, where only a single band can be observed with antennas included in the same array. Where concurrent MeerKAT multi-band observations are indicated in Table 2.1, the array was split into two independent subarrays[28] with a roughly 50:50 split of available antennas.

The JVLA observations were calibrated using AIPS [58]. The basic workflow is briefly discussed in Appendix D.2 of this document. The MeerKAT data, apart from the off-axis leakage datasets, were all independently reduced in CASA [104] and AIPS [58] to guard against software or method inconsistencies. The reduction workflows are discussed in Appendix D.1 of this document. Both the reductions and instruments agree well within the error bars. The error is driven mostly by uncertainties in ionospheric corrections to the EVPA at the lower end of the observed frequency range.

2.4.2 Off-axis leakages, HV phase calibration and absolute leakage calibration limitations on MeerKAT observations

Part of this section was distributed to the observatory as a note dated 7 February 2023[29] for the benefit of the user community before the 2023 open time call. We include the same discussion of off-axis leakages due to multi-modal limitations to the wideband OMT design in use by the MeerKAT telescope, because it is necessary to quantify errors.

[27] With the MeerKAT system the observer is restricted to only observing a subband of the available S-band bandwidth during an observation (per sub-array)

[28] In this mode of operation the subarrays effectively act as independent telescopes with their own allocated resources (from antenna, through correlator and Science Data Processor). The mode is regularly used by the Thousand Pulsar Timing (TPA) array.

[29] Available here: `https://docs.google.com/document/d/1vhO99l2uqX9T7iQRosuyk-lPpyJPYWs2Ct1qVQ8NmtE/edit?usp=sharing`

One of the most prominent drivers of error on the linear angle measurement is the crosshand phase (systemic ellipticity) induced by the instrument between the two feeds. This can be calibrated, assuming that the polarized calibrator (a quasar here) should have little to no intrinsic circular polarization. A model of the linear flux is not strictly necessary[30]. Under these assumptions, the residual circular flux can, typically, be calibrated to two orders of magnitude below the total linear power after carefully calibrating the time and spatially variable phases using the known position of the sources and gradually building sky models in Stokes I in the process discussed in Appendix D.1 of this document. Whether the assumption on minimal circular power of quasars, like 3C286, holds is worth checking by transference onto the Moon — where we expect little intrinsic circular polarization through the radial refractive process induced by the regolith, discussed in Section 2.2. The result is shown in Fig. 2.14.

The off-axis leakage performance of the MeerKAT telescope was verified in the observations indicated as "off-axis leakage qualification" in Table 2.1. We observe 3C286 pointings at raster offset positions, in declination only, for an LST span of 5 hours, cyclically alternating between PKS B1934-638, 3C286 and 10 offset positions. This allows for a large sweep of the far-field response over the offset positions as a function of parallactic angle,[31] and allows us to check for temporal variability induced by leakages both on and off-axis. For all offset positions we rephase the observations to fringe stop on the position of the source (thus the source dominates in the real part of the visibilities, without the need for imaging).

We show, for UHF, L, S0, S2, and S4 bands the frequency dependence of off-axis leakages (mainly from diagonal Stokes I into diagonal Q and off-diagonal U). The red curves in Figs. 2.16, 2.18, 2.20, 2.22 and 2.24 indicate the mean linear ($\sqrt{Q^2+U^2}$) polarization fraction on-axis. As we move off the pointing axis the variable cross-hand polarization sweeps over the source as a function of frequency and / or time, inducing a variability that cannot easily be removed due to unknown observables: squint, frequency-dependent reference pointing, and per receiver OMT multimodal and optical characteristics through all bands (up to date measurements of the latter is not yet available for use by the user community although average products have been published, see [47]). We summarize the scatter as a function of offset (with the antenna primary lobe FWHM at the high end of each band indicated[32]) in Fig. 2.15. Results showing the leakage-induced frequency structure for UHF, L, S0, S2 and S4 are shown in Figs. 2.16, 2.18, 2.20, 2.22 and 2.24 respectively. Breakdowns showing the scan-average parallel and crosshand visibility terms (with leakages from total intensity dominating the frequency structure seen in the crosshand terms), are shown in Figs 2.17, 2.19, 2.21, 2.23 and 2.25. Overall these results match well the instrumental polarization behaviour reported by [46] from holographic measurement and serves as independent measure of system off-axis performance.

It is clear that for all usable Lunar data captured at UHF, L and S0-bands the band average leakage at the average Lunar radius of 0.26 degrees is about 1% or less. The expected error induced on the measured EVPA on the limb is at the level of 2 degrees at most across all three bands. The contribution of frequencies above 1.46 GHz is removed by the fitting procedure in the case of L-band.

[30] A simple mathematical derivation from Jones calculus shows that the crosshand phase is given by $\arctan(V/U)$ under the assumption of 0 intrinsic circular polarization. See the discussion in EVLA memo 219 [128] for more details.

[31] Due to the alt-azimuth mounts employed, the antenna far field response effectively rotates around the pointing axis as a function of parallactic angle for all positions on sky sufficiently far away from the pole (where parallactic angle becomes highly direction dependent).

[32] For the reader's reference, the following are the FWHM of the antenna primary beams for the various bands at highest frequency: UHF 0.7°, L-band 0.5°, S0 0.31°, S2 0.25° and S4 0.22°

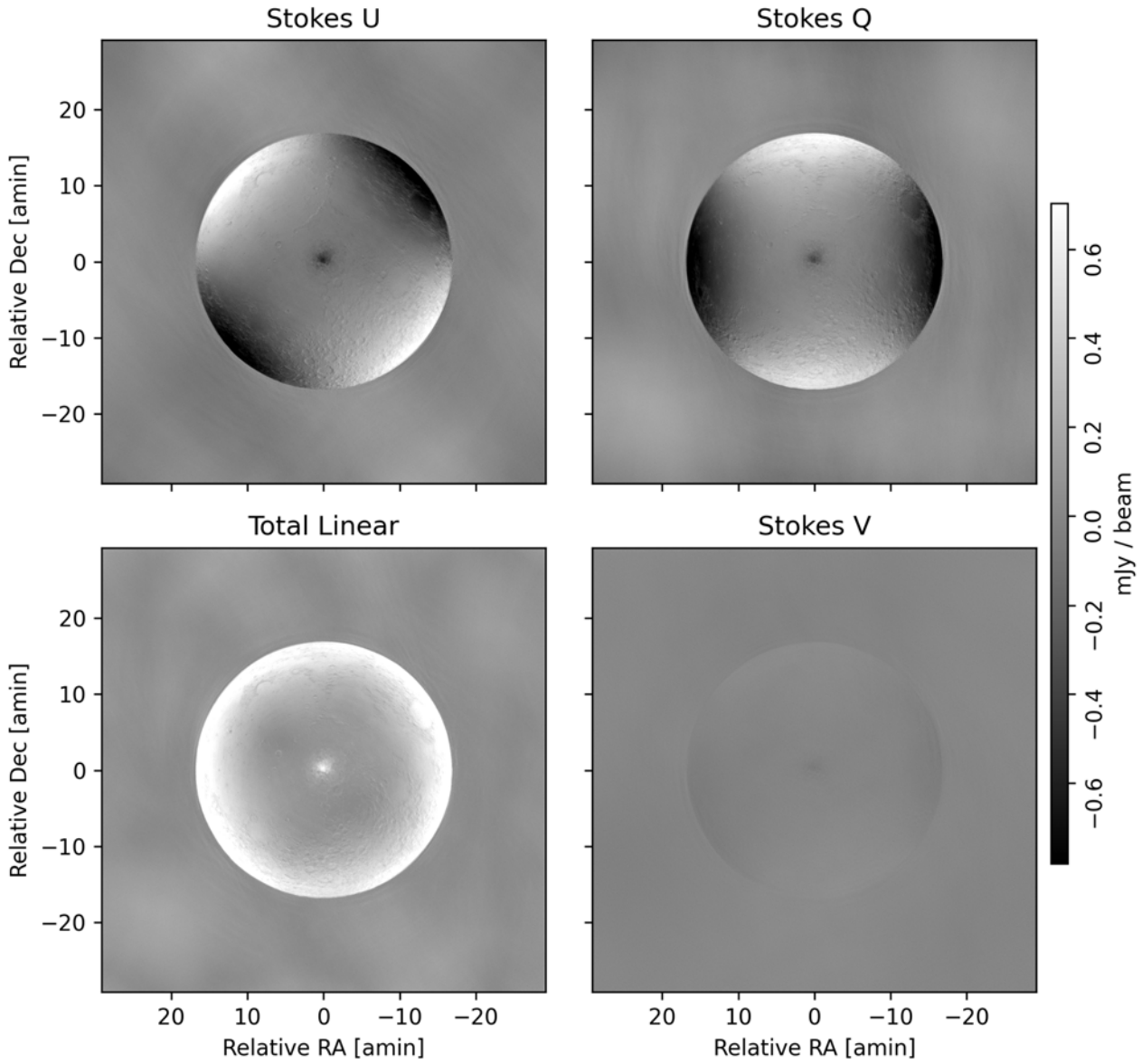

Figure 2.14: (Locked to the same minima and maxima, left to right, top to bottom) Stokes U, Q, total linear power, Stokes V Multi-Frequency-Synthesis ("MFS") maps of the Moon at 816 MHz (UHF). The images are corrected for the rotational effects of parallactic angle and MeerKAT handedness convention issues as discussed in EVLA memo 219 [128]. Up is in the direction of increasing declination towards NCP and right is east towards increasing right ascension. As expected vertical Q is positive north rotating counter-clockwise (north through east) through $+U$ (45 degrees) to horizontal $-Q$ at an EVPA of 90 degrees. There is little to no elliptical polarization visible at the limb as expected after transference. The bright spot at the center is reflected terrestrial RFI.

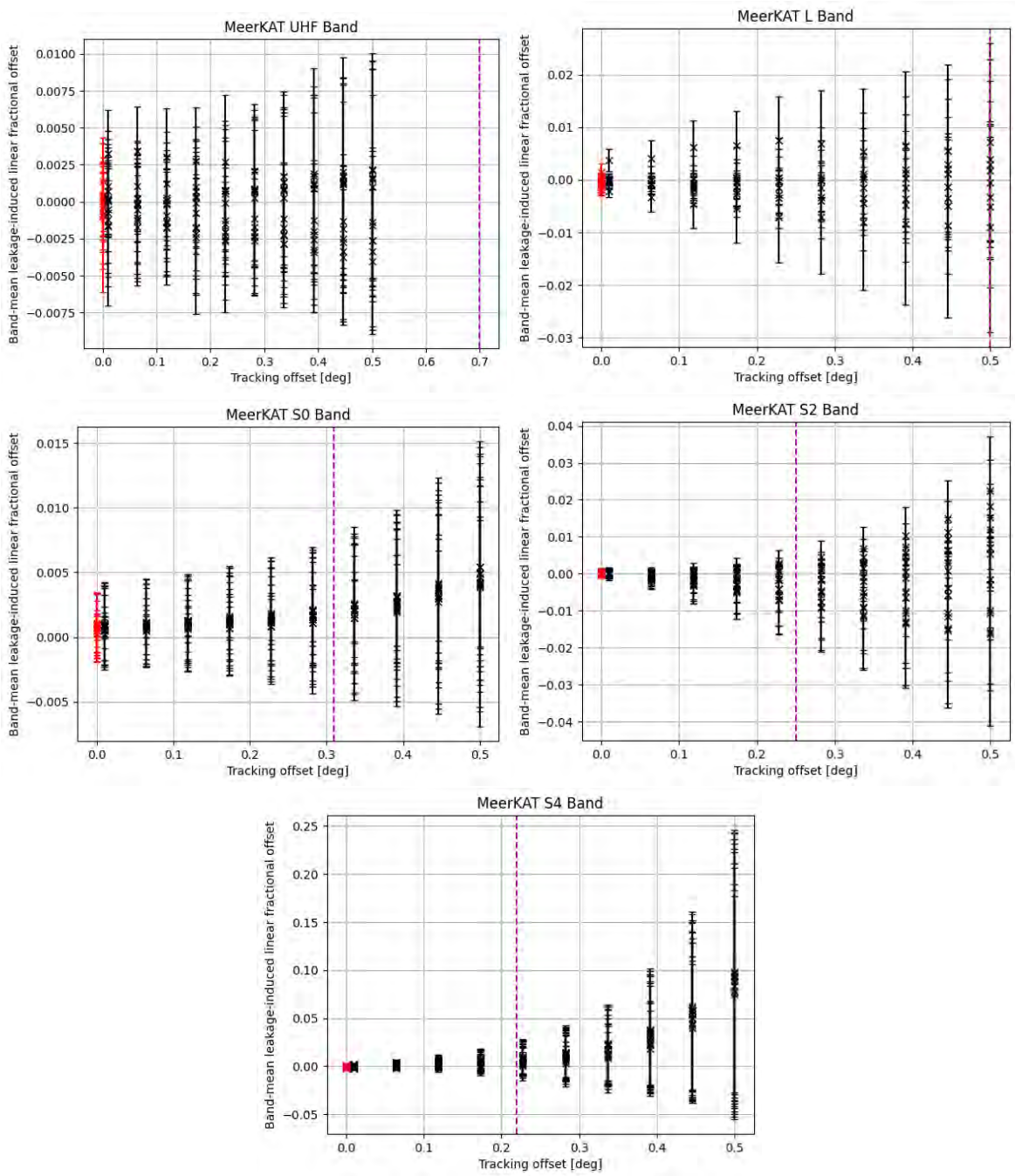

Figure 2.15: MeerKAT off-axis leakage performance across UHF, L, S0, S2 and S4-bands out to a separation of 0.5 degrees. Throughout we show the FWHM of the antenna primary beam at the highest frequency of the band as a vertical magenta line for performance comparison relative to effective observable sky area. On-axis measurement scatter from the mean is shown in red. The scatter on-axis is indicative of the level of contribution from gain errors, save for UHF where the structure seems to be mainly dominated by field sources. Scatter beyond the on-axis levels in the off-axis measurements are due to leakage. It is worth noting leakage on the off-axis positions at 2% level or lower at 0.25 degrees on all bands, save for S4. This implies that our Lunar limb measurements should be relatively free of leakage contribution. See also Figs. 2.16 through 2.24.

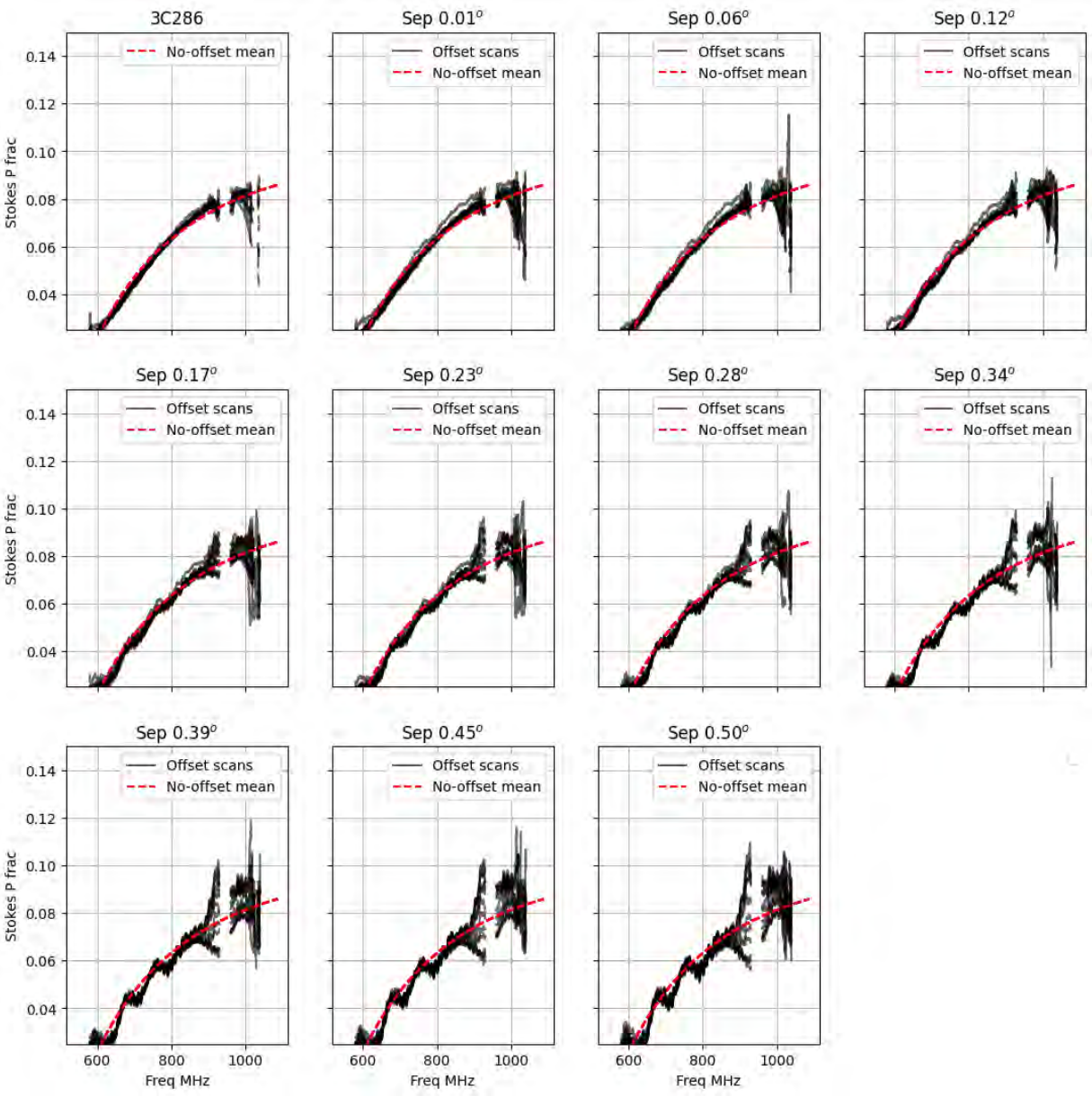

Figure 2.16: MeerKAT off-axis performance out to a separation of 0.5 degrees from the pointing center for UHF band (FWHM 0.7 deg at highest frequency). Per scan averages are shown in gray curves for the 5-hour round-robin visits to each offset position, observing the offset position through various parts of the antenna beam as a result. The average on-axis response (shown top-left) is fitted and overplotted at all offset pointings for reference. Some sub-percent rippling is seen above 0.23 degree offset.

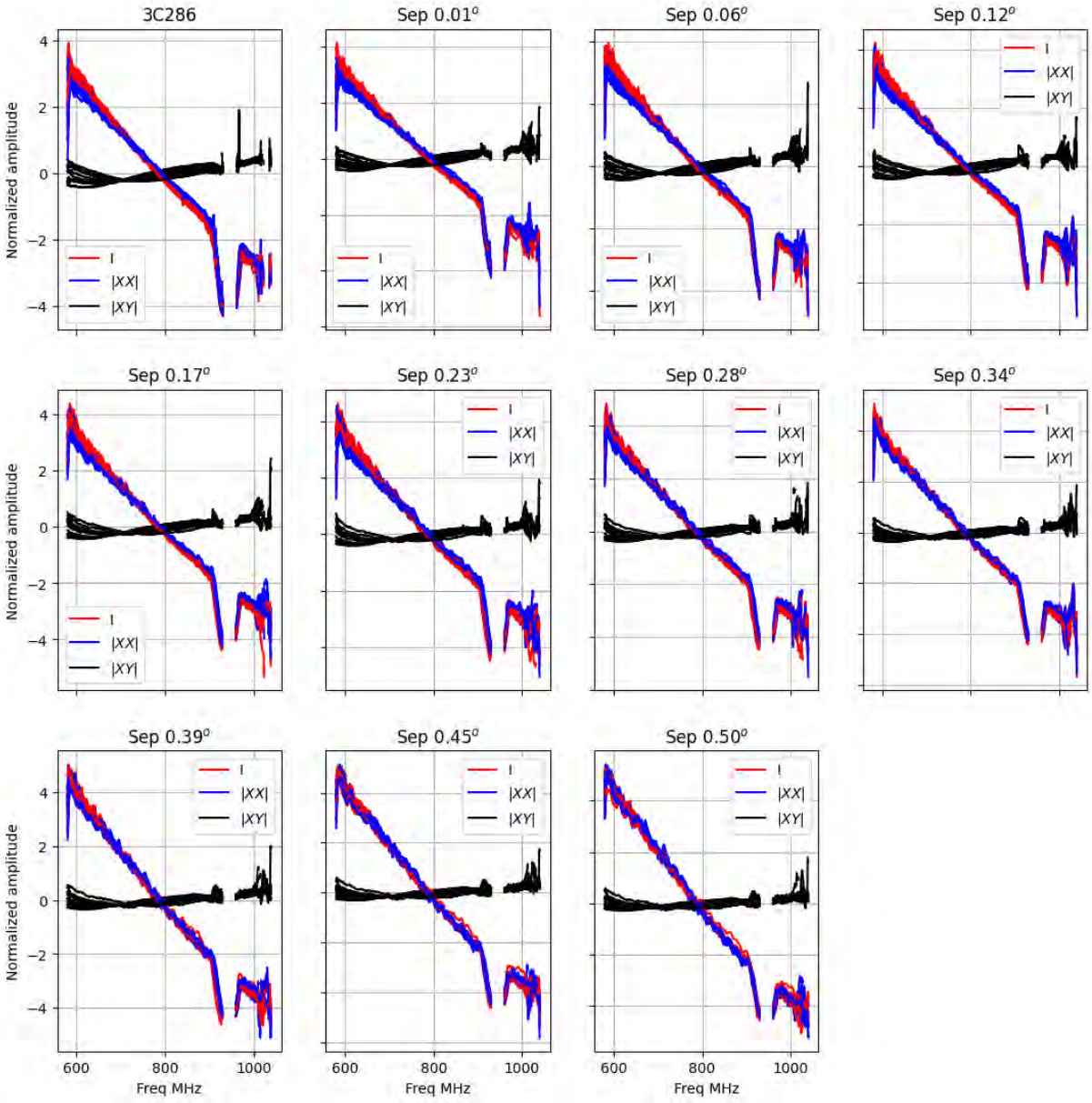

Figure 2.17: Parallel and cross-correlation products for UHF band. Here we separate the contributions to polarization seen in Fig. 2.16. It appears that the rippling seen at larger offsets may in part be dominated by total intensity contribution from off-axis sources. The cross-correlations in the UHF out to 0.5 radius are flat across the band

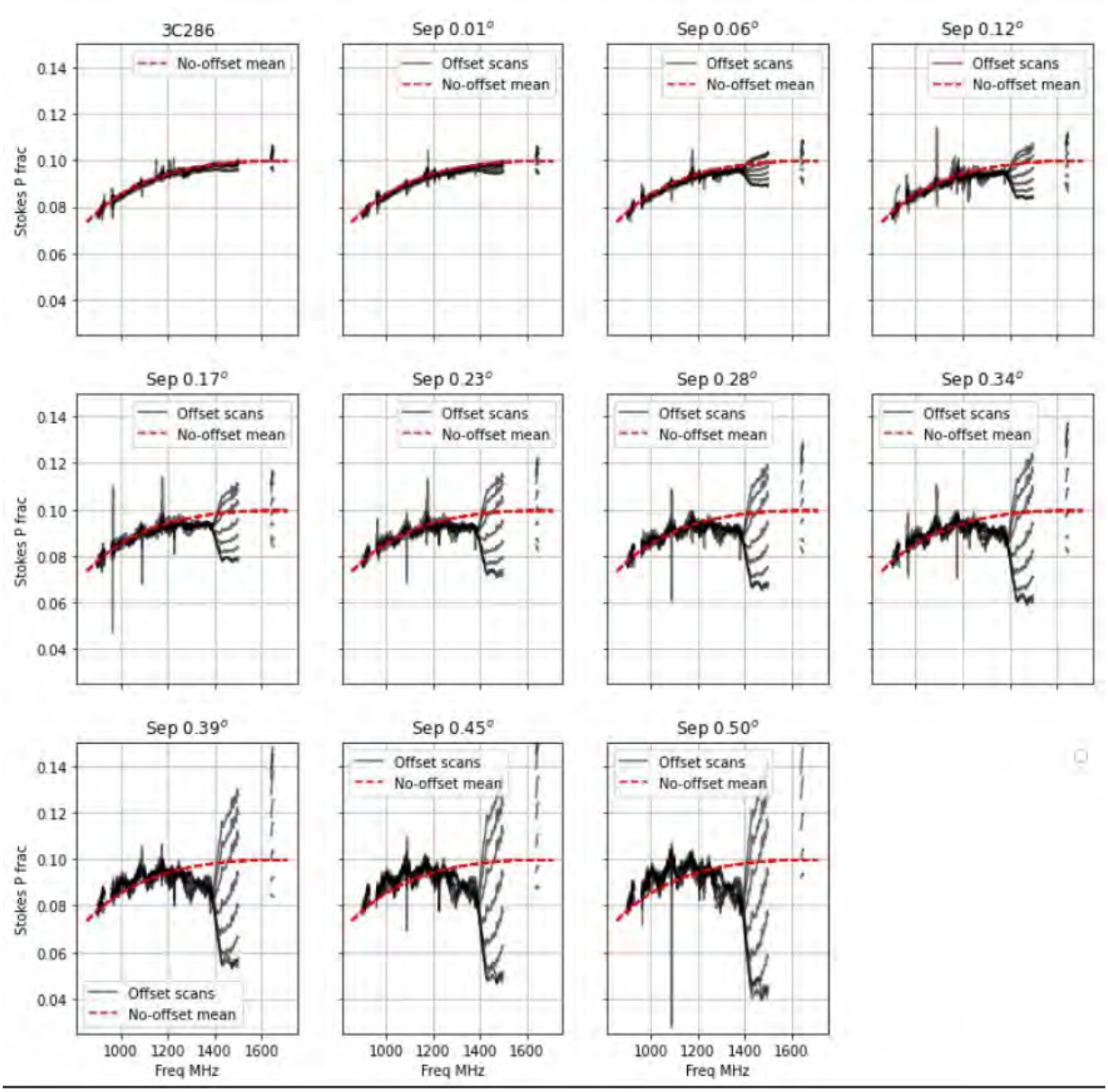

Figure 2.18: MeerKAT off-axis leakage performance out to a separation of 0.5 degrees from the pointing center for L-band (FWHM 0.5 deg at highest frequency). Per scan averages are shown in gray curves for the 5-hour round-robin visits to each offset position, observing the offset position through various parts of the antenna beam as a result. The average on-axis response (shown top-left) is fitted and overplotted at all offset pointings for reference. Well-known multimodal effects are visible at frequencies above 1400 MHz to a few percent level beyond 0.23 degrees separation. Furthermore the leakage seems to be highly variable with parallactic angle coverage.

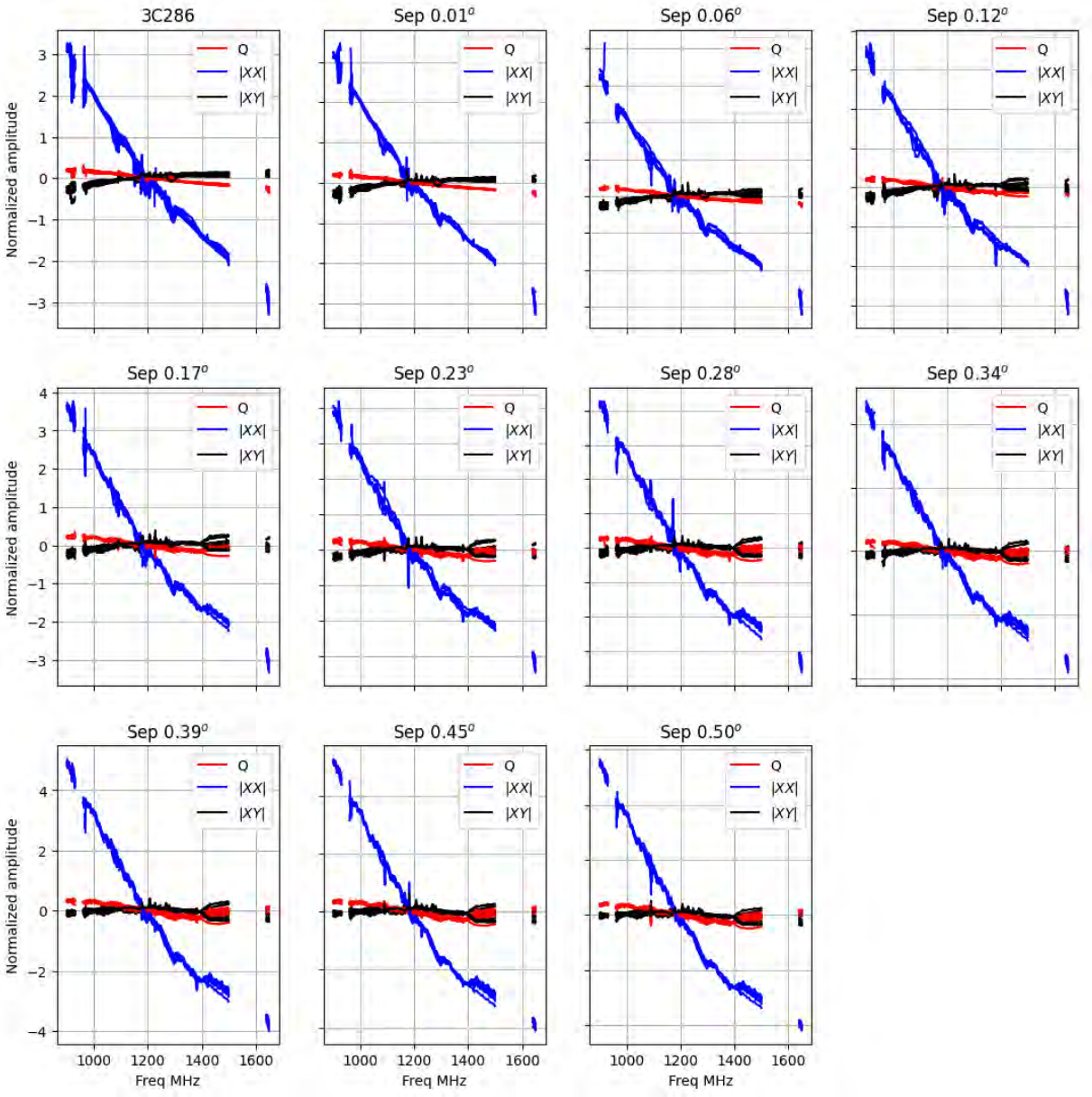

Figure 2.19: Parallel and cross-correlation products for L-band. Here we separate the contributions to polarization seen in Fig. 2.18. The stucture above 1400 MHz stems from polarized structure in the cross-correlation and polarization component of the parallel hand products. This is in line with the observed asymmetrical TE21 waveguide modes in the parallel and cross correlation noted by [46] from holographic results.

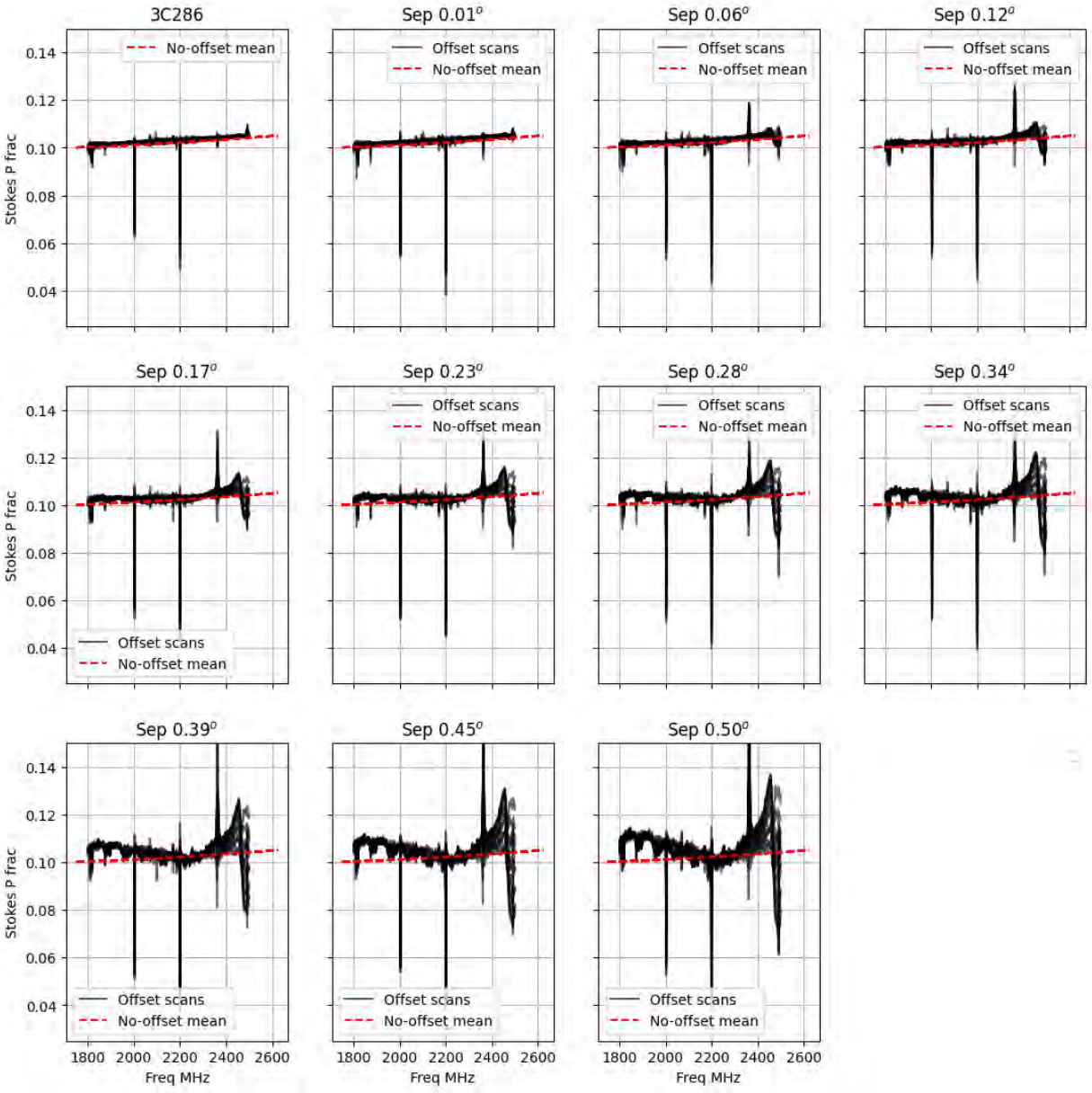

Figure 2.20: MeerKAT off-axis leakage performance out to a separation of 0.5 degrees from the pointing center for the first (S0) spectral window of the S-band system (FWHM 0.31 deg at highest frequency). Per scan averages are shown in gray curves for the 5-hour round-robin visits to each offset position, observing the offset position through various parts of the antenna beam as a result. The average on-axis response (shown top-left) is fitted and overplotted at all offset pointings for reference. The spectral variation is worst at the very top of the first spectral window of the S-band system, but overall has less spectral leakage compared to the L-band system.

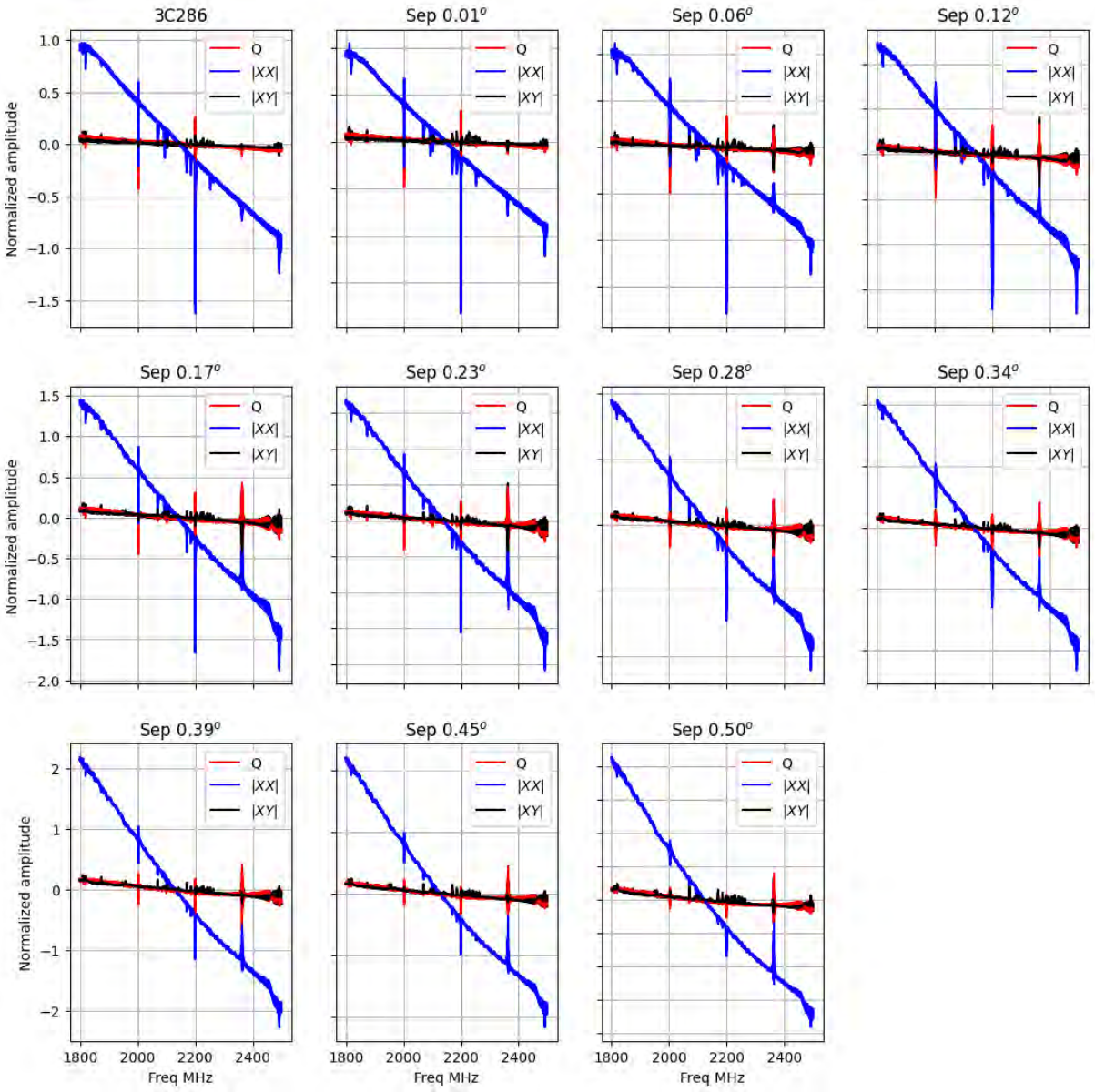

Figure 2.21: Parallel and cross-correlation products for S0-band. Here we separate the contributions to polarization seen in Fig. 2.20. As in [46] the bottom part of the observable S-band has markedly flat parallel and cross-polarization.

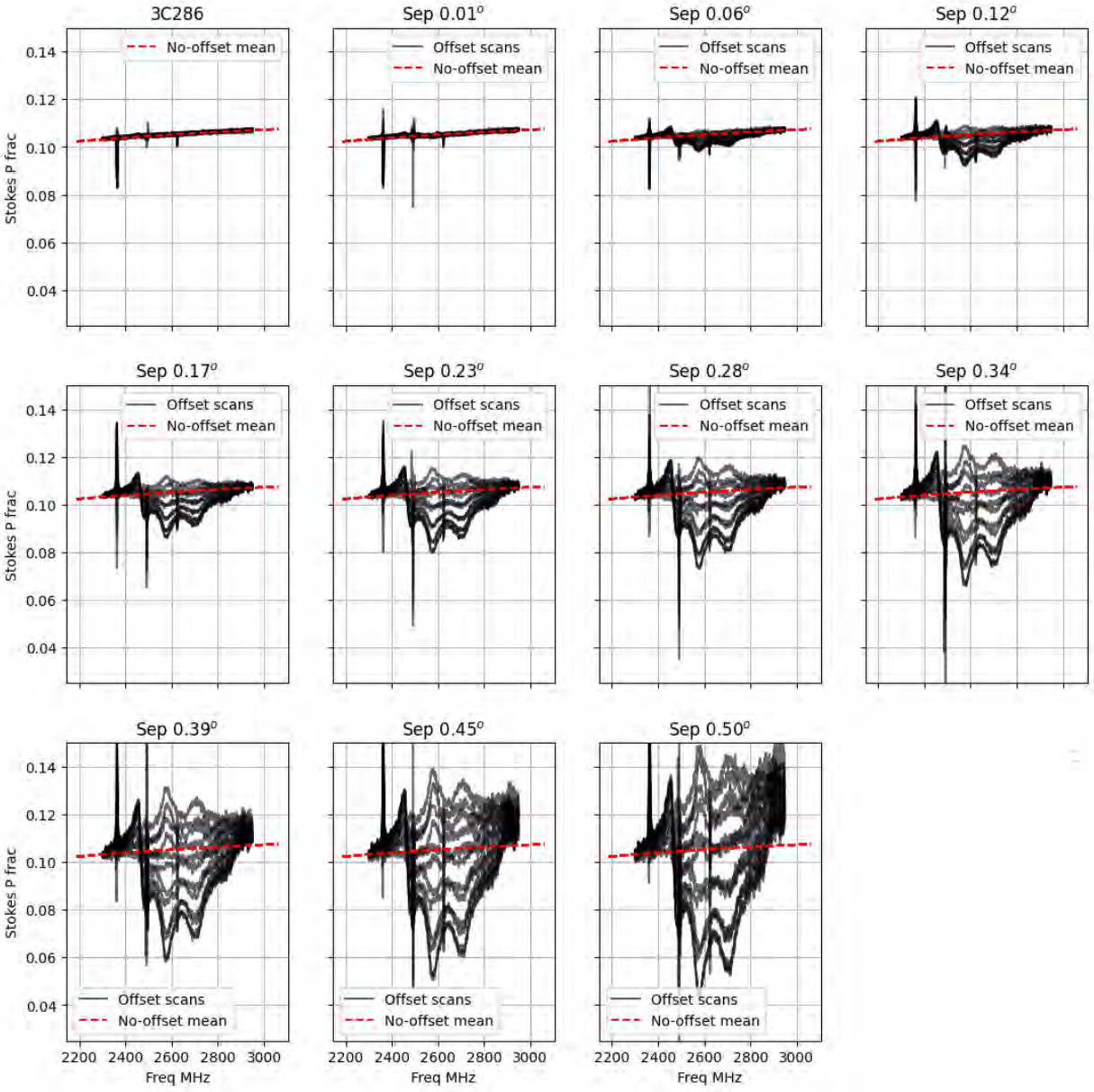

Figure 2.22: MeerKAT off-axis leakage performance out to a separation of 0.5 degrees from the pointing center for the third (S2) spectral window of the S-band system (FWHM 0.25 deg at highest frequency). Per scan averages are shown in gray curves for the 5-hour round-robin visits to each offset position, observing the offset position through various parts of the antenna beam as a result. The average on-axis response (shown top-left) is fitted and overplotted at all offset pointings for reference. The spectral variation, like that seen in L-band, is highly variable as a function of parallactic angle and is at multi-percent level beyond a separation 0.28 degrees.

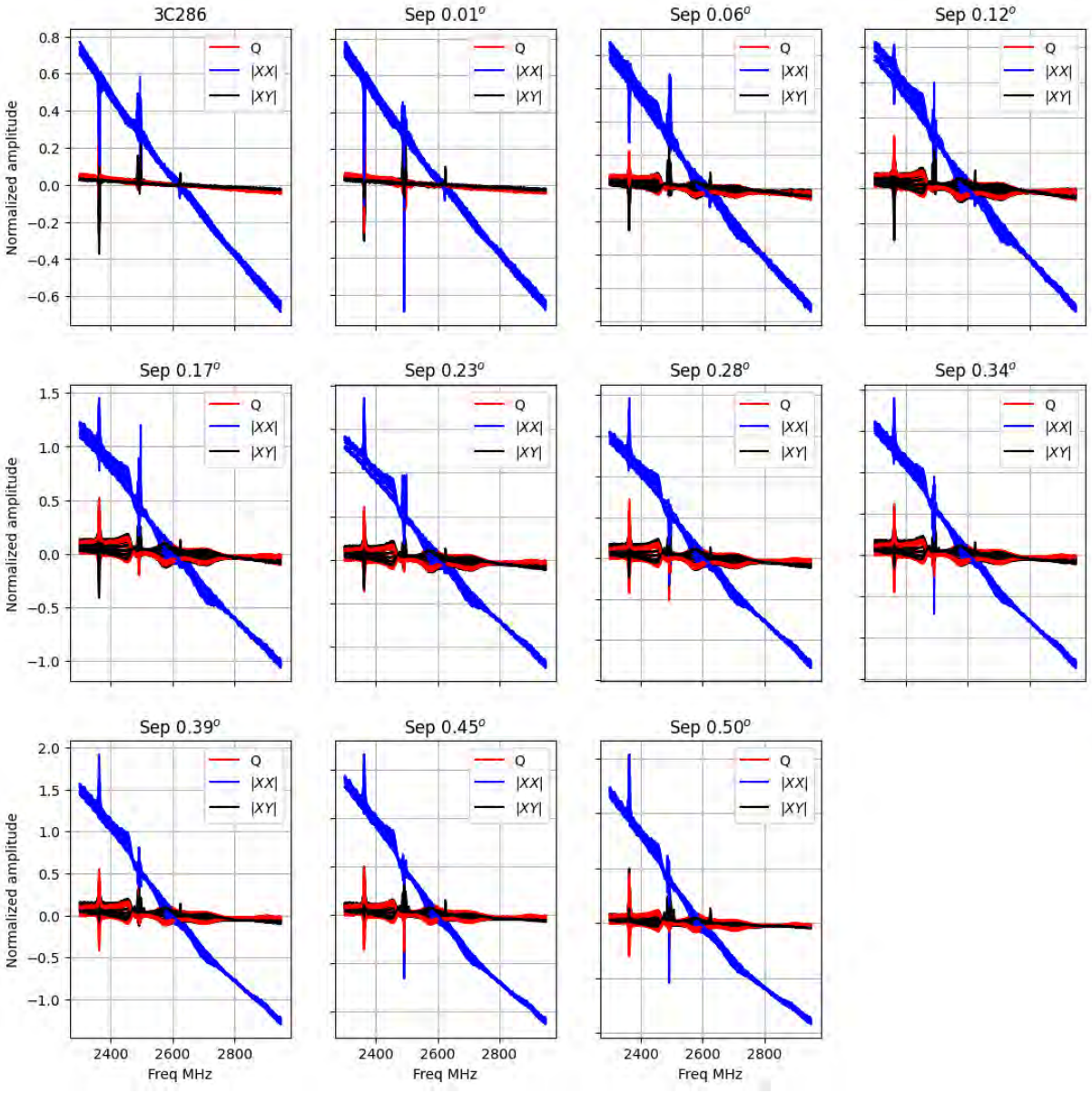

Figure 2.23: Parallel and cross-correlation products for S2-band. Here we separate the contributions to polarization seen in Fig. 2.22. Parallel and cross-polarization are dominated by TE21 waveguide modes above 2500 MHz to levels very comparable to what is observed in [46] at FWHM.

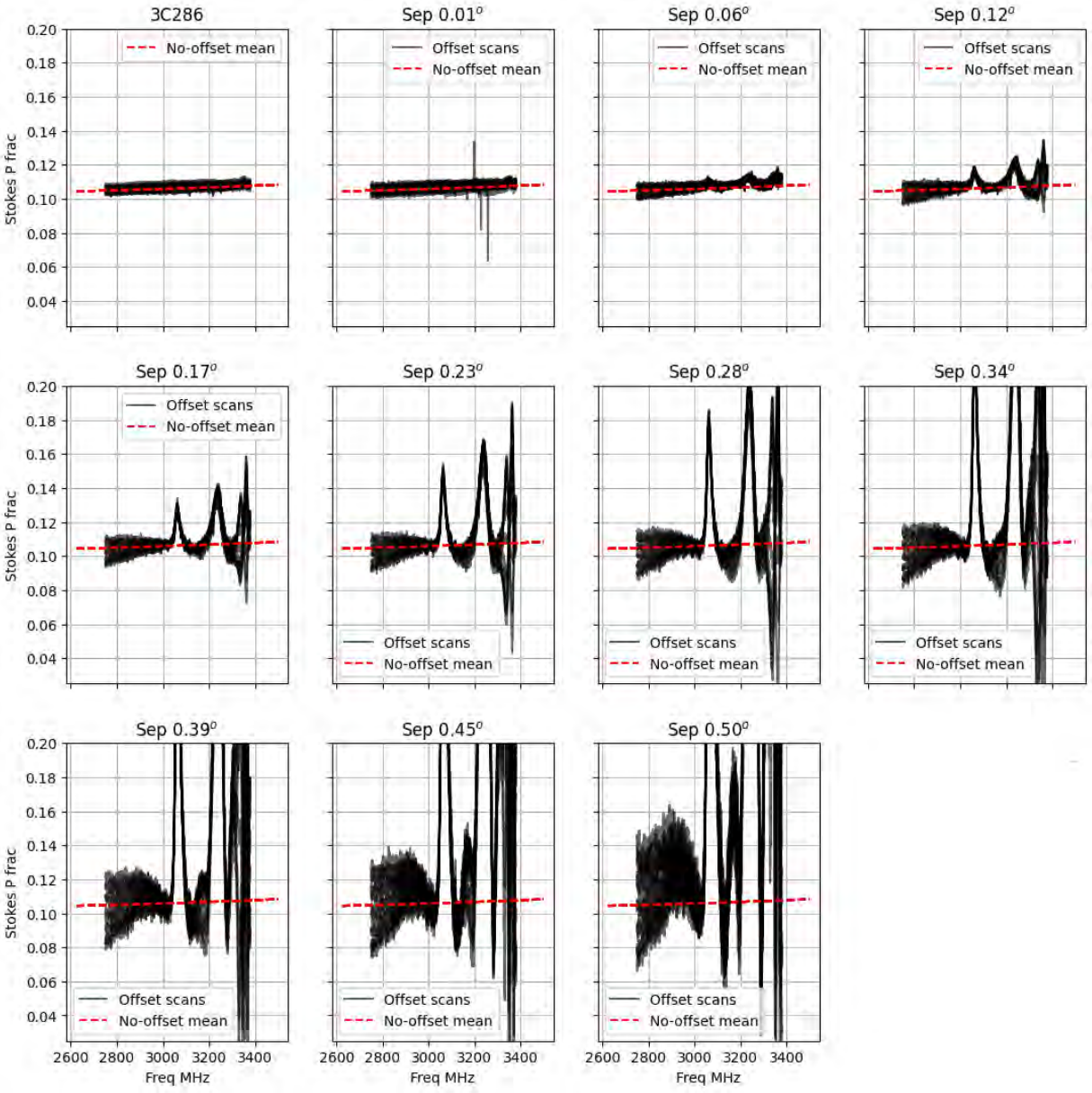

Figure 2.24: MeerKAT off-axis leakage performance out to a separation of 0.5 degrees from the pointing center for the highest (S4) spectral window of the S-band system (FWHM 0.22 deg at highest frequency). Per scan averages are shown in gray curves for the 5-hour round-robin visits to each offset position, observing the offset position through various parts of the antenna beam as a result. The average on-axis response (shown top-left) is fitted and overplotted at all offset pointings for reference. Unlike the L and S2 systems the spectral variation appears not highly variable as a function of parallactic angle but the leakages display distinct notches beyond 3GHz which rapidly increase in magnitude to many percent level beyond a separation of 0.17 degrees.

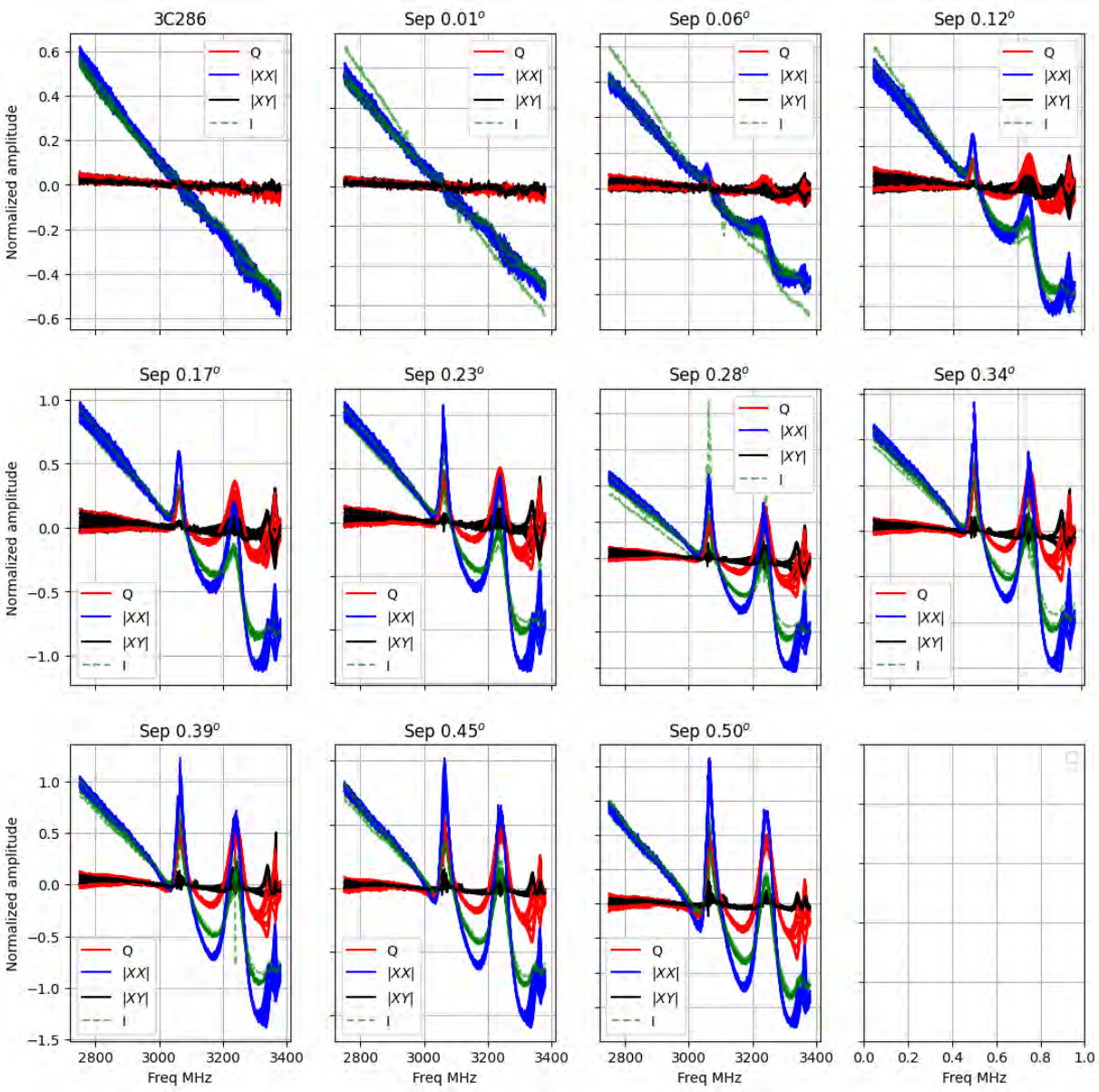

Figure 2.25: Parallel and cross-correlation products for S4-band. Here we separate the contributions to polarization seen in Fig. 2.24. Overall the structure of the cross correlation attenuation follows the usual λ/D relationship, however the band is dominated by frequency dependent TM11 modes which elongates the primary beam above 3 GHz and very closely matches the stucture observed by [46]. The band has strong off-axis polarization at these frequencies and closely matches the observed levels at FWHM stated by [46].

We note that, to our knowledge, no existing modern software satisfactorily corrects for absolute leakages at lower frequencies. Although one can theoretically solve for such leakages without a model of a (simple compact) polarized calibrator over a wide range of parallactic angle [for details see e.g. 62, 140], by fitting to the periodicity induced by parallactic angle rotation on Stokes Q and U of a polarized source and solving for a (presumed) temporally stable leakage solution, the discussion in those papers are done at higher frequencies and neglect the temporal effects induced by the ionosphere at low frequencies.

In [140] one of the authors (Rick Perley), with his collaborators, rotated receivers on the array by 90 degrees between observations to establish absolute leakage measurements and compared these against absolute leakage terms derived from solving from observations of a polarized calibrator spanning a large sweep in parallactic angle. Such an extensive mechanical engineering endeavor is not possible for MeerKAT to the authors' knowledge, nor can it be sufficiently motivated. Theoretically, it may be possible to solve for these but no commonly-available software can achieve this[33].

The fitted frequency-independent angular offsets on the Moon presented in the next subsection are therefore a combination of absolute leakage uncertainties and feed angle offsets. These, however, sufficiently quantify uncertainties on measurement and appear not to drive the measurement error, which is very clearly a wavelength-squared effect — in line with ionospheric measurement error. More on this later in this section.

2.4.3 Corrections based on radial EVPA of the Moon, Venus and Mars

In this subsection we quantify the angular offsets measured on the Moon after transfer calibration and fitting procedure as outlined in Section 2.2. As discussed in Section 2.2 both the ionospheric-induced Rotation Measurement and the constant feed angle misalignment can be fitted for directly from the offsets of the EVPA from their nominal radial alignment. This is corrected for (and later compared to GNSS differential measurement in Sub-section 2.4.4) in the vector plots shown in this Sub-section. The measurements and corrections are treated differently for linearly and circularly polarized systems. To come back to the points briefly mentioned in Section 2.1:

- During calibration of a circularly polarized system the assumed model for the crosshand angle (phase in circular basis) calibrator sets the value of the corrected angle. Assuming this phase is temporally stable on the reference antenna (at least stable enough to transfer onto interleaved scans of the Moon / Venus / Mars) any errors in the assumed model show up as offsets on the radial angles on the rocky body. ionospheric corrections are subtracted from the frequency-independent corrective term. The latter is fitted using routines developed at the NRAO. These were used in [127] to model 3C286 at higher frequencies using observations of Mars and were again employed on the VLA data taken for this study.
- The calibration of a linear system does not need a known absolute angle for the calibrator — the uncertainty is bound mainly by the accuracy of system-induced crosshand[34] phase calibration, which biases the instantaneous measurement of Stokes U, as well as feed misalignments in the absence of ionospheric terms. Once the HV phase and (assumed) low-level leakages are accounted for the response should be nominally aligned with the array-average feed angle in the absence of the ionosphere. We can use the fitted frequency independent component of the

[33]The authors tried, without success, the Df+QU solver mode in the "polcal" task of CASA [104] (which is marked in the documentation as a circular only mode). The authors also attempted transfer calibration using the QUARTICAL [88] package (available at `https://github.com/ratt-ru/quartical`) by assuming a model for 3C286 and solving for frequency dependent D terms as was done in related work undertaken by Rick Perley and Jonathan Kenyon at X band. The absolute leakages experiment in [140] was effectively replicated using QUARTICAL and assuming a model for 3C286 (which has been well established at high frequencies by Perley and Butler, 2013 and is not subject to significant ionospheric effects). The error in the assumed model appears to drive error on the solutions at low frequencies. The solutions fail to reduce leakages on an unpolarized source through transference to similar levels as achieved by relative leakage calibration. The authors briefly looked at MIRIAD and the documentation clearly states that although models for Q and U are not necessary, reference antenna zero'ing is enforced. Writing a solver to attempt to solve for Q and U and D terms on linear feed systems is beyond the scope of this undertaking and left as a future exercise.

[34]On a plane-polarized signal the system crosshand phase, ρ, splits power between the 45 degree U polarization and circular polarization modes. See Eqn. 2.1.

fitting routine, independently developed at SARAO, discussed in Section 2.2 to measure the remaining offset (plus absolute and off-axis leakage uncertainties).

The ionospheric and offset-corrected radial EVPA of the MeerKAT Lunar observations are shown in the extended Table 2.2, along with angle offset distributions for MFS sub-bands ranging from UHF to S0 frequencies. Throughout we use the established WSCLEAN [112] imager to image MeerKAT wideband data. The EVPA quivers are scaled with linear polarization fraction and overplotted on the Stokes *I* map (without zero-spacing observation) of the Moon in all instances. Polarization vectors are only shown for high (20 sigma) polarized emission. It is noted that there is some overlap between the bands in frequency.

Table 2.2: Feed (plus relative leakage induced errors) offset distributions from Lunar fitting. Overall the MeerKAT feeds are very well aligned with nominal assumed positions.

Lunar EVPA	Residual EVPA offset distribution
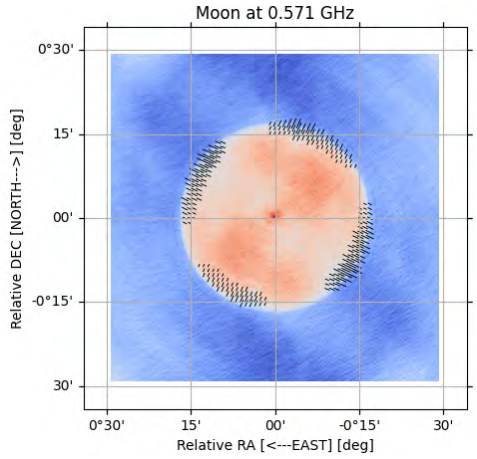	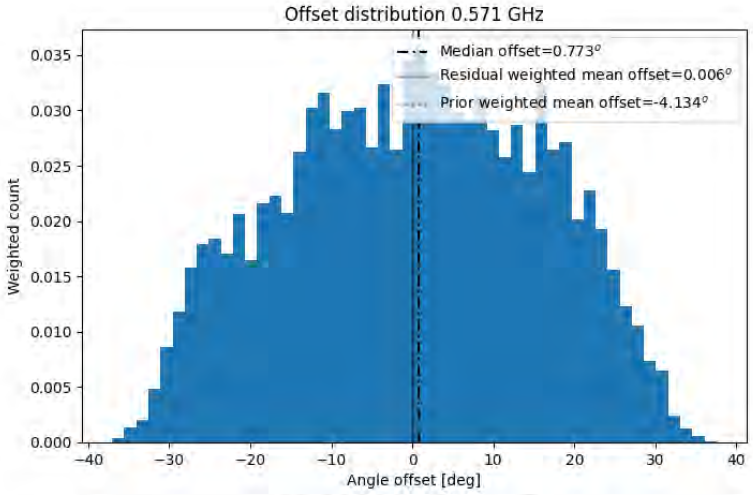
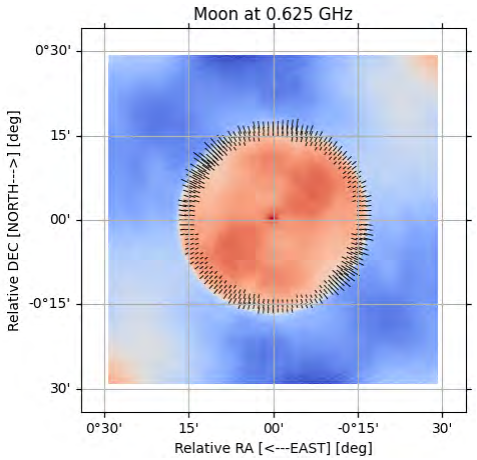	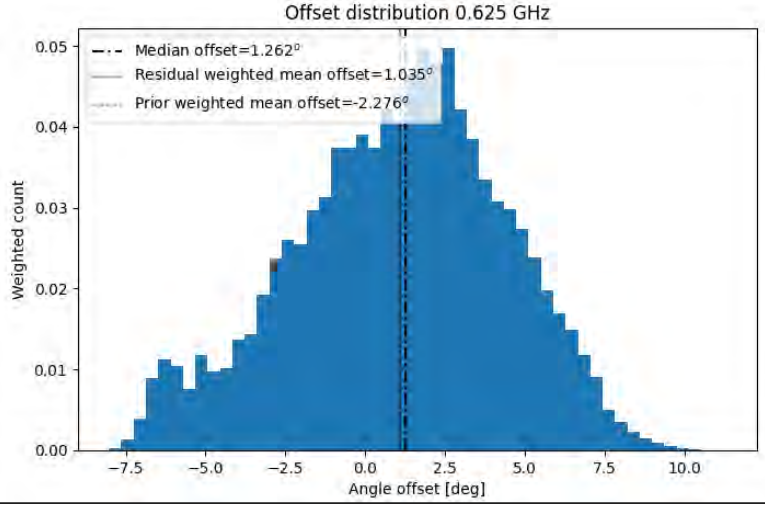

Continuation of Table 2.2

Lunar EVPA	Residual EVPA offset distribution
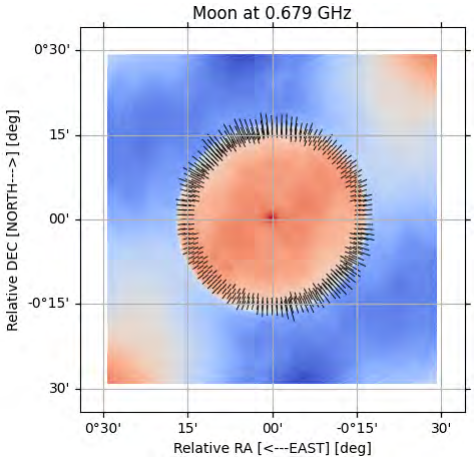	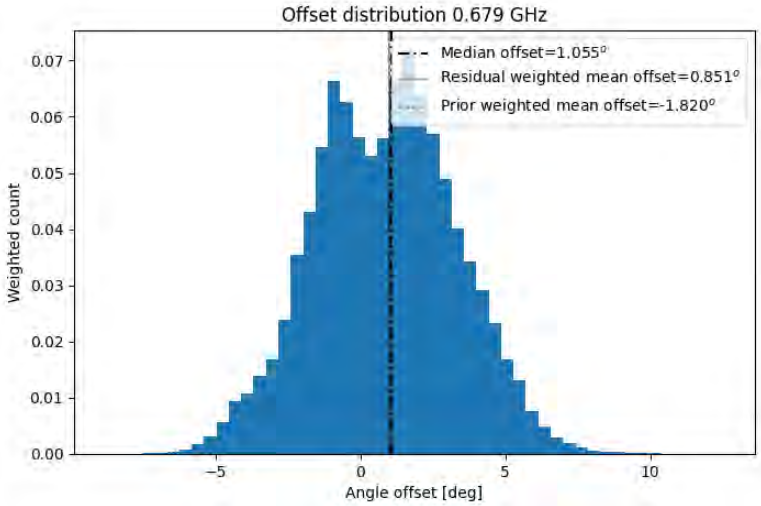
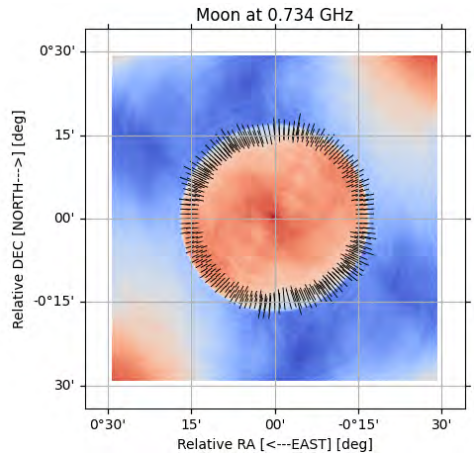	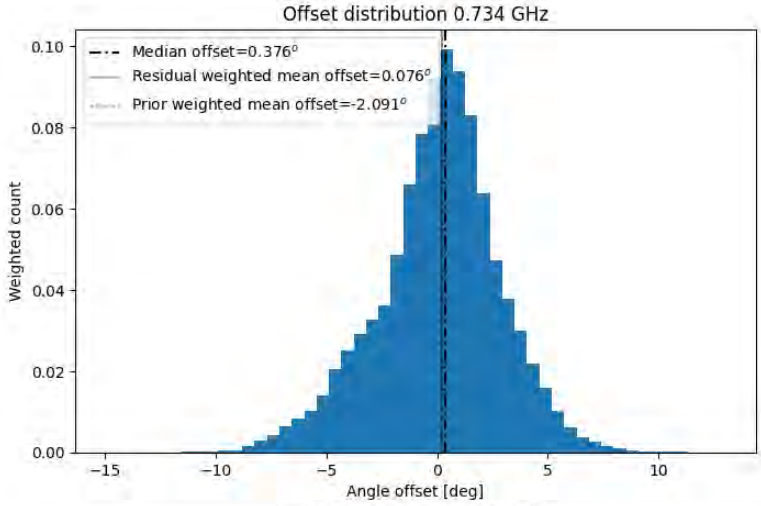
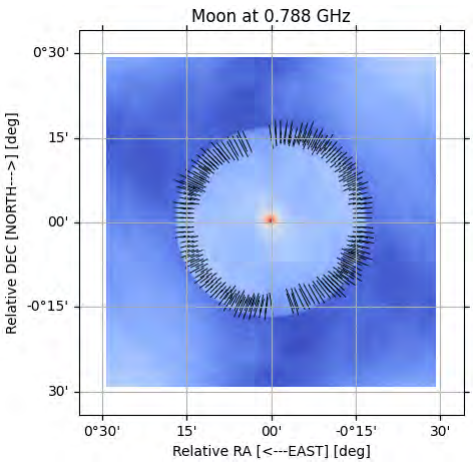	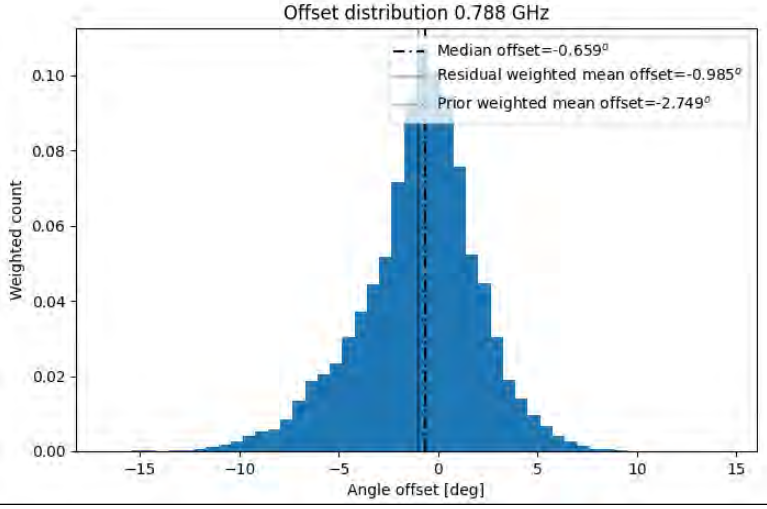

Continuation of Table 2.2

Lunar EVPA	Residual EVPA offset distribution
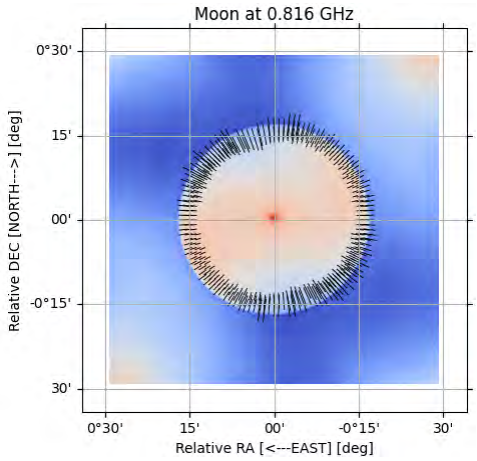	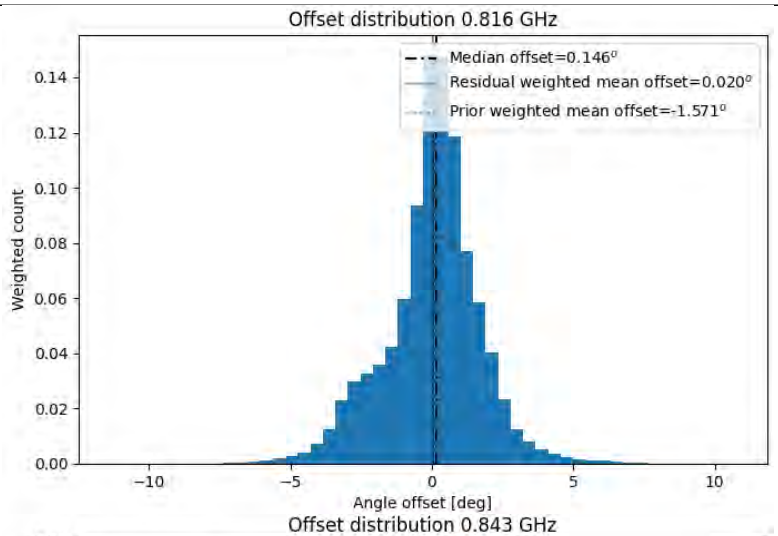
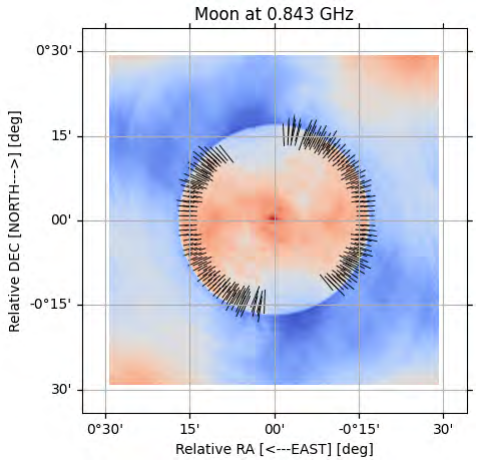	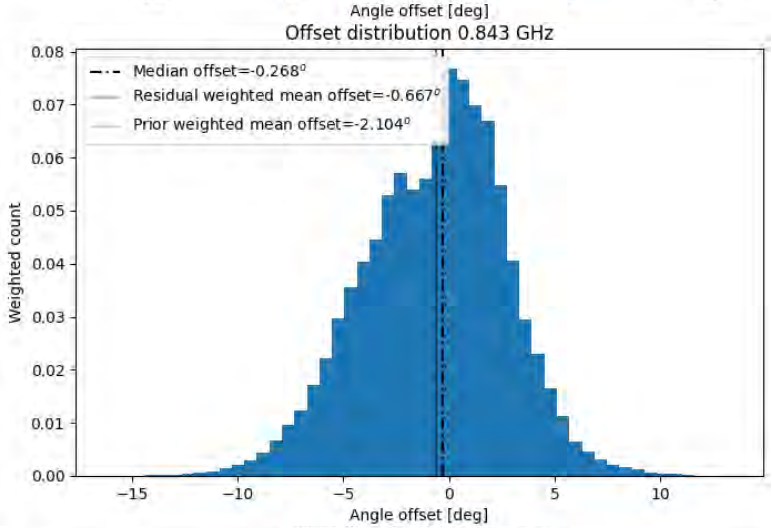
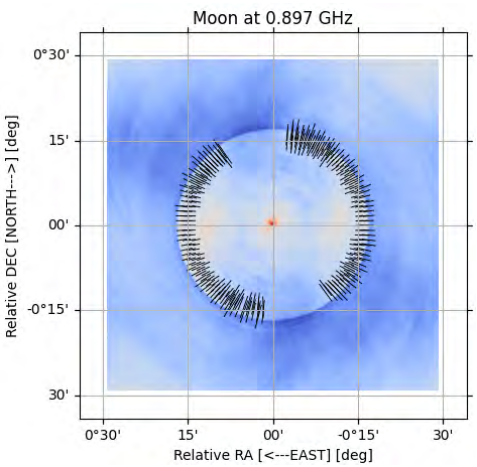	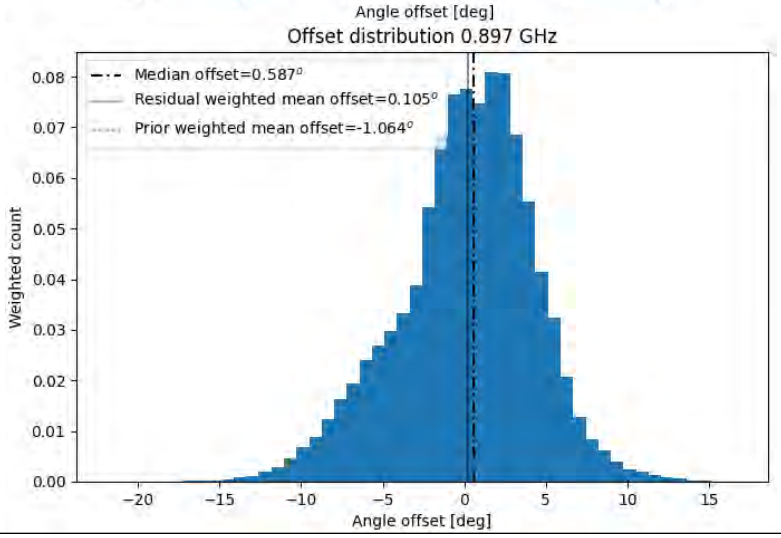

Continuation of Table 2.2

Lunar EVPA	Residual EVPA offset distribution
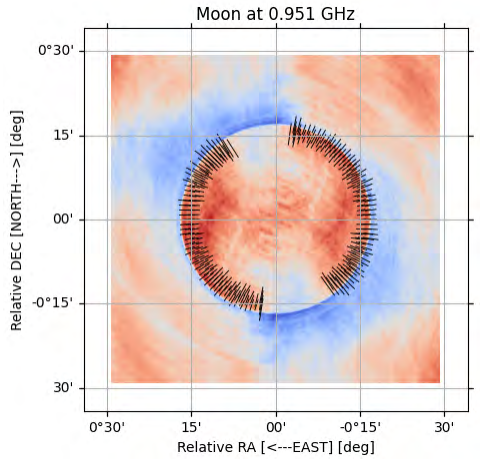	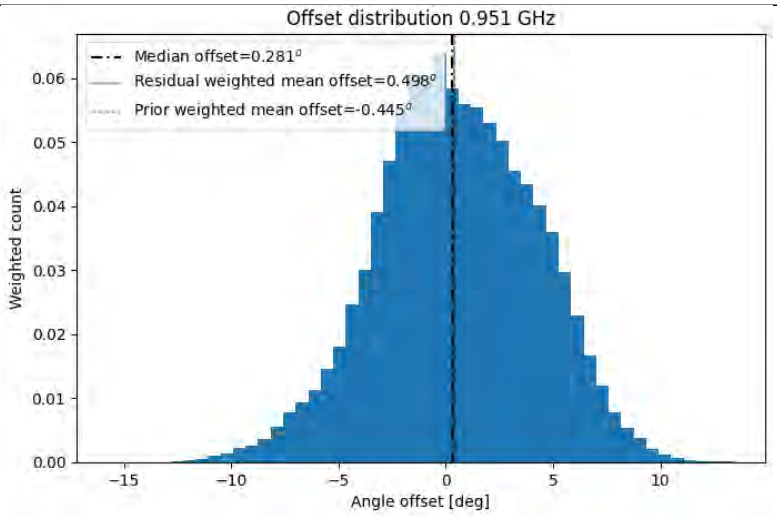
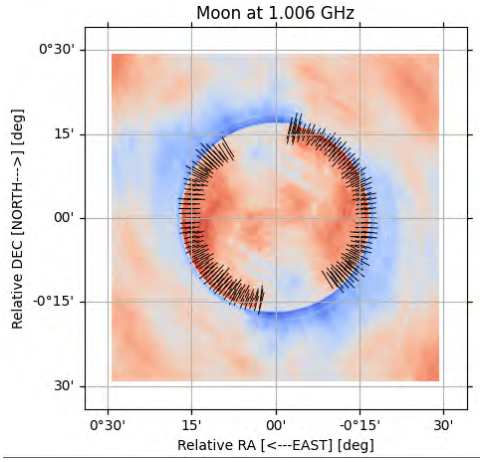	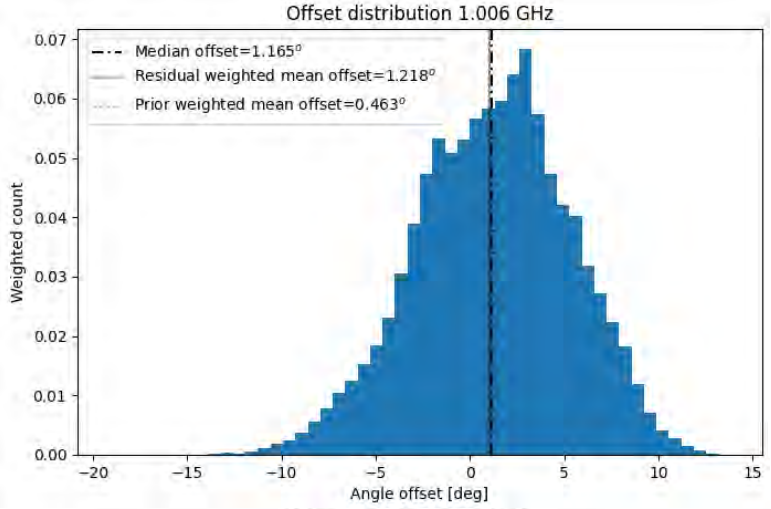
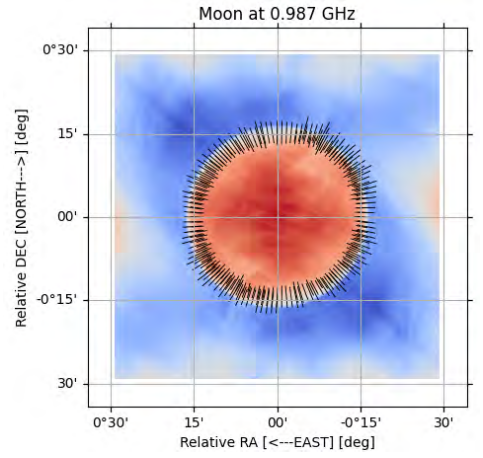	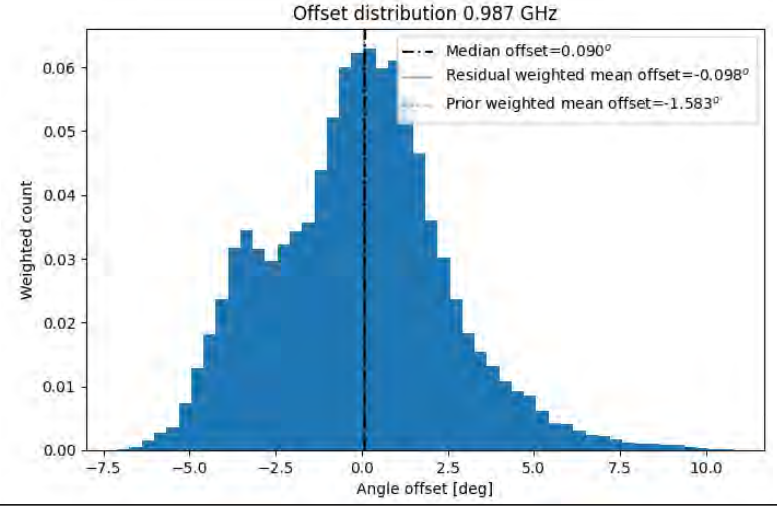

Continuation of Table 2.2

Lunar EVPA	Residual EVPA offset distribution
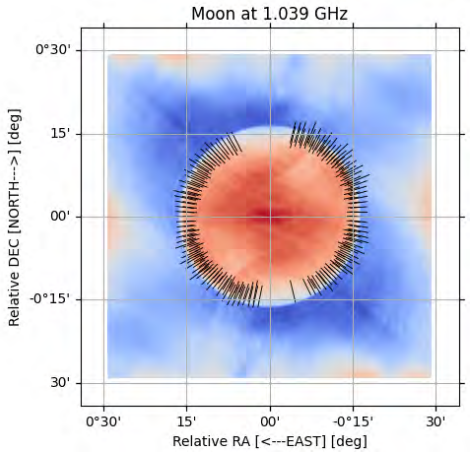	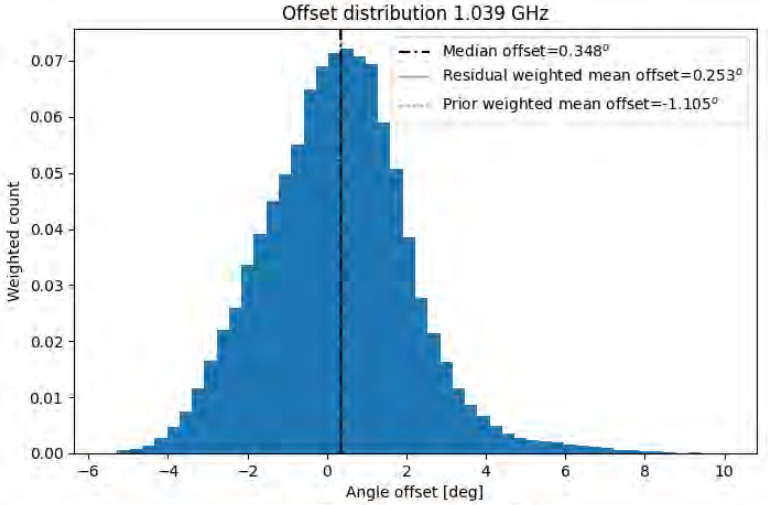
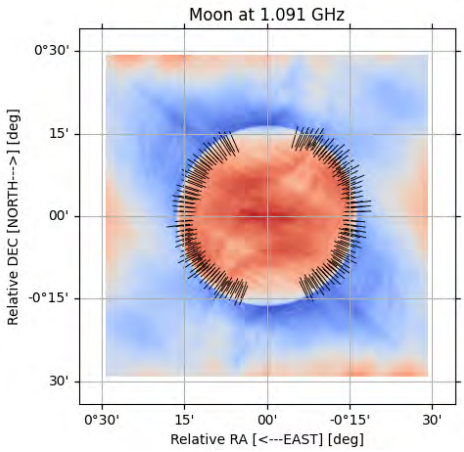	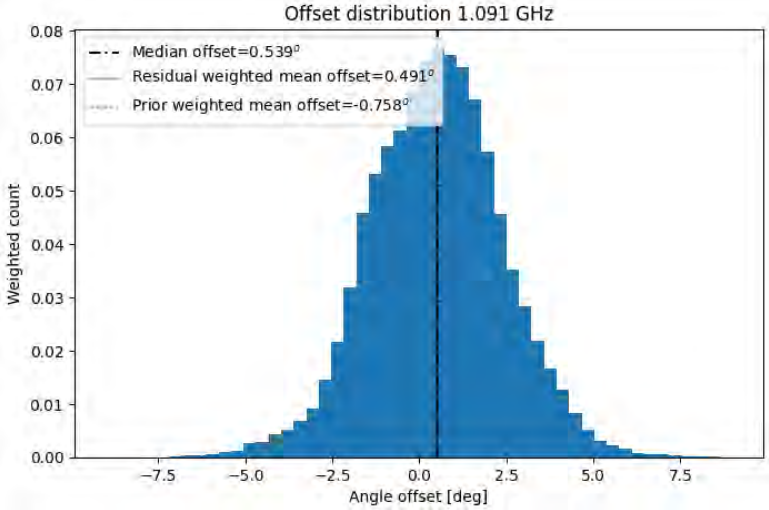
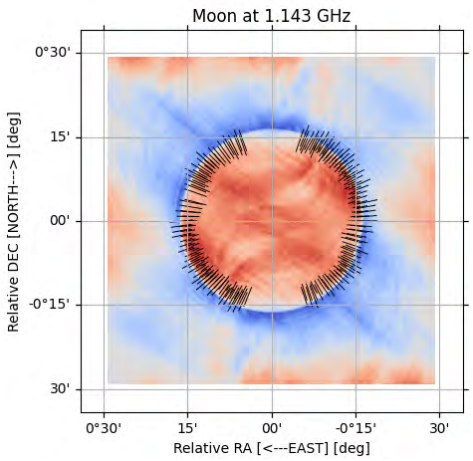	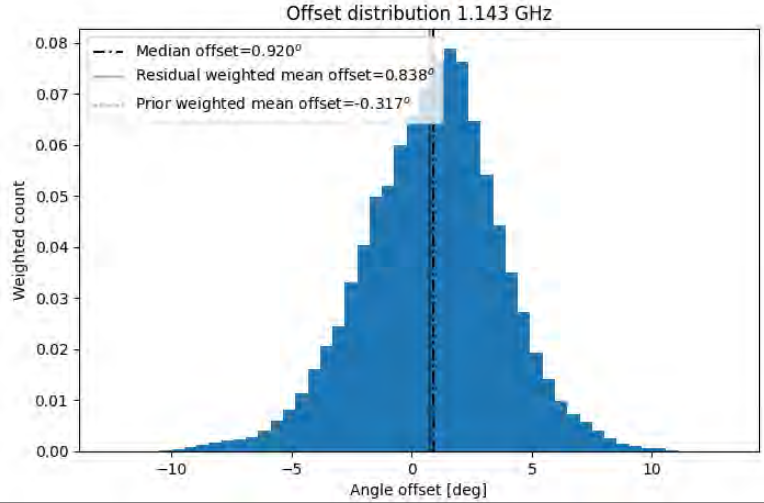

Continuation of Table 2.2

Lunar EVPA	Residual EVPA offset distribution
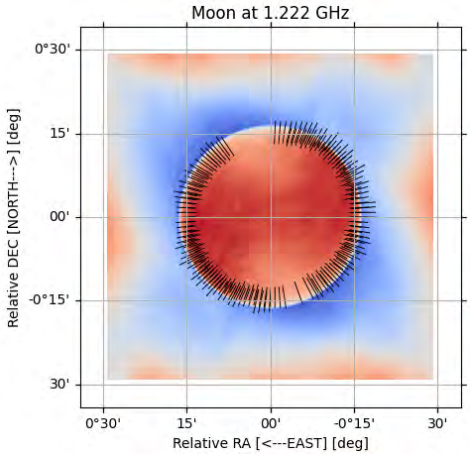	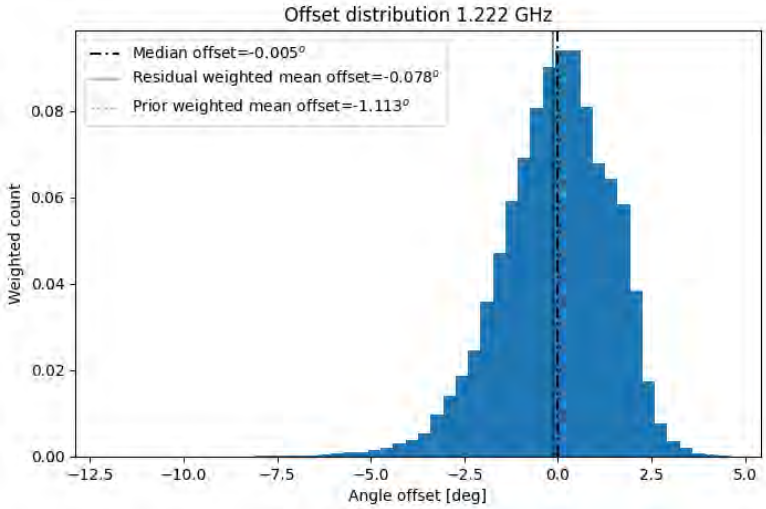
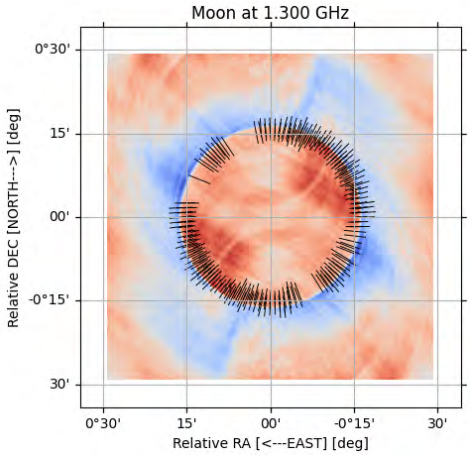	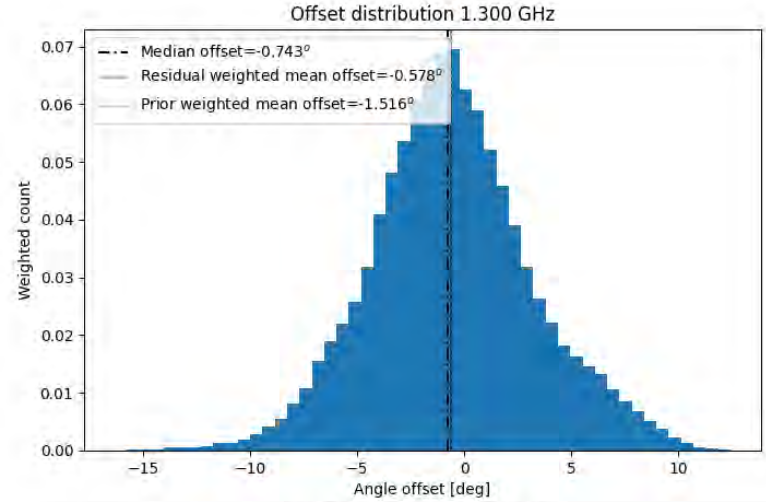
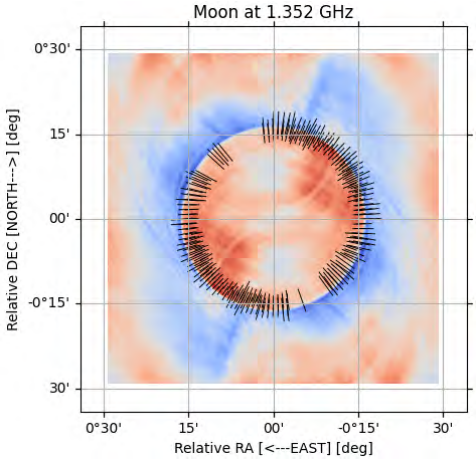	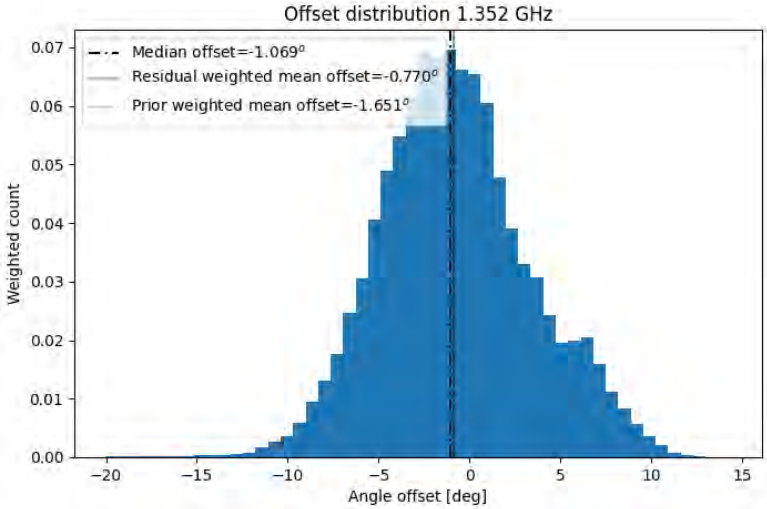

Continuation of Table 2.2

Lunar EVPA	Residual EVPA offset distribution
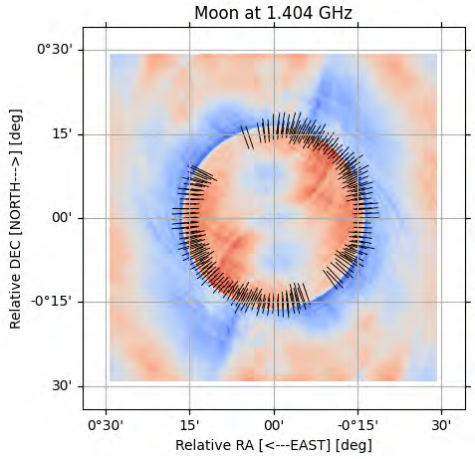	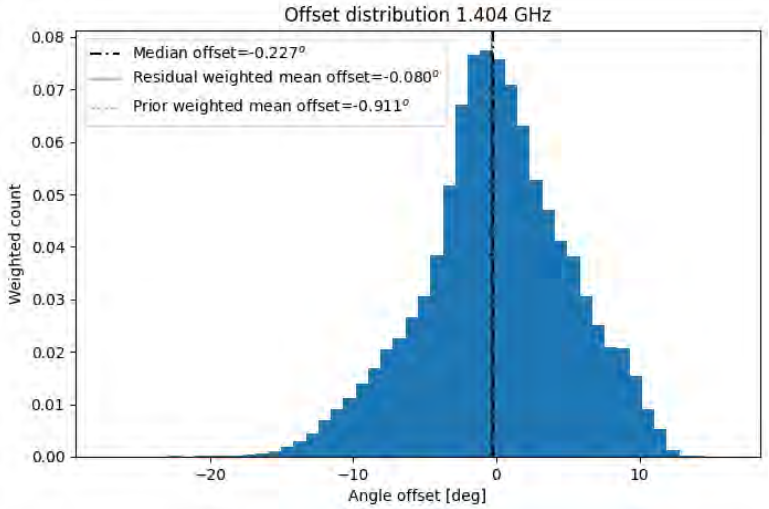
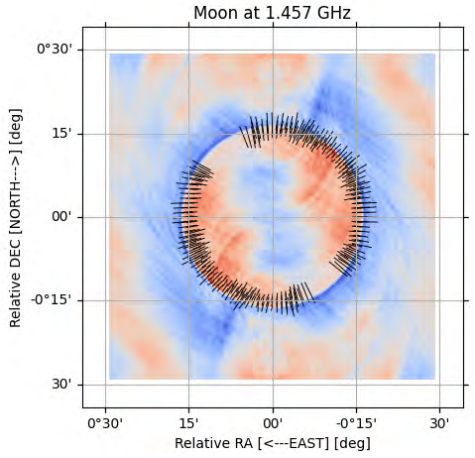	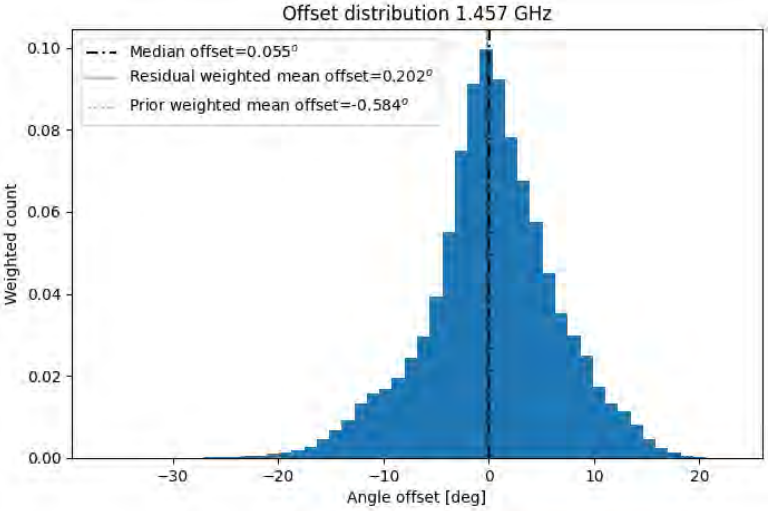
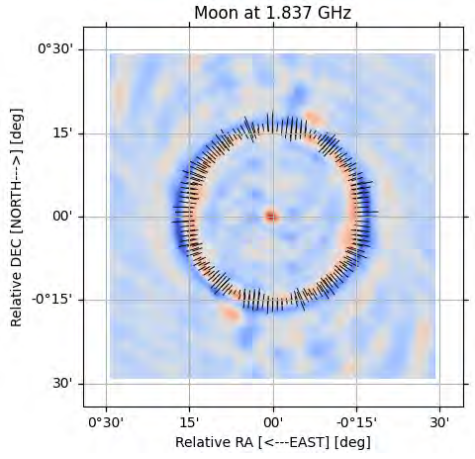	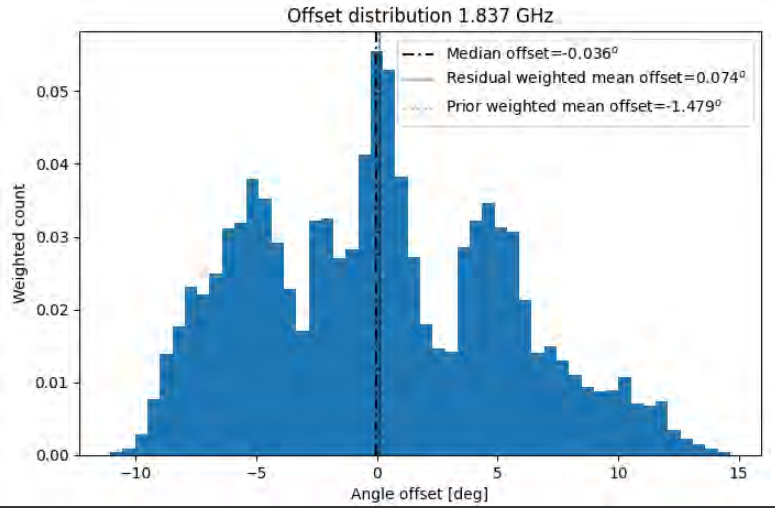

Continuation of Table 2.2

Lunar EVPA	Residual EVPA offset distribution
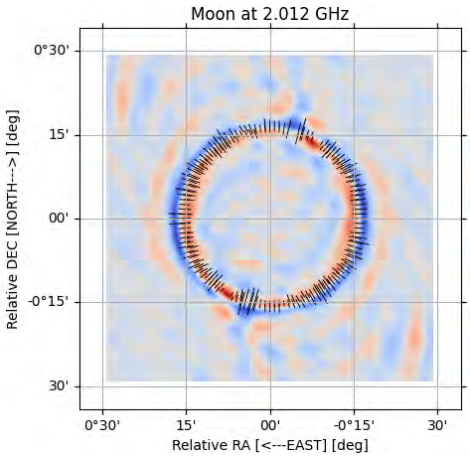	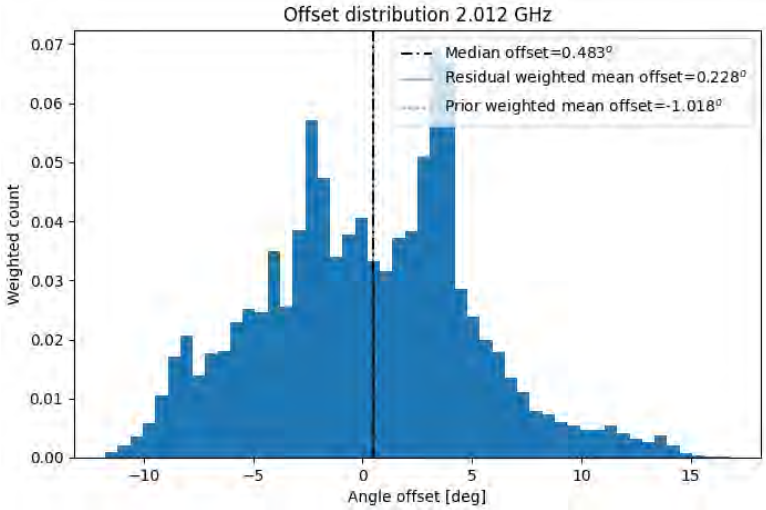
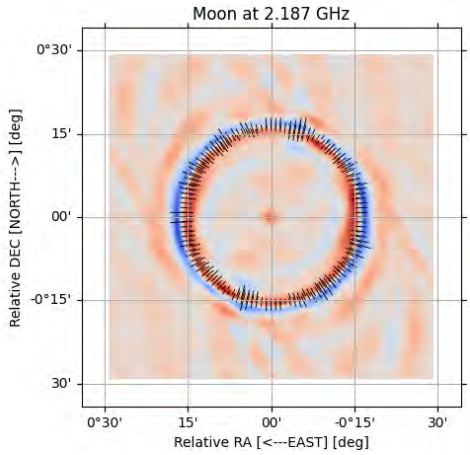	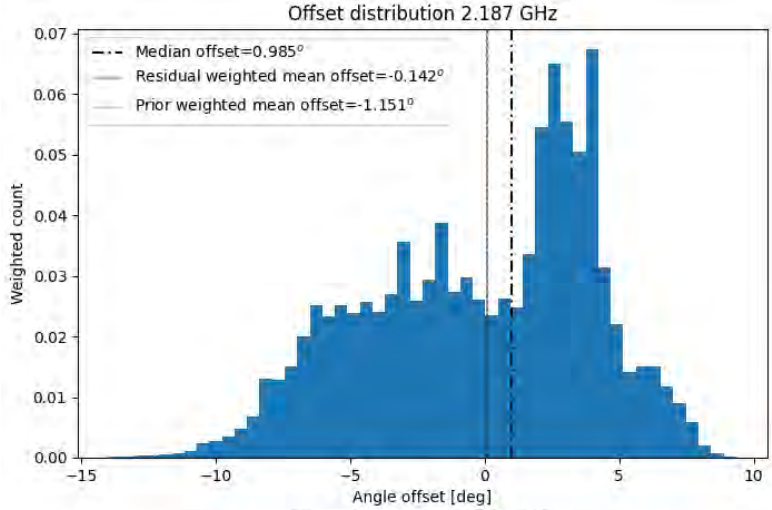
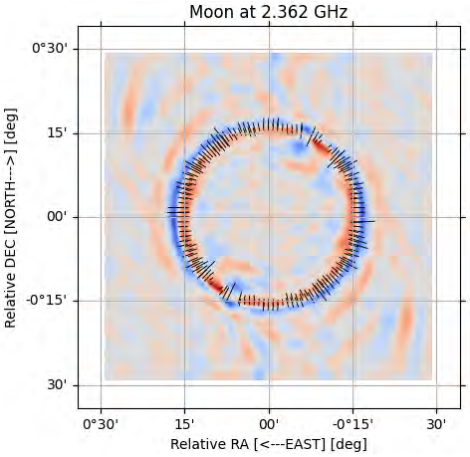	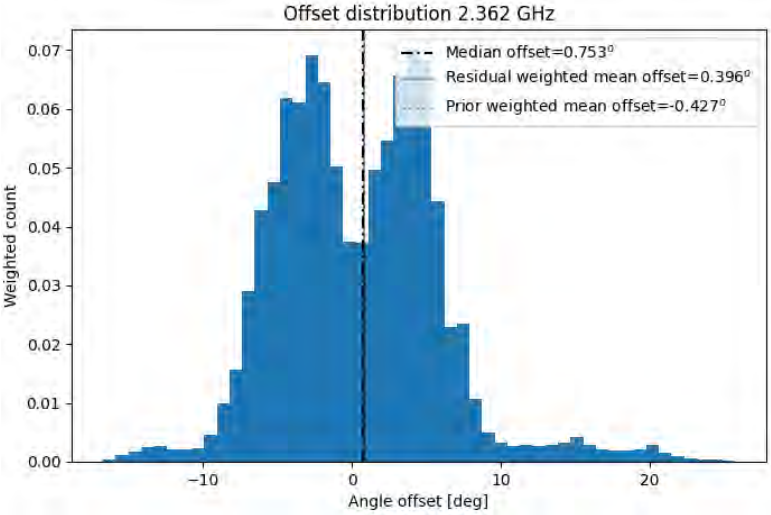

Continuation of Table 2.2

Lunar EVPA	Residual EVPA offset distribution
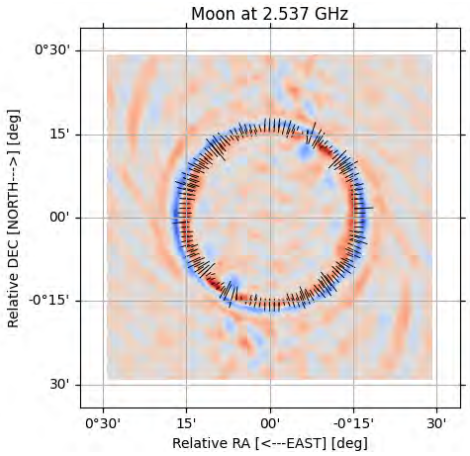	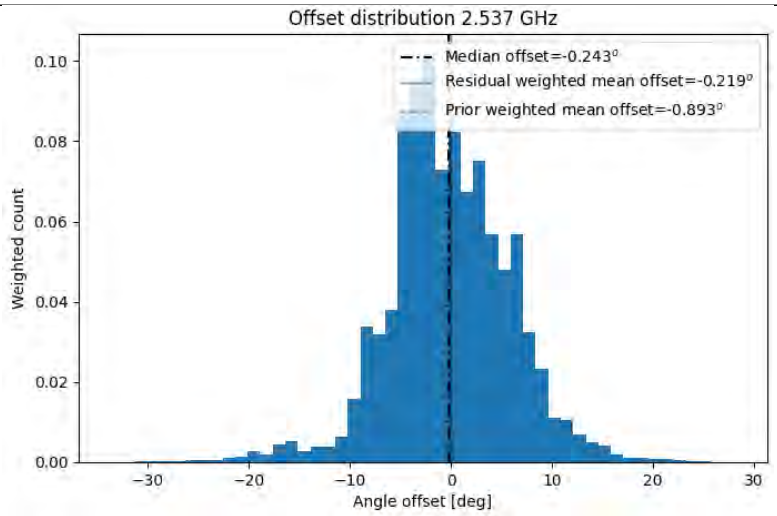

At S0-band we start losing SNR on the limb due to a combination of a lack of spacings sensitive to large spatial scales and the limb emission being attenuated by the main lobe (close to being at the FWHM point in the beam at highest frequencies). At S0-band we expressly tapered off spacings below 75m and higher than 400 m because we found that the shortest spacings had significant residual phase errors (not seen in the other bands) and spacings longer than 400m resolved out the broadscale refractive limb emission we needed to constrain the measurement. We further constrained the fit to a toroidal region between 0.265 and 0.255 degrees where most of the high SNR refractive linear power was concentrated in S0-band.

We suspect that the tailedness at some frequencies through all three bands is dominated by sidelobe emission from the overall disk (and crater structure on the disk). Where the distribution is significantly tailed or non-Gaussian it is excluded in the fitting procedure. Sub-band images are not locked to a scale minimum and maximum. The spread in the distributions are well above the spread that would exist from thermal noise levels. We have implemented an image space simulation of the refractive model presented in Section 2.2 for a regolith dielectric constant of 2.5. On the limb the absolute scale of the polarized emission matches that seen on the UHF Lunar data. The variance seen in the distribution of EVPA offsets depends on signal-to-noise and is shown in Fig. 2.26. We readily achieve dynamic ranges in the many tens to few hundred in our observation (limited by Lunar disk sidelobe contribution), and therefore expect our measurements not to be bound by instrumental sensitivity.

At UHF the fitted offset (feed plus absolute leakages) is 0.4 ± 0.1 degrees (3 sigma). At L-band this is -0.1 ± 0.1 degrees (3 sigma). S0 had a much poorer fit (for reasons of beam attenuation and lack of spacings sensitive to the large scale structure of the disk discussed) at 0.1 ± 2.1 degrees (3 sigma), although it is noted that the error bars on the RM was large (between -2.5 and -3.0 rad.m^{-2} predicted by ALBUS vs. -1.211 ± 3.39 rad.m^{-2} from the Lunar fit). **In all instances, the feeds (on average across the entire array) appeared well aligned to the nominal position.** From discussion with Mattieu de Villiers (SARAO) the relative orientations on the dipoles reflect, to within tenths of a percent, rotations measured through holography. **It is noted that strong 1-2 degree changes are seen in the dipole orientations on some antennas at elevation ranges in the 70-80 degree range.**

As discussed in Section 2.2, we can get the relative feed offsets from this array average absolute position angle, which was referenced to a user-picked reference antenna (m002 for all three bands). This is summarized in Figure 2.27 for the three bands. We note that the scatter across the array is mostly within about a degree from nominal IAU alignment (vertical

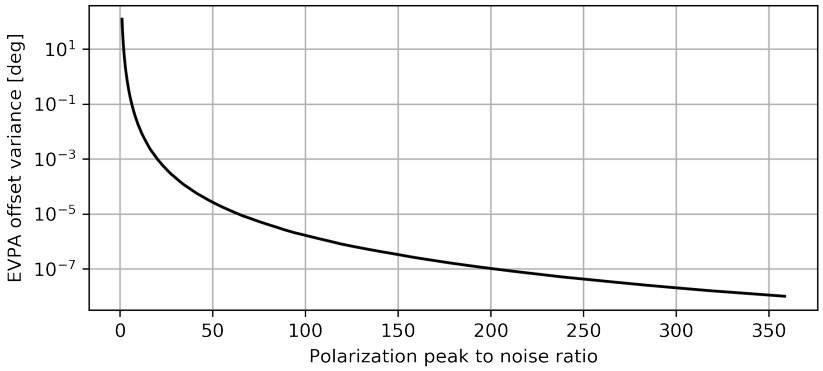

Figure 2.26: Simulations showing the expected scatter in the measured EVPA offsets from thermal noise. We assume a dielectric constant of 2.5 and constrain measurements to the polarized limb of the Moon. A dynamic range of a few tens is sufficient to remove the dependance of the distribution variance on thermal noise. The distribution variances seen in Table 2.2 is therefore expected to be predominantly driven by sidelobe emission and irregularities in the Lunar regolith.

towards pole position, horizontal towards east) with no significant outliers outside the assumed 5 degree engineering tolerances.

At the JVLA, at higher frequencies, Venus and Mars (shown in Fig. 2.28) are corrected for the assumed angle of the RL phases. We used RM corrections using global maps of the ionospheric TEC (JPLG [108] model) provided by the AIPS [58] `TECOR` program. After applying the measured offset and `TECOR` ionospheric corrections to 3C286, the observed EVPA matches well between the telescopes. The results are discussed further in Section 2.4.4. In Fig. 2.28 beam polarization and power attenuation are much less of a concern at these scales, compared to the Moon. Table 2.3 shows measured radial offsets on the Moon and Venus before and after applying RM corrections using `TECOR` with JPLG [108] IONEX databases. In D configuration not all the SPWs have results due to substantial RFI. This is less of an issue at A configuration for the Venusian data.

Table 2.3: Measured radial offsets in the linear EVPA measured on the Moon and Venus at L-band using the AIPS [58] `MARSP` program, where the ionospheric RM contribution is expected to be maximum for the observed VLA data

Observation	Frequency [MHz]	Offset without RM correction [deg]	Offset with RM correction [deg]	Fit error [deg]
Moon May '21	1044	8.4	-0.6	0.3
	1104	6.8	-1.1	0.3
	1312	5.6	0.1	0.2
	1360	5.9	0.6	0.2
	1424	5.5	0.7	0.2
	1488	5.2	0.8	0.2
	1639	4.8	1.2	0.2
	1676	3.8	0.3	0.2
	1744	3.9	0.7	0.3
	1807	4.4	1.5	0.3
	1872	3.8	1.0	0.3

Continuation of Table 2.3

Observation	Frequency [MHz]	Offset without RM correction [deg]	Offset with RM correction [deg]	Fit error [deg]
	1920	3.6	1.0	0.3
Moon Sep '22	1040	6.6	-6.4	0.2
	1102	4.3	-7.4	0.2
	1316	4.4	-3.8	0.3
	1359	4.3	-3.4	0.2
	1424	4.2	-2.8	0.3
	1487	4.3	-2.2	0.2
	1636	3.5	-1.9	0.2
	1675	4.1	-1.2	0.3
	1743	3.2	-1.5	0.4
	1807	3.4	-1.0	0.4
	1872	3.2	-0.9	0.3
	1932	2.6	-1.3	0.3
Venus March '22	1041	10.3	-2.3	0.6
	1104	9.9	-2.1	0.6
	1167	8.7	-1.1	0.5
	1232	8.3	-0.8	0.5
	1298	7.8	-0.2	0.3
	1359	7.4	-0.1	0.3
	1424	6.8	0.0	0.3
	1487	6.2	0.1	0.2
	1616	5.7	0.4	0.3
	1679	5.5	0.6	0.2
	1743	5.2	0.7	0.2
	1807	4.8	0.5	0.2
	1871	4.9	1.0	0.2
	1935	4.3	0.6	0.2
	2000	4.0	0.6	0.3

The error bars on the ionospheric corrections cannot be quantified from the limited observations we have on that telescope here. In separate work [129] the error bars at the VLA site from usage of JPLG[108] models through the `TECOR` routines are established at ~ 0.2 rad m^{-2}. This is significantly less than quoted by [102].

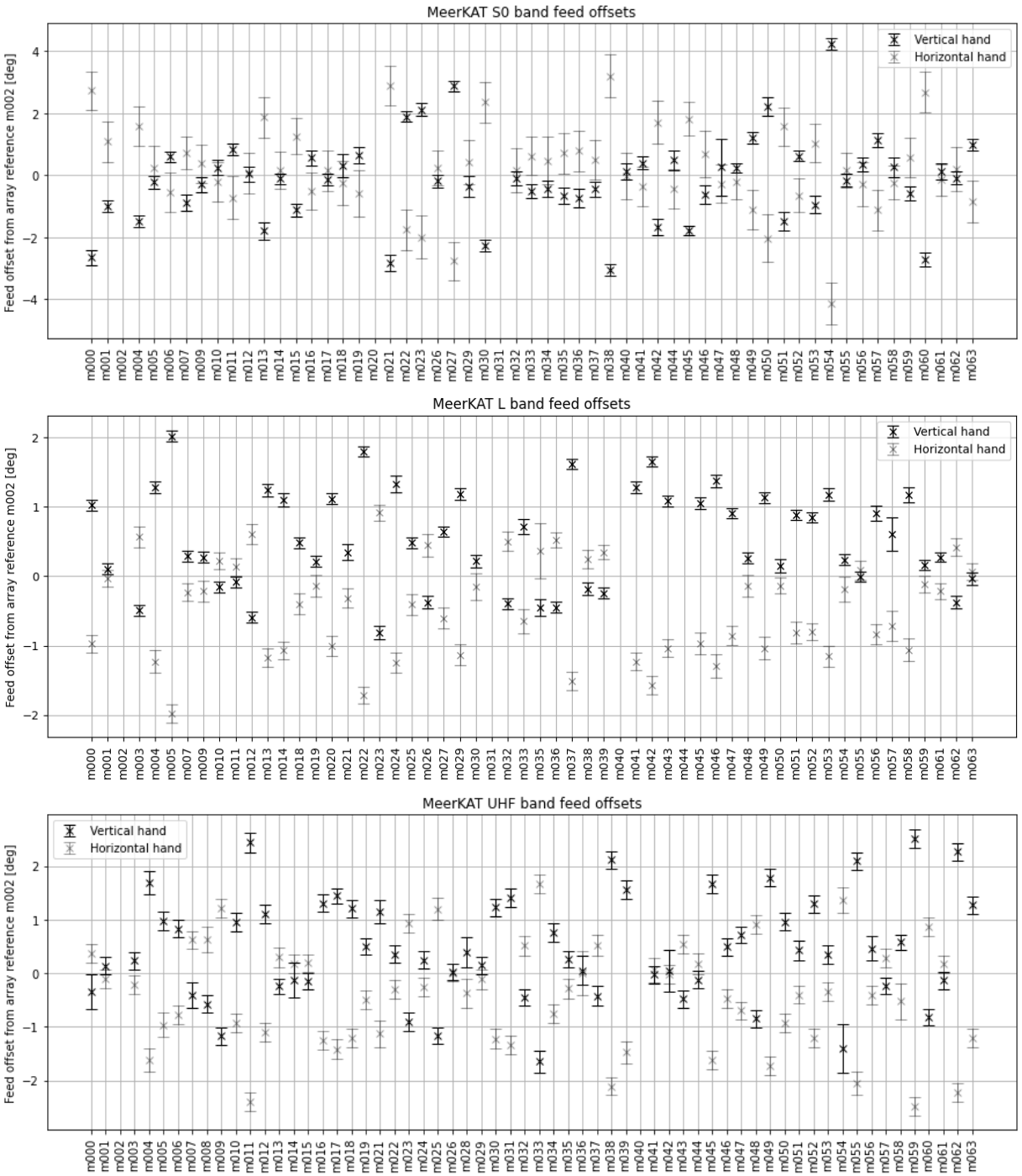

Figure 2.27: Relative feed angle offsets derived from relative leakage measurements and the global array offset measured on the Moon. We expect that these numbers will, from time to time, change as the receiver analog components are refurbished.

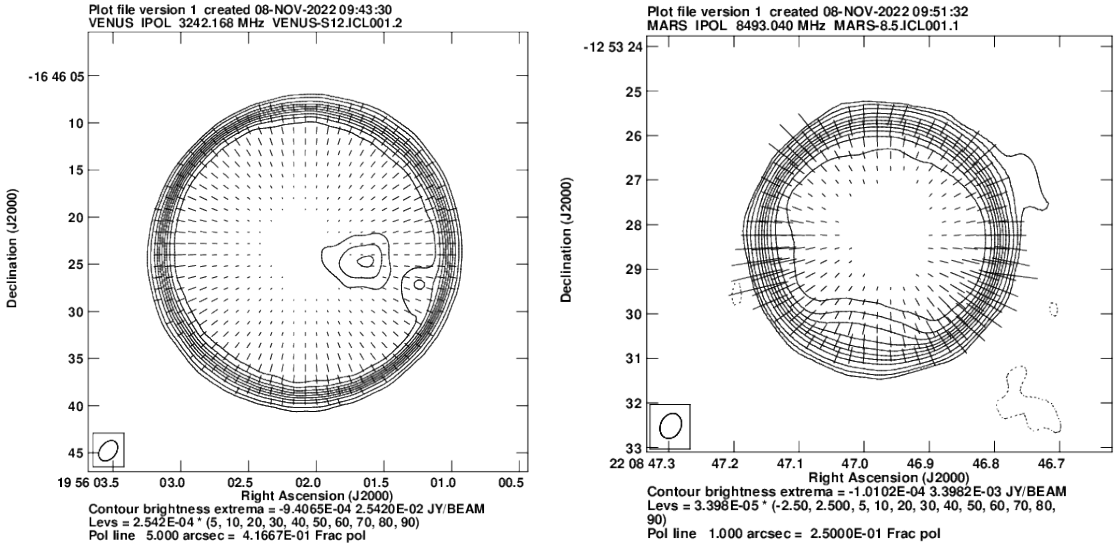

Figure 2.28: Venus and Mars shown left and right respectively. Polarization quivers are overplotted on total intensity maps showing the planetary temperature variations. The temperature depreciation seen on the Venus Equatorial region is a mountainous region with the contours showing a marked cooling due to its altitude. The temperature of Venus is markedly more radially homogenous than that of Mars, which shows a clear drop in temperature towards the southern ice caps on the planet.

2.4.4 A new low-frequency model for 3C286

Through our long-term study we present a new low frequency model of 3C286 which can be used to calibrate the absolute angle of circular feed systems, such as the JVLA, and check results on linear feed systems, such as MeerKAT by the user community. We show the ionospheric uncorrected measurements on MeerKAT for reference, as well as the residual scatter from various corrective regimes in Fig. 2.29. It is important to note that we correct, per scan, the ionospheric RM for the final measurements in both the AIPS and CASA datasets in the final measurements presented in this work.

Results from using the Lunar fitting procedure outlined in Section 2.2 yields an average (as determined from the entire observation) ionospheric contribution of -0.3 rad m^{-2} for the UHF observation and -0.2 rad m^{-2} for the L-band observation. Whether the global TEC model gives superior results over a local model is thus inconclusive — we can only establish that the RM signage and RM is correct to within an order of magnitude. This is supported by the measured scatter post ionospheric corrected measurements we see on long term observation of 3C286. A comparison of the predicted and measured TEC (directly fitted on the Moon) between the various IGS, local GNSS measurement using the TrigNET beacon network is presented in Fig 2.30.

In all cases, we have a residual of about 1 rad m^{-2} with both TEC estimates from local stations and TEC estimates from global JPLG [108] and UQRG [114] models, at the MeerKAT site. The measurements made on MeerKAT and the JVLA (after correction based on the Moon, Mars and Venus) matches to within the scatter induced by the ionosphere. For the local measurements we used the United States Air Force PIM model [42] of the ionospheric density using up to date 21cm data from the DRAO.

The evidence presented here strongly supports complaints from the MeerKAT user community that the intrinsic angle of 3C286 is significantly offset from the 33 degree extrapolation commonly assumed by the community. Curiously, we note that the drop in EVPA is accompanied by a substantial dog-legged depolarization in the source starting at the bottom of L-band, dropping sharply in power towards the low end of MeerKAT UHF band, as shown in Fig. 2.31.

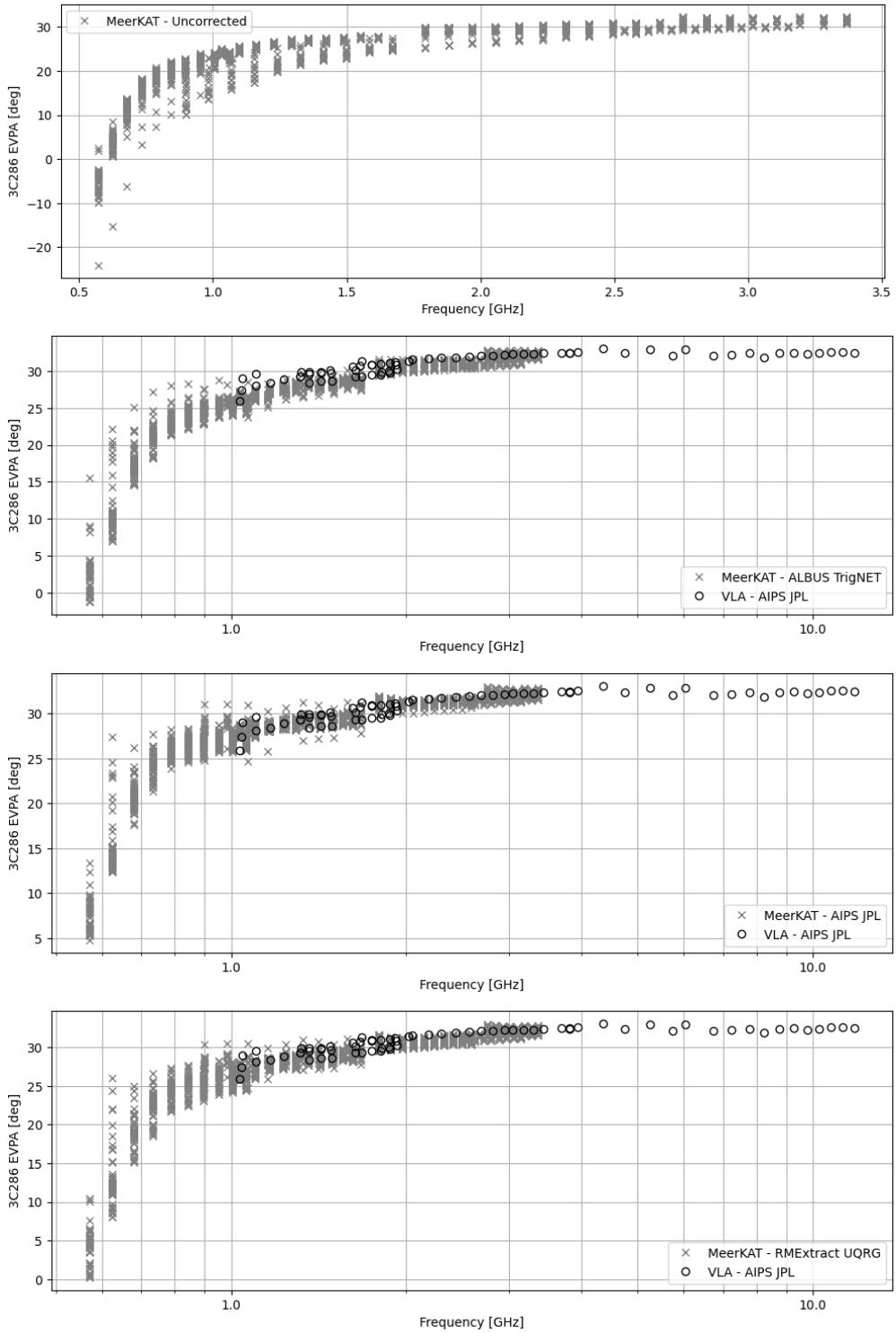

Figure 2.29: Measured EVPA of 3C286 on MeerKAT before (top) and after (comparative, bottom three plots) correction for ionospheric RM contribution. We show the ionospheric-induced scatter on the angle as observed over the course of three years as we headed towards the current Solar high (top). We show the residual scatter after applying corrections from distributed JPLG [108], UQRG [114] models as well as locally-derived (TrigNET) models. Corrections are applied on a scan-by-scan basis.

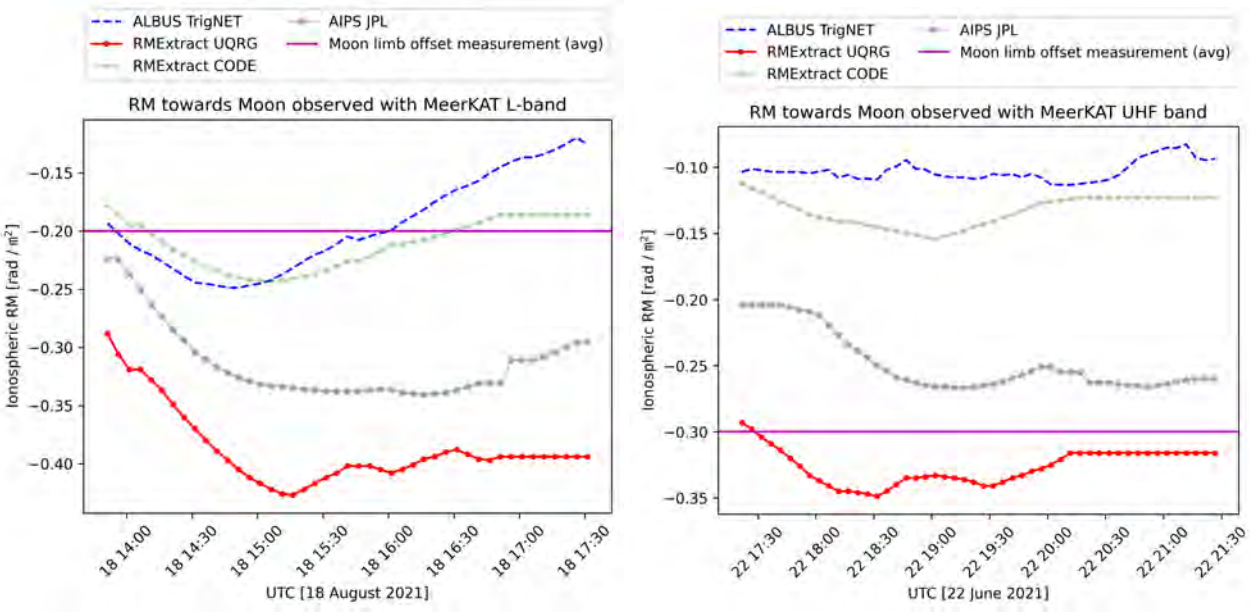

Figure 2.30: A comparison between predicted Rotation Measure towards the Moon from various IGS databases (CODE, JPLG, UQRG), direct differential GNSS TEC measurement using the TrigNET beacon network and direct fitting of the frequency dependent component of the polarized Lunar limb (average across the entire observation to ensure sufficient SNR on the fit) is shown. Both L (left) and UHF (right) observations of the Moon were taken during relatively quiescent ionospheric conditions. We take the direct measurement of the ionospheric conditions on the Moon as the most accurate measurement of the ionospheric RM available from the observed data. In line with long term monitoring none of the IGS-derived or local differential TEC measurements using the TrigNET GNSS beacon network show a marked improvement in the absolute scaling relative to the other products.

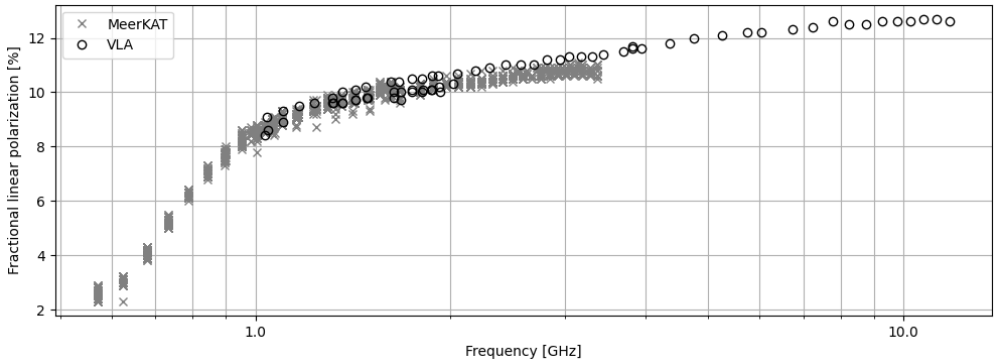

Figure 2.31: Strong depolarization is observed for 3C286 at sub-Gigahertz frequencies.

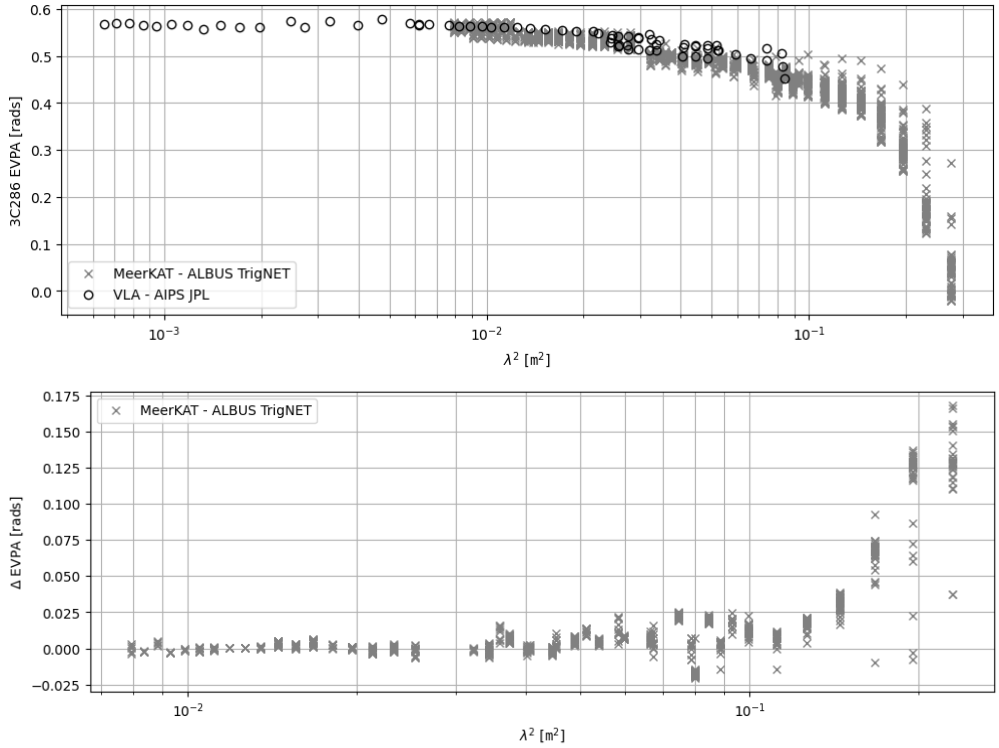

Figure 2.32: 3C286 EVPA (here in radians) along with its gradient as a function of squared wavelength. We see a marked change in rotation measure from near 0 at higher frequencies (and historically extrapolated by the community to frequencies below the C/X-band) to about 0.12 rad.m^{-2} at the bottom of the MeerKAT UHF band. Differential scatter is computed on an observation-by-observation basis.

It must be noted that, because the intrinsic EVPA (after ionospheric correction) drops only gradually, the depolarization in the linear power cannot be because of a singular strong RM screen. An alternative view is presented in Fig. 2.32. The RM of the source is markedly not constant — it shows curvature after about 1 GHz.

If we apply a filter to select scans that are observed strictly during night-time on ALBUS-corrected MeerKAT data and is at least 60 degrees in arc away from the Sun to avoid the worst issues due to Solar wind then we obtain the following broken power law fit of the EVPA, with frequency specified in units of GHz. These are shown in Fig. 2.33.

$$\mathrm{EVPA}(\nu_{\mathrm{GHz}})\ [\mathrm{deg}] = \begin{cases} 32.64 - 85.37\lambda^2 & \text{if } \nu_{\mathrm{GHz}} \in [1.7, 12] \\ 29.53 + \lambda^2(4005.88\log_{10}^3 \nu_{\mathrm{GHz}} - 39.38) & \nu_{\mathrm{GHz}} < 1.7 \end{cases}$$

$$P(\nu_{\mathrm{GHz}}) = \begin{cases} 0.080 - 0.053\lambda^2 - 0.015\log_{10}\lambda^2 & \text{if } \nu_{\mathrm{GHz}} \in [1.1, 12] \\ 0.029 - 0.172\lambda^2 - 0.067\log_{10}\lambda^2 & \nu_{\mathrm{GHz}} < 1.1 \end{cases}$$

Here λ is the wavelength in meters and ν_{GHz} is the frequency in gigahertz.

2.5 Conclusions

In this chapter we addressed the lingering issue of the intrinsic polarization angle of 3C286 at low frequencies which is intended to be a counterpart to [127]. We find that the angle is substantially less than the invalid 0 rad m^{-2} extrapolation

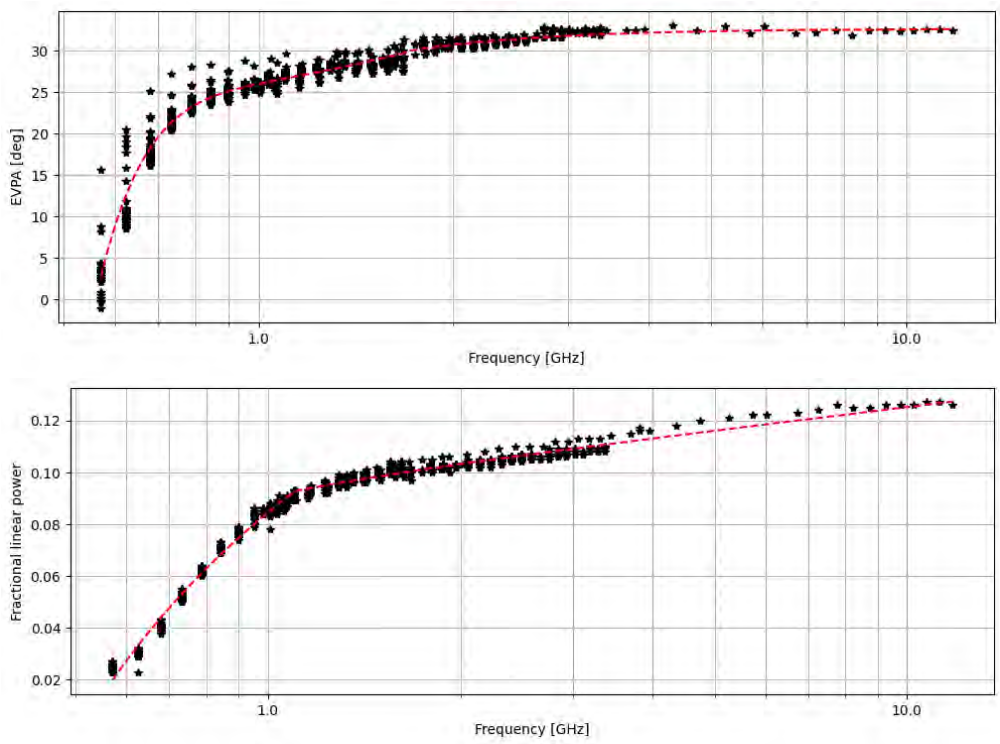

Figure 2.33: Broken power law fit of the EVPA and linear polarization fraction of 3C286. Error indicated as scatter from filtered measurements as discussed in the text.

of 33 degrees (measured only at higher frequencies by [16, 127]) widely assumed by the community, which has spread throughout the working knowledge in the literature. We find that the source has an intrinsic rotation measure that gradually increases to about 0.12 rad m^{-2} below 1 GHz.

From our analysis, it is clear that MeerKAT off-axis leakages account for many-percent-level errors beyond 1.4 GHz in L-band and the higher frequencies in S-band (S1 and beyond) when observing beyond 0.3 degrees from the pointing center. It is also clear that the MeerKAT feeds, as a global average, are well aligned with nominal IAU convention, with all antennas conforming to well within their dipole alignment specification (a scatter of at most about 2 degrees is seen at S-band), once the software convention is corrected as per EVLA memo 219 [128].

Correcting for the ionospheric contribution is the main limitation to our analysis. We have tested corrective schemes using a thin shell model with global IONEX data, as well as a local model (based on stations in the South African TrigNET network and US Air Force PIM model of the three-dimensional ionospheric profile) with no definitive improvement in the residuals between corrective regimes. From long-term observation at the MeerKAT site we determine that these residuals are on the order of ~ 1 rad m^{-2}. We suspect that these errors are primarily driven by our lack of understanding of the ionization densities in the upper ionosphere coupled with very few contributing IGS stations around the MeerKAT site. It is important to stress that, although there are significant residuals, ionospheric corrections significantly improve the diurnal and spatio-temporal variability in the Rotation Measure contributed by the ionosphere, and these corrections must be applied in science observations where the EVPA is measured, especially at frequencies below 1.0 GHz.

Future work entails properly characterizing the variable 3C138 at cm wavelengths over the long term. Multiband subarray MeerKAT data for this calibrator has already been taken at the time of writing.

Chapter 3

Multi-directional simultaneous peeling

In this chapter we discuss the development of a streamlined workflow for direction-dependent calibration of interferometric data in the CUBICAL [87] calibration framework. This is achieved through model prediction using targeted faceting in user-defined lattices. We show how this is incorporated into an end-to-end reduction framework for MeerKAT data using containerization technology through the STIMELA [101] workflow orchestration package.

3.1 Motivation

Hand-in-hand to the imaging problem is the dual problem of telescope calibration. Without calibrating, at minimum, the semi-random phases (due to impedance differences) of an interferometer, it is not possible to synthesize an image. Yet, calibrator fields (dominated by compact bright quasars or stellar objects) are often far and few between. They are often spatially separated by tens of degrees from target fields, and by tens of minutes in their observation. They, therefore, do not capture the full effect of system calibration error. This calibration error, effectively, decorrelates the system reponse to a source of emission from the idealized response of the interferometer, in turn causing artifacts around sources of emission in synthesized maps.

Given that the distribution of sources on the sky is usually relatively sparse (save perhaps for the well resolved emission of the galactic plane) and modern large interferometric arrays are well-engineered (both electrically and mechanically), the problem of deriving time, frequency and directional gains are, usually, substantially overdetermined — by several orders of magnitude depending on the complexity needed to model the distribution of flux on the sky. Solution intervals are usually driven by signal-to-noise constraints and the dominance of residual systemics, such as the intereference of terrestrial transmitters. To counter the slowly-varying, spatially-smooth gains introduced by the system electronics and the environment, both the model and the gains (derived through non-linear least squares) are iteratively improved through a process of imaging (which constructs a model of the sky flux distribution from calibrated measurements — the "visibilities") and calibrating the measured visibilities to this model, starting only with an initial map of the target field (calibrated by interpolation of temporal and frequency-dependent gains derived from known compact calibrators). This modern "self"-calibration process dates at least as far back as [141].

Calibration error can be both direction independent (as in the case of system impedance gains) and direction dependent (most prominent is the dispersive effects of the ionosphere and the attenuating antenna far field beam, driven by pointing error). Although the CUBICAL [87] calibration package significantly simplifies the steps required to apply a direction-dependent treatment over traditional approaches as implemented in CASA [104] the model prediction component remained a reasonably laborious task. In the direction dependent case the sky flux contribution to the measured visibility on each

pair of antennas have to be decomposed between their region of origin on the celestial sphere, in order to solve for, and apply, a direction dependent gain correction. This could be done in two approaches:–

- Requiring that the user tag and predict each patch where they wish to affect directional dependent gains into separate data columns (each the size of the original database — prohibitatively expensive in terms of storage), which require multiple iterations of invoking an imager to predict visibilities corresponding to a subset of sky, or
- Requring fitting for components and storing them in a TIGGER `Local Sky Model` catalog for on-the-fly model prediction during calibration through computing a Direct Fourier sum, which has limited capacity to capture frequency dependence in the model and is prohibitatively expensive for larger numbers of components due to the poor scaling of such direct sum approaches. Such approaches scale linearly with the number of sources, M, instead of the $\log M$ scaling achieved through inversion through convolutional Fast Fourier Transform approaches, as is widely implemented in imaging packages.

This work expands on the flexibility introduced by the CUBICAL [87] calibration package and adds on-the-fly fast $\log M$ prediction of model visibilities, which substantially improves the usability of the software.

We will start by formally introducing the spatial relationship between the sky flux distribution and the measured visibility product and the treatment of non-coplanar visibility samples in Section 3.2, before returning to the general calibration problem and extending the CUBICAL [87] calibration package with our on-the-fly predictive regime in Section3.3. In Section 3.4 we showcase a comparison between our augmented peeling approach in CUBICAL and KILLMS, before discussing incorporating our augmented approach in an end-to-end data reduction framework, called VERMEERKAT, in Section 3.5.

3.2 Background - the problem of non-coplanar baselines

The discussion here is summarized from [153] and the RATT Fundamentals of Interferometry interactive book[1].

A Radio Interferometer Measurement Equation (hereafter "RIME") for a perfectly calibrated noiseless omnidirectional single feed interferometric system observing a single unresolved unpolarized source with brightness $I(l,m)$ Jy at cosine position $l,m,n=\sqrt{1-l^2-m^2}$ on the celestial sphere is given by Eqn. 3.1.

$$V(u,v,w)=\frac{I(l,m)}{n}\exp\left[-2j\pi(ul+vm+w(n-1))\right] \tag{3.1}$$

Here $V(u,v,w)$ is the complex-valued "visibility" product, as measured in a local Euclidean space. For a specified hour angle each pair of interferometer stations (forming a "baseline" vector) define a single measurement coordinate in this uvw space that forms the virtual aperture. A radio interferometer is used to observe spatial scales on the sky. Interferometers with short spacings close to the origin of this space are sensitive to large scales on the sky, whereas interferometers with longer spacings are sensitive to smaller structures on the sky. This can be seen from the complex fringe defined in Eqn. 3.1: as baseline length is increased (and shortening of the associated fringe response period) scales on the sky become resolved out and sensitivity to large scales drops off (hence why this is referred to as a "visibility" function).

The uvw coordinates are defined such that the w direction points towards a point on the sky where the fringes defined in Eqn. 3.1 is a constant function (ie. the fringes are "stopped"). At this position $l=m=0,n=1$ as indicated in Fig. 3.1.

The uvw basis are defined relative to a nominal Equatorial coordinate frame where X points south on the celestial equator, Y points east on the celestial equator and Z points towards NCP. This frame is given, to first order, by the azimuth, $\mathscr{A}$,

[1] Available from `https://github.com/ratt-ru/fundamentals_of_interferometry`

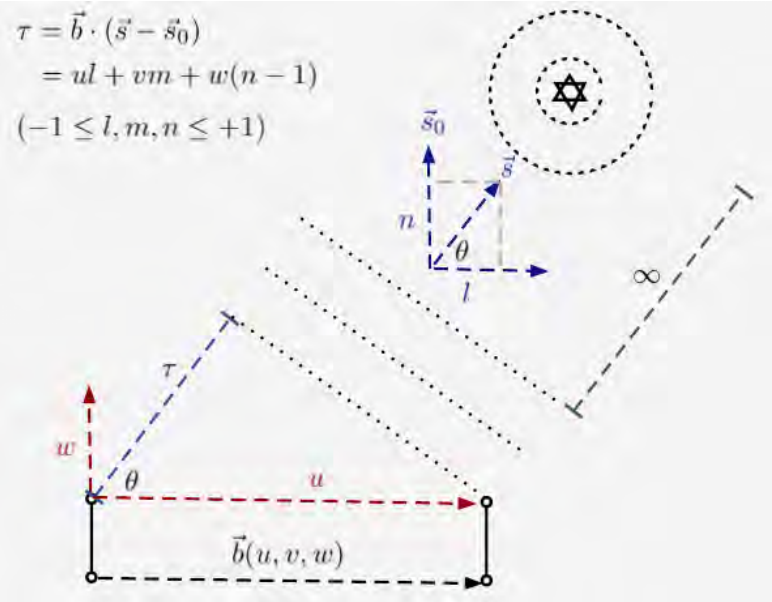

Figure 3.1: The two element interferometer showing the geometric relationship between a source at cosines l, m off the fringe- stopping direction on the celestial sphere in the direction of $\vec{s}_0$, or equivalently, the direction of the w basis vector. In the far field (here illustratively indicated by ∞) the propagation delay is given by the scalar projection of the source cosines onto the baseline vector $\vec{b}$. The cosines are assumed to lie on the unit sky sphere, with $n := \sqrt{1-l^2-m^2}$. This illustration is confined to the lu-dimension for illustrative purposes.

(north-through-east) and elevation, $\mathscr{E}$, angles of the baseline between an antenna/station pair on a plane tangent to the horizon of the local observer at latitude, L_a according to the Eqn. 3.2. The coordinates depend on the hour angle, H, and declination, δ, towards the fringe-stopped position on the sky, and scale inversely with the observing wavelength λ. $|\vec{b}|$ is the vector distance between the pair of antennas that defines the baseline.

$$\begin{bmatrix} u \\ v \\ w \end{bmatrix} = \begin{bmatrix} \sin H & \cos H & 0 \\ -\sin\delta\cos H & \sin\delta\sin H & \cos\delta \\ \cos\delta\cos H & -\cos\delta\sin H & \sin\delta \end{bmatrix} \begin{bmatrix} \cos L_a \sin\mathscr{E} - \sin L_a \cos\mathscr{E}\cos\mathscr{A} \\ \cos\mathscr{E}\sin\mathscr{A} \\ \sin L_a \sin\mathscr{E} + \cos L_a \cos\mathscr{E}\cos\mathscr{A} \end{bmatrix} \frac{|\vec{b}|}{\lambda} \tag{3.2}$$

The source cosines lmn are defined relative to the baseline-orthogonal $\vec{s}_0 =< 0,0,1 >$ direction in Fig. 3.1. In practice this vector $\vec{s}_0$ may lie in any direction on the sphere: one only needs to multiply the complex voltages with the appropriate delay to shift the fringe stopping position to another position on the celestial sphere. We note that the cosines are related to the celestial coordinates as (where α_0, δ_0 is the coordinate of the fringe stopping position):

$$\begin{aligned} l = &\quad \cos\delta\sin(\alpha-\alpha_0) \\ m = &\quad \sin\delta\cos\delta_0 - \cos\delta\sin\delta_0\cos(\alpha-\alpha_0) \\ n = &\quad \sqrt{1-l^2-m^2}, ||l,m|| \leq 1 \end{aligned}$$

For all hour angles at a given declination on any east-west baseline on a flat plane one may linearize Eqn. 3.1 to the

following

$$
\begin{aligned}
V(u,v) &= \frac{I(l,m)}{\sqrt{1-l^2-m^2}} \exp\left(-2j\pi(ul'+vm')\right) \\
&\quad (\forall u,v \exists \beta,\gamma \in \mathbb{R}) \\
l' &:= l+\beta\left(\sqrt{1-l^2-m^2}-1\right) \\
m' &:= m+\gamma\left(\sqrt{1-l^2-m^2}-1\right)
\end{aligned}
\tag{3.3}
$$

From Eqn. 3.3 it is clear that there is a simple two-dimensional Fourier relationship between any point in the visibility domain and its sky brightness, because all points in the *uvw* space are coplanar and a linear transformation exists between their position on the w basis and the $w=0$ plane.

This general two-dimensional relationship is only applicable to a limited number of physical interferometric arrays, such as the Westerbork Synthesis Radio Telescope. For an array containing non-east-west spacings such as MeerKAT, generally, there is no such simple linear relationship between all measurements. The measurements taken with such an array are non-coplanar. For such a north-south component array, if one were to synthesize a two dimensional map of the sky the $\xi = w(n-1)$ term must then be treated as a source of error that depends on the physical size of the array, the hour angle, and radial distance off the fringe stopping position of an observation. One may think of this phase error on the visibility term as introducing a baseline and angular offset dependent smearing in the image space. Luckily there are several approximate methods that can be used to do this three-to-two-dimensional transformation between sampled visibilities and image space.

Faceted imaging is a traditional approach in imaging to solve the problem of non-coplanar baselines associated with non-east-west interferometric arrays when synthesizing maps over a wide field of view. The approach is discussed in [35] and generally entails the following steps:

1. Split the field of view into patches (for instance a grid of square patches), each with a celestial centroid coordinate.
2. For each patch take all measured visibilities and rephase to the center of the facet. This has the effect of shifting the sky over the facet field of view, such that it has zero phase at the center of the facet.
3. Optionally, further minimize error at the edge of the field of view in each facet by convolution of the remaining w term (W-projection [36]) or by tilting the geometry of each facet to be tangent to the sky sphere such that the w coordinate points towards the facet center [153, ch 19] (see Eqn. 3.2).

Formally, step two is implemented by multiplying each visibility with a phasor

$$
V'(u,v,w) = V(u,v,w)\exp\left[2j\pi(u(l_0-l_f)+v(m_0-m_f)+w(n_0-n_f))\right] \tag{3.4}
$$

where l_f, m_f, n_f is the centroid coordinate of the facet in question and l_0, m_0, n_0 is the original phase stopping center of the observation. With a smaller field of view around this new phase center the total error at the edge of the field of view is reduced, ie. ξ decreases from a geometric error with respect to the original phase center of the image ($n_0 = 1$) to an error with respect to the new tangent point n_f. The geometry of the rephased problem is illustrated in Fig. 3.2.

Although a full templated implementation of the tilted geometry approach is provided in the codex-africanus[2] library, using the NUMBA [95] LLVM just-in-time compiler for PYTHON [162], the implementation in the calibration routines discussed in Section 3.3 currently use the parallel-planes approach implemented in the DDFACET [152] imaging package.

[2] See `https://github.com/ratt-ru/codex-africanus/tree/master/africanus/gridding/perleypolyhedron`

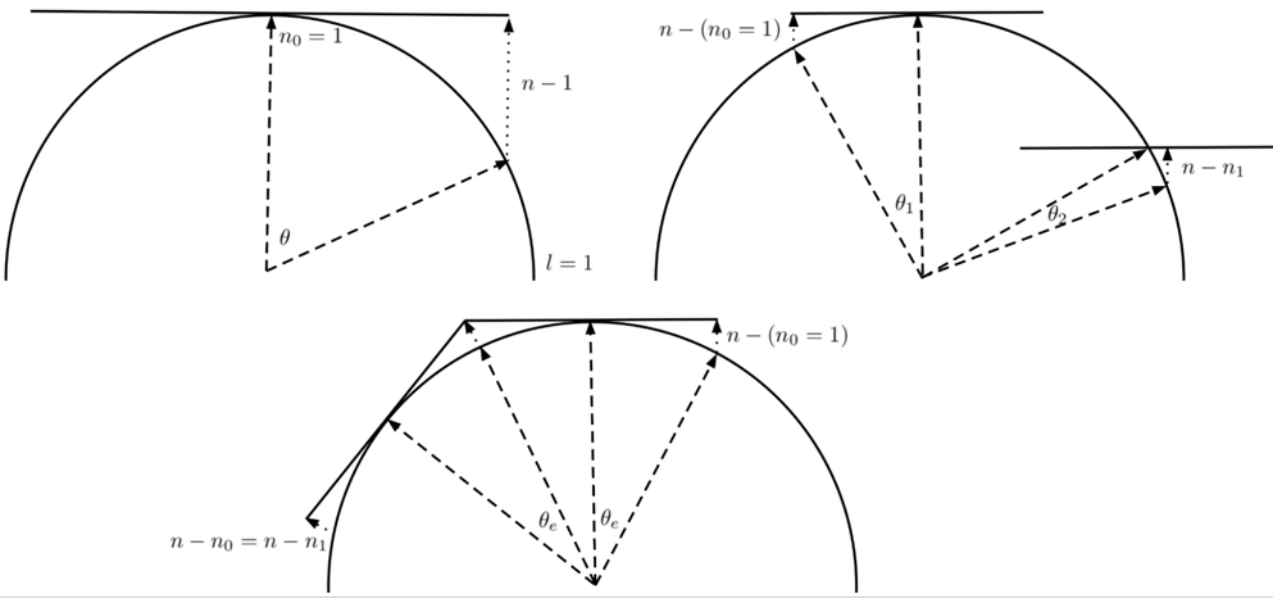

Figure 3.2: Illustration of faceted geometry. Top left we show the geometric projection error associated with taking a two-dimensional transform of a large field of view (shown in dotted lines as $n-1$). Top right we show the geometric error associated with parallel-plane facets (formed by rephasing). Here the error, albeit much smaller than associated with a large field of view, is dependent on the angular distance of the facet center to the original phase center. Consequently the distortion-limited field of view θ_1 and θ_2 decreases the further away n_1 is placed from n_0, and many more facets are needed towards the edge of an image formed with such an approach if further corrections are not applied. Lastly, in the bottom illustration, we show the approach to equal-sized faceting developed by [35]. Here the geometry of the facet is rotated such that the image plane is kept tangent to the sphere. This ensures that the undistorted field of view is constant ($\theta_0 = \theta_1 = \cdots = \theta_e$) regardless of the angular separation between n_0 and n_1.

I briefly discuss the approach outlined in the paper here. Applying the phasor defined in equation 3.4 to the visibilities one obtain the following measurement equation

$$V'(u,v,w) = \frac{I(l,m)}{\sqrt{1-l^2-m^2}} \exp\left[-2j\pi(u(l-l_f)+v(m-m_f)\right] \exp\left[-2j\pi w(n-n_f))\right]$$

For a more complicated sky brightness distribution this generalizes to the following convolution

$$\begin{aligned} V'(u,v,w) &= \int_{(l,m)} \left[\frac{I(l,m)}{\sqrt{1-l^2-m^2}} \exp\left(-2j\pi(u(l-l_f)+v(m-m_f))\right) \right] * \bar{G} \\ \bar{G} &:= \exp\left(-2j\pi(w(n-n_f))\right) \end{aligned} \tag{3.5}$$

Where $\bar{G}$ can be applied as part of a convolution kernel while the visibilities are resampled onto a regular grid for two-dimensional transformation with a Fast Fourier Transform. This approach is analogous to the original w-projection algorithm discussed by [36]. The support for these kernels grows as the square of the image diameter. Typically they are combined with an anti-aliasing kernel and pretabulated at predetermined stepping (e.g. a linear stepping in our implementation) with adequate number of steps to keep the separation in the projected distance between steps small.

As [90] notes there exists a linearization for such $\bar{G}$. By first order Taylor expansion we may approximate

$$n - n_f \approx -\frac{l_f(l-l_f)+m_f(m-m_f)}{\sqrt{1-l_f^2-m_f^2}}$$

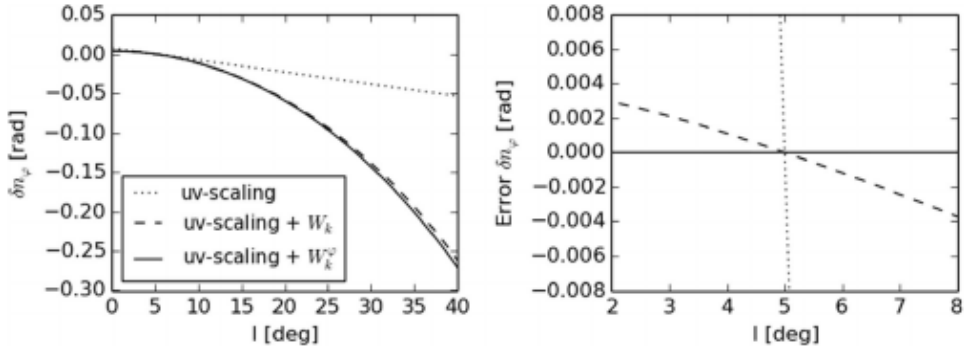

Figure 3.3: Comparison of the error associated with the approaches discussed in this section taken from [152]. Left: $n-n_f$ as a function of radial distance from the facet center as implemented with the [90] linearization approach (dotted), [90] with a traditional w-term added (dashed) and our polynomial approach (solid). Right: residual error from the three approaches. As shown, the polynomial approach works best.

which can conveniently be applied by a change in uv coordinates while resampling

$$u' = u - w\frac{l_f}{\sqrt{1-l_f^2-m_f^2}}, \text{ and}$$
$$v' = v - w\frac{m_f}{\sqrt{1-l_f^2-m_f^2}}$$

This linearization still leaves higher order (curvature) phase errors from the geometry, but greatly reduces the support needed in the kernel when modeling the residual convolution term. We increase the accuracy of the approximation by evaluating a polynomial fit to $n-n_f$. This is given as $n-n_f \approx \vec{\Delta_l}^T \mathbf{P}_{k,N_f} \vec{\Delta_m}$ where Δ_l and Δ_m are polynomial basis vectors of order k and $\mathbf{P}_{k,N_f}$ is a matrix with fit coefficients for the N_f facets. Then the first order terms may again be expressed as coordinate transformation

$$u' = u + w\mathbf{P}_{k,f}[1,0], \tag{3.6}$$

$$v' = v + w\mathbf{P}_{k,f}[0,1], \text{ and} \tag{3.7}$$

$$\bar{G} \approx \bar{G}' = \exp\left(-2j\pi(w\vec{\Delta}_l^T \bar{\mathbf{P}}_{k,N_f} \vec{\Delta}_m)\right) \tag{3.8}$$

where $\bar{\mathbf{P}}_{k,N_f}$ is just $\mathbf{P}_{k,N_f}$ with coefficients $[1,0]$ and $[0,1]$ set to unity.

Then substituting 3.6, 3.7 and 3.8 into the rephased measurement equation in 3.5 we obtain the forward and backward transformation operator, 3.9, used for DDFACET [152] and the modeling system we implemented for direction-dependent calibration discussed in section 3.3.

$$V'(u,v,w) = \int_{(l,m)} \left[\frac{I(l,m)}{\sqrt{1-l^2-m^2}} \exp\left(-2j\pi(u'(l-l_f)+v'(m-m_f))\right)\right] * \bar{G}' \tag{3.9}$$

Typically polynomials of order 4th or 5th are sufficient for general use in this w-correcting parallel plane faceting approach. Through this coordinate transformation approach the support needed for $\bar{G}'$ is not substantially larger than the typical few-pixel support needed for the anti-aliasing kernels. This limits the per facet resampling and transformation time. The two approaches are compared in Fig. 3.3, where the functions are plotted as a function of radial distance from the facet phase centre to the left, as well as the error to the true $n-n_f$ term to the right. We show the improvement of our approach over the linear approach taken by [90], where the linearization rapidly breaks down as a function of radial distance from the facet phase centre.

3.3 Targeted faceting for direction-dependent calibration

In Section 3.2 we discussed how the measurement operator is implemented to go between image and measurement space for a perfectly calibrated interferometer. In this section we apply the faceting approach to substantially simplify direction-dependent calibration through an easy-to-use interface implemented within the CUBICAL framework [87].

The software developed for this section is freely available under GNU General Public License v2.0 within the CUBICAL [87] software package: `https://github.com/ratt-ru/cubical`. As such no source code will be printed in this section.

We start by formally expanding the radio interferometric measurement equation in Eqn. 3.1 to an orthogonal set of basis (needed to fully describe the polarization state of the transverse wavefront being measured). We will only discuss the linear basis here. For a single emitting source, measured on an interferometer between antennas p and q we have

$$V_{pq}(u,v,w) =< \mathbf{K}_p[e_{Xp},e_{Yp}].[e_{Xq},e_{Yq}]^H\mathbf{K}_q^H > \tag{3.10}$$

Where $<>$ denotes a short term average over channelized voltages (e) captured on the two orthogonal feeds X and Y on two antennas p and q. $\mathbf{K}$ is a diagonal-scalar matrix containing the geometric delay we first introduced in Eqn. 3.1, ie.

$$\mathbf{K}_p = \begin{bmatrix} e^{-2j\pi(u_pl+v_pm+w_p(n-1))} & 0 \\ 0 & e^{-2j\pi(u_pl+v_pm+w_p(n-1))} \end{bmatrix}$$

Here the geometric delays are applied in fine-enough temporal resolution to satisfy the astrometric requirements of the system, within an averaging interval that is set by the allowable time-smearing tolerance at the edge of the field of view. The non-coplanar phased corrections discussed in Section 3.2 can be analogously applied to the 2x2 coherencies defined in Eqn. 3.10 and we do not consider them a source of error.

For an interferometer with linear bases with $+X$ pointing towards NCP and $+Y$ pointing east (increasing right ascension) the coherency matrix $\mathbf{B}$ measures [64]

$$\mathbf{B} = [e_{Xp},e_{Yp}].[e_{Xq},e_{Yq}]^H = \begin{bmatrix} I+Q & U+jV \\ U-jV & I-Q \end{bmatrix}$$

As with Eqn. 3.1 Eqn. 3.10 still describes a perfectly calibrated system. Additional sources of error on the propagation of the measured signal can be fully described by a chain of 2x2 complex Jones [82] matrices along the following "onion" form [146]:

$$V_{pq}(u,v,w) =< \mathbf{J}_{pN}\mathbf{J}_{pN-1}\dots\mathbf{J}_{p1}\mathbf{K}_p\mathbf{B}\mathbf{K}_q^H\mathbf{J}_{q1}^H\dots\mathbf{J}_{qN-1}^H\mathbf{J}_{qN}^H > \tag{3.11}$$

Here the N^{th} 2x2 matrix describes a propagation effect (or polarizer) closest to the observer and the matrix closest to the geometric delay a propagation effect closest to the emitting source. These terms may be frequency, time and direction-dependent. If we assume that the variation on these terms are longer than the typical few-second integration periods then we can move the Jones terms outside of the averaging product. For a more spatially-complex sky distribution, Eqn. 3.11 can then be rewritten as follows

$$V_{pq}(u,v,w) = \mathbf{G}_p(\nu,t)\int_{(l,m)}\left[\Delta_p(l,m,\nu,t) * \mathbf{K}_p\mathbf{B}\mathbf{K}_q^H * \Delta_q^H(l,m,\nu,t)\right]dldm\mathbf{G}_q^H(\nu,t) \tag{3.12}$$

Here the **G** terms are systemic errors on the signal chain that apply equally to all directions. The Δ terms are direction-dependent Jones matrices, and in the most general case may vary across the source extent. The most prominent example of this is the convolution with the far field voltage response of the antenna (which in itself is approximately a Fourier relationship with the voltage distribution, so-called "grading", along the surfaces of the antenna / station). These far field patterns are typically not completely symmetric (especially when struts are used to support secondary reflectors) and are subject to per antenna shifts (pointing errors), rotation over the sky when the reflectors are placed on alt-azimuth mounts (as a function of time-variable parallactic angle) and inversely scales spatially with increasing observing frequency.

If we include the system noise and make further simplifications: firstly, that most extragalactic sources are spatially compact, and secondly that these far-field effects are spatially smooth (therefore roughly constant over small areas of sky), then Eqn. 3.12 may be further simplified to Eqn. 3.13.

$$V_{pq}(u,v,w) = \mathbf{G}_p(\nu,t) \sum_{(l,m)} \left[\Delta_p(l,m,\nu,t)\mathbf{K}_p\mathbf{B}\mathbf{K}_q^H\Delta_q^H(l,m,\nu,t)\right]\mathbf{G}_q^H(\nu,t) + \eta_{pq}(\{p,q\} \in \{\text{ant}\} \times \{\text{ant}\}) \tag{3.13}$$

η_{pq} is the baseline-dependent correlated noise term that stems primarily from the low noise amplification circuitry of the receiver electronics, but includes other terms such as spillover, atmosphere temperature, etc. A full treatment is not necessary for the discussion here — the reader is referred to [153, ch 9] for a detailed statistical treatment.

In its simplest form, Eqn. 3.13 defines the direction-dependent calibration problem we are solving in this work that is encountered with radio interferometers. One may further generalize this to chains of terms for both the direction-independent and dependent terms. In the centimeter regime, the calibration errors show up, for the most part, around the brightest field sources. Depending on the proximity of these calibration artifacts to the science target this may preclude the derivation of imaging products at sufficient fidelity to achieve the science goals of the observer.

We use faceting to predict the model visibilities in direction (l,m) in Eqn. 3.13 via Fourier transform, denoted $\mathscr{F}$. It is easy to see how this can be reformulated to be applicable to patches of model visibilities

$$V(u,v,w) \approx \mathbf{G}_p(\nu,t)\left[\mathscr{F}\mathbf{B}_{\text{DIE}} + \sum_{(\hat{l},\hat{m})} \Delta_p(\hat{l},\hat{m},\nu,t)(\mathscr{F}\mathbf{B}(\hat{l},\hat{m}))\Delta_q^H(\hat{l},\hat{m},\nu,t)\right]\mathbf{G}_q^H(\nu,t) + \eta_{pq}(\{p,q\} \in \{\text{ant}\} \times \{\text{ant}\}) \tag{3.14}$$

Here $\mathbf{B}_{\text{DIE}}$ is the portion of celestial emission deemed not to contain significant direction-dependent gains by the user. At the same time $\mathbf{B}(\hat{l},\hat{m})$ describe areas of sky $(\hat{l},\hat{m})$ which are affected by direction dependent effects that are relatively invariant over the extent of those regions. The Fourier transform $\mathbf{B}_{\text{DIE}}$ is all the field flux as predicted by the imaging software into a model data column with the contributions in the patches defined by $\mathbf{B}(\hat{l},\hat{m})$ removed. Alternating between a chain of direction-independent and direction-dependent gains in this definition has the advantage of limiting the potential for flux absorption, by taking into account as much of the sky flux as possible during solving.

A typical workflow to solve for direction-dependent effects toward multiple patches of sky emission with this approach entails:

1. Imaging, using DDFACET [152], typically with a binary mask to constrain image deconvolution to real emission and to avoid the sidelobe structure of the gain decorrelated Point Spread Function. Like most other imagers the imaging software will write back the model visibilities into the Measurement Set database for use in calibration. The imager also writes out image model (CLEAN) components into a DicoModel file.

2. Opening and marking of regions. These areas can be made arbitrarily complex in their morphology. The interface we specify allows the user to define convex latices around patches of sky affected by direction-dependent effects.

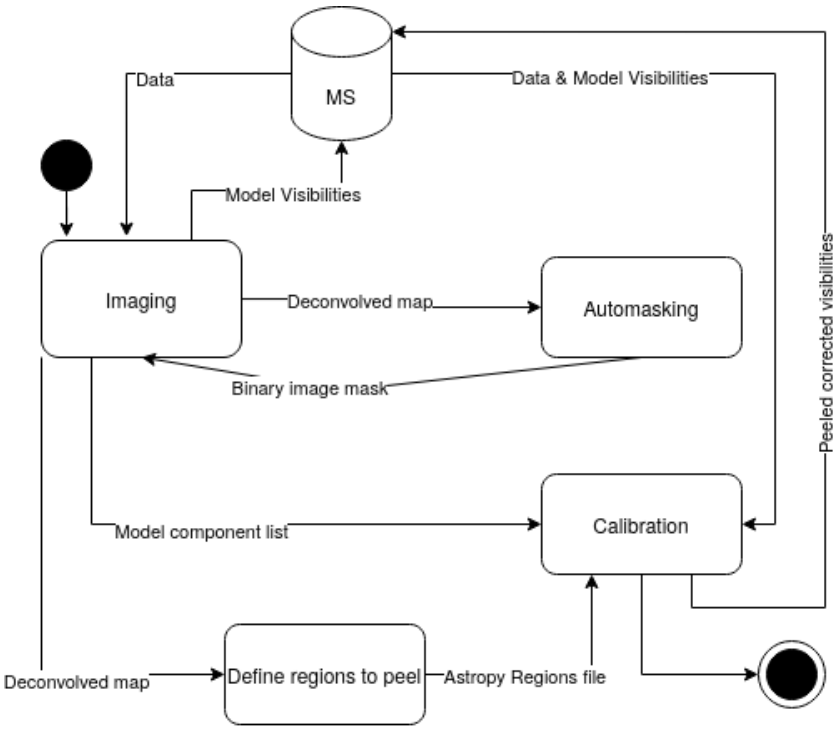

Figure 3.4: One round of self-calibration as outlined above. Multiple regions can be peeled off simultaneously per Eqn. 3.14

These lattices can be drawn visually using the popular SAODS9 FITS viewer [83] and stored in an ASTROPY [136] regions lattice format file.

3. The user supplies both the regions file, the DicoModel component list file, and the database with all-sky model visibilities to CUBICAL [87]. CUBICAL is set to solve for a chain of direction-independent and direction-dependent complex gains and to subtract the gain-corrupted visibilities of the various regions to simultaneously peel the flux and errors in the targeted regions. The implementation makes provision for splitting each region further (by a maximum facet size parameter) and applying sampled antenna far-field response per sub-region-facet).

A single such cycle of simultaneous multi-direction peeling is indicated in Fig. 3.4. This direction-dependent calibration framework is implemented as part of the VERMEERKAT [3] Introspect calibration pipeline via the container-based STIMELA pipelining framework [101].

The equivalent steps in other packages, such as OBIT [38], consists of a somewhat involved recipe of steps to fourier transform and subtract out the components not solved for and solved for before and after solving respectively that have to be executed on a source-by-source basis without the ability to iterate between differential gain terms during a single global solve. The process is discussed in [39].

3.4 A comparison between direction-dependent calibration through KILLMS and CUBICAL

A detailed comparison of this peeling approach with that followed in the KILLMS[4] calibration package is presented by [121]. See co-authored paper list, Appendix A. For the benefit of the reader, we will briefly highlight the differences in approaches implemented by the two packages.

[3] Available from `https://github.com/ratt-ru/vermeerkat.git`
[4] Available from `https://github.com/saopicc/killms.git`

The core difference between the two approaches is that KILLMS subdivides the entire image into a user-controllable number of Voronoi tessellations based on the amount of flux available per tessel. Optionally, similar to the outlined peeling approach, each tessel may be divided further by a number of facets that applies the antenna far-field response if provided. It solves for a direction-dependent (frequency and/or temporally variable) gain for the entirety of the tessellation which can be loaded and applied in image space through the DDFACET [152] imaging package. This approach has two drawbacks that we can see:

- It is hard to control the exact size of each of the tesselations where direction-dependent solutions are to be applied
- The entire sky is ultimately subject to direction-dependent solutions, even patches where there may not be sufficient flux to solve for direction-dependent gains, or where it may not be needed. This second problem is, however, mitigated by smoothing solutions post-calibration and prior to application in image space.

The main advantage the KILLMS approach has over the peeling scheme discussed, is that the solutions are applied in image space to correct both the residuals and the source fluxes, as opposed to only forming corrected residuals (with source fluxes peeled off) in the peeling approach.

We now showcase the main results presented by [121], as applied to observations of the Saraswati supercluster ZwCl2341+0000, see Fig. 3.5. Both approaches significantly reduce sidelobe emission, especially visible around the source labeled "E" in Fig. 3.5 (top). Side-by-side comparison cutouts of "A" through "E" are supplied in Fig. 3.6. Statistics for the residuals corresponding to these 8' cutouts are given in Table 3.1.

Both the dynamic range (DR) and statistics reflecting the fidelity of the maps are measured. Dynamic range is useful to quantify the level of calibration / deconvolution artifacts relative to the peak flux. We provide three definitions of DR, both relative to the local and global RMS noise, these are:

$$\begin{aligned} \text{DR1} &:= \frac{\text{flux}_{\text{peak}}}{\text{rms}_{\text{local}}}, \\ \text{DR2} &:= \frac{\text{flux}_{\text{peak}}}{\text{min}_{\text{local}}}, \\ \text{DR3} &:= \frac{\text{flux}_{\text{peak}}}{\text{rms}_{\text{global}}} \end{aligned}$$

As CUBICAL [87] peels sources (ie. forms only a corrected residual, with model flux removed), the peak flux for these compact sources is defined as the peak flux in the direction-independent calibrated maps. The other statistical quantities (rms, Min, Sum, MAD, Kurt and Norm) are computed from the residual maps.

Table 3.1 quantitatively shows that there are, overall, significant improvements in all measures of dynamic range (ie. the artifacts are reduced both locally and globally). We find that the peeling solution we discussed here works better than KILLMS to reduce sidelobe emission locally around strong sources, whereas a KILLMS-based solution-per-tessel yields slightly improved global residual noise. The amount of integrated and peak negative (unphysical) fluxes are substantially improved in both cases with mostly comparable levels in the integrated negative fluxes in both methods. The skew and kurtosis indicate that the residual distribution is not Gaussian in both direction-independent and direction-dependent cases, and are of limited use.

In Chapter 4 we deployed the peeling methodology developed in this section to calibrate data significantly limited by dynamic range problems. A full worked example is given in Section 4.3.

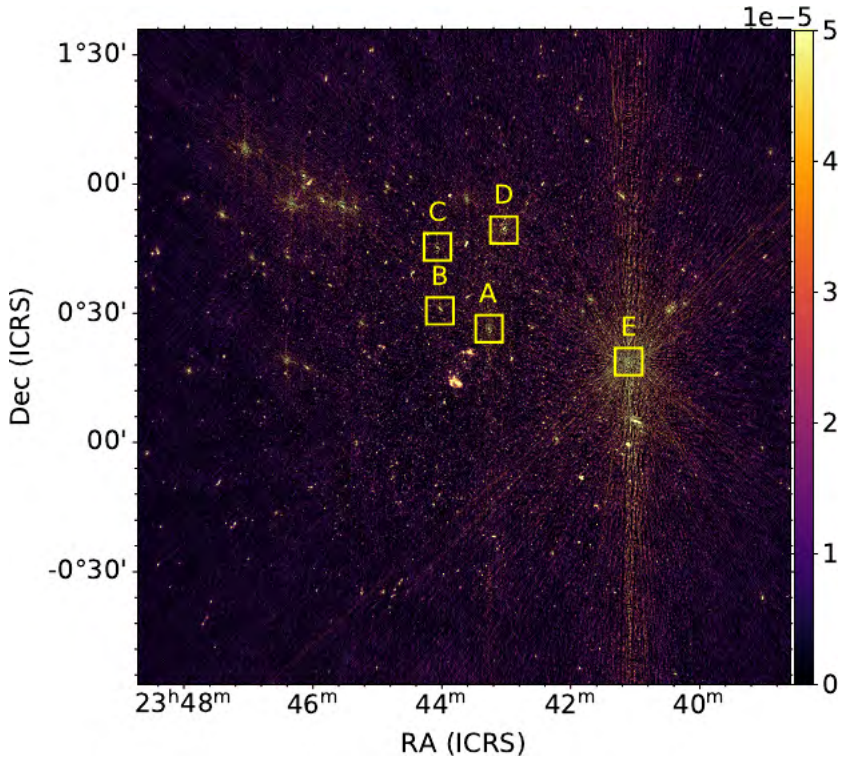

(a) Direction-independent calibration only

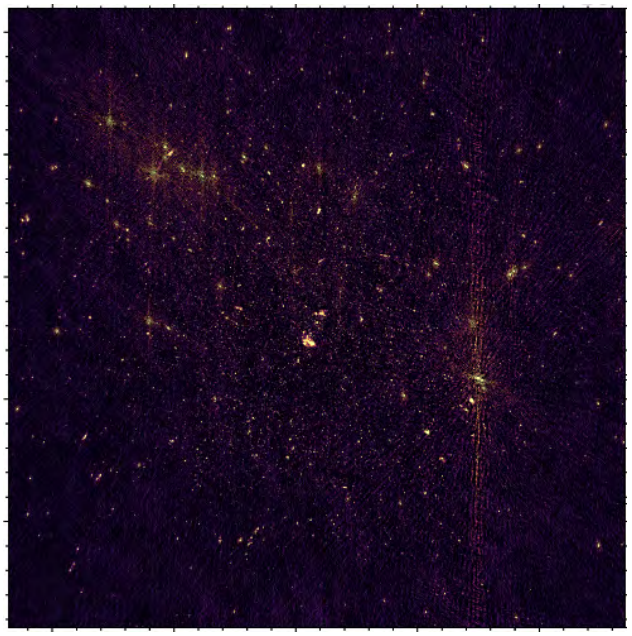

(b) Direction-dependent peeling using CUBICAL [87]

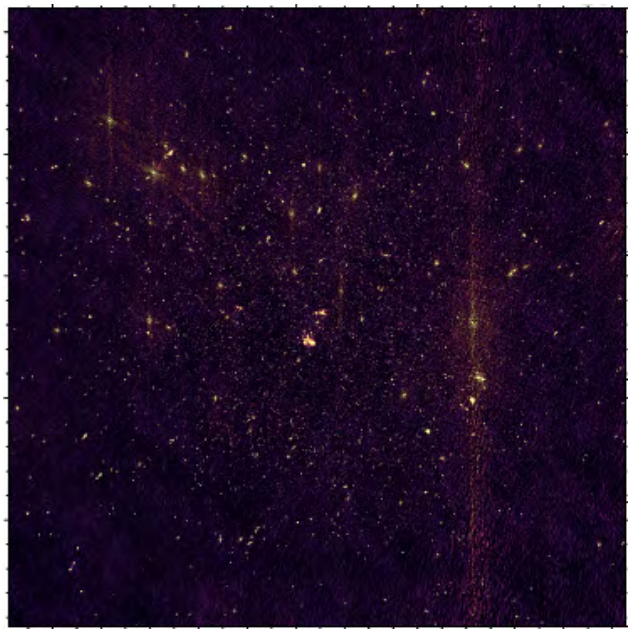

(c) Direction-dependent calibration using KILLMS

Figure 3.5: Side-by-side comparison between direction-dependent calibration through our faceting approach in CUBICAL [87] and the tessellation-wide scheme implemented in KILLMS. Images locked to the same scale. Taken from [121]

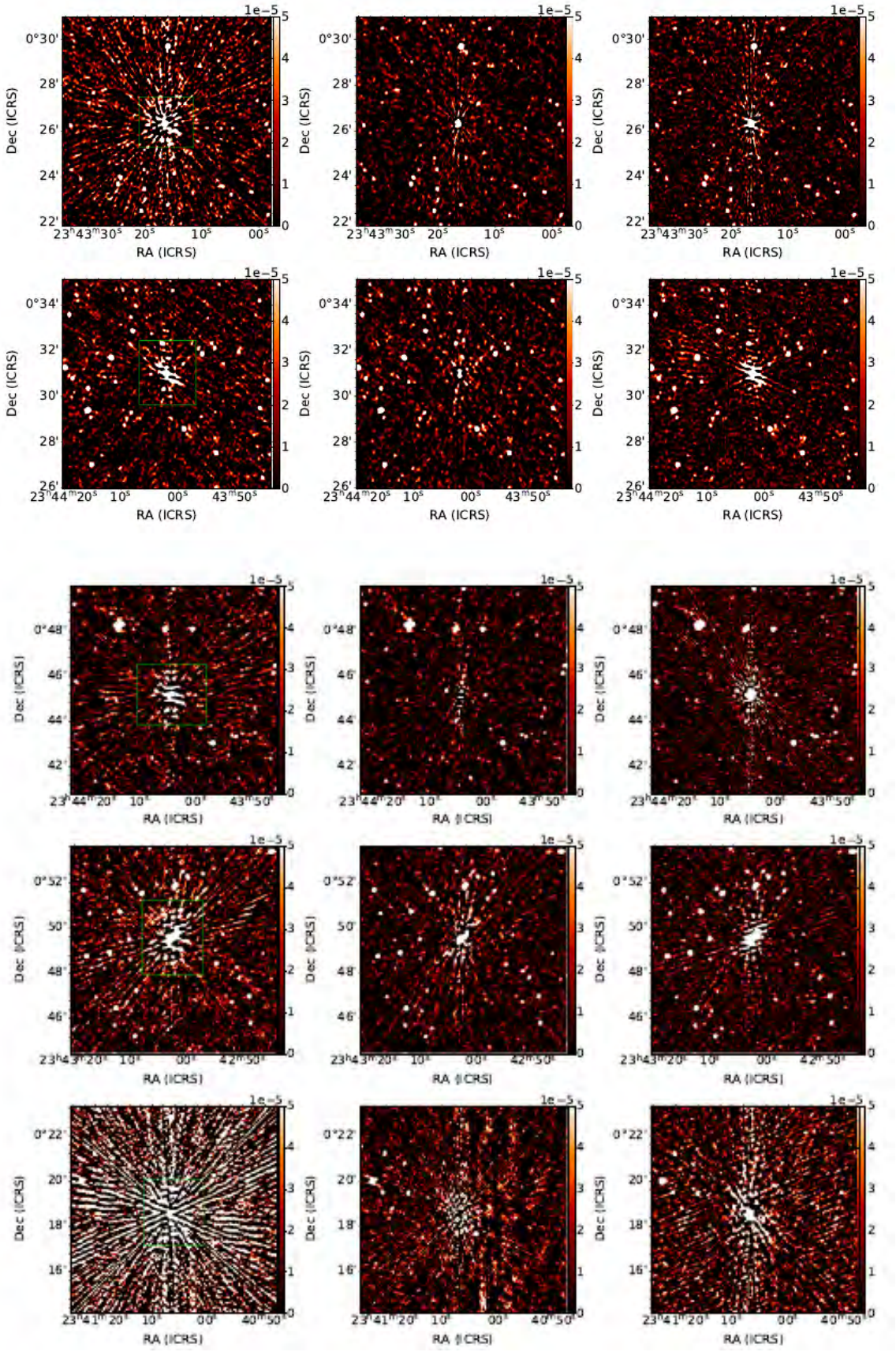

Figure 3.6: Cutouts "A" through "E", top to bottom. Left column is the image with only direction-independent self-calibration performed, middle column is direction-dependent peeling through CUBICAL [87], and right column is direction-dependent solutions from KILLMS applied through DDFACET [152]. Images locked to the same scale. Taken from [121]

Table 3.1: Statistics for extracts “A” through “E”, calculated in the residual images in the ZwCl 2341.1+0000 field. Taken from [121]

Source	RMS μJy/beam	DR1	DR2	DR3	MAD μJy/beam	MIN mJy/beam	MAX mJy/beam	SUM NEG mJy/beam	SKEW	KURT	NORM
					A						
DI	37.0	2288.95	66.77	4282.69	15.0	-1.27	84.61	-1170.39	-6.59	175.62	132287.84
DD CC	16.0	5384.67	521.17	6011.81	9.0	-0.16	1.93	-642.60	1.2	12.53	32982.4
DD KMS	18.0	4819.0	207.25	6728.32	8.0	-0.41	84.35	-648.68	-2.19	61.92	68730.32
					B						
DI	23.0	1452.71	89.54	1703.88	11.0	-0.38	33.66	-780.03	1.26	41.87	48327.62
DD CC	17.0	1948.45	203.95	2391.82	9.0	-0.17	1.11	-640.55	1.53	13.83	40406.3
DD KMS	19.0	1729.23	89.72	2616.98	8.0	-0.37	32.80	-525.23	0.78	63.84	43861.46
					C						
DI	37.0	859.03	35.10	1703.88	12.0	-0.89	31.37	-974.88	2.47	161.56	81404.9
DD CC	18.0	1786.54	123.52	2391.82	9.0	-0.25	3.19	-683.07	0.56	23.3	29623.6
DD KMS	23.0	1329.44	39.44	2616.98	9.0	-0.77	30.30	-647.93	-6.74	207.55	134959.27
					D						
DI	38.0	823.34	39.83	1596.63	15.0	-0.79	31.54	-1009.09	-1.06	91.05	52000.85
DD CC	24.0	1335.30	57.60	2241.26	10.0	-0.55	2.09	-668.20	-3.96	86.19	97598.32
DD KMS	23.0	1293.42	52.52	2414.77	9.0	-0.58	30.27	-672.90	-4.67	102.88	107886.23
					E						
DI	201.0	903.81	31.46	9191.59	47.0	-5.77	181.59	-4077.27	-5.1	196.17	117774.02
DD CC	30.0	6097.83	237.53	12902.67	14.0	-0.76	2.60	-895.05	0.29	76.61	38640.5
DD KMS	36.0	4446.85	233.40	12927.69	17.0	-0.69	162.08	-1178.32	-1.13	33.72	43613.94
					Full image						
DI	20.0	-	31.46	9191.59	9.0	-5.77	181.59	-196953.75	-15.45	5995.31	75889133.9
DD CC	14.0	-	115.12	12902.67	7.0	-1.58	42.21	-154531.51	-1.59	636.36	26984110.1
DD KMS	12.0	-	122.20	12927.69	7.0	-1.33	162.08	-154750.56	-4.86	531.9	43647231.0

3.5 VERMEERKAT: an end-to-end MeerKAT 3GC reduction framework

The software developed for this section is freely available under GNU General Public License v2.0 at `https://github.com/ratt-ru/vermeerkat`. As such no source code will be printed in this section. This Section briefly summarizes containerized software deployment and recipe development using STIMELA [101] and discuss how the STIMELA framework was used to develop an end-to-end direction-dependent – colloquially referred to 3^{rd} Generation Calibration ("3GC") – reduction framework called VERMEERKAT.

VERMEERKAT is a scripted reduction framework based on the STIMELA [101] pipelining framework. STIMELA combines a heterogeneous set of commonly-used software into a common scriptable PYTHON [162] Application Programmer Interface (hereafter "API"). We leverage the now widely-adopted containerization technologies natively supported by the Linux Kernel (with hypervisor support on other platforms). Each software package (or constituent task as in the case with e.g. CASA [104]) is run in isolation of the host system. At the time of writing multiple containerization backends are supported: DOCKER [105], SINGULARITY (recently renamed APPTAINER) [56] and PODMAN[5] runtime environments.

The layered approach to reduction strategy development and execution followed here is illustrated in Fig. 3.7. Each release version of STIMELA [101] is bundled with the image specifications of the versioned binary images that are uploaded onto an open container image registry. In this way a high degree of reproducibility is achieved: the science user can specify both a version of STIMELA and provide an end-to-end recipe for the reduction of their data. Current versions of STIMELA uses QUAY.IO, although previous versions used the DOCKERHUB registry, which since had restrictive rate limits introduced. The images for earlier versions are still however available on that registry.

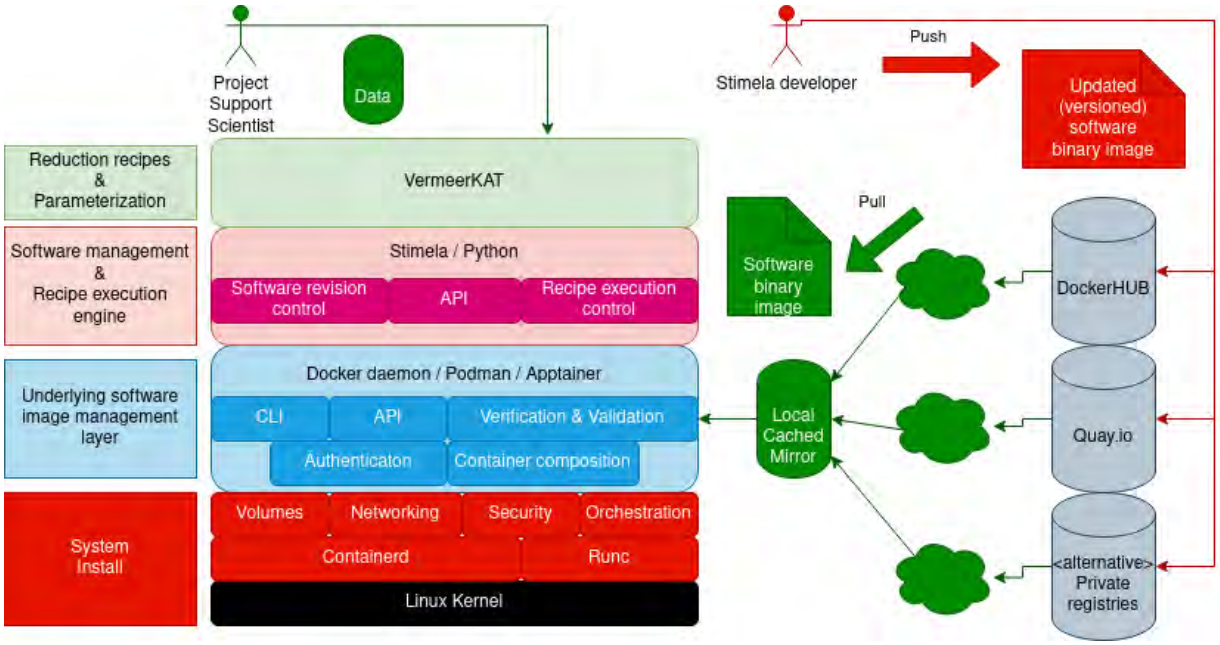

Figure 3.7: Containerized recipe execution through the STIMELA [101] framework. STIMELA provides a common task parameterization specification language and interface to commonly-used astronomical packages (which is easily extendable). VERMEERKAT provides a set of STIMELA-based recipes for the continuum-reduction of MeerKAT data. Underneath the hood STIMELA manages the deployment of (versionned) software binary images on the user's system (user indicated as green actor) and presents a common PYTHON [162] API to the reduction recipe developer. Each step in such a recipe runs inside a container (runtime instance of the software installation binary kept in the local image library) which is isolated from the system and libc installations. The software image specifications are version-controlled by STIMELA developers (indicated as red actor) who push pre-build images to container registries, e.g. DOCKERHUB, where they can be easily accessed by the user community.

[5] Available from `https://github.com/containers/Podman`

The system-wide management of the binary images is left to the underlying containerization technology, and differs slightly between the supported platforms. However, the three (at the time of writing) supported platforms uses interoperable protocols and formats, known as the Open Container Initiative ("OCI"). For instance the STIMELA [101] developers build images using the build specification system provided by DOCKER [105], but users are not restricted to using DOCKER to run their reductions with STIMELA. Often due to root escalation capabilities of the powerful DOCKER daemon system administrators give preference to user-space, non-daemonized, container technologies such as APPTAINER [56] and PODMAN.

This containerized approach have significant advantages over traditional bundled package installs through e.g. UBUNTU-specific APT binary distribution or pre-compiled binary wheels:

- **Portable** — the necessary system libraries, e.g. GLIBC, is effectively bundled with the base distribution image (e.g. Ubuntu 20.04) on which the software was compiled. It is decoupled from system installations, which can be newer with conflicting library Application Binary Interfaces ("ABI") or on distributions where dependencies cannot easily be met. In principle the images can also be run, using hypervisor support, on completely different operating systems (e.g. running software compiled on UBUNTU 20.04 through DOCKER for Microsoft WINDOWS), although STIMELA [101] at present does not support Microsoft WINDOWS.
- **Installation compatibility between a diverse heterogeneous set of software tooling** — adding to portability, the isolation provided by the containerization approach helps to install software and tooling provided by a diverse community. Often-conflicting dependency requirements is easily resolved by isolating package binary file systems using containers.
- **Ease of deployment** — a full library of commonly-used radio astronomy software can be pulled with a single command, and executed within the span of an hour, depending on network speed (a full deployment needing downloads on the order of a few tens of gigabytes at the time of writing). Users additionally do not need to meet dependencies or compile software themselves. STIMELA [101] is distributed with minimal additional PYTHON [162] dependencies by design, all of which are available through the PYTHON PACKAGE INDEX (PYPI).
- **Software versionning and reproducible reduction environments** — binary images are a sequential composition of differences, secure hashed at byte-level, representing the state of the isolated file system into which a specific software, and its dependencies, were compiled for every step of the installation and dependency collection. With each release version of STIMELA [101] we tag these images with version numbers and upload them to the container registry. Each STIMELA task (what we refer to as a "cab") has a revision-controlled binary image tag specification. It is therefore easy to roll back and forth between package versions.

Each task / "cab" specification definition in STIMELA [101] contains the typed parameters for that task, which serves as a schema file against which a user's reduction recipe is validated prior to execution. These cab schema are automatically loaded from a namespace-structured directory within the STIMELA installation, and can easily be expanded to include additional software packages.

Based on these cab specifications a user can construct a recipe of steps to reduce a dataset. The recipe, of arbitrary complexity, is written in PYTHON [162]. An example for a simple UV simulation and imaging (at various different Briggs [25] robustness factors) is shown below, and is adapted from the user documentation:

```
import stimela
INPUT      = "input"
OUTPUT     = "output"
PREFIX     = "stimela-example"
MSDIR      = "msdir"
```

```
MSNAME     = "meerkat_example_simulation.ms"
SKYMODEL   = "nvss1deg.lsm.html"

# Create an empty database for MeerKAT configuration of the
# specified channelization and time sampling
recipe.add("cab/simms",# this is the full name of the executor image
   "create_emmpty_ms",# container label
   {
       "msname"       : MSNAME,
       "telescope"    :  "meerkat",
       "synthesis"    : 4, # Synthesis time in Hours
       "dtime"        : 5, # integration time in seconds
       "freq0"        : "1400MHz", # Start frequency
       "dfreq"        :    "1MHz",
       "nchan"        : 10
   },
   input=INPUT,
   output=OUTPUT,
   label="Create empty MS") # Task label. For logging purposes

# DFT predict visibilities
recipe.add("cab/simulator",
   "simulate_visibilities",
   {
       "msname"    : MSNAME,
       "skymodel"  :  SKYMODEL,
       "column"    : "CORRECTED_DATA"
   },
   input=INPUT,
   output=OUTPUT,
   label="simulate visibilities into MS")

# image at different robustness settings using WSClean
for robust in [-1, 0, +1]:
   recipe.add("cab/wsclean",
       "image_data_robust_%d"%robust,
       {
           "msname"            :   MSNAME,
           "npix"              :   2048,
           "cellsize"          :   2, # in arcseconds
           "column"            :   "CORRECTED_DATA",
           "clean_iterations"  :   3000,
           "weight"            :   "briggs %f" % robust,
           "prefix"            :   "%s-%d" % (prefix, robust)
       },
```

```
        input=INPUT,
        output=OUTPUT,
        label="Image data. Robust=%d" % robust)

# finally run
recipe.run()
```

VERMEERKAT is a semi-interactive reduction framework consisting of a set of STIMELA [101] recipes for transfer calibration (or "1st Generation Calibration"), self calibration – both direction-independent (or "2nd Generation Calibration") and direction-dependent (or "3rd Generation Calibration") – and separate polarimetric calibration routines. For a discussion of the calibration of the MeerKAT polarimetric response, see Chapter 2. The framework is aimed at assisting the user in creating continuum imaging products. It was specifically developed for galaxy cluster analysis. The recipes are interruptable (for user intervention when needed) and their execution is controlled through a basic NCURSES command line interface menu system.

Transfer calibration is largely completed with CASA [104] tasks, with additional antenna and baseline flagging routines and RFI flagging through TRICOLOUR [72]. The transfer calibration recipe includes an extensive set of diagnostic plotting steps. It would typically entail the user doing multiple rounds of calibration of the bandpass, gain, and alternative calibrators (backup primary and polarization calibrators). The implemented transfer calibration recipe is summarized in Fig. 3.8.

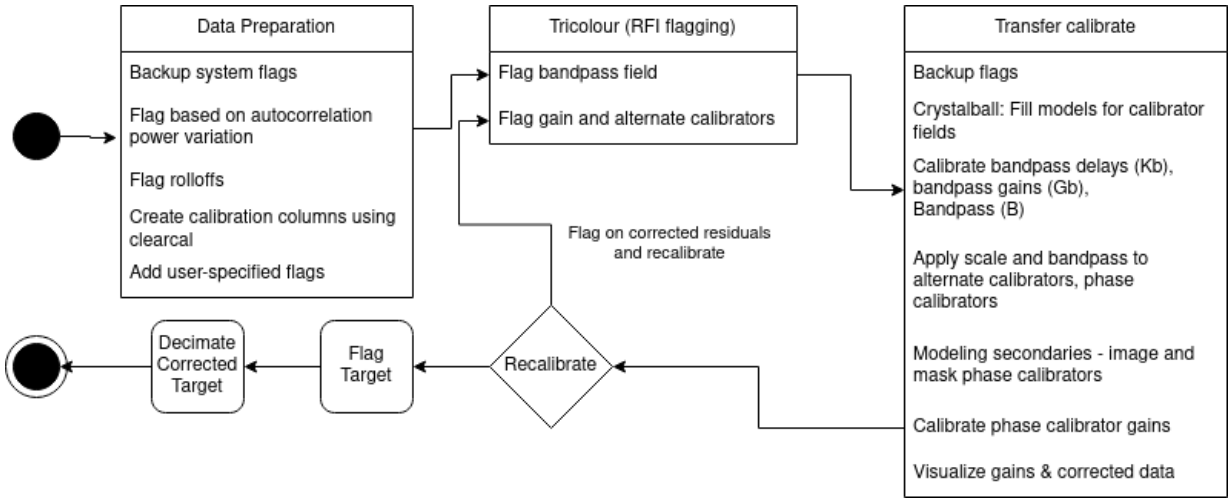

Figure 3.8: Transfer calibration, as implemented in the VERMEERKAT `Basic Apply Transfer` calibration recipe. The recipe consists of multiple cycles of calibration refinement, which includes a set of diagnostic plots.

Here the transfer calibration steps refine the phases between fields. We incorporate the apparent-scale (antenna beam attenuated) flux scale models that includes the calibrators PKS B1934-638 and PKS B0407-65 and their surrounding field sources through a DFT (see the modeling in Chapter 1) during the bandpass field calibration process. We image the gain calibrator sources and then refine the phase solutions per calibrator source — the phase is expected to change substantially across the horizon and with time due to ionospheric phase gradients and system impedance changes.

The process of self-calibration calibrates the variability in the system and (especially at low frequencies) environmental gains that exist due to the inaccuracies that stems from interpolating gains from a secondary calibrator to a target field, as well as temporal variability that is not fully captured by using secondary sources, such as the effects of pointing errors in the flanks of the antenna primary beams on strong off-axis sources. Self-calibration achieves this through an iterative process of modeling (through imaging and deconvolution) the target field and calibrating the per-antenna gains towards

the constructed model. After transfer calibration VERMEERKAT implements self-calibration in the `Introspect` recipe. The worker includes a compact specification language that makes it highly configurable and can be tuned to the user's needs. We illustrate the flexibility through the default self-calibration strategy:

```
p(35,256s),p(35,64s),dp(35,16s),dd(45,4.0,20,50,CORRECTED_DATA,DE_DATA),i(DE_DATA,0.0),
s(DE_DATA),i(SUBTRACTED_DATA,0.0)
```

Here we iteratively refine the phase in three steps (plus delays in the third), before solving for direction dependent solutions in the fourth, imaging in the fifth, subtracting the model from the fifth step in the sixth and imaging the subtracted residuals in the seventh. Direction-independent calibration solutions are derived with CASA [104], Imaging is performed with DDFACET [152] and direction-dependent solutions are derived with CUBICAL [87] through the targeted faceting approach discussed in this Chapter. Currently the language specification is as follows:

- `p` — Direction-independent frequency-independent phase, with the first parameter indicating the auto-Cleanmasking threshold to be used when imaging before solving and second parameter the solution interval cadence.
- `dp` — Direction-independent frequency-independent delay and phase, with the the parameters the same as the `p` solution.
- `ap` — Direction-independent frequency-independent amplitude and phase gains, with parameters the same as the `p` solution.
- `s` — (no gain refinement) Subtract `MODEL_DATA` column predicted by the previous imaging iteration from the specified data column. The option is useful when the goal is to e.g. image cluster residuals in subsequent steps at various resolutions.
- `i` — (no gain refinement) Image data column provided in the first parameter at the robust weighting specified by the second parameter.
- `dd` — Direction-dependent frequency-dependent solutions (optional — cadences set by user). The first parameter specifies Auto-Cleanmasking threshold, second parameter sets the direction-dependent region auto-tagging thresholds (based on local noise estimates), and third and fourth parameters sets solution interval in number of time intervals and frequency channels. The last two parameters control the input and output data columns. The peeling RIME constructed internally solves for phase-only solutions using the direction-independent part of the model and full 2x2 Jones matrices for the tagged regions of the model requiring direction-dependent treatment, as specified in Eqn. 3.14.

The rest of the most critical parameters needed to control imaging and calibration are set via command-line arguments, but are left at sensible defaults for MeerKAT L-band reduction. We show an example of a VERMEERKAT-processed database in Fig. 3.9, taken from the user documentation. VERMEERKAT was extensively tested on MeerKAT L-band data and includes useful strategy files for Tricolour on which users can expand. Future work includes expansion of the defaults to the other MeerKAT bands.

These generic 3^{rd} Generation Calibration tooling and frameworks presented in this chapter were developed with the hope that they will be useful for the MeerKAT astronomer community at large. They are also in active use in e.g. the CARACAL framework [84] which is a STIMELA-based reduction framework.

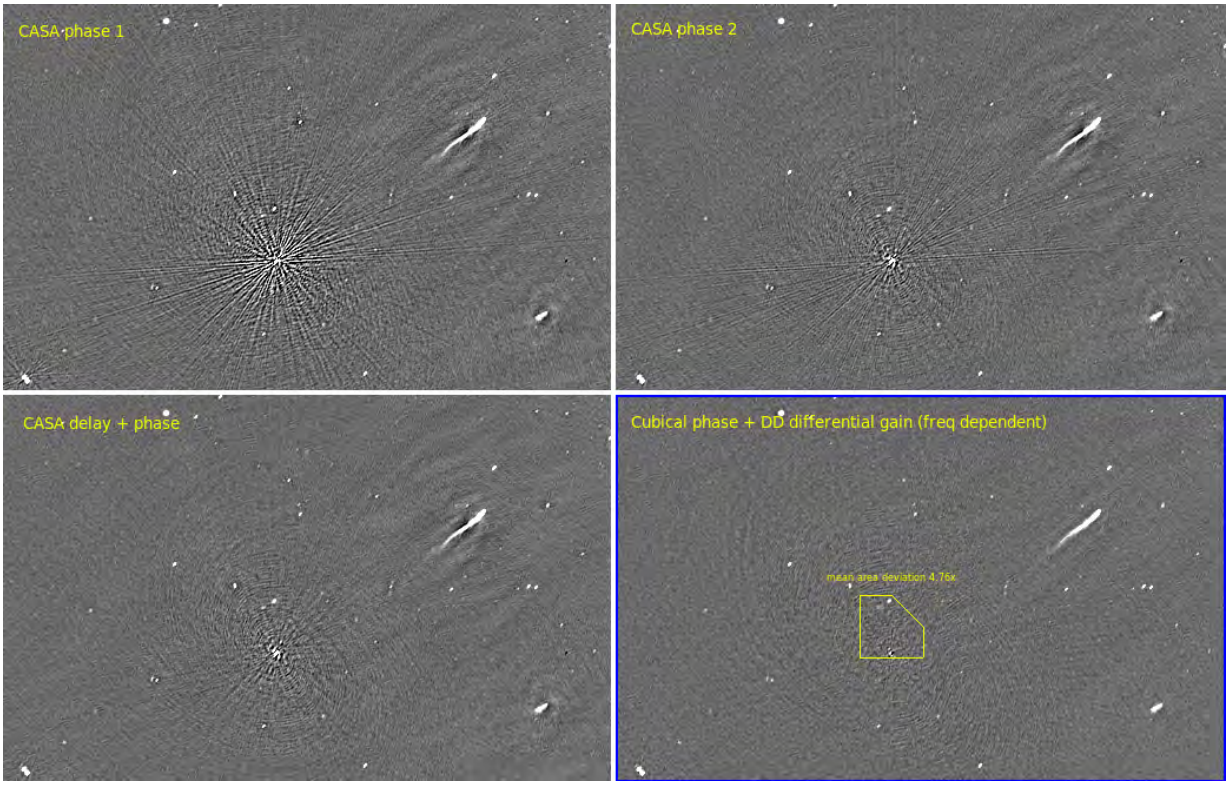

Figure 3.9: Here we show an example case study in the Triangulum Australis cluster taken with the MeerKAT Early Science Data call, under proposal code SCI-20180212-BH-01, using the 16-antenna ROACH I correlator.

Chapter 4

Detection of a radio counterpart to transitional MSP candidate using MeerKAT

In this chapter the direction-dependent calibration methodology developed in chapter 3 is applied to a transitional millisecond pulsar (hereafter "tMSP") candidate CXOU J110926.4-650224. The detection of a radio counterpart to this X-ray pulsar is published in [37], see co-authored papers in Appendix A. In this multi-wavelength study I led the MeerKAT component. This section will focus, primarily, on the radio component. I thank Francesco Coti Zelati for the useful discussions on the science case for these X-ray systems in preparation of this chapter.

Throughout this chapter the positive convention for radio power-law spectra and negative convention X-ray energy power-law spectra are assumed.

4.1 Recycling theory background

Radio pulsars are highly regular periodic stars first discovered in 1967 [66]. The discovery of pulsars with periodicity in the tens of millisecond range (e.g. PSR B0531+21 [147]) suggested that these may be neutron stars (hereafter "NS") [115, 57].

When stars reach end of life in supernovae explosions their total magnetic flux is conserved. However, the decrease in diameter from 10^6 to roughly 10 km amplifies the magnetic field strength by a factor of 10^{10} and the conservation of angular momentum implies that the period of rotation is sped up by about the same factor. At NS densities ($\sim 4.74 \times 10^{17}$ kg m^{-3} for a canonical NS) much of the content is a neutron superfluid that serves as superconductive material. The high rate of rotation of this material serves to make these stars act as a dynamo with a strong dipole magnetic field of field strengths ranging between 10^8 and 10^{14} G. Young pulsars (known as magnetars) are found at the the top end of this scale. The magnetic field lines of pulsars, responsible for accelerating highly colimated synchrotron emission, are forced open within a "light cylinder" radius when they co-rotate at relativistic speeds as is shown in Fig. 4.1. For suitable viewing angles, the emitted radiation is detected in the form of periodic pulses [33, ch. 6].

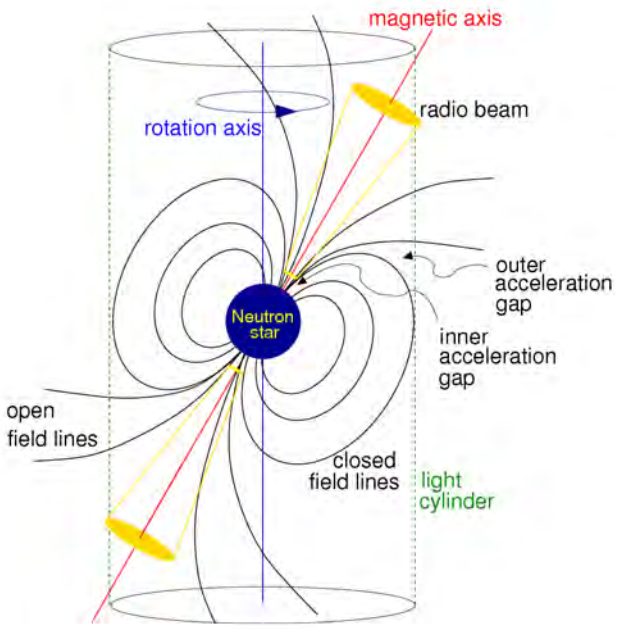

Figure 4.1: The bipolar magnetic field of an NS with spin and magnetic axis offset at an inclination angle. The light cylinder radius is defined as the radial distance from the neutron star at which the magnetic field lines would corotate at the light velocity. It is aligned with the spin axis of radius $R_{\mathrm{LC}} = 80\nu_{600}$ km, where ν_{600} is the spin frequency in units of 600 Hz [118]. Illustration from [99]

Over time this energy is primarily lost due to dipole radiation, given as [33, eqn. 6.12]:

$$P_{\mathrm{rad}} = \frac{2}{3c^3}(BR^3 \sin\alpha)^2 \left(\frac{2\pi}{P}\right)^4 \tag{4.1}$$

Here α is the magnetic inclination angle (see Fig. 4.1), P the pulse period, B magnetic field strength and R radius. If this is the dominant driver of energy loss, the magnetic field strength is directly equatable to the rate of energy loss given by [33, eqn. 6.15, 6.20]

$$-\dot{E} = \frac{4\pi^2 \dot{P} 2MR^2}{5P^3} \tag{4.2}$$

Where $\dot{E}$ is the energy loss rate, M is the mass estimate and $\dot{P}$ is the measured rate of change in the pulse period.

This gradual dissipation of energy during the lifetime of pulsars is best viewed in what is known as a $P\dot{P}$-diagram, shown in Fig. 4.2. Young pulsars in the middle and upper right of this diagram (magnetars) are often still associated with their supernova shell. It is thought that, progressively, these pulsars move down and to the right of the diagram as their energy is radiated away. The group to the middle right ("RRATs" - Rapidly Rotating Radio Transients) are thought to be pulsars that have reached the end of their lifespan. These only emit radio pulses at irregular intervals. The group of millisecond and subsecond pulsars are shown to the left. This last group of millisecond pulsars (hereafter "MSP") is of particular interest in this work.

Theories to explain the origin of this MSP group have been put forward since the 1980s. It is thought that they have to be re-accelerated by accretion from – and gravitational tidal interaction with – binary companions. The explanation for the physical processes behind the creation of this old-but-not-dead group requires multi-wavelength observation spanning the

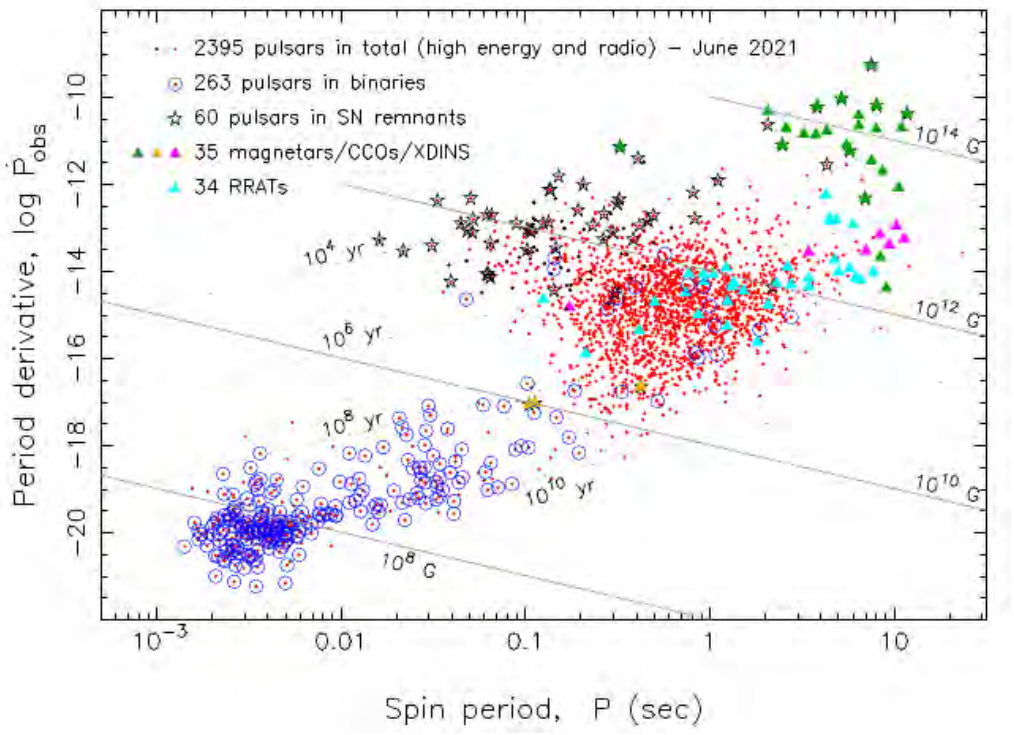

Figure 4.2: A $P\dot{P}$ diagram taken from [78]. Here the spin period derivative is plotted as a function of spin period. The magnetic field strength, energy loss rate are plotted as minor grid lines. Red dots represent radio pulsars, triangles represent magnetars, core compact objects (CCOs), X-ray dim isolated neutron stars (XDINSs) and rotation radio transients (RRATs). Objects still associated with supernovae remnants or binary systems are overplotted with stars and circles respectively.

entire electromagnetic spectrum from cm through to gamma-ray observation. Much of the discussion here is drawn from the recent review of [118, and references therein].

From the orbital variations in the pulse time of arrival (hereafter "TOA") it has been established that this older population of MSPs, for the most part, are part of binary systems. Potential donors range from main sequence to dwarf stars. The accretor type is strongly influenced by the donor mass and orbital period. A variety of pulsing transient objects have been detected by multi-wavelength studies. Radio pulsars are generally found in systems with roughly circular orbits measured in days. A sub-class of low-mass X-ray binary MSPs[1] (hereafter "LXMP") show X-ray pulsations in accreting state (hereafter "AMXP") and are typically found in systems with orbits much less than one day. A third class of "spider" radio binary systems are found in low orbital period ranges. In these systems the pulsar winds irradiate and ablate the companion star, ensuring a steady flow of intrabinary material. Although the majority of spider orbits are highly circular, the orbits of some of these systems are significantly eccentric in their shape, thought to be due to the presence of intrabinary material in the system. The "black" widow" spider systems have donor star masses less than $0.06M_{\odot}$ while systems with a hydrogen-rich donor (minimum mass $0.1M_{\odot}$) are known as "redbacks" . This is shown in Fig. 4.3.

Although there are now[2] 622 MSP with periods less than 30 ms known, only around 100 are deemed "spider" class in compact orbital systems. **The interplay between radio, optical, X-ray, and gamma-ray modes within this group is of critical importance in understanding how the magnetosphere of these stars interact with infalling matter accreted from binary companions.**

The recycling model [145, 4, 133] suggests that within binary systems matter is accreted from a donor. The inflow of this

[1] Contrary to radio transients the designation of "pulsar" in the context of X-ray transient sources may formally refer to either an NS or blackhole (hereafter "BH") accretor.

[2] As of December 2021 see [118]

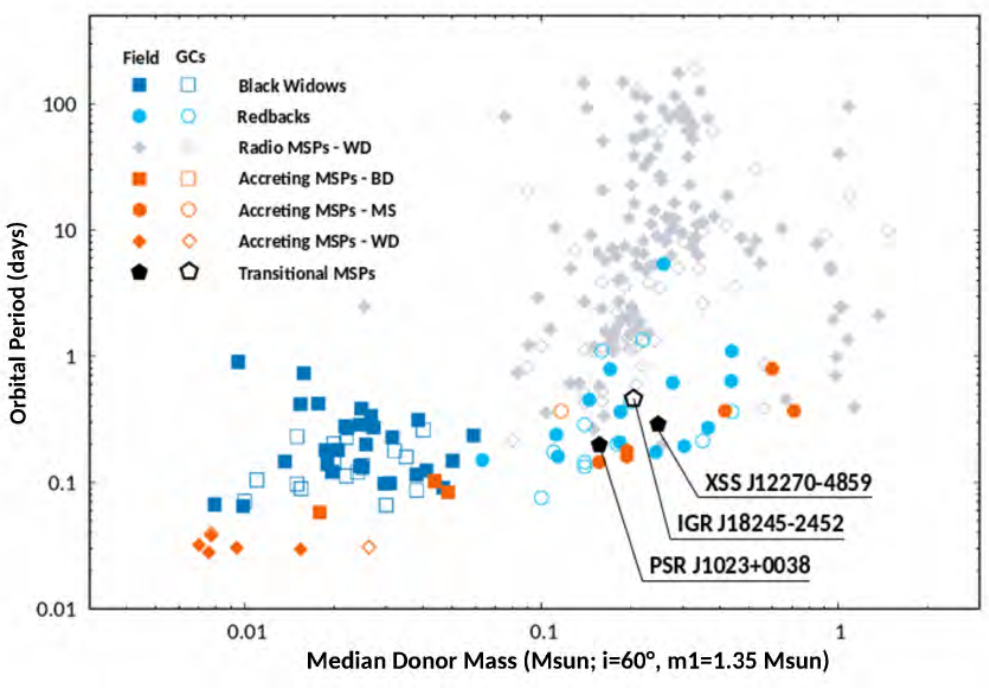

Figure 4.3: Orbital period vs. median donor mass of binary systems showing the populations of radio and X-ray pulsars. Taken from [118]. Solid and unfilled symbols indicate sources in the Galactic field and globular clusters respectively. Orange squares indicate AXMP. Designations "WD", "BD", "MS" refer to white dwarf, brown dwarf and main sequence donor stars respectively. "Black-widow" and "redbacks" indicated in blue.

interbinary material is thought to form a viscous co-rotating disk with a centrifugal boundary set by the pressure exerted from the rotating magnetosphere. The relative radial position of this boundary determines the emission state of the system: if the accreting matter falls into the light cylinder (Fig. 4.1) it is thought that the rotational-driven pulsar winds, responsible for the regular pulsing seen in radio, is shock quenched. If the ram pressure exerted by the gravitational infall is smaller than the pressure exerted by the magnetosphere the system is said to be in a co-rotation "propeller state" [74].

The accretion disk truncation and co-rotation radii are given as [118]

$$R_{\rm acc} = \xi \frac{(0.5BR^3)^{4/7}}{\dot{M}^{2/7}(2GM)^{1/7}}, \text{ and} \tag{4.3}$$

$$R_{\rm co} = \left[\frac{GM}{(2\pi\nu)^2}\right]^{1/3} \tag{4.4}$$

Here ν is the spin frequency, ξ is a factor (still debated) that relates the accretion radius to Alfven (magnetic/kinetic equilibrium) radius. Matter accretes onto the NS if $R_{\rm acc} < R_{\rm co}$, otherwise if $R_{\rm co} < R_{\rm acc} < R_{\rm LC}$ the system is in a propeller state, with torque possibly still lost due to some magnetic field lines intersecting beyond the co-rotation radius. When $R_{\rm acc} > R_{\rm LC}$ the pulsar wind is free to travel down the light cylinder, switching on the rotation-powered radio pulsar.

The detection of a confirmed radio MSP [7] in the J102347.6+003841 (PSR J1023+0038) system finally confirmed the elusive link between radio MSP and accreting systems. The system was observed accreting from a stellar disk[3] before 2009 prior to transitioning to a system with G-type stellar spectra [155, 163]. After the disappearance of the Balmer series pulsed radio emission was detected from the system. The disk episode at the turn of the century was short-lived

[3] Seen from the existence of doubly peaked lines in the Balmer series HI and HII spectra and a flickering light curve [22, 150, 164]. This is indicative of the presence of circular motion of matter around the NS in the form of an accretion disk.

($\sim 1.5-2$ years) [22, 150, 165, 163]. In 2013 the system entered a fresh accretion phase where all traces of radio pulsar activity ceased [148] and the double-peaked lines made a fresh appearance in the optical accompanied by a brightening in gamma-ray [63], UV and X-ray observations [123]. With these observations the system was therefore confirmed to be the first known tMSP.

Currently, three confirmed transitional MSPs (hereafter "tMSPs") are known, with a handful of candidates (at the time of writing):

- J102347.6+003841 (PSR J1023+0038)
- IGR J18245-2452 (PSR J1824-24521)
- XSS J12270-4859 (PSR J1227-4853)

For a full list, see [118, and the references therein]

From existing multi-wavelength observations of tMSPs it is now known that these systems spend their time existing within 3 distinctly dominant phases:

- **A rotationally-powered phase** where redback behavior is noted with occasional mass ejections (thought to stem mostly from the increased stripping of ionized material from an eclipsing donor). These eclipses are hard to detect due to highly frequency-dependent scattering and absorption effects of the interstellar material. The X-ray spectra of observation of sources in this state suggests that the X-ray emission stems from high-energy synchrotron (ie. relatively quiescent/non-thermal) winds in the magnetosphere, with unbroken power law spectra extended to $\sim$ 70 keV. The radiation X-ray luminosity is in the range $1-2\times10^{32}$ erg s^{-1} . This accounts for $0.1-0.2\%$ of the total spin-down budget. Synchrotron radiation at a luminosity of the order of $\sim 10^{33}$ erg s^{-1} ($0.1-100$ GeV) is visible in the gamma-ray band, accounting for a few percent of the total spindown budget.
- **Accretion disk (sub-luminous) state** where all three confirmed tMSP show an increase in X-ray activity of between $\sim 1-2$ orders of magnitude in luminosity (ie. $\sim 10^{33}-10^{34}$ erg s^{-1}). Although still substantially fainter than the population of AMXPs (by at least 3 orders of magnitude) in this mode they are overall more luminous than the general population of rotation-powered radio MSP ($10^{30}-10^{32}$ erg s^{-1}). These tMSP disk states may last for spans of years. Moreover this mode is characterized by sharp transitional modes in radio, optical and X-ray. J1023+0038 spends about 80% of its time in the high mode ($\sim 3\times10^{33}$ erg s^{-1}) with sharp transitions to flat bottomed (stable) lower states on the scales of tens of seconds. See Fig. 4.4. There is evidence of increasing hardening (ie. flattening) of the X-ray spectrum towards the high mode. Similar mode switching is seen in XSSJ12270-4859. Strong anti-correlated temporal behavior is seen (Fig. 4.4, b) in simultaneous X-ray/cm-radio observations of J1023+0038 with a significant steepening of the radio spectrum from an inverted to a moderately steep spectrum source, suggesting that optically thin jet emission becomes dominant over when the source drops to a low X-ray mode. The optical emission of tMSP is $1-2$ orders of magnitude brighter than in the rotational state with double-peaked Balmer lines. Optical observation of flares in J1023+0038 and XSSJ12270-4859 suggest these flares are optically thin. Pulsed X-ray emission is only seen in the high modes of these two sources whereas optical pulsation is only detected for J1023+0038.
- **Accretion outbursts** where X-ray luminosities approach those of the AXMP population. Only IGR J18245-2452 is known to have had such an outburst, lasting around three weeks, with a (pulsed) X-ray luminosity of 5×10^{36} erg s^{-1} with a significantly softer X-ray spectrum than in the sub-luminous state.

The radio emission (with a distinct lack of pulsing) seen in the sub-luminous (accretion disk) state, at least in part, is thought to have its origins in jets launched by the accretion disk. This is supported by e.g. VLA C- and X-band observations of tMSP J1023+0038 [48] where the radio spectra switches from a partially self-absorbed flat to steep

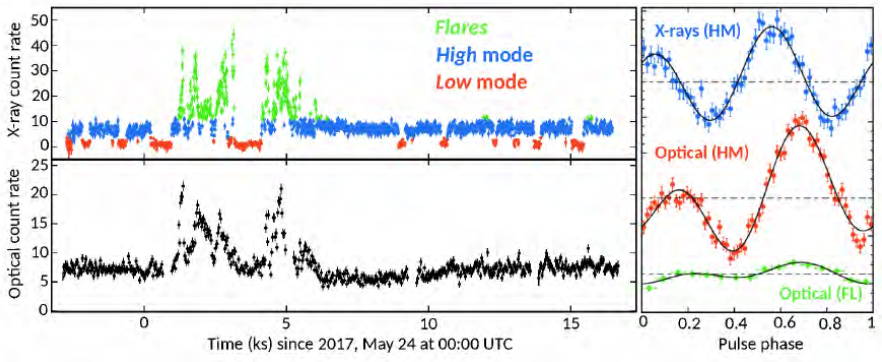

(a)

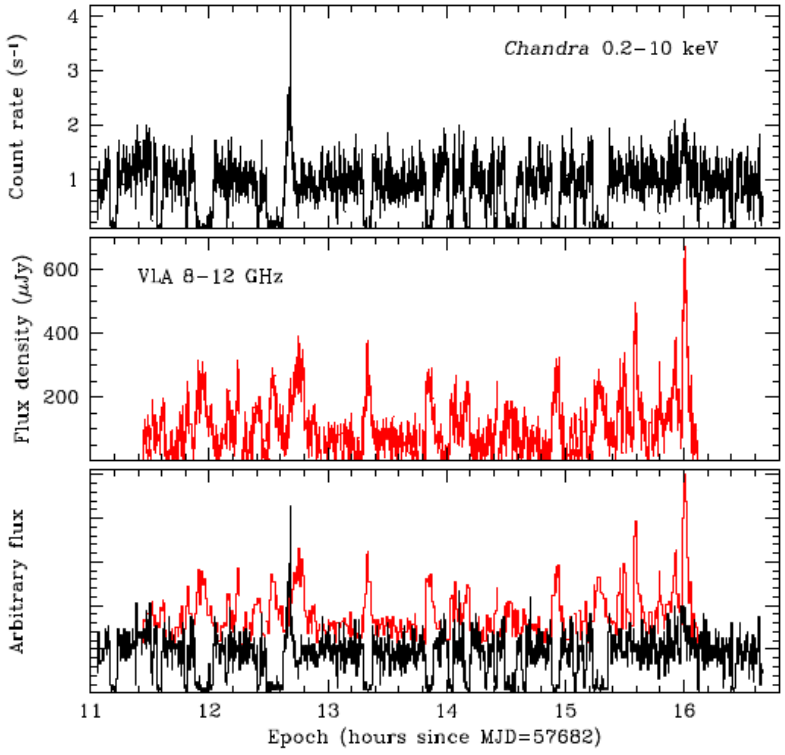

(b)

Figure 4.4: (a) Low and high modes for accretion disk state tMSP J1023+0038 in optical (SiFAP, INAF Telescopio Nazionale Galileo) and X-ray (0.5 – 10 keV XMM-Newton) simultaneous observations adapted from [116]. X-ray flares, high and low modes are plotted in green, blue and red respectively. High mode X-ray pulse profile is plotted in blue in the right panel. The pulse profile for the optical high and flare modes are plotted in red and green in the right panel respectively. (b) Strongly temporal anti-correlated high and low modes of radio (VLA 8 – 12 GHz, middle) and X-ray (Chandra 0.2 – 10 keV) simultaneous observation of J1023+0038 [20]

spectra in more radio luminous stages to inverted optically thin spectra in low activity modes. Jet based-radio emission is also seen in the most X-ray luminous NS LXMB population (the so-called "Z" sources) [50, e.g.]. It should be noted that the steep radio spectra of J1023+0038 in its enhanced activity mode of -0.27 ± 0.07 [48] is still far shorter than the steep spectrum radio emission (-2.8, [7]) seen in its rotation powered mode[4]. A notable increase in the spin-down rate of PSR J1023+0038 of $26.8 \pm 0.4\%$ is observed when the system enters the accretion phase [6, 75].

The physics at play in the transitioning phases between these states is currently not clearly understood. This is partly due to the lack of population size at lower X-ray luminosities, and the difficulty to detect these transitional systems due to their non-predictable state transitions. Although debated in literature it is now thought that the X-ray spectra of transitional sources are non-thermal over a large range of X-ray energies and do not stem from accretion directly onto the NS surface. It is known that radio continuum emission from lower-luminosity BH systems is due to self-absorbed jets due to their flat radio spectra, high radio temperatures, and the correlation between radio and X-ray emission [19]. The now well-established radio-X-ray luminosity relation for BH is shown in Fig. 4.5 coded as the black population [54, and references therein]. BH systems are accepted as being substantially more radio loud than NS systems at various X-ray energy ranges (by a factor of 6.5x [54]). It is thought that the wide range of correlations between the NS systems depend on whether these systems are in an efficient (or inefficient, respectively) radiative regime [55]. At higher accretion rates the system is dominated by X-ray radiative output, while at lower accretion rates the system is radiatively inefficient and is jet-dominated. The high radio luminosity, accompanied by the radio spectra of the three known tMSP systems indicate that these systems are radiatively inefficient jet-dominated systems [48].

The radio luminosity at distance d is related to the flux at 5 GHz ($S_{5\mathrm{GHz}}$) through

$$L_R = 4\pi d^2 \nu_{5\mathrm{GHz}} S_{5\mathrm{GHz}} \tag{4.5}$$

The significantly higher-than-expected luminosity in these tMSP systems put them around a factor of 5 from the BH radio-X-ray luminosity correlation — within its confidence level, but well above the radio-X-ray luminosity of the hard NS population if the inefficient accretion correlation is extended downwards [48].

In addition to the higher-than-expected radio luminosity, an uptick in gamma ray emission in the $0.1 - 10$ GeV band, associated with the sub-luminous disk states of PSR J1023+0038 and XSS J12270-4859, is observed. This emission ($\sim 10^{34}$ erg s^{-1}) is an order of magnitude above the gamma-ray emission seen when the source was in its rotation-powered state [45, 68, 120, 148, 151]. This increase is contrary to what was expected from rotationally-powered radio pulsar multi-wavelength observations. It is thought that gamma ray emission stems predominantly from high-energy (and coherent) magnetospheric curvature radiation in the higher parts of the magnetosphere through a process of further upscattering from populations of lower energy photons [33, ch. 6]. Recent sensitive polarimetric timing experiments with the MeerKAT beamforming system [143, see co-authors list] undertaken on a population of high spin-down young (non-recycled) pulsars shows that the engine driving gamma-ray emission may not, necessarily, require that radio-synchrotron emission be emitted at the same magnetospheric altitudes.

[4]These steep radio spectra are typical of rotationally powered pulsars, J1023+0038 is placed towards the top of the range, although some pulsars have spectral indices < -3. The population mean spectral index is on the order of -1.7. Only a handful are flat spectrum ($\alpha > -0.5$) [33, ch. 6].

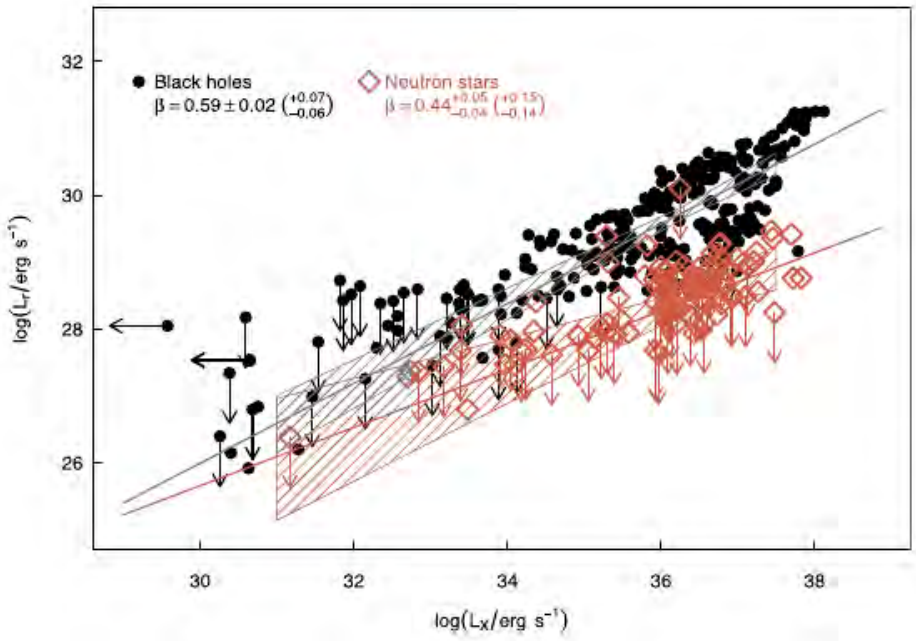

(a)

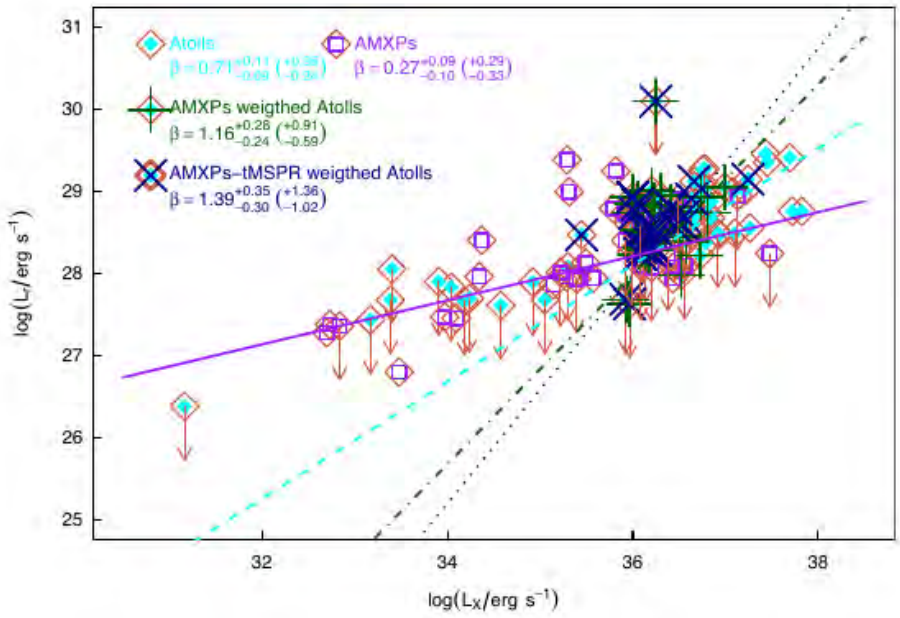

(b)

Figure 4.5: (a) Radio-X-ray luminosities for BH and NS systems taken from [54, and references therein]. The correlations for BH systems (black) and NS systems (red) are indicated in the legend, with 3σ errors indicated as filled regions. (b) Radio-X-ray luminosities for different classes of NS systems taken from [54, and references therein] where the differences in slopes of the Atolls and AMXP populations are found to be statistically significant.

[119] puts forward Spectral Energy Distribution (hereafter "SED") modeling that shows that a weak propeller state, where only a small fraction of the infalling accreted matter makes it down to the surface, may be behind these unusually high luminosities. Their model is compatible with the detection of pulsed X-ray emission in both PSR J1023+0038 [5] and XSSJ12270-4859 [117]. It also can explain the uptick in gamma-emission in PSR J1023+0038. In short, it is thought that:

1. the magnetosphere shock-accelerates (Fermi I[5]) a portion of the available electron content to relativistic speeds near the edge of the accretion disk, where
2. they interact with the magnetic field lines to produce synchrotron emission in the X-ray energy band (which is in addition to the small thermal component thought to stem from the NS surface) which is then
3. further up-scattered to gamma energy levels by the population of, now relativistic, electrons in a Synchrotron Self-Compton upscattering.

This periodic weak propeller as proposed by [119] (assuming a $\sim 20\%$ accretion efficiency of the disk) also explains the observed uptick in radio emission. The highly anti-correlated radio-X-ray temporal behavior [20] observed favours such a weak propeller model, see Fig. 4.4 (b) and is supported by simulation of strong propellers that indicate that short episodes of accretion are accompanied by ejection of a radio jet, with short (order of a few rotations) pauses where neither occur. An interpretation more consistent with this observation is that the flat-spectrum radio flux may stem from interaction in the rotating magnetosphere and accretion disk boundary instead of a highly collimated outflow and that the disk is periodically pushed out beyond the co-rotation boundary where the weak propeller may take over.

As much of the existing understanding of MSP systems are drawn from observation of hard-state NSs, a larger population of transitional low radio luminosity NS systems are necessary to further our understanding of the processes at play when the pulsar accretion and rotation-based luminosities are comparable. This is, however, a difficult undertaking as these systems are seemingly variable on the spans of only a few years, and are necessarily left to discovery in optical and higher energy bands (due to their relatively low radio luminosity), but requires subsequent co-observation (preferably co-temporal) at wavelengths ranging from centimeter to gamma-ray bands to fully explain magnetospheric-accretion-disk interactions.

4.2 The transitional pulsar candidate CXOUJ110926.4-650224

In a search for X-ray counterparts to unclassified gamma-ray sources observed with the Fermi Large Area Telescope (LAT) [167] identified CXOUJ110926.4-650224 (hereafter "J1109" for brevity) as the only possible X-ray counterpart to gamma source listed as FL8Y J11098-6457. J1109 was identified as the soft X-ray counterpart to hard X-ray source IGRJ11098-6457 by [156] using Chandra and listed in the Swift Burst Alert Telescope source catalog as 4PBCJ1109.3-6501 [40].

In a first study of J1109 [167] reprocessed X-ray data spanning nearly three decades of observation (starting January 1991 through 2018), as observed with ROSAT (1991, 0.1-2.4 keV), Swift soft X-ray monitoring (2008, 2009, 2018, 1.5keV) and continuous hard X-ray monitoring between 2004 and 2017 in the 15-150keV band, Chandra (2008 0.5-7.0keV), slew observations using XMM-Newton (2012, 2014 and 2017 0.2-12keV) and simultaneous soft and hard X-ray band observation with XMM-Newton and NuSTAR in the 0.3-10 and 3-79 keV bands respectively (June 2018). Archival INTEGRAL observations spanning the period 2003 to 2018 were also reprocessed. Optical observations were obtained from both the Optical Monitoring (hereafter "OM") camera on-board XMM-Newton and dedicated observations using the SALTICAM camera and Robert Stobie Spectograph on SALT during March 2018. Finally, the team obtained dedicated

[5]It is noted that [48] points out that the assumption of Fermi-based acceleration has not yet been noted for other LMXB.

continuum radio observation of the source using ATCA C/X band in 2018, entirely overlapping with the aforementioned NuSTAR hard X-ray observations.

The optical counterpart for the source is located at 11h09m26.4057(9)s, -65d02m24.8216(4)s (J2000) [26]. [167] noted that the luminosity distance obtained from parallax angle of the source is still subject to relatively large error. Using a Bayesian method, discussed in [13, 14], they calculate the luminosity distance from an assumption of an expotentially decreasing volume prior that is heavily dependent on the choice of length scale (based on the expected distribution of stellar distances in the galaxy). The spread in distance ranges between 1.7 to 15.5 kpc at the 16th and 84th percentiles for length scales of 2.1 and 3.4 kpc. In the interpretation we will quote luminosities at both 4 and 11 kpc, the luminosity distances for these are denoted d_4 and d_{11} respectively.

The main findings of this first detailed multi-wavelength study of [167] are summarized here:

- An optical counterpart showing variations of 0.3-0.4 mag on timescales of tens of minutes was detected in the 3300-10500 Å range. Observations using the OM indicate that this variability extends to few 10 ks. Doubly peaked Balmer lines are clearly evident in the spectroscopic data indicative of a system with an accretion disk in motion.
- X-ray observation spanning an energy spectrum between $0.3-79$ keV showed highly variable transitions between flat-bottomed low, high and flaring states comparable to what has been observed for e.g. tMSP J1023+0038. The source spends about 60% of its time in a high mode. Irregular transitions to a flat-bottom stable low state lasting anywhere between a few tens of seconds to tens of minutes is seen. After a lengthy dip to the low state during the second half of joint soft-hard X-ray observation significantly more variable and flare activity were seen. Unlike J1023+0038 there is no statistically significant evidence for hardening of the energy spectra when it spends time in the high state. The low and high mode luminosities differ by about an order of magnitude ($\sim 2.7\times10^{34}d_4^2$ erg s^{-1} vs. $\sim 3\times10^{33}d_4^2$ erg s^{-1} in the $0.3-79$ keV range at a distance of 4 kpc)
- Apart from short term relative variability in the sub-luminous accretion state, over the long term there is no statistically significant variation in the soft X-ray. This suggests no switching between rotation-powered and accretion-powered states is taking place. It is, however, cautioned that the authors cannot definitively exclude that the source did not experience a mode flip reversion between a rotation powered and accretion powered state in the timespan between 1991 and 2003 due to the lack of observation.
- Both the high state X-ray and gamma-ray (100 MeV $-$ 300 GeV) have luminosities at comparable magnitude. The gamma-ray energy spectrum is softer than the X-ray spectrum ($\Gamma_\gamma \sim 2.6$ and $\Gamma_X \sim 1.6$ respectively).
- No radio counterpart detections were made in the band at a stacked 3σ sensitivity of 18μJy beam^{-1}, nor when stacking low, high and flare intervals separately, hence any anti-correlated phenomenological similarities to J1023+0038 could not be investigated. The fact that the source spends only between $\sim 10-20\%$ of its time in a stable flat-bottomed low X-ray mode further complicates any detection of a corresponding radio high. It is noted that no pulsar spatially coincident with J1109 is listed in the most recently updated version of the Australia Telescope National Facility (ATNF) pulsar catalog v1.67[6] [69].

Even though the source is yet to be confirmed to transition between accretion and rotationally powered stages, the observed short-period and characteristically-stepped X-ray luminosity transitions match behavior in other confirmed tMSP and candidates. In our published work [37] we carried out a followup simultaneous observation campaign using XMM-Newton, MeerKAT, Swift and ATCA. We will draw much of the discussion here from the publication and its supporting internal memorandum. This followup observation campaign is summarized in Table 4.1. Two sets of overlapping observations were scheduled to monitor the source in X-ray and radio, firstly, using XMM-Newton and deep MeerKAT observation between 2019 Jun 14 and 16 and, secondly, using Swift and ATCA.

[6]Rechecked from the v1.59 catalog checked by [167]

Table 4.1: Observation execution schedule for the 2019 followup to the 2018 multi-wavelength study of J1109.

Telescope	Start - End time	Exposure
	Mmm DD hh:mm:ss (UTC)	ks
XMM-Newton/EPIC MOS1	Jun 14 18:46:04 - Jun 15 02:26:26	26.8
	Jun 15 14:24:17 - Jun 16 00:51:19	36.5
XMM-Newton/EPIC MOS2	Jun 14 18:46:25 - Jun 15 02:26:31	26.8
	Jun 15 14:24:40 - Jun 16 00:51:25	36.5
XMM-Newton/EPIC pn	Jun 14 19:23:42 - Jun 15 02:30:37	24.9
	Jun 15 15:01:55 - Jun 16 00:51:39	34.4
XMM-Newton/OM	Jun 14 18:54:26 - Jun 15 02:29:47	25.5
	Jun 15 16:56:13 - Jun 16 00:24:40	25.1
MeerKAT	Jun 14 15:31:32 - Jun 14 23:23:45	28.4
	Jun 15 14:44:26 - Jun 15 22:31:34	28.1
Swift XRT	Sep 6 21:01:34 - Sep 6 21:29:56	1.7
	Sep 6 22:37:03 - Sep 6 23:04:56	1.7
	Sep 7 00:14:23 - Sep 7 00:17:53	0.2
ATCA	Sep 6 22:36:30 - Sep 7 07:09:20	30.8

The XMM-Newton observatory has a dual X-ray imaging (the European Photon Imaging Camera "EPIC" Metal Oxide Semiconductor "MOS") and spectrometer system (the Reflection Grating Spectrometer "RGS"), an unobstructed EPIC "pn" X-ray camera and an Optical/UV Monitoring camera on board [149, 157, 103]. For these observations both the MOS and pn EPIC cameras were employed (in small window and fast timing modes respectively). The $0.3-10$ keV band data was analized with the Science Analysis Software v. 19. Note that the first 10 ks worth of the first X-ray observation had to be discarded due to strong background flare contamination. The OM observation in the second epoch started late due to technical problems.

In the MOS data a $60''$ radius was used for subtraction of background photons, while photons from the source itself were extracted from a $30''$ radius, using the outer and inner CCDs respectively. A ten pixel-wide strip was used to collect source photons with the pn camera, while background photons far away from the source was read from a three pixel-wide strip. Single and double pixel events > 0.7 keV were extracted with the pn camera, while the MOS captured up to quadruple pixel events. J1109 was detected at the count rates summarized in Table 4.2. The second set of X-ray observations were taken with the Swift X-ray Telescope (XRT) [29] in photon counting mode in the $0.3-10$ keV band. We detected J1109 at an average net rate of 0.040 ± 0.003 counts s^{-1} ($\sim 10.5\sigma$ detection) between three epochs as listed in Table 4.2. The net count rates between the three obervation epochs (latter two concurrent with ATCA observation) was constant between the epochs, within the uncertainties. From the combined observation a source and background spectrum was extracted at a radius of 47.2" and source-free annulus of 94.4" and 188.8" respectively, both centered on target.

Radio observations of J1109 were made with MeerKAT at L-band ($856-1712$ MHz) and ATCA in C/X-band with two subbands centered at 5.5 and 9 GHz respectively, each with a bandwidth of 2 GHz. The MeerKAT reduction is detailed in Section 4.3. ATCA observed the J1109 field in an extended 6 km configuration (6C). The data was edited and reduced with CASA [104] and imaged at robust UV weighting ranging between 0-2 (2 roughly equating to Natural weighting). As with the 2018 observations no detection was made from these 2019 observations either. A 3σ sensitivity of 18 μJy beam^{-1} was again achieved in this setting in both subbands. Stacking both subbands together did not yield a detection either at 15 μJy beam^{-1} 3σ sensitivity. Stacking the 2018 and 2019 observations achieved resulted in a 12 μJy beam^{-1} 3σ sensitivity with no detection either.

Table 4.2: Count rates from the readouts of the various cameras on XMM-Newton and the Swift XRT. Only an upper estimate of 0.15 counts s^{-1} can be derived for each 4 ks image and 0.3 counts s^{-1} for the final 1.2 ks image for the first day observing using the OM system due to strong variable interference from background flares near J1109.

Telescope	Start - End time	Net count rate
	Mmm DD hh:mm:ss (UTC)	counts s^{-1}
XMM-Newton/EPIC MOS1	Jun 14 18:46:04 - Jun 15 02:26:26	0.186 ± 0.003
	Jun 15 14:24:17 - Jun 16 00:51:19	0.159 ± 0.002
XMM-Newton/EPIC MOS2	Jun 14 18:46:25 - Jun 15 02:26:31	0.199 ± 0.003
	Jun 15 14:24:40 - Jun 16 00:51:25	0.161 ± 0.002
XMM-Newton/EPIC pn	Jun 14 19:23:42 - Jun 15 02:30:37	0.580 ± 0.009
	Jun 15 15:01:55 - Jun 16 00:51:39	0.498 ± 0.005
XMM-Newton/OM	Jun 14 18:54:26 - Jun 15 02:29:47	No detection
	Jun 15 16:56:13 - Jun 16 00:24:40	$0.4 - 0.8$
Swift XRT	Sep 6 21:01:34 - Sep 6 21:29:56	0.043 ± 0.005
	Sep 6 22:37:03 - Sep 6 23:04:56	0.039 ± 0.005
	Sep 7 00:14:23 - Sep 7 00:17:53	0.03 ± 0.01

4.3 A direction-dependent MeerKAT treatment

MeerKAT co-temporal observations were taken with the XMM-Newton soft X-ray observations to study the interplay between the magnetosphere and ongoing subluminous accretion process and to hopefully contribute a firm radio detection to aid in classification of J1109. To this end, MeerKAT observations (capture blocks 1560526258 and 1560609072) were taken under proposal code SCI-20190418-DB-01, as listed in Table 3.1, using 61 and 63 antennas with the 4k channelizer full-polarimetric correlator of the MeerKAT system with frequency coverage spanning $856 - 1712$ MHz and 8 s integration. A short system overview is given by [81].

We started by reducing the dataset taken on 15 June 2019, for which the largest portion of usable X-ray observation is available.

Standard transfer calibration is applied using CASA where flux and passband calibration is performed using ATCA standard flux calibrator PKS B1934-638 [135]. Temporal variability (phase and amplitude) calibrated using secondary J0906-6829 (09h06m52.23s -68d29m39.90s J2000).

The data was flagged by hand, applying a dilated mask to the passband in the process[7]. A total of 72.1% of the target field data was flagged, inclusive of flagged antennas. This is slightly more than typical flag percentages of 55-65% using automated methods [see co-authored proceedings 72]. Fig. 4.6 indicates the flag percentages as a function of frequency, time and baseline length. Antennas m023, m038 and m061 were fully flagged due to temporal dropout, possibly due to digitizer faults in observation on June 15^{th}. It also shows the percentages for the first epoch data where it was flagged with a static mask and further culling by hand.

This relative scale is transferred to the observation taken on June 14^{th} through transfer of the derived self-calibrated (discussed next) sky model of the target field, after deriving and applying gain normalized bandpass solutions to ensure that we have relatively consistant fluxes across both epochs for stacking and deriving time-series.

The transfer calibrated image (more information in the next section) is fitted with PYBDSF [107] and total fitted flux cross matched within 5" resolution for the high S/N (dominantly AGN) population at detection threshold of 50σ ($\sigma \sim$

[7] I note that this initial data inspection was done by Ruby van Rooyen within the collaboration. These pre-flagged visibilities were used for further transfer and self-calibration.

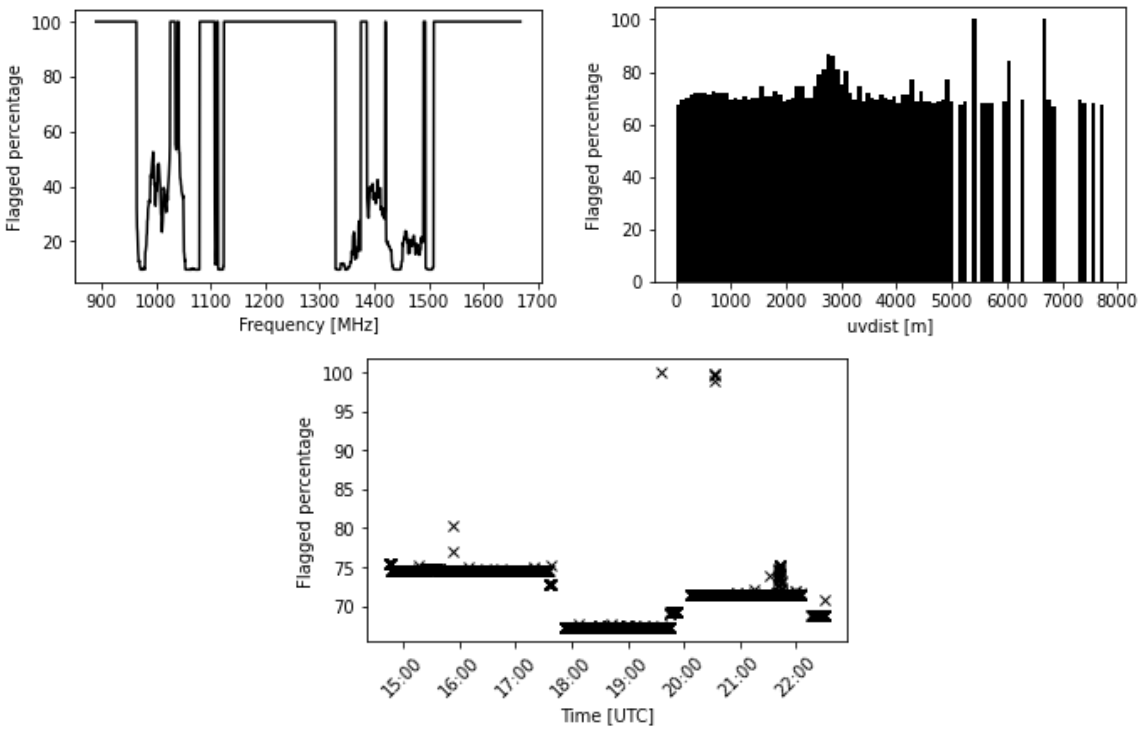

(a)

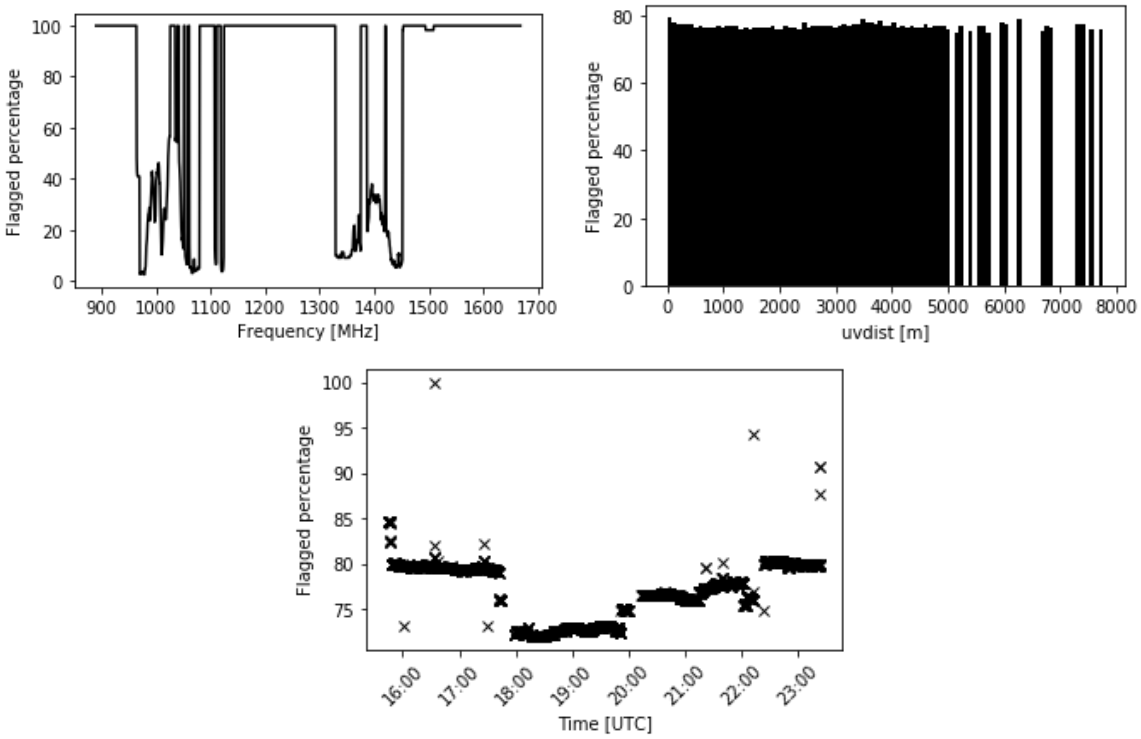

(b)

Figure 4.6: (a) Flag percentages as a function of frequency, baseline length and time for the Jun 15 epoch MeerKAT observation. (b) Flag percentages as a function of frequency, baseline length and time for the Jun 14 epoch MeerKAT observation

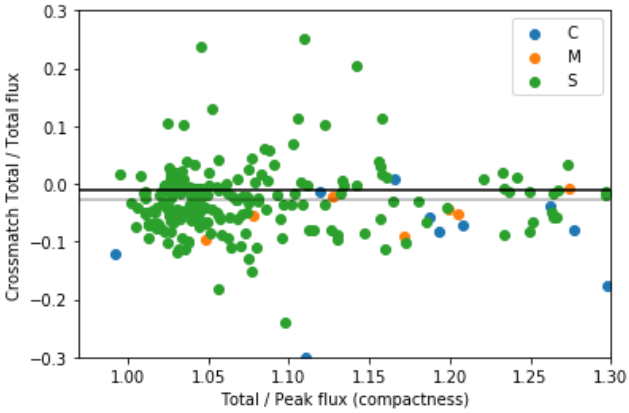

Figure 4.7: Absolute error of cross-matched integrated flux between epochs Jun 14 and 15 as a function of integrated to peak flux of a selection of the most high SNR compact field sources. The majority of the population are therefore the "(S)ingle" fitted Gaussian per island category, with a few from the "(M)ultiple" fitted Gaussian and "(C)omplex multi-Gaussian per island source" as classified by BDSF.

5 μJy beam^{-1} for both epochs) as shown in Fig. 4.7. The second observation flux scale is, relatively, fractionally higher as shown. The gray line is the median fractional offset of 2.8%, while the black line is the mean fractional offset of 0.95%. We correct the scale of the second observation to that of the first observation with the median fractional offset, which brings the two Multi-Frequency Synthesis maps into closer match (by manual inspection of compact sources). This correction ensures accurate stacking and comparison between epochs.

We also checked the applied flux scale of the first observation against the known flux scale of PKS B0407-65 from long-term monitoring (see Chapter 1). After accounting for the 2.8% adjustment outlined above, this absolute error (stemming from the flux scale calibration of the second epoch) overestimates the scale of PKS B 0407-65 by 7% at the bottom of the L-band spectrum, which was taken as the absolute flux scale error of both observations.

Direction-dependent self-calibration of this field was performed using DDFACET [152, see co-authors list] and CUBICAL [87]. We used the CLEANMASK[8] utility to constrain clean models for calibration to local sigma of 10, manually including faint extended emission from a supernova remnant complex to the south-east of the field. Throughout we used Briggs [25] -0.3 weighting in the imager giving near optimal sensitivity while avoiding the potential for confusion introduced through the non-gaussian flanks of the MeerKAT PSF that become apparent at robust scales greater than 0.3. The image extent is 2d29m at a fitted resolution of $7.38'' \times 6.10''$ and $6.70'' \times 5.91''$ for the first and second epochs respectively. Images of both epochs are continuum radio Multi Frequency Synthesis images at 1.284 GHz. We highlight how to practically use the interface and framework developed in Chapter 3 here more verbosely as an example on its practical use.

The field had substantial direction-dependent errors that required us to go directly to direction-dependent calibration techniques after applying transfer calibration. This ensured that direction-independent gains were not influenced by flux variability due to the effects of the antenna far field response (coupled with pointing errors) on bright off-axis sources. The Radio Interferometric Measurement Equation (RIME) used for calibration is given by Eqn. 3.14 (see Chapter 3 for a theoretical treatment).

The advantage of using the RIME in Eqn. 3.14 is that most of the sky flux (within 10σ of the local RMS in this instance) is taken into account during solving of direction-dependent gains. This, to a large extent, avoids the flux suppression that is typically seen in implementation of traditional peeling through e.g. the CASA [104] framework, if the flux in the rest of the field is not first removed before gains are solved and applied to the field sources. This "traditional" peeling approach has to be done source-by-source with no automatic iteration between directions to consider gain coupling, in a laborious

[8] Available from `https://github.com/SpheMakh/cleanmask`

multi-step process. We started by tagging sources using the SAODS9 [83] viewer and saving a region file for use in to demarcate direction-dependent regions for calibration and storing the regions in pixel coordinates, matching that of the image, using the SAODS9 [83] viewer, see Fig. 4.8 (a).

The following options (non-exhaustive, but sufficient to demonstrate direction-dependent calibration functionality) are specified to CUBICAL [87], after imaging. This results in outputting residuals for directions `[1,n]`:

```
out-mode            = sr
out-subtract-dirs   = 1:
out-correct-dir     = 0
model-list          = MODEL_DATA+-
DDF_CXOUJ110926_1GC.DicoModel@dE.reg:DDF_CXOUJ110926_1GC.DicoModel@dE.reg
sol-jones           = G,dE
dist-ncpu           = 16
dist-nworker        = 16
dist-nthread        = 16
dist-max-chunks     = 16
g-update-type       = phase-diag
g-diag-only         = 1
g-freq-int          = 0
de-fix-dirs         = 0
de-time-int         = 8
de-freq-int         = 16
```

The expression in the `model-list` reads the model visibilities (as written by the imager) from `MODEL_DATA`, subtracting all flux from demarcated regions and uses this product as direction-independent part (so-called direction `0`) of the model. The specification after the semicolon in the `model-list` specifies a series of direction-dependent models from the component model output by the imager (here a `DicoModel`-formatted catalog), where each such direction/region is demarcated by our ds9 region file (here `dE.reg`). These are directions `1:` in NUMPY [161] slice notation. The result from this calibration is a substantial improvement in the residuals around the bright off-axis sources, as well as the residuals at phase center stemming, mostly from the marked source to the north.

We then apply the same treatment again, but to sources closer to the target coordinates. This time subtracting directions `[0,n]` (ie. including the 10σ masked flux of the rest of the field). This mask expressly excludes the science target coordinates. This time we calibrated with slightly longer intervals to increase signal-to-noise, because the directional models contain less flux. The cyan circle indicates reported optical position of the target. The result is a relatively interference-free central region in Fig. 4.9.

The same treatment was then applied to the the first epoch data before stacking and making lightcurves from snapshot imaging of the residuals (with all but the immediate vicinity – few times the resolution – of J1109 subtracted, apart for a separate series of diagnostic snapshot images which will be discussed in the next section).

4.4 Stacking and variability searches

The X-ray co-temporal observations taken with XMM-Newton again showed distinct trimodal behaviour in the counts, with the variability strikingly similar to what was seen in the 2018 observations. We use the following definitions to classify the count rates (CR, binned to 50 s):

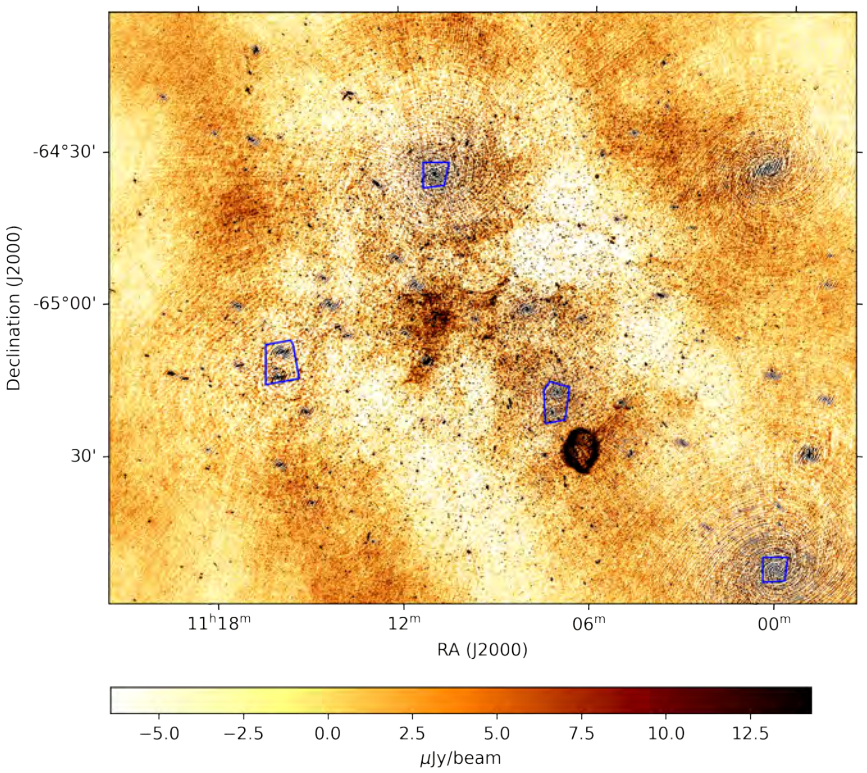

(a)

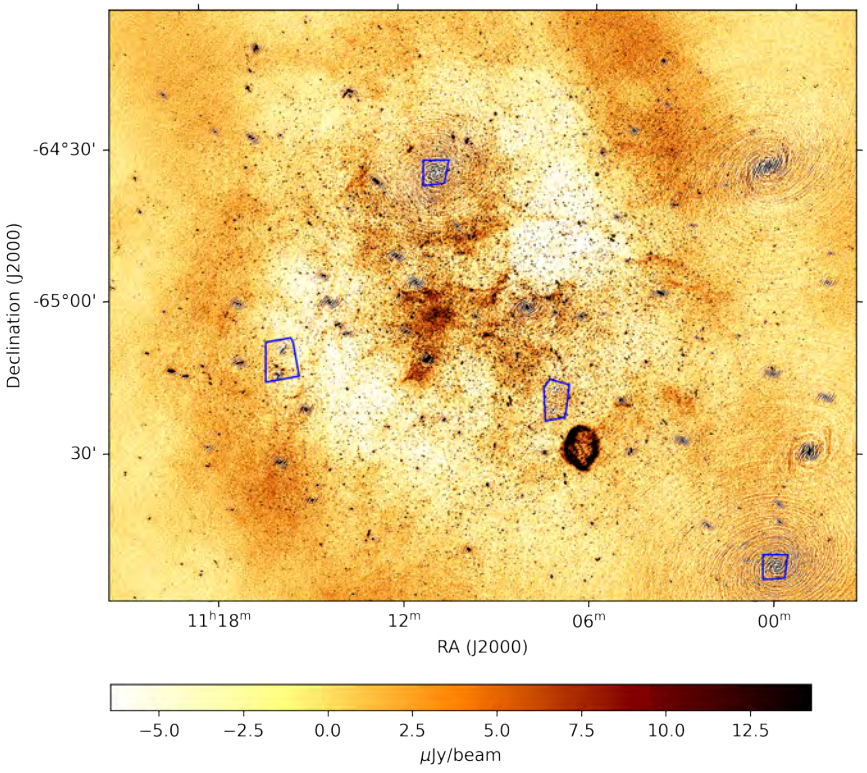

(b)

Figure 4.8: (a) Regions (blue convex polygons) where direction-dependent solutions should be solved for is specified inside the SAODS9 [83] viewer. (b) peeled residuals after correcting and peeling regions marked. Images here locked to the same scale. Here we show the image constructed only with the June 15^{th} epoch.

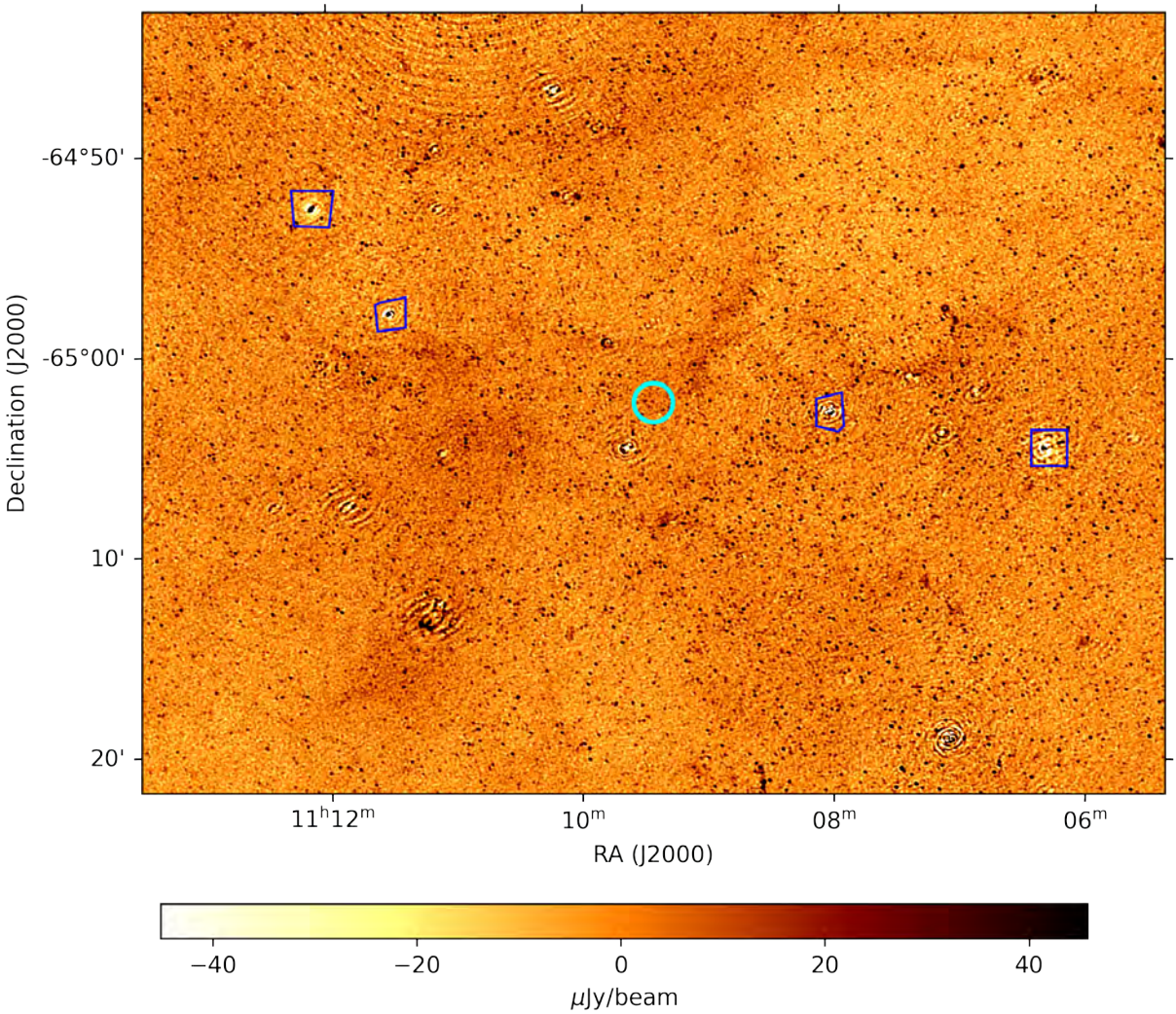

Figure 4.9: The relatively sidelobe interference-free central region (position of J1109 marked with cyan circle) after two rounds of multi-direction direction-dependent calibration. Here scales are adjusted to show the interference free target position at an RMS sensitivity of 5 μJy beam^{-1} for the observation taken on 15 Jun.

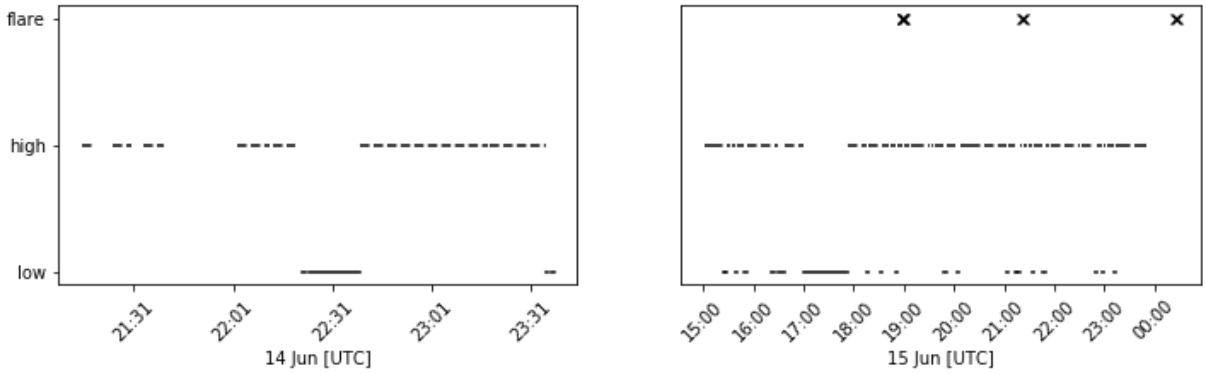

Figure 4.10: Stable low, high and flare states as determined from the X-ray counts for the two observation epochs.

- Low mode: CR < 0.4 counts s^{-1}
- High mode: $0.4 \leq$ CR < 2.0 counts s^{-1}
- Flares: CR ≥ 2.4 counts s^{-1}

The periods corresponding to the trimodal states under this definition are given in Appendix B of this document and we show a viewgraph of state time series in Fig. 4.10 for visual reference. We will be referring to these periods later on when we discuss stacking. Periods prior to June 14^{th}, 2019 21:15 UTC were subject to background flaring activity in X-ray and no mode information was available during this time period.

As was seen from the 2018 observations, J1109 spends the majority of its time in a stable high state with periodic transitions to a flat-bottomed low state, which may last time periods ranging from tens of seconds to several minutes. During the second observation the source experienced a particularly long (~ 50 min) flat-bottom low state for which we have co-temporal MeerKAT data.

From the DD-corrected, flux subtracted, residuals we formed a series of dirty snapshot (ie. non-deconvolved) images of one minute each using the CASA `clean` imaging task[9]. We kept imaging at maximum MeerKAT untapered and non-sidelobe-confused sensitivity weighting of robust 0. Since most of the bright AGN emission had already been subtracted from the field through previous self-calibration steps, the imager was operated in narrow-field mode on a 256 pixel region (image radius of $2.8'$) around the science target coordinate to speed up processing by disabling w-corrections.

The sensitivity achieved from the stacking of all available radio data is ~ 4 μJy beam^{-1}.

We find evidence of radio emission at the position of CXOU J110926.4-6502 in these stacked images, where a statistically significant (7.9σ - 33 ± 4 μJy beam^{-1}) detection is made for the first time, see Fig. 4.11. We fitted for the position of this emission using PYBDSF [107], adopting an island threshold of 3σ and confidence cutoff of 5σ. The compact radio emission (with a peak to integrated flux ratio of ~ 1.8) is centered at 11h09m26.53 $\pm$ 1.15s $-$65d02m23.65 $\pm$ 0.93s (J2000.0). This is fully consistent with the position quoted from Gaia and Chandra X-ray data [167], within the uncertainties.

Using the defined X-ray-count states we further selected and stacked the radio images corresponding to these states. These are shown in Fig. 4.12. As the X-ray counterpart do not spend an equal amount of time in each state, the local noise levels differed substantially between the panels.

We made a very marginal detection of at around 30 μJy beam^{-1} (2.7σ) of the source while it was in low periods (at most

[9]We used this imager simply due to ease of its time-based data selection switches. Similar time-based switches have since been added to DDFACET which we used for the data calibration, but was not as easy to use at the time of reduction.

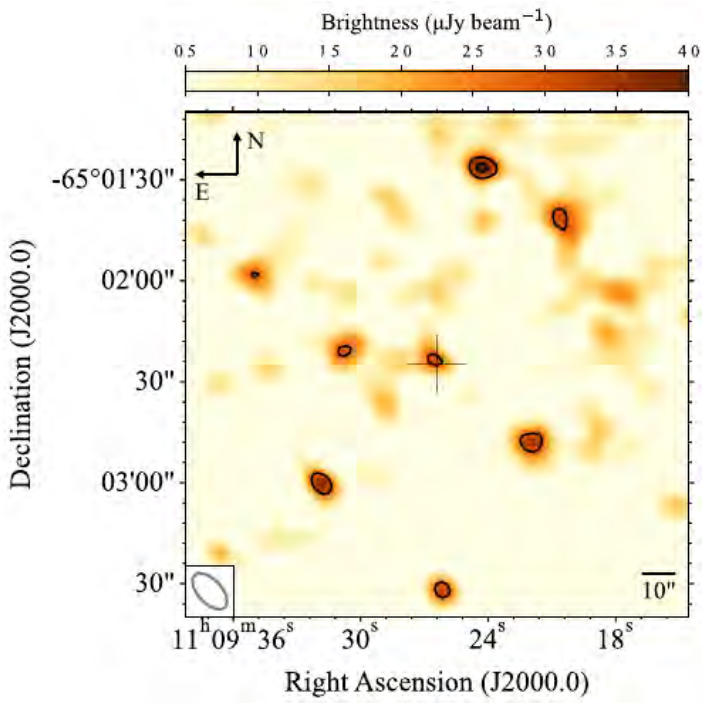

Figure 4.11: 1.28 GHz MeerKAT image of the region immediately around J1109. This image is published in [37]. Here all data acquired during the first and second epochs are stacked. Radio emission is shown here in color with contours overlaid at intervals of $2^{n/2} \times 30$ μJy beam^{-1}, $n \in \{0,1\}$. The position of the optical counterpart is marked with a gray cross. The stacked synthesized beam is shown by the ellipse with $13.2'' \times 7.0''$, PA 43^o.

about 20% of the observed time). On the contrary, we make a very significant detection during high periods (peak flux at 51.3 ± 5.5 μJy beam^{-1} — a $\sim 9\sigma$ detection). This is well above the detection obtained by stacking all available radio data. To understand this seeming discrepancy, we also stacked the flare period data for which we could not determine an X-ray state. Here the 30 μJy beam^{-1} contours we plot are at 4.65σ confidence, however the coinciding centimeter emission clearly disappears. This is not due to a lack of sensitivity and indicates that some time within the time frame where our X-ray data was unusable the coinciding centimeter flux density decreased markedly.

In order to investigate if there is any indication of correlated or anti-correlated behaviour between the centimeter-emission and the soft X-ray, especially during the periods where the source is in X-ray low periods for prolonged times, we extract light curves from the 1min snapshots made earlier, using the peak flux detected flux density within the resolution of the confirmed position.

To exclude misinterpretation due to short term system gain errors, we also computed the field temporal flux gain variability (middle of the following figure) by extracting the mean of the light curves on stronger surrounding AGNs in a series of fields synthesized to $44.37'$, after peeling of the first sequence of interfering AGN. For this latter reference scale we enabled widefield corrections during imaging. The following positions, corresponding to identified compact sources within a few arcminutes of J1109 (and therefore not strongly influenced by potential pointing errors) are used:

- 11h08m03.42s -65d02m48.97s, J2000
- 11h09m39.58s -65d04m41.55s, J2000
- 11h09m28.17s -64d58m30.40s, J2000
- 11h08m44.74s -65d10m03.84s, J2000

The results of stacking these one minute exposures at various length scales to search for short temporal behaviour is shown

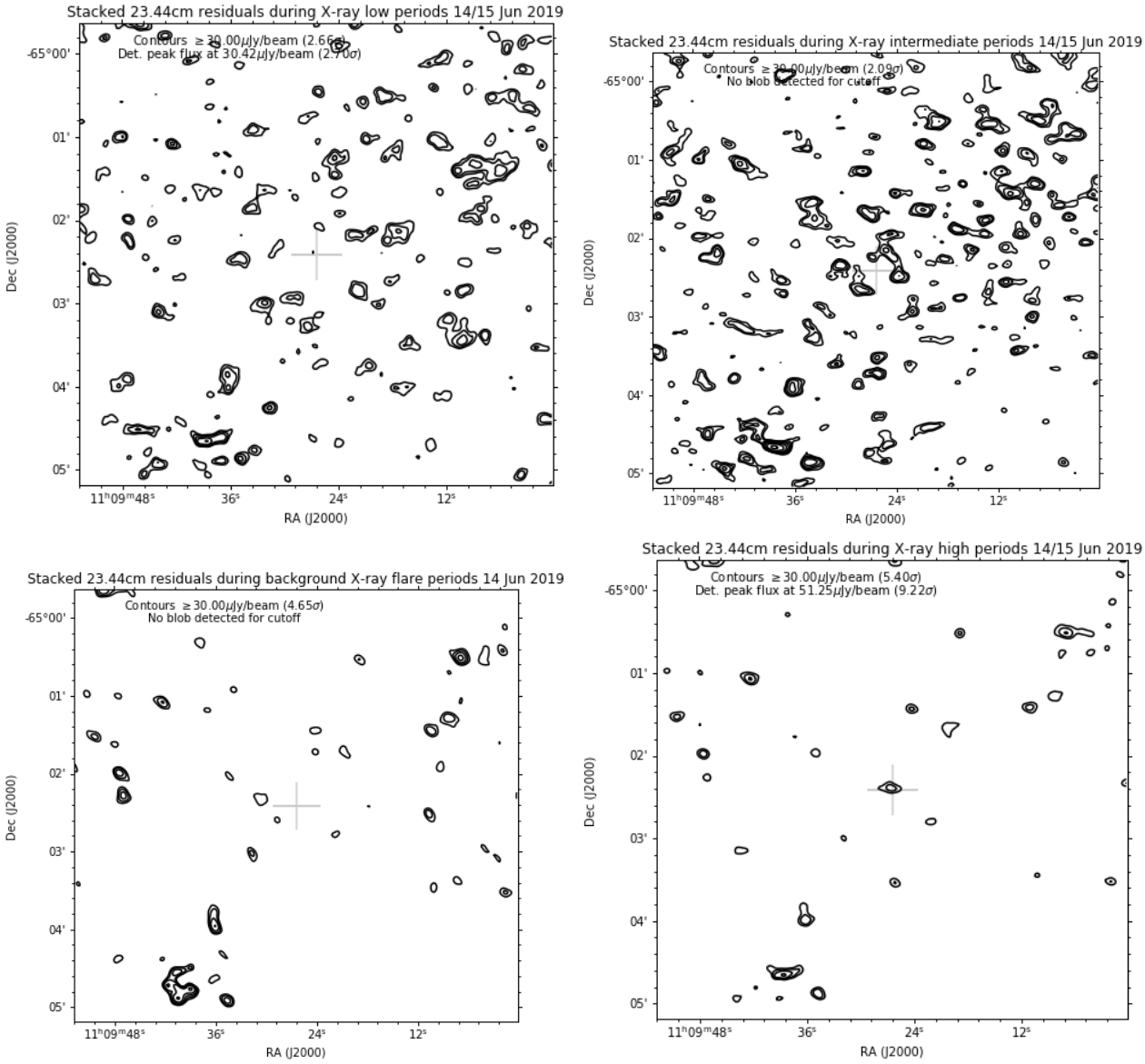

Figure 4.12: Stacked images for various states. In the top-left panel residuals for X-ray low periods during the two epochs are shown. Top-right panel shows the residuals during all intermediate periods not captured by the piecewise state definition defined above. Bottom-left panel shows the residuals for the period where there were background flare activity affecting the X-ray observation (ie. it was not possible to classify the accretion state behaviour based on X-ray counts) and bottom-right panel shows the stacked residuals during the X-ray high periods, in which the source spent the vast majority of its time. In all cases contours starting at 30 μJy beam^{-1} are drawn.

in Fig. 4.13[10]. We found that the system gain variation with each observation is bound to about $\pm 5\%$ (see the middle panels in the respective exposure curves).

4.5 Results and discussion

The radio data, binned at 1.5 hrs, is shown with the measured EPIC and OM count rates in Fig. 4.14. Overall we note:

- That there is a smooth many-hour long variability in the source flux level (more than a 5-fold increase).
- Unlike confirmed tMSP J1023+0038, there is no clear anti-correlation between the radio and X-ray flux. During the ~ 50 min low mode we measure a radio flux of 50 ± 12 μJy beam^{-1} vs. a measurement of 59 ± 5 μJy beam^{-1} during a 30 minute high mode directly next to the low mode. These levels are comparable to within errorbars and suggests no definitive correlation or anti-correlation behaviour.
- A substantial increase in radio flux after flaring starts in the X-ray, and a possible radio flare is detected within ~ 15 mins from the most significant X-ray flare.
- Although the early OM measurements were affected by an extended scattered light feature resulting in non-detections we see a mild variability around the time that there is an increase in radio activity and X-ray flaring. Unfortunately these detections were also too faint to study any strong temporal correlations with the X-ray flares.
- Based on the high confidence MeerKAT detection, we re-examined the ATCA observations by binning the ATCA data into 30 min intervals. Although there was one possible detection at 93 ± 25 μJy beam^{-1} (3.8σ) the instantaneous uv coverage was too poor to definitively localize the source of the emission.

The bright X-ray flare at around 45.4 hours of ~ 7 counts s^{-1} is brighter than the flares measured in the 2018 XMM-Newton observations by more than a factor of 2. The energy spectrum over the $0.3-10$ keV band was fitted with an absorbed power-law and showed a slight softening of the spectrum between average/high and flaring modes ($\Gamma = 1.60 \pm 0.01$ vs $\Gamma = 1.76 \pm 0.05$ respectively). Assuming an absorption column density of 5.3×10^{21} cm^{-2} the average unabsorbed flux is $\sim 3.3 \times 10^{-21}$ erg cm^{-2} s^{-1}. The magnitude of the companion remains largely unknown, owing to the uncertainties in the contribution from the companion star and the dominant accretion disk at optical wavelengths. Coupled with a large uncertainty in the parallax of 449 ± 637 μas the luminosity distance 1σ confidence interval spans $1.9-6.6$ kpc assuming an exponentially decreasing space density [27, 98] or the range $8.9-13.9$ kpc from a photogeometric prior discussed in [12]. We conservatively computed the 5 GHz[11] radio and X-ray luminosities at both 4 and 11 kpc. These measurements are shown on the radio-X-ray plane in Fig. 4.15.

As the non-detection of a radio-X-ray anti-correlation is not due to lack of sensitivity, it is suggestive that the radio emission in J1109 may not directly be linked to the process driving the X-ray mode switching, unlike with J1023. Assuming that the X-ray mode-switching in J1109 operates close to the NS, we can speculate that the majority of the low frequency emission of J1109 stems from a compact jet and/or ejection processes close to the NS. This does not exclude a propeller contribution, but merely suggests that it may be contributing below the detection threshold. The position occupied by J1109 on the radio-X-ray luminosity plane is consistent with that of other tMSPs and hard-state BH binaries and are substantially brighter than other accreting NSs at a given X-ray luminosity.

[10] The datapoints for these may be found in Appendix C to this document.

[11] As the MeerKAT detections are too faint to confidently fit for an in-band spectral index and there is no ATCA detection at higher frequencies, we assume a flat spectrum source as is seen in other accreting systems, as discussed in the background section 4.1. It is likely that the non-detection is due to variability observed, evident at L-band. Comparable variability has been observed for tMSP J1023 [48] and candidate 1RXS J154439.4-112920 [76].

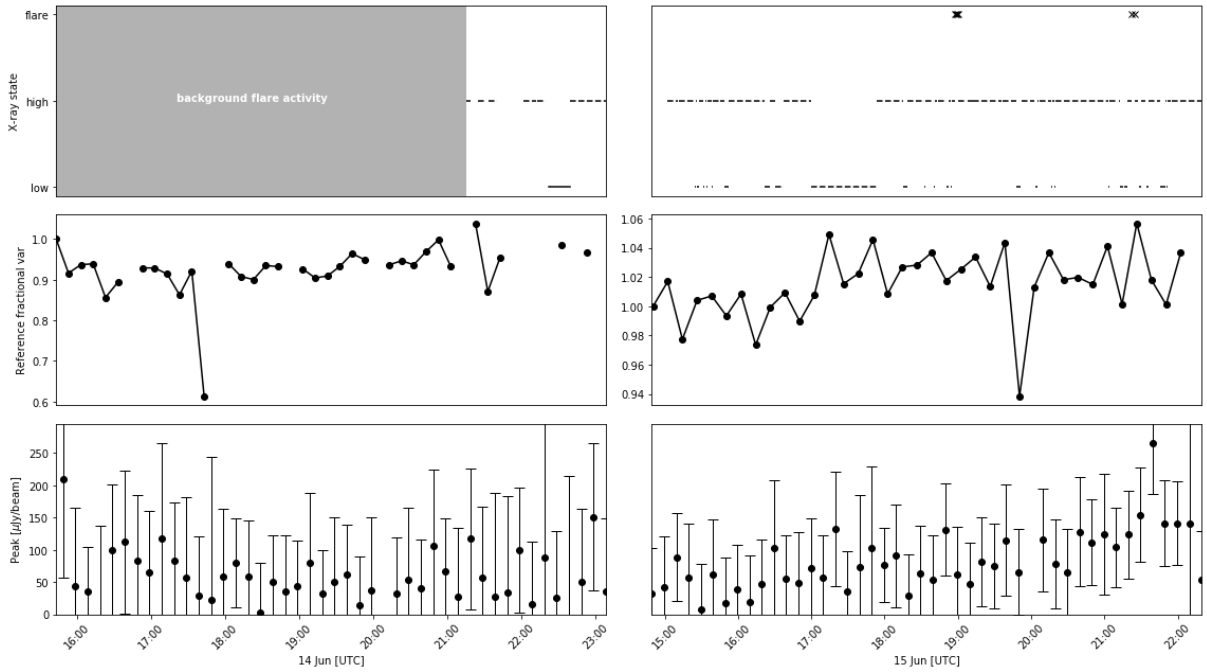

(a) 10 min exposure (average sensitivity of ~ 30 μJy beam^{-1})

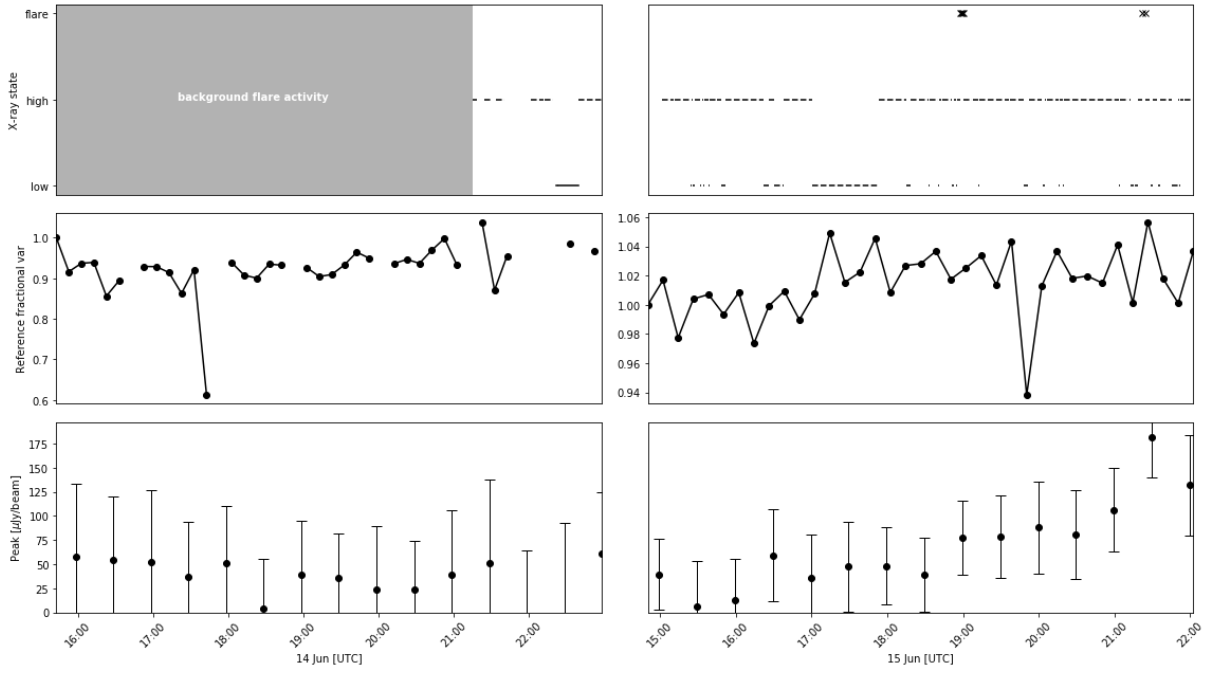

(b) 30 min exposure (average sensitivity of ~ 17 μJy beam^{-1})

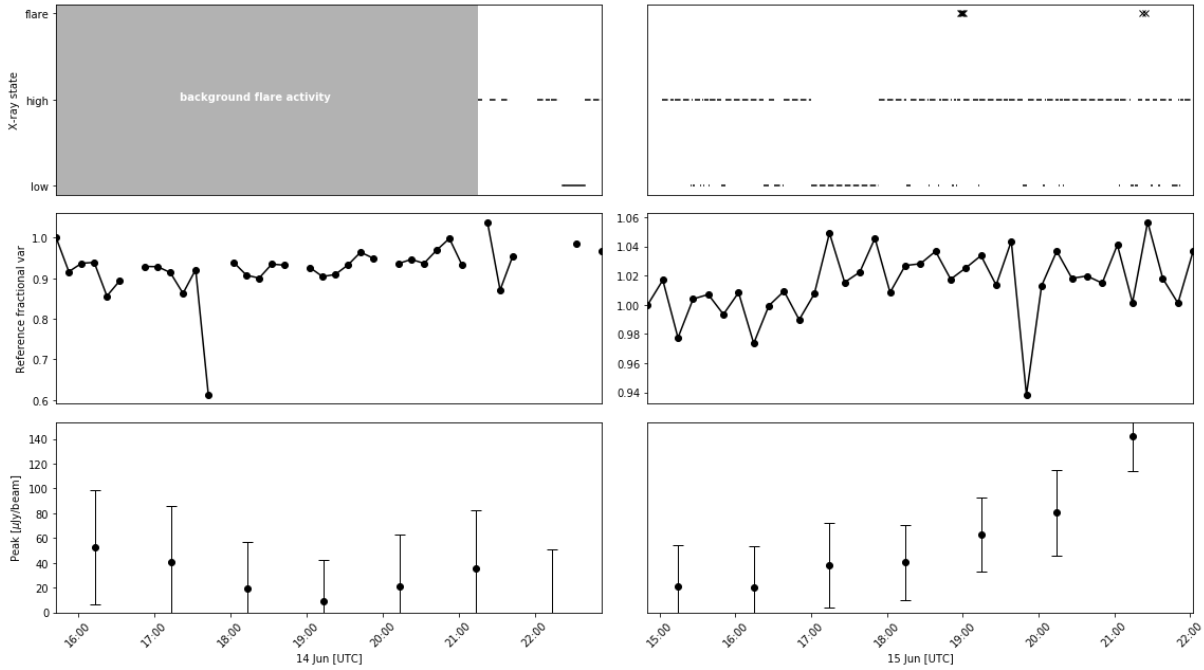

(c) 1 hr exposure (average sensitivity of $\sim 13\ \mu$Jy beam^{-1})

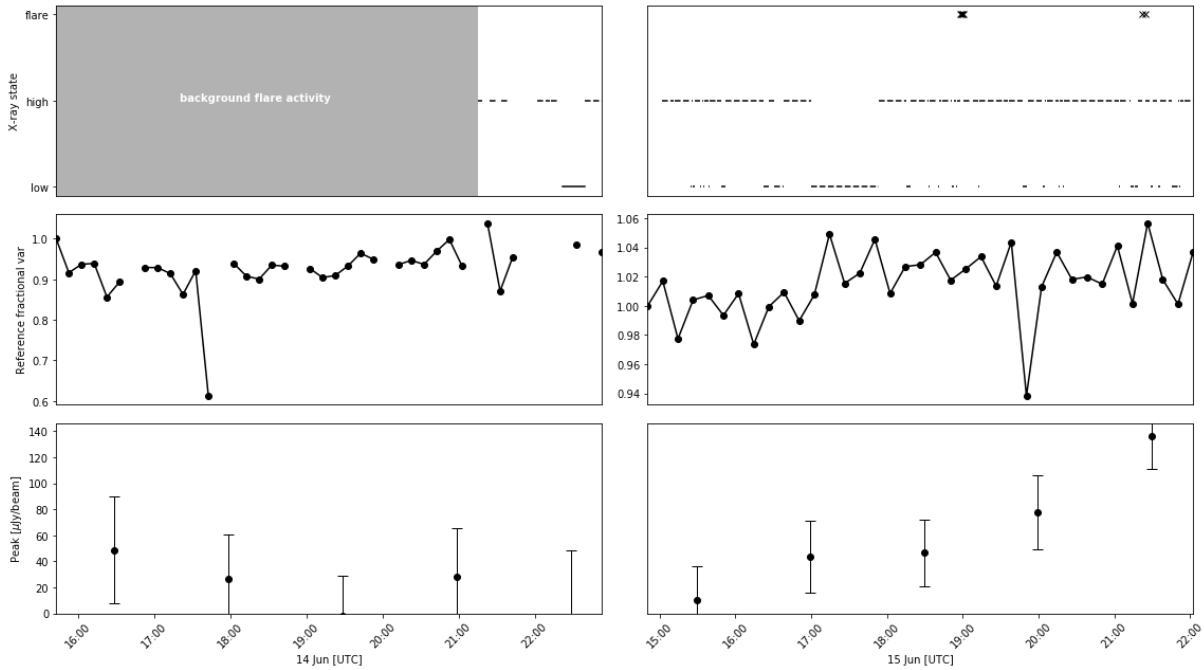

(d) 1 hr 30min exposure (average sensitivity of $\sim 10\ \mu$Jy beam^{-1})

Figure 4.13: Light curves extracted for J1109 for various exposures to trade signal-to-noise for temporal cadence. For each stacking exposure the top plot indicates X-ray state, middle plot the estimated system gain fluctuation (with reference to the first point in the June 15^{th} plot) and bottom plot the light curve around J1109 with local noise levels indicated as error bars (3σ confidence level)

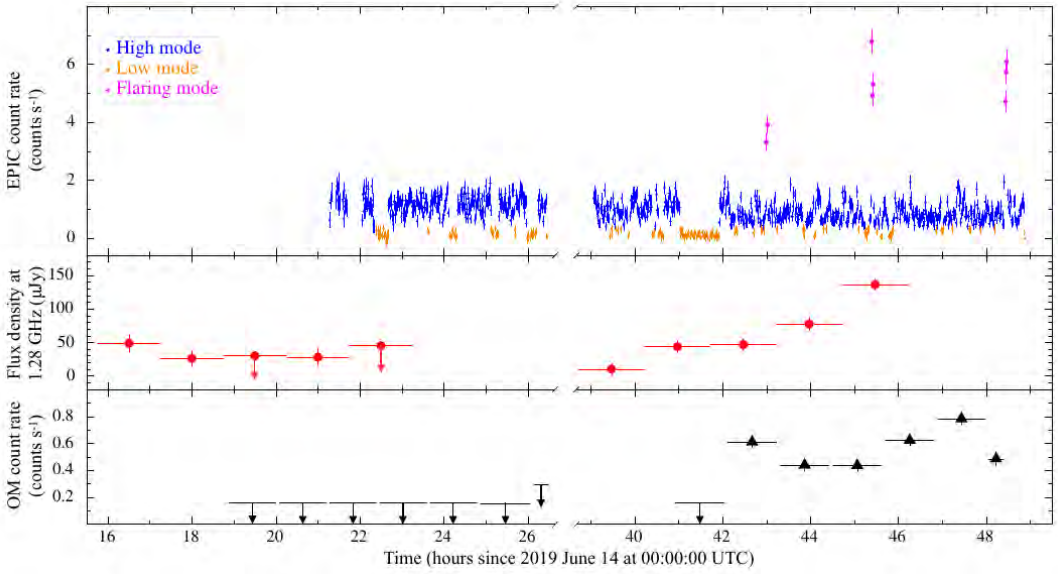

(a)

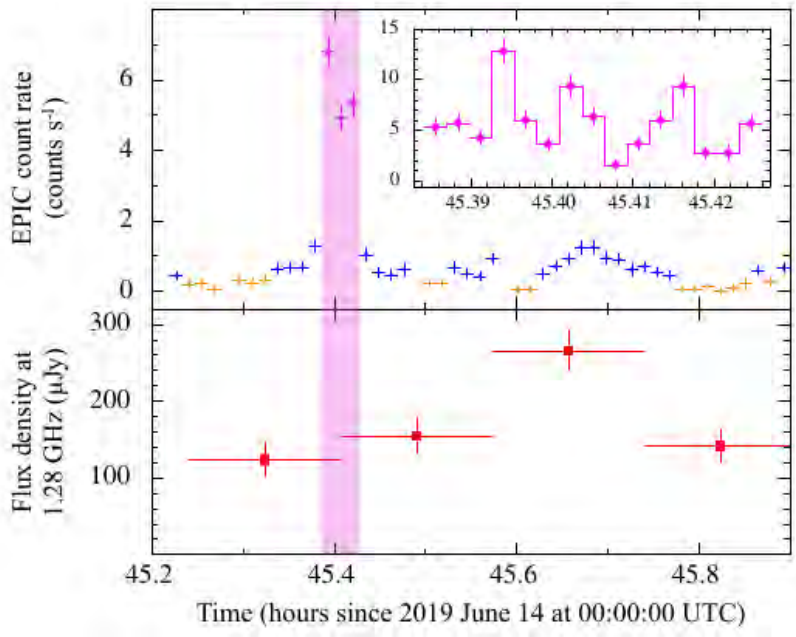

(b)

Figure 4.14: (a) Multi-wavelength lightcurves of J1109 observed between 14-16 June 2019. Top: soft X-ray, binned at 50 s exposures, between 0.3 – 10 keV is shown — color-coded by state as previously defined. Middle: MeerKAT 1.28 GHz flux densities are shown with stacked exposure of 1.5 $t$hrs. Bottom: the white light curve as measured in single images (lengths 4 or 1.2 ks). (b) Zoom of the light curves around the brightest X-ray flare, here showing the 10 min exposure stacked MeerKAT measurements. The shaded area indicates the X-ray flare time period. The insert in the EPIC panel shows a further zoom in of the X-ray data binned at 10 s intervals. All error bars here are plotted at 1σ level. Upper limits are shown where the source is undetected at 3σ. This figure is published in [37].

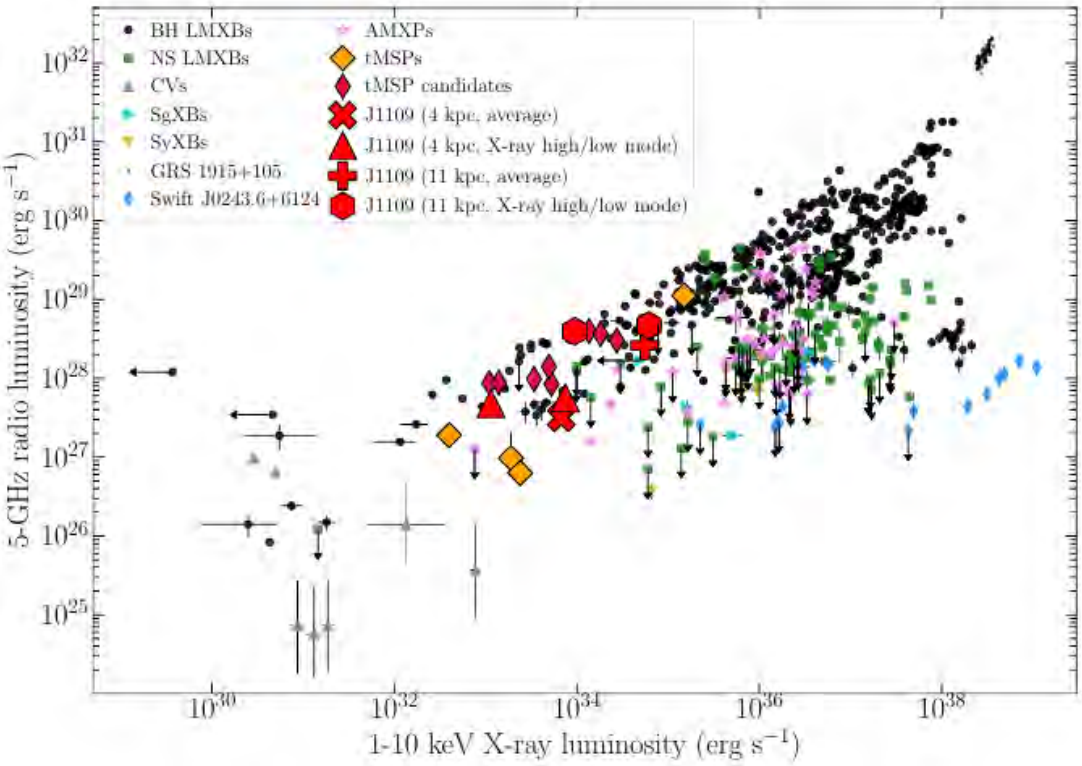

Figure 4.15: Here we show radio and X-ray luminosities for different classes of binary systems. Both BH and NS LXMBs are shown. Cataclismic variables (CVs), supergiant X-ray binaries (SgXBs), symbiotic X-ray binaries (SyXBs), Be X-ray binary SwiftJ0243+6124, AXMPs and both confirmed and candidate tMSPs. We plot the luminosities for both the average and high/low mode X-ray states of J1109 at both 4 kpc. Error bars indicate 1σ confidence and are in many cases smaller than the marker (including J1109). Upper limits are marked with arrows. Figure published in [37].

The process behind the (possible) radio flare is more uncertain. We speculate that it may stem from a quick expansion of plasma, which in the process quickly rarifies and becomes transparent to synchrotron radiation at low frequencies. In this framework, the X-ray flare emission may be due to Fermi interaction of the particle wind and the accretion disk as it suddenly becomes substantially thicker. Reconnection of the magnetic field lines at the edge of this termination shock interaction may serve to launch outflows of plasmoids and could also explain the increase in optical flux variability seen around the X-ray flares. It remains possible that this uptick in emission is due to the presence of a yet-undetected rotation-powered pulsar mechanism. In the future more sensitive co-observation with the full SKA-MID array may shed further light on this candidate.

Chapter 5

Baseline Dependent Averaging: improved archiving tooling for MeerKAT data

In this chapter I present a procedural verification of the DASK-based [137] XOVA [8] averaging utility which supports Baseline Dependent Averaging (hereafter "BDA") of Measurement Set v2 [86] formatted interferometric visibility products, primarily for data archival purposes. Although the BDA averager supports time and frequency variable averaging on a baseline-by-baseline basis, in this work I only verify the smearing and astrometrical accuracy of the averager. Even with this conservative verification approach, compression factors at an order of magnitude better than what can be achieved with regular averaging on a typical MeerKAT wideband L-band dataset is achieved while introducing no significant further flux decorrelation due to time-smearing of the visibility phases.

The XOVA [8] software was, in large, developed by Simon Perkins (SARAO) with minor improvements and fixes by myself. The work presented here is only in verification and qualification of the software on simulated and calibrated MeerKAT data (presented in Chapter 4). I will, however, briefly outline the theory behind BDA for the sake of discussion. The chapter is presented as a walkthrough for simulations with the hope that this will be useful to the reader in their own interferometry characterization work.

5.1 Motivation

We tested the baseline-regular and BDA capabilities of the XOVA [8] averager as a replacement to the CASA [104] averaging capabilities in `split` and `oldsplit`. Even in the Square Kilometer Array (SKA) precursor era it has become increasingly hard to store fully calibrated visibility products (in the MSv2 standard [86]) on archive for later re-imaging due to increasing dataset size, even when averaged. The following scenarios exemplify the absolute necessity in keeping calibrated visibilities on hand, although there are many more:

- Tapering *uv* coverages to correspond to sister instruments for detailed and accurate spectral index analysis at a later date,
- Subtracting of continuum field emission in the *uv* space in order to re-image at different weighting to improve sensitivity to diffuse emission, as is regularly done in, for instance, galaxy cluster studies,
- Re-imaging to improve sensitivity when more data eventually becomes available.

BDA is consistent with traditional visibility averaging, with the only exception being in adjusting the length of the

time interval of the averaging bin — depending on the length scale of the interferometer spacing (or baseline) being averaged.

In traditional averaging, where a single integration length scale is applied to all baselines, the length scale of such an operation is driven by the longest spacing, which has a maximally-variable fringe rate. This means that the error introduced across an interferometric array is not constant: the complex visibility function measured by a long spacing is smeared (or "fringe washed") more than the short spacings.

This is, of course, not ideal — the effective compression ratio can be substantially improved, by also maximally averaging the shorter spacings (in a lossy sense), considering the data reduction goals of the particular observation through specifying a maximum amount of decorrelation tolerated at some radius away from the fringe stopping center of the interferometer.

Although on-the-fly BDA is implemented in DDFACET [152], WSCLEAN [112] and OBIT [38], no ready tool exists to create archival databases, consistent with existing interoperability standards, using this technique to our knowledge. This chapter deals only with implementation verification of our archiving tool XOVA [8] [1]. In short, we need to verify that the tolerated smearing that comes from data compression by means of averaging is within the boundaries set. These boundaries are ultimately dependent on, the field of view needed for subsequent imaging, and also, further calibration and science requirements. It is understood that datasets produced in this fashion cannot, currently, be further calibrated with CASA [104] or CUBICAL [87] due to the assumptions of regularity imposed by the packages. Tentative work has been done to illustrate that BDA-compressed data can be calibrated within the QUARTICAL [88] calibration package, but this is still a long way from any practical use. All recommendations, therefore, are made for fully calibrated data ready to be archived for future imaging operations.

We verified that the time-averaged products can be imaged with the following imaging packages:

- CASA [104] v5.4 clean,
- DDFACET [152] v0.6.0. A small modification is currently under review to be able to image frequency discretized BDA data as produced with Xova. This will be included in an upcoming release,
- WSCLEAN [112] v2.6. This version of WSCLEAN only supports XOVA-produced time-averaged BDA maps, although future versions may support frequency averaged products.

CASA [104] v5.4 `tclean` does not support imaging these BDA averaged products due to the lack of rest frame information. We are looking into writing these optional products into the Measurement Set metadata to support imaging in CASA 6.0 with `tclean`.

We restrict our core analysis to time-averaged products. To achieve these results, users must disable frequency averaging by setting the minimum number of channels (`-mc` switch) to the number of channels in their dataset. If the frequency averaging switch is used, users are advised to use CASA [104] `clean` until such time that the above issues are fully resolved.

5.2 Fundamentals

We quickly review the core principles related to averaging of the visibility function produced with interferometers. We refer the reader to [10] for a detailed discussion on the method of BDA.

The geometric phase (in the absence of residual calibration errors — assumed throughout) measured by two unique

[1] Open Source. Available here: `https://github.com/ratt-ru/xova`

antennas of a single source offset from the fringe stopping position of the interferometer is:

$$\exp\phi = \exp(-2j\pi\tau), \text{ where } \tau = \vec{b}\cdot(\vec{s}-\vec{s}_0) \tag{5.1}$$

Where $\vec{s}_0$ is the direction in which the interferometer is fringe stopped (where the fringes are maximally sensitive to an omni-directional antenna). $\vec{s}$ is the direction of the source of which we want a flux measurement and $\vec{b}$ is the baseline vector between two antennas in the interferometric array. There are $N_a(N_a-1)/2$ such unique spacings (each corresponding to a two-element interferometer) in the set cartesian product of the antennas. This excludes any correlation products formed between antennas with themselves (ie. the zero-spacings of the array, which are not typically used in the interferometric imaging, save for single dish intensity mapping operations). The baseline vector is dependent both on the source hour angle and the observing frequency of the instrument.

It is this phase information from many interferometers that enables synthesis of maps of the sky brightness distribution which must be preserved in any averaging operation. As with all averaging operations on complex numbers, averaging the phase of the measured visibility results in a drop in amplitude of the norm of the complex vector. The measured visibility fringes defined above are compact for both long spacings and large cosines of source separation from the fringe stopping position on the sky, ie. large values of τ. The averaging must therefore be done well within the Nyquist rate sampled by the longest fringe in the array — averaging beyond this rate will decorrelate the amplitude of the reconstructed source in image space.

The level of decorrelation is therefore dependent on the rate of change of the *uvw* coordinates of the baseline vector $\vec{b}$. The *uvw* bases is defined such that *w* points towards the fringe stopping center of the telescope, with L_x, L_y and L_z basis pointing south, east and towards NCP respectively in the Equatorial frame. H is the hour angle to the source and δ is the source declination.

$$\begin{bmatrix} u \\ v \\ w \end{bmatrix} = \frac{1}{\lambda}\begin{bmatrix} \sin H & \cos H & 0 \\ -\sin\delta\cos H & \sin\delta\sin H & \cos\delta \\ \cos\delta\cos H & -\cos\delta\sin H & \sin\delta \end{bmatrix}\begin{bmatrix} L_x \\ L_y \\ L_z \end{bmatrix}$$

From Eqn 5.1 we can then define a differential cumulative error in phase introduced by Earth rotation of the baseline vector within an averaging interval. r is the angle cosine of the source offset vector $\vec{s}-\vec{s}_0$ (subtending a field of view given by $\sin\theta$) on the celestial sphere. The latter can be reasonably approximated by an angle in radians for small angles.

$$\xi = \Delta t\frac{d\phi}{dt}, \text{ where } \frac{d\phi}{dt} = -2\pi r\left(\frac{du}{dt}+\frac{dv}{dt}+\frac{dw}{dt}\right)$$

Noting that only right ascension, α is a function of time — $\alpha := H_{\text{LST}} - H$, H being the hour angle to the source and H_{LST} the observatory Local Sidereal Clock. The change in u, v and w are given as:

$$\begin{aligned}
\frac{du}{dt} &= \frac{1}{\lambda}(L_x\cos H - L_y\sin H)\frac{dH}{dt} \\
\frac{dv}{dt} &= \frac{1}{\lambda}(L_x\sin\delta\sin H + L_y\cos H\sin\delta)\frac{dH}{dt} \\
\frac{dw}{dt} &= \frac{1}{\lambda}(-L_x\cos\delta\sin H - L_y\cos H\cos\delta)\frac{dH}{dt}
\end{aligned}$$

Furthermore, the derivative of the hour angle, H, is a derivative of the sidereal time of the planet, ie.

$$\frac{dH}{dt} = \omega_e \approx 7.292118516 \times 10^{-5} \text{ rad s}^{-1}$$

The decorrelation D is, therefore, given as a relative drop in amplitude resulting from averaging, here shown for a source with flux density of unity (to arbitrary scale):

$$D = \frac{I_{\text{avg}}}{I_{\text{unavg}}} = \frac{\sin(0.5|\xi|)}{0.5|\xi|}$$

Inside the software we approximate the rate change by direct evaluation of the change in *uvw* coordinates, scaled to the highest frequency in the passband. We average a baseline in time until the length of the interval exceeds a maximum decorrelation factor set by the user for a specified field of view radius (θ above) that is to be used for imaging in subsequent imaging operations.

5.3 Verification based on simulation

5.3.1 Verification of smearing tolerances

The objective of these tests is to verify a replacement averaging tool for the CASA `split` / `mstransform` averaging tool for the v2 specification of the Measurement Set [86] — the *defacto* standard visibility distribution and interoperability format. We, therefore, describe a method of verifying the effects of compression on image quality is within the bounds specified by user input and that the regular averaging components of XOVA [8] give comparable results to that given by standard CASA [104] tasks. We use CASA v5.4 throughout for this purpose.

We start by simulating a empty database with the RATT SIMMS tool[2]. The following command simulates a database with MeerKAT layout for a synthesis time of half an hour at integration rate of 2s with a single channel at 1712MHz with channel width of 208kHz on sky position 19h39m25.02671s -63d42m45.6255s (J2000).

```
simms -dir "J2000,19h39m25.02671s,-63d42m45.6255s" -T meerkat -dt 2 -st 0.5 -nc 1 \
-f0 1712MHz -df 208kHz -pl XX XY YX YY -n mk64.0.5hr.2s.1712.208khz.1939-6342.cross.ms
```

Next we simulate the following cross sky pattern into the database using the MEQTREES [109] `TurboSim` Tree Definition Language script. Here no DI or DD gain terms have been enabled

```
[turbo-sim]
dipole_model = lba_model
img_sel.imaging_column = DATA
me.e_module = Siamese_OMS_analytic_beams
me.l_module = Rotation
me.sky.tiggerskymodel = 1
me.z_module = Siamese_OMS_oms_ionosphere
model_type = use_wsrt_cos3
ms_sel.ddid_index = 0
ms_sel.field_index = 0
ms_sel.input_column = DATA
ms_sel.model_column = DATA
ms_sel.ms_channel_end = 0
ms_sel.ms_channel_start = 0
```

[2]Open Source. Available here `https://github.com/ratt-ru/simms`

```
ms_sel.ms_channel_step = 1
ms_sel.ms_corr_sel = 2x2
ms_sel.ms_polarization = XX XY YX YY
ms_sel.msname = mk64.0.5hr.2s.1712.208khz.1939-6342.cross.ms
ms_sel.output_column = DATA
ms_sel.tile_size = 32
noise_from_sefd = 0
noise_sefd = 425.0
noise_sefd_bw_khz = 208.0
noise_sefd_integration = 8.0
noise_stddev = None
oms_gain_models.err-gain.offset = 59438.857422
oms_gain_models.err-gain.scale = 0.499444444444
oms_gain_models.err-phase.offset = 59438.857422
oms_gain_models.err-phase.scale = 0.499444444444
oms_pointing_errors.pe_l.offset = 59438.857422
oms_pointing_errors.pe_l.scale = 0.499444444444
oms_pointing_errors.pe_m.offset = 59438.857422
oms_pointing_errors.pe_m.scale = 0.499444444444
selname = Lions_PiercePoints_modules_TID_MIM
tiggerlsm.filename = model_cross.txt
```

We use the following TIGGER ASCII sky model, with sources laid out in the shape of a cross with a maximum separation from the sky phase center of 1 degree in declination and 0.5 degree in right ascension.

```
#format: ra_h ra_m ra_s dec_d dec_m dec_s i freq0 spi emaj_s emin_s pa_d
19 39 25.02671 -63 42 45.6255 1.0 1.2e9 0.0 0.0 0.0 0.0 #primary
19 39 25.02671 -63 12 45.6255 1.0 1.2e9 0.0 0.0 0.0 0.0
19 39 25.02671 -62 42 45.6255 1.0 1.2e9 0.0 0.0 0.0 0.0
19 39 25.02671 -64 12 45.6255 1.0 1.2e9 0.0 0.0 0.0 0.0
19 39 25.02671 -64 42 45.6255 1.0 1.2e9 0.0 0.0 0.0 0.0
19 37 25.02671 -63 42 45.6255 1.0 1.2e9 0.0 0.0 0.0 0.0
19 35 25.02671 -63 42 45.6255 1.0 1.2e9 0.0 0.0 0.0 0.0
19 41 25.02671 -63 42 45.6255 1.0 1.2e9 0.0 0.0 0.0 0.0
19 43 25.02671 -63 42 45.6255 1.0 1.2e9 0.0 0.0 0.0 0.0
```

Throughout we assume unresolved (ie. delta scale / point) sources. This is important to simplify measurement of the drop in amplitude brought about from decorrelation in the following sense:

- The interferometer measures the visibility function — that is the amplitude and phase as a function of baseline length. By simulating delta scale sources, we expect the amplitude to be constant for all spacings of the interferometer,
- The peak flux of an unresolved source equals its integrated flux for high SNR sources. By simulating only unresolved sources, we are guaranteed that our measurement of a relative drop from unity in image space is not subject to changes in the shape of the dirty beam (Point Spread Function) of the instrument.

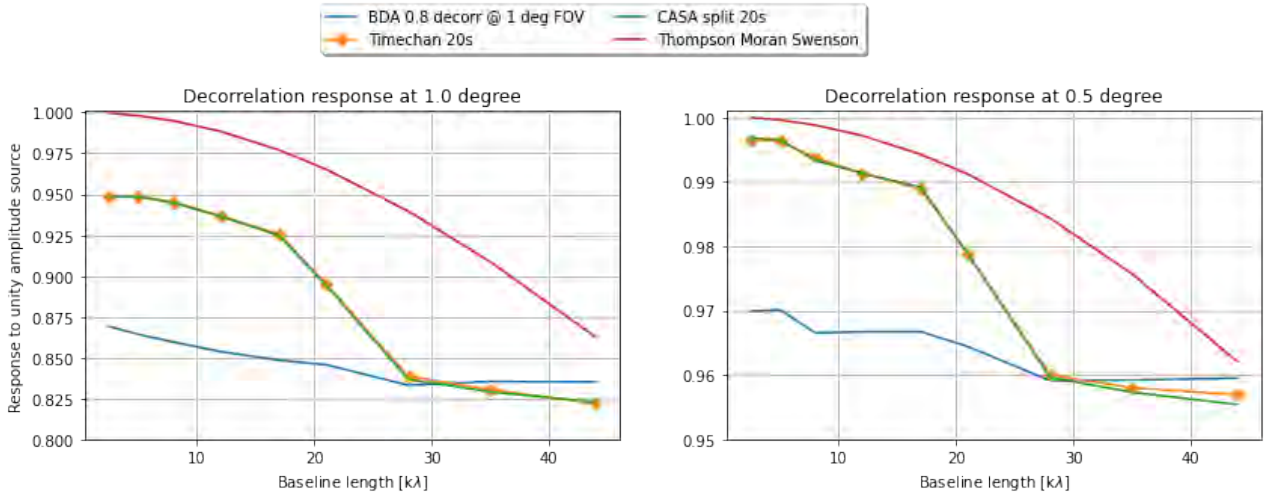

Figure 5.1: Decorrelation level of a source 1 (left) and 0.5 (right) degrees from the phase center shown for regular averaged datasets using CASA (green) [104] and XOVA [8] (orange) and a BDA averaged dataset using XOVA (blue). The theoretical decorrelation, given by [154] (red) is plotted for reference only — it assumes a circularly symmetric Gaussian distribution of sampling points on the *uv* plane (a sampling distribution different to what is achieved with MeerKAT in other words) and an idealized rectangular bandwidth.

Baseline Dependent Averaging must maintain a constant decorrelation factor for all interferometer spacings. To measure this, we use the `maxuv-l` flag of the WSCLEAN [112] imager, in the following command:

```
for i in 43955 35000 28000 21000 17000 12000 8000 5000 2500 1000; do \
wsclean -data-column DATA -channels-out 1 -weight briggs \
0.0 -niter 2000 -nmiter 25 -mgain 0.85 -size 6000 6000 \
-scale 1.4asec -maxuv-l $i -no-update-model-required \
-name xova.${i}uvlambda -mem 65.0 mk64.0.5hr.2s.1712.208khz.1939-6342.cross.xova.ms; \
done
```

Commands with the same cleaning thresholds are used to average the data in a regular fashion (at 20 s intervals) using the CASA [104] `split` task and the equivalent regular averaging implementation (`TimeChan`) in XOVA [8]. The results are summarized in Fig 5.1, with theoretical smearing estimates from [154] overplotted. The XOVA datasets were produced with the following commands:

Firstly, a BDA-averaged dataset at a maximum decorrelation of 0.8 (ie 20% drop in amplitude) at 1.0 degree radius is produced by:

```
xova bda mk64.0.5hr.2s.1712.208khz.1939-6342.cross.ms  -fov 1.0 -d 0.8 \
-dc DATA -mc 4096 --force -o mk64.0.5hr.2s.1712.208khz.1939-6342.cross.xova.ms -rc 2000000
```

Regular averaging (`TimeChan`) mode at 20 s, no frequency averaging is produced by

```
xova timechannel mk64.0.5hr.2s.1712.208khz.1939-6342.cross.ms -dc DATA -c 1 -t 20 \
--force -o mk64.0.5hr.2s.1712.208khz.1939-6342.cross.xova20s.ms -rc 500000
```

We find comparable levels of smearing for both the CASA [104] and XOVA [8] regular averaging implementations. In fact, the absolute difference between the maps synthesized and cleaned with the same parameters between these two averaging implementations is -23.6 dB. This sub-percent difference is well within the normal error bars generally accepted for flux scale calibration.

We also find that the BDA implementation overall satisfies our requirement that spacings are largely averaged to the same extent as the longest spacing. The decorrelation is slightly above the level specified by the user, but, importantly, does not

exceed the maximum decorrelation factor requested. It is worth noting, however, that the averager is designed to chunk the data in the row dimension (ie. the baseline by time by data descriptor axis of the Measurement Set [86] database). To achieve this level of averaging across all the baselines it is vitally important that the user specify enough rows per chunk, as averaging bins, at the time of writing, do not span across chunk boundaries.

5.3.2 Verification of astrometry of averaged products

Modern interferometers, including the pathfinders, are generally large interferometric arrays with high resolution (to the scale of few arcseconds or better at radio frequencies). Coupled with the high sensitivity of these instruments their resolution requires high accuracy in the array geometry (ie. the *uvw* coordinates) to produce maps with accurate source positions to well within the instrument resolution.

To this end, XOVA [8] does not apply a simple geometric mean to the *uvw* coordinate corresponding to the centroid time and channel of an output average bin. Such an approach breaks down for long spacings — where the Euclidean mean is offset from the ellipse traced out on the *uv* plane. We use the established high precision CASACORE[3] libraries to recompute *uvw* coordinates from the ITRF antenna positions of the array. We note here that this operation requires the user to keep an updated ephemeris set obtainable from the NRAO ephemeris server[4].

We again simulate a database using the combination of MEQTREES [109] and SIMMS, this time with a cross model sky out to just over 3 degrees. The following SIMMS command is used to simulate this:

```
simms -dir "J2000,19h39m25.02671s,-63d42m45.6255s" -T meerkat -dt 2 -st 0.5 \
-nc 1 -f0 1712MHz -df 208kHz -pl XX XY YX YY -n mk64.0.5hr.2s.1712.208khz.1939-6342.star.ms
```

The following Tree Definition Language definition for a MEQTREES [109] `TurboSim` simulation is used — no DI or DD gain terms have been enabled:

```
[turbo-sim]
dipole_model = lba_model
img_sel.imaging_column = DATA
me.e_module = Siamese_OMS_analytic_beams
me.l_module = Rotation
me.sky.tiggerskymodel = 1
me.z_module = Siamese_OMS_oms_ionosphere
model_type = use_wsrt_cos3
ms_sel.ddid_index = 0
ms_sel.field_index = 0
ms_sel.input_column = DATA
ms_sel.model_column = DATA
ms_sel.ms_channel_end = 0
ms_sel.ms_channel_start = 0
ms_sel.ms_channel_step = 1
ms_sel.ms_corr_sel = 2x2
ms_sel.ms_polarization = XX XY YX YY
ms_sel.msname = mk64.0.1hr.2s.1712.208khz.1939-6342.star.ms
ms_sel.output_column = DATA
ms_sel.tile_size = 32
noise_from_sefd = 0
```

[3] Open Source. Available from `https://github.com/casacore/casacore/`

[4] Available at `rsync://casa-rsync.nrao.edu/casa-data`. See also `https://casadocs.readthedocs.io/en/latest/notebooks/external-data.html`

```
noise_sefd = 425.0
noise_sefd_bw_khz = 208.0
noise_sefd_integration = 8.0
noise_stddev = None
oms_gain_models.err-gain.offset = 59441.8492079
oms_gain_models.err-gain.scale = 0.499444444444
oms_gain_models.err-phase.offset = 59441.8492079
oms_gain_models.err-phase.scale = 0.499444444444
oms_pointing_errors.pe_l.offset = 59441.8492079
oms_pointing_errors.pe_l.scale = 0.499444444444
oms_pointing_errors.pe_m.offset = 59441.8492079
oms_pointing_errors.pe_m.scale = 0.499444444444
selname = Lions_PiercePoints_modules_TID_MIM
tiggerlsm.filename = model_star_astrometry.txt
```

The following star-shaped Tigger ASCII sky model is used. The maximum separation from the phase center is 3.3 degrees:

```
#format: ra_h ra_m ra_s dec_d dec_m dec_s i freq0 spi emaj_s emin_s pa_d
19 39 25.026710 -63 42 45.625500 1.0 1712e6 0.0 0.0 0.0 0.0
19 40 25.026710 -63 42 45.625500 1.0 1712e6 0.0 0.0 0.0 0.0
19 38 25.026710 -63 42 45.625500 1.0 1712e6 0.0 0.0 0.0 0.0
19 39 25.026710 -63 27 45.625500 1.0 1712e6 0.0 0.0 0.0 0.0
19 39 25.026710 -63 57 45.625500 1.0 1712e6 0.0 0.0 0.0 0.0
19 40 25.026710 -63 27 45.625500 1.0 1712e6 0.0 0.0 0.0 0.0
19 38 25.026710 -63 27 45.625500 1.0 1712e6 0.0 0.0 0.0 0.0
19 38 25.026710 -63 57 45.625500 1.0 1712e6 0.0 0.0 0.0 0.0
19 40 25.026710 -63 57 45.625500 1.0 1712e6 0.0 0.0 0.0 0.0
19 41 25.026710 -63 42 45.625500 1.0 1712e6 0.0 0.0 0.0 0.0
19 37 25.026710 -63 42 45.625500 1.0 1712e6 0.0 0.0 0.0 0.0
19 39 25.026710 -63 12 45.625500 1.0 1712e6 0.0 0.0 0.0 0.0
19 39 25.026710 -64 12 45.625500 1.0 1712e6 0.0 0.0 0.0 0.0
19 41 25.026710 -63 12 45.625500 1.0 1712e6 0.0 0.0 0.0 0.0
19 37 25.026710 -63 12 45.625500 1.0 1712e6 0.0 0.0 0.0 0.0
19 37 25.026710 -64 12 45.625500 1.0 1712e6 0.0 0.0 0.0 0.0
19 41 25.026710 -64 12 45.625500 1.0 1712e6 0.0 0.0 0.0 0.0
19 42 25.026710 -63 42 45.625500 1.0 1712e6 0.0 0.0 0.0 0.0
19 36 25.026710 -63 42 45.625500 1.0 1712e6 0.0 0.0 0.0 0.0
19 39 25.026710 -62 57 45.625500 1.0 1712e6 0.0 0.0 0.0 0.0
19 39 25.026710 -64 27 45.625500 1.0 1712e6 0.0 0.0 0.0 0.0
19 42 25.026710 -62 57 45.625500 1.0 1712e6 0.0 0.0 0.0 0.0
19 36 25.026710 -62 57 45.625500 1.0 1712e6 0.0 0.0 0.0 0.0
19 36 25.026710 -64 27 45.625500 1.0 1712e6 0.0 0.0 0.0 0.0
19 42 25.026710 -64 27 45.625500 1.0 1712e6 0.0 0.0 0.0 0.0
19 43 25.026710 -63 42 45.625500 1.0 1712e6 0.0 0.0 0.0 0.0
19 35 25.026710 -63 42 45.625500 1.0 1712e6 0.0 0.0 0.0 0.0
19 39 25.026710 -62 42 45.625500 1.0 1712e6 0.0 0.0 0.0 0.0
19 39 25.026710 -64 42 45.625500 1.0 1712e6 0.0 0.0 0.0 0.0
19 43 25.026710 -62 42 45.625500 1.0 1712e6 0.0 0.0 0.0 0.0
19 35 25.026710 -62 42 45.625500 1.0 1712e6 0.0 0.0 0.0 0.0
```

```
19 35 25.026710 -64 42 45.625500 1.0 1712e6 0.0 0.0 0.0 0.0
19 43 25.026710 -64 42 45.625500 1.0 1712e6 0.0 0.0 0.0 0.0
19 44 25.026710 -63 42 45.625500 1.0 1712e6 0.0 0.0 0.0 0.0
19 34 25.026710 -63 42 45.625500 1.0 1712e6 0.0 0.0 0.0 0.0
19 39 25.026710 -62 27 45.625500 1.0 1712e6 0.0 0.0 0.0 0.0
19 39 25.026710 -64 57 45.625500 1.0 1712e6 0.0 0.0 0.0 0.0
19 44 25.026710 -62 27 45.625500 1.0 1712e6 0.0 0.0 0.0 0.0
19 34 25.026710 -62 27 45.625500 1.0 1712e6 0.0 0.0 0.0 0.0
19 34 25.026710 -64 57 45.625500 1.0 1712e6 0.0 0.0 0.0 0.0
19 44 25.026710 -64 57 45.625500 1.0 1712e6 0.0 0.0 0.0 0.0
19 45 25.026710 -63 42 45.625500 1.0 1712e6 0.0 0.0 0.0 0.0
19 33 25.026710 -63 42 45.625500 1.0 1712e6 0.0 0.0 0.0 0.0
19 39 25.026710 -62 12 45.625500 1.0 1712e6 0.0 0.0 0.0 0.0
19 39 25.026710 -65 12 45.625500 1.0 1712e6 0.0 0.0 0.0 0.0
19 45 25.026710 -62 12 45.625500 1.0 1712e6 0.0 0.0 0.0 0.0
19 33 25.026710 -62 12 45.625500 1.0 1712e6 0.0 0.0 0.0 0.0
19 33 25.026710 -65 12 45.625500 1.0 1712e6 0.0 0.0 0.0 0.0
19 45 25.026710 -65 12 45.625500 1.0 1712e6 0.0 0.0 0.0 0.0
19 46 25.026710 -63 42 45.625500 1.0 1712e6 0.0 0.0 0.0 0.0
19 32 25.026710 -63 42 45.625500 1.0 1712e6 0.0 0.0 0.0 0.0
19 39 25.026710 -61 57 45.625500 1.0 1712e6 0.0 0.0 0.0 0.0
19 39 25.026710 -65 27 45.625500 1.0 1712e6 0.0 0.0 0.0 0.0
19 46 25.026710 -61 57 45.625500 1.0 1712e6 0.0 0.0 0.0 0.0
19 32 25.026710 -61 57 45.625500 1.0 1712e6 0.0 0.0 0.0 0.0
19 32 25.026710 -65 27 45.625500 1.0 1712e6 0.0 0.0 0.0 0.0
19 46 25.026710 -65 27 45.625500 1.0 1712e6 0.0 0.0 0.0 0.0
19 47 25.026710 -63 42 45.625500 1.0 1712e6 0.0 0.0 0.0 0.0
19 31 25.026710 -63 42 45.625500 1.0 1712e6 0.0 0.0 0.0 0.0
19 39 25.026710 -61 42 45.625500 1.0 1712e6 0.0 0.0 0.0 0.0
19 39 25.026710 -65 42 45.625500 1.0 1712e6 0.0 0.0 0.0 0.0
19 47 25.026710 -61 42 45.625500 1.0 1712e6 0.0 0.0 0.0 0.0
19 31 25.026710 -61 42 45.625500 1.0 1712e6 0.0 0.0 0.0 0.0
19 31 25.026710 -65 42 45.625500 1.0 1712e6 0.0 0.0 0.0 0.0
19 47 25.026710 -65 42 45.625500 1.0 1712e6 0.0 0.0 0.0 0.0
19 48 25.026710 -63 42 45.625500 1.0 1712e6 0.0 0.0 0.0 0.0
19 30 25.026710 -63 42 45.625500 1.0 1712e6 0.0 0.0 0.0 0.0
19 39 25.026710 -61 27 45.625500 1.0 1712e6 0.0 0.0 0.0 0.0
19 39 25.026710 -65 57 45.625500 1.0 1712e6 0.0 0.0 0.0 0.0
19 48 25.026710 -61 27 45.625500 1.0 1712e6 0.0 0.0 0.0 0.0
19 30 25.026710 -61 27 45.625500 1.0 1712e6 0.0 0.0 0.0 0.0
19 30 25.026710 -65 57 45.625500 1.0 1712e6 0.0 0.0 0.0 0.0
19 48 25.026710 -65 57 45.625500 1.0 1712e6 0.0 0.0 0.0 0.0
19 49 25.026710 -63 42 45.625500 1.0 1712e6 0.0 0.0 0.0 0.0
19 29 25.026710 -63 42 45.625500 1.0 1712e6 0.0 0.0 0.0 0.0
19 39 25.026710 -61 12 45.625500 1.0 1712e6 0.0 0.0 0.0 0.0
19 39 25.026710 -66 12 45.625500 1.0 1712e6 0.0 0.0 0.0 0.0
19 49 25.026710 -61 12 45.625500 1.0 1712e6 0.0 0.0 0.0 0.0
19 29 25.026710 -61 12 45.625500 1.0 1712e6 0.0 0.0 0.0 0.0
19 29 25.026710 -66 12 45.625500 1.0 1712e6 0.0 0.0 0.0 0.0
```

```
19 49 25.026710 -66 12 45.625500 1.0 1712e6 0.0 0.0 0.0 0.0
19 50 25.026710 -63 42 45.625500 1.0 1712e6 0.0 0.0 0.0 0.0
19 28 25.026710 -63 42 45.625500 1.0 1712e6 0.0 0.0 0.0 0.0
19 39 25.026710 -60 57 45.625500 1.0 1712e6 0.0 0.0 0.0 0.0
19 39 25.026710 -66 27 45.625500 1.0 1712e6 0.0 0.0 0.0 0.0
19 50 25.026710 -60 57 45.625500 1.0 1712e6 0.0 0.0 0.0 0.0
19 28 25.026710 -60 57 45.625500 1.0 1712e6 0.0 0.0 0.0 0.0
19 28 25.026710 -66 27 45.625500 1.0 1712e6 0.0 0.0 0.0 0.0
19 50 25.026710 -66 27 45.625500 1.0 1712e6 0.0 0.0 0.0 0.0
19 51 25.026710 -63 42 45.625500 1.0 1712e6 0.0 0.0 0.0 0.0
19 27 25.026710 -63 42 45.625500 1.0 1712e6 0.0 0.0 0.0 0.0
19 39 25.026710 -60 42 45.625500 1.0 1712e6 0.0 0.0 0.0 0.0
19 39 25.026710 -66 42 45.625500 1.0 1712e6 0.0 0.0 0.0 0.0
19 51 25.026710 -60 42 45.625500 1.0 1712e6 0.0 0.0 0.0 0.0
19 27 25.026710 -60 42 45.625500 1.0 1712e6 0.0 0.0 0.0 0.0
19 27 25.026710 -66 42 45.625500 1.0 1712e6 0.0 0.0 0.0 0.0
19 51 25.026710 -66 42 45.625500 1.0 1712e6 0.0 0.0 0.0 0.0
```

The data was then averaged with the BDA averager in time using the following command:

```
xova bda mk64.0.5hr.2s.1712.208khz.1939-6342.star.ms -fov 1.5 -d 0.98 -dc DATA \
-mc 4096 --force -o mk64.0.5hr.2s.1712.208khz.1939-6342.star.xova.ms -rc 200000
```

It was then imaged with WSCLEAN [112], including the longest spacings (no tapering applied):

```
wsclean -data-column DATA -channels-out 1 -weight briggs 0.0 -niter 15000 \
-nmiter 25 -mgain 0.85 -size 9000 9000 -scale 1.3asec -auto-mask 7.0 \
-no-update-model-required -name astrometry.xova.98.1.5fov -mem 50.0 \
mk64.0.5hr.2s.1712.208khz.1939-6342.star.xova.ms
```

Finally, we cross-matched a PYBDSF [107] fit to the WSCLEAN [112] cleaned map to verify that the newly synthesized *uvw* coordinates are not corrupted. Overall, we find excellent agreement on tens of milliarcsecond level, as shown in Fig. 5.2. These differences are two orders of magnitude smaller than the MeerKAT instrumental resolution at L-band, and on levels an order of magnitude below the expected variations due to expected Tropospheric path length delays. We deem them acceptable.

5.4 Verification with MeerKAT observations

To verify the software, we used a dataset taken of the X-ray pulsar candidate CXOUJ1109072 investigated in Chapter 4. The data is heavily flagged ($\sim 72\%$) and at this point had transfer calibration applied before being averaged down to 624 kHz resolution at an integration interval of 8 s using regular averaging through CASA[104] `split`. The data spans the period 15-Jun-2019 14:44:26 - 22:31:34 UTC with an array of 63 antennas. The observation was taken with the wideband L-band observation mode of the MeerKAT system.

We already performed direction-dependent self-calibration on the data, as discussed in Chapter 4. The map is shown in Fig 5.3 for reference. Decorrelation due to smearing at a field radius of 1 degree is estimated to be on the order of 0.89 on the long spacings with this level of averaging, applying the estimation from [154]. As we saw in Fig. 5.1 this estimation is optimistic for the MeerKAT layout. Nonetheless, it provides a useful lower bound to averaging the other spacings to comparable levels. The following invocation was then used to BDA average the dataset:

```
xova bda CXOUJ110926_1560609072_split.avg.ms -fov 1.0 -d 0.89 -dc CORRECTED_DATA \
-mc 4096 --force -o CXOUJ110926_1560609072_split.avg.xovabda0.89.radius1deg.ms -rc 3000000
```

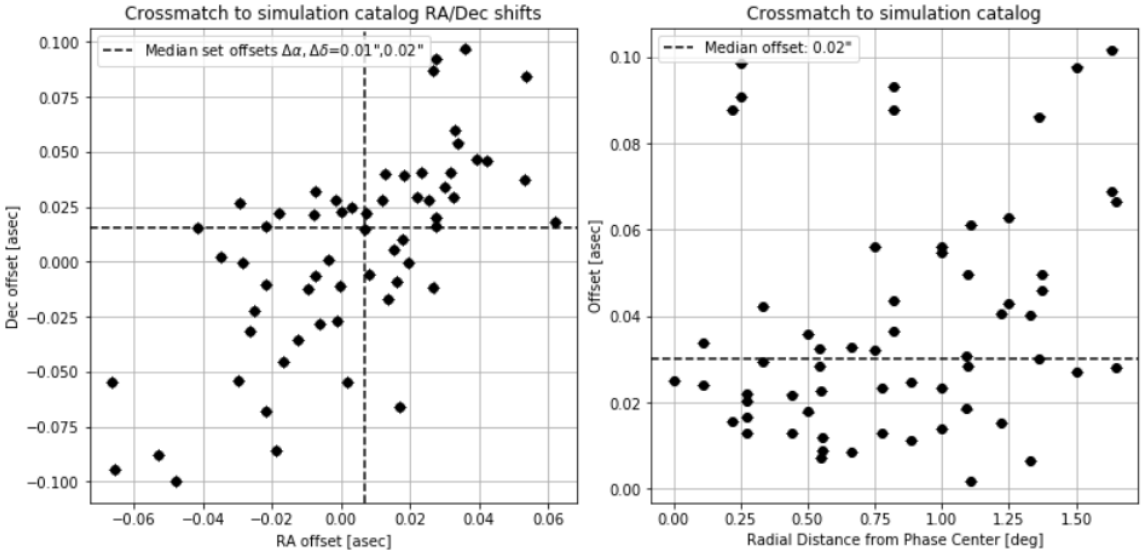

Figure 5.2: Median offsets from the known (noiseless) simulated positions crossmatched to a radius of 3". Overall we are assured the averaging operation do not corrupt the astrometry of datasets.

We show the absolute difference map for the considered Field of View radius in Fig. 5.4. The differences in decorrelation are best seen in the sidelobes of the bright AGN which still had calibration errors. The maximum absolute difference is on the level of around 10%, although the majority of this error map is empty and increases radially as expected due to slight differences in the estimated decorrelation levels between the two datasets. However, this is perhaps not the best test of flux scale accuracy. To improve the error estimation, we fitted for a catalog on the image synthesized from the regular averaged database, as well as the BDA averaged database. The crossmatch is shown in Fig. 5.5. Again we find excellent agreement in the astrometry out to a matched radius of 1.4 degrees from phase center, definitively showing that the (recomputed) *uvw* coordinates of the XOVA [8] averaged database are within acceptable tolerances. We further find an average difference in the apparent scale flux scales at the 2.5% level. This is well within acceptable margin of error usually assumed for flux scale calibration – the difference is most likely stemming from slight differences in decorrelation between the two sets – we emphasise that it is only possible to estimate for simulated data where the true sky is known.

Compared to time-averaging with standard averaging routines the compression ratio achieved by only applying time-variable BDA averaging is 9.96x — an order of magnitude difference in size over the regularly averaged database. Re-imaging the BDA-averaged and non-BDA averaged databases to the exact same shallow cleaning parameters took 30m23.4s and 01h10m51.6s respectively — more than halving the time needed for image synthesis.

5.5 Conclusions

We have extensively tested the averaging capacity of the XOVA [8] averaging software written to compress Measurement Set v2.0 format [86] interferometric visibility products. We verified only the time-averaging capability of the Baseline Dependent Averaging mode. We find that it performs as expected and introduces no serious astrometrical error, flux scale errors (beyond the decorrelation tolerance specified by the user) or morphological errors on both simulated and observed MeerKAT data. **Using only time-based BDA averaging we find that a general MeerKAT database can be compressed a further order of magnitude compared to typically used values in regular averaging.** This keeps phase decorrelation levels constant across all baselines, without compromising the science quality of the databases, save for continuum science cases where minute-level temporal variability studies are the primary science goal. BDA shows great

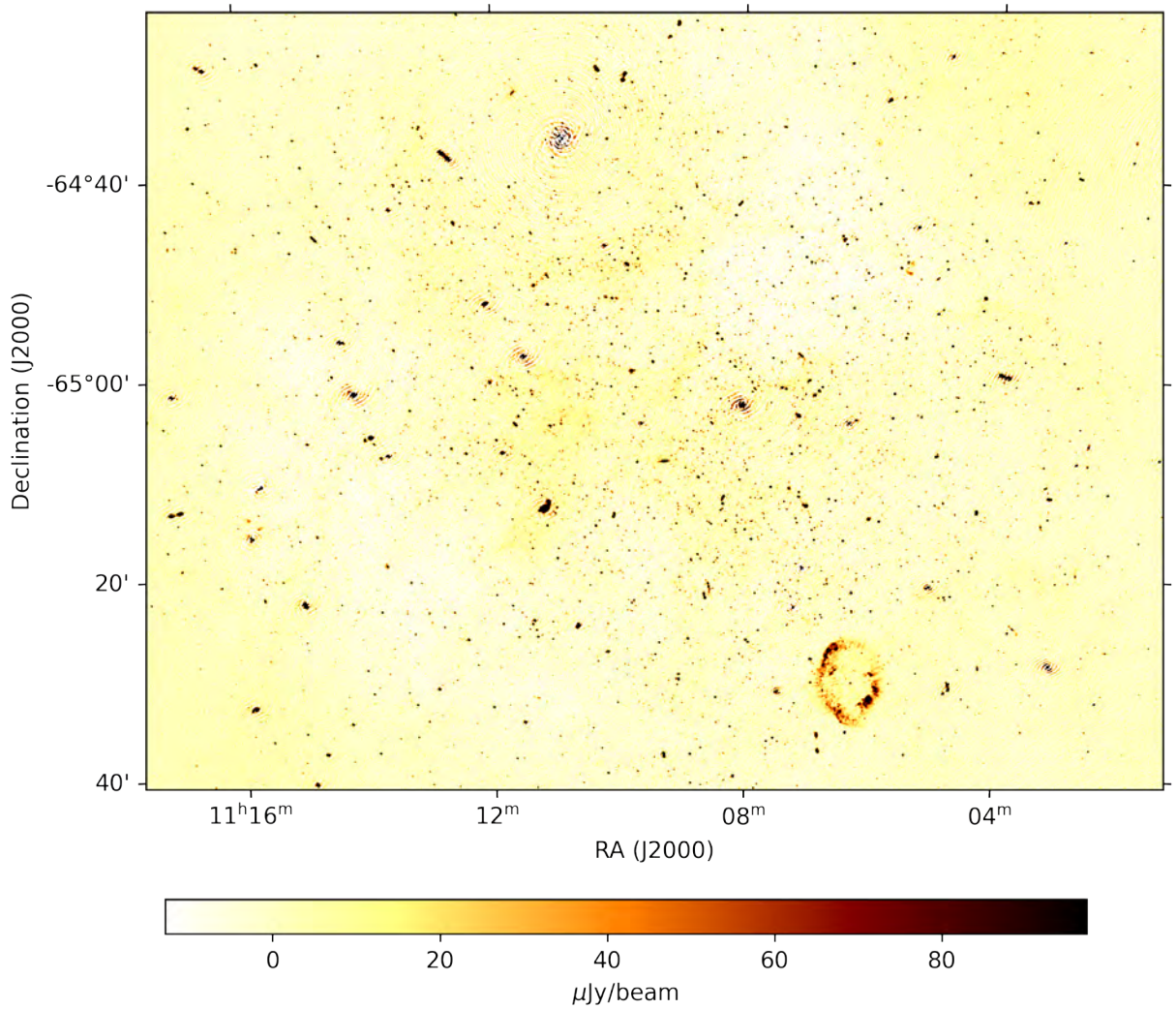

Figure 5.3: The field surrounding pulsar candidate CXOUH110926. Although low level artifacts remain, they are substantially reduced at this point, after an initial round of multi-source peeling using CUBICAL[87]. The 1σ noise is ~ 5 μJy beam^{-1} (synthesized beam size $8.97'' \times 6.83''$)

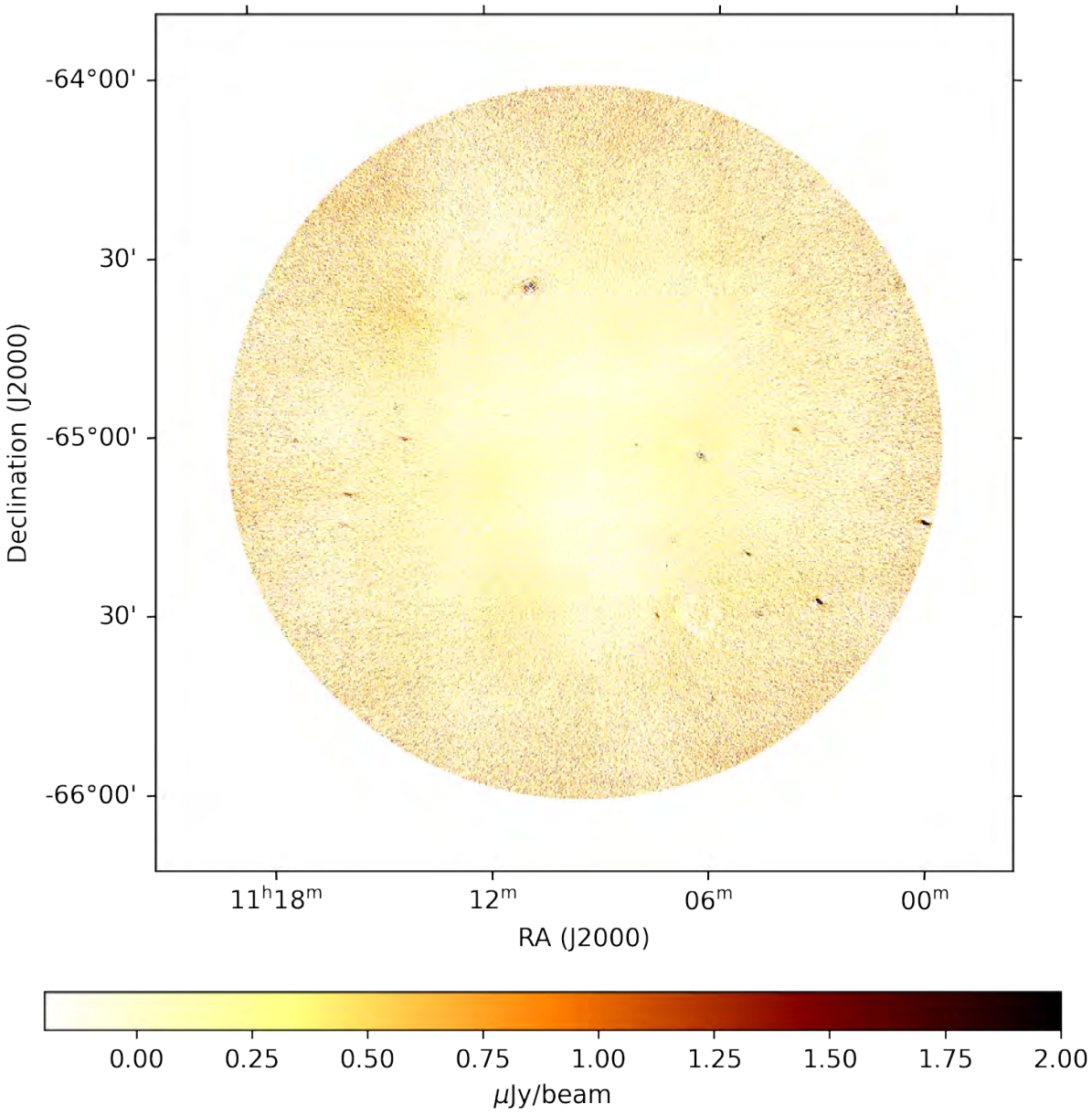

Figure 5.4: Absolute difference between the BDA and non-BDA averaged datasets within a 1 degree radius FoV. The most substantial differences are in the residual sidelobes of the brightest AGN (at a level of 7σ)

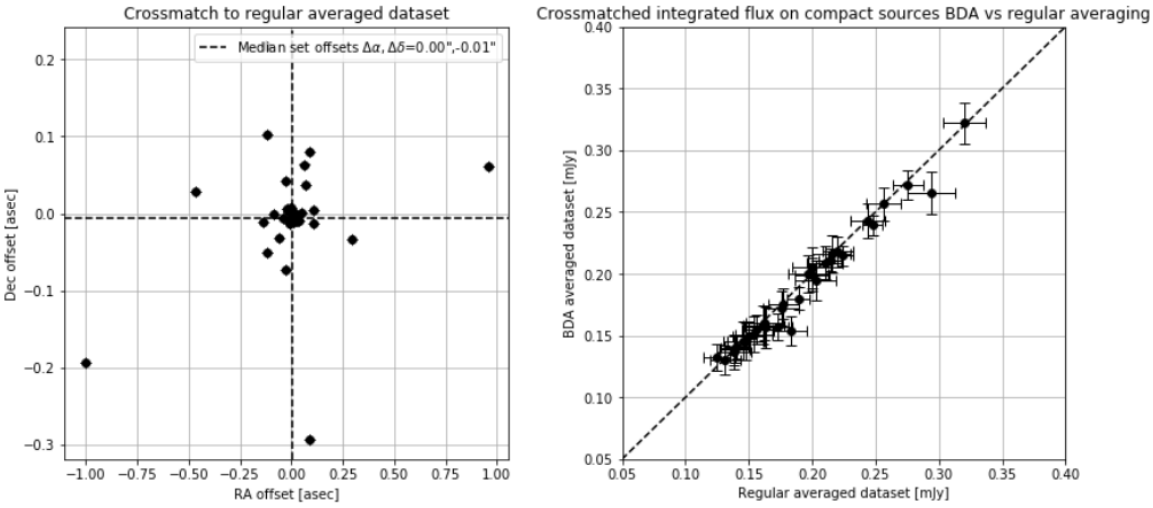

Figure 5.5: Crossmatch to 30σ compact sources between the regular averaged and BDA averaged datasets. Compact sources are here defined to have an absolute integrated to peak flux ratio of better than 1.25. Radial distances up to 1.4 degrees from phase center were considered. Left: As in the simulated case we find excellent agreement in terms of the astrometry. Right: The integrated flux for the crossmatched compact sources are shown (along with a 45 degree matching line in dashes for visual reference). We find good agreement: with errors at -16dB level — well within the usually acceptable flux scale error levels. The differences may be attributed to varying decorrelation factors between the two datasets, which can only be approximated on real data.

potential for significantly reducing storage requirements of archiving calibrated visibility products. It is our hope that the software will be useful for MeerKAT science teams and that these archiving strategies will be adopted for upcoming SKA and ngVLA calibrated data products. The work presented in this chapter, however short, illustrates the potential of reworking commonly used tooling in data reduction pipelines and extends theoretical and simulation work done by others, e.g. [11, 10] to production-quality tooling operating on observed data. That said, several questions remain to be adequitely addressed in future work, both in terms of new research and production-ready tooling implementation:

- Preliminary work is undergoing to investigate whether the long-spacing data (where the averaging time intervals are shortest, and where the effects of phase-calibration errors are most pronounced) can be further calibrated in such products.
- Currently the XOVA implementation is limited to baseline-dependent averaging with a basic (non-overlapping) rectangular (boxcar) filter window. As in the case of regular averaging this decorrelates / smears responses within the desired field of view (up to a tolerence limit as discussed). An improvement on this could be to implement a baseline-dependent lowpass fringe filtering function that more sharply defines the unsmeared field of view, while filtering sources beyond the science target, as discussed in [11].
- It must be pointed out that baseline-dependent averaging / windowing is not the only form of lossy compression in the literature:
  - In non-peer-reviewed work [9] we explored the idea of using SVD-based lossy (low-rank) compression to archive visibility data [5]. The main advantage of that approach over the BDA-based work presented in this chapter is that the compressed visibility data can be reinstated to a regular grid which is more compatible with existing calibration tooling (and could therefore be further calibrated without the additional complications arising from defining solution intervals on irregular-sampled data in calibration routines), while providing superior decorrelation within the field of view. However, the main limitation of the approach is the need

[5] I provide a conceptual prototype for the approach here: `https://gist.github.com/bennahugo/97723d3e50641fab83c7be62029d1a55`, although it must be stressed that this is not meant as production tooling

to inpaint RFI-masked visibilities and the effect this additional source of modelling has on science data. Additional testing and validation of this approach should be done, as well as the provision of production-ready software that can be readily used within workflows.

– The compression discussed in this chapter is driven by an argument of tolerances based on phase decorrelation — no assumptions on the noise properties of the data are made. Further bit-level compression is likely still possible, especially on the long spacing (ie. higher time-frequency sampling cadence) BDA data. For low signal to noise fields (ie. those without strong fringes from bright objects) [111] shows that bitrate reduction of renormalized visibility data can lead to substantial compression factors (order of a few on LOFAR and MWA array data) and is already implemented at MSv2 [86] STORAGEMANAGER level. Some research is needed to show if BDA data can be further effectively compressed by effectively utilizing the existing bitrate-reduction offered in the DYSCO STORAGEMANAGER for MSv2 datasets included in the CASACORE table system.

Appendices

A List of publications

The following is the list of publications I contributed to over the duration of these studies, as part of contributions to MeerKAT commissioning for the South African Radio Astronomy Observatory. This includes work contributed towards understanding MeerKAT polarimetric response for the interferometric and tied-array beamformer modes, as well as pipeline development or development of flagging, imaging and calibration routines which enabled data reductions.

Lead author papers / proceedings:

- Hugo, B., et al. "Radio multifrequency observations of Abell 781 with the WSRT." Monthly Notices of the Royal Astronomical Society 526.4 (2023): 5278-5291.
- Hugo, B., et al. "Tricolour: an optimized sum-threshold flagger for MeerKAT." Proceedings of the Astronomical Data Analysis Software and Systems XXX, Astronomical Society of the Pacific (2021).
- Hugo, B., et al. "ADASS XXXI: Hybrid Conferencing in the Time of Pandemic" Proceedings of the Astronomical Data Analysis Software and Systems XXXI, Astronomical Society of the Pacific (2023).
- Hugo, B., et al. "ALBUS: Modelling the Ionosphere with GNSS Interchange Data from the South African TrigNET." Proceedings of the Astronomical Data Analysis Software and Systems XXXII, Astronomical Society of the Pacific (2023).

Papers / proceedings in print (accepted):

- Józsa, Gyula IG, et al. "MeerKATHI–an end-to-end data reduction pipeline for MeerKAT and other radio telescopes." Proceedings of the Astronomical Data Analysis Software and Systems XXX, Astronomical Society of the Pacific (2021).
- Atemkeng, M. "Xova - a Baseline-Dependent Time and Channel Averaging Implementation" (2020). Proceedings of the Astronomical Data Analysis Software and Systems XXX, Astronomical Society of the Pacific (2021).

Through contributions to the Dask-ms API and data reduction eco-system, Cubical, MeqTrees, DDFacet and KillMS Direction dependent imaging and calibration packages:

- Tasse, C., et al. "Faceting for direction-dependent spectral deconvolution." Astronomy & Astrophysics 611 (2018): A87.
- Tasse, C., et al. "The LOFAR Two-meter Sky Survey: Deep Fields Data Release 1-I. Direction-dependent calibration and imaging." Astronomy & Astrophysics 648 (2021): A1.
- Shimwell, T. W., et al. "The LOFAR two-metre sky survey-II. First data release." Astronomy & Astrophysics 622 (2019): A1.
- Shimwell, T. W., et al. "The LOFAR Two-metre Sky Survey-V. Second data release." Astronomy & Astrophysics 659 (2022): A1.
- Heywood, I., et al. "MIGHTEE: total intensity radio continuum imaging and the COSMOS/XMM-LSS Early Science fields." Monthly Notices of the Royal Astronomical Society 509.2 (2022): 2150-2168.
- Parekh, V. et al. "Third-Generation Calibrations for MeerKAT Observation." Galaxies 9.4 (2021): 90.
- Parekh, V., et al. "MOSS I: Double radio relics in the Saraswati supercluster." Monthly Notices of the Royal Astronomical Society 509.2 (2022): 3086-3101.

- Perkins, Simon J., et al. "A Dask Distributed Radio Astronomy Reduction Framework." 2021 XXXIVth General Assembly and Scientific Symposium of the International Union of Radio Science (URSI GASS). IEEE.
- Makhathini, Sphesihle, et al. "The Panchromatic Afterglow of GW170817: The Full Uniform Data Set, Modeling, Comparison with Previous Results, and Implications." The Astrophysical Journal 922.2 (2021): 154.

Through development of the CARACAL pipeline:

- Namumba, Brenda, et al. "MeerKAT-64 discovers wide-spread tidal debris in the nearby NGC 7232 galaxy group." Monthly Notices of the Royal Astronomical Society 505.3 (2021): 3795-3809.
- Ramatsoku, M., et al. "GASP–XVII. H i imaging of the jellyfish galaxy JO206: gas stripping and enhanced star formation." Monthly Notices of the Royal Astronomical Society 487.4 (2019): 4580-4591.
- Serra, P., et al. "Neutral hydrogen gas within and around NGC 1316." Astronomy & Astrophysics 628 (2019): A122. Ianjamasimanana, Roger, et al. "MeerKAT-16 H i observation of the dIrr galaxy WLM." Monthly Notices of the Royal Astronomical Society 497.4 (2020): 4795-4813.
- Józsa, Gyula IG, et al. "Anomalous gas in ESO 149-G003: a MeerKAT-16 view." Monthly Notices of the Royal Astronomical Society 501.2 (2021): 2704-2723.

Through contributions to early commissioning of the MeerKAT array (Array Release 1 and 1.5) reductions of imaging data and polarimetric calibration of beamforming modes:

- Mauch, T., et al. "The 1.28 ghz meerkat deep2 image." The Astrophysical Journal 888.2 (2020): 61.
- Heywood, I., et al. "Inflation of 430-parsec bipolar radio bubbles in the Galactic Centre by an energetic event." Nature 573.7773 (2019): 235-237.
- Heywood, I., et al. "The 1.28 GHz MeerKAT Galactic Center Mosaic." The Astrophysical Journal 925.2 (2022): 165.
- Bailes, M., et al. "The MeerKAT telescope as a pulsar facility: System verification and early science results from MeerTime." Publications of the Astronomical Society of Australia 37 (2020).
- Camilo, F., et al. "Revival of the magnetar psr j1622–4950: Observations with meerkat, parkes, xmm-newton, swift, chandra, and nustar." The Astrophysical Journal 856.2 (2018): 180.
- Kramer, M., et al. "The relativistic binary programme on MeerKAT: science objectives and first results." Monthly Notices of the Royal Astronomical Society 504.2 (2021): 2094-2114.
- Johnston, Simon, et al. "The Thousand-Pulsar-Array programme on MeerKAT–I. Science objectives and first results." Monthly Notices of the Royal Astronomical Society 493.3 (2020): 3608-3615.
- Song, Xiaoxi, et al. "The Thousand-Pulsar-Array programme on MeerKAT–II. Observing strategy for pulsar monitoring with subarrays." Monthly Notices of the Royal Astronomical Society 505.3 (2021): 4456-4467.
- Serylak, M., et al. "The thousand-pulsar-array programme on MeerKAT IV: Polarization properties of young, energetic pulsars." Monthly Notices of the Royal Astronomical Society 505.3 (2021): 4483-4495.
- Asad, K. M. B., et al. "Primary beam effects of radio astronomy antennas–II. Modelling MeerKAT L-band beams." Monthly Notices of the Royal Astronomical Society 502.2 (2021): 2970-2983.

- Smirnov, O. M., et al. “MeerKAT Primary Beam Models: Derivation and Application In Calibration and Imaging.” 2018 International Conference on Electromagnetics in Advanced Applications (ICEAA). IEEE, 2018.
- Parthasarathy, A., et al. “Measurements of pulse jitter and single-pulse variability in millisecond pulsars using MeerKAT.” Monthly Notices of the Royal Astronomical Society 502.1 (2021): 407-422.
- Knowles, K., et al. “The MeerKAT Galaxy Cluster Legacy Survey: I. Survey Overview and Highlights.” Astronomy & Astrophysics 657 (2022): A56.

Through commissioning and/or continued characterization efforts:

- Heywood, Ian, et al. “Field sources near the southern-sky calibrator PKS B1934-638: effect on spectral line observations with SKA-MID and its precursors.” Monthly Notices of the Royal Astronomical Society 494.4 (2020): 5018-5028.

Through observation proposals submitted:

- (B. Hugo, Project PI, technical lead) Terni de Gregory, B., et al. “A MeerKAT view on galaxy clusters: a radio–optical study of Abell 1300 and MACS J1931. 8— 2634.” Monthly Notices of the Royal Astronomical Society 504.2 (2021): 2924-2939.
- (B. Hugo, MeerKAT technical lead) Zelati, F. Coti, et al. “Simultaneous X-ray and radio observations of the transitional millisecond pulsar candidate CXOU J110926. 4–650224.” A&A 655 (2021): A52.
- Parekh, V., et al. “MeerKAT’s discovery of a radio relic in the bimodal merging cluster A2384.” Monthly Notices of the Royal Astronomical Society 499.1 (2020): 404-414.
- Bernardi, G., et al. “A MeerKAT view on galaxy clusters.” arXiv preprint arXiv:1708.07728 (2017).

B XMM-Newton J1109 trimodal states

B.1 X-ray flare periods

```
# The photon arrival times were referred to the UTC standard


TSTART (MJD)     TSTOP (MJD)

!!!2019/06/15
58649.79009600377   58649.79067470747
58649.79125341118   58649.79183211488
58649.89021174451   58649.89194785563
58650.01694785563   58650.01868396674
```

B.2 X-ray high flux level periods

```
# The photon arrival times were referred to the UTC standard
```

TSTART (MJD) TSTOP (MJD)

!!!2019/06/14
58648.88566233 58648.88797715
58648.89202807 58648.89607900
58648.89839382 58648.90302345
58648.91806974 58648.92501419
58648.92559289 58648.93022252
58648.94411141 58648.97073178
58648.97131048 58648.98288456
58648.98462067 58649.00371789

!!!2019/06/15
58649.62632286 58649.63268860
58649.63326730 58649.64194786
58649.64252656 58649.64310526
58649.64426267 58649.64715619
58649.64831360 58649.64889230
58649.64947100 58649.65178582
58649.65236452 58649.65583674
58649.65641545 58649.65873026
58649.66104508 58649.68187841
58649.68477193 58649.68766545
58649.69287378 58649.70849878
58649.74553582 58649.76058211
58649.76289693 58649.77273489
58649.77331360 58649.77794323
58649.77852193 58649.77967934
58649.78025804 58649.78546637
58649.78662378 58649.78778119
58649.78835989 58649.79009600
58649.79183211 58649.79646174
58649.79704045 58649.79993397
58649.80051267 58649.81382286
58649.81440156 58649.81671637
58649.81729508 58649.82481823
58649.82771174 58649.83523489
58649.83697100 58649.83754971
58649.83812841 58649.84449415
58649.84507286 58649.84680897
58649.84738767 58649.87748026
58649.87805897 58649.88268860
58649.88326730 58649.88384600
58649.88789693 58649.89021174

58649.89194786 58649.89426267
58649.89599878 58649.89831360
58649.90004971 58649.90641545
58649.90988767 58649.91046637
58649.91104508 58649.91278119
58649.91335989 58649.93824415
58649.93882286 58649.95097563
58649.95155434 58649.95618397
58649.95849878 58649.95965619
58649.96023489 58649.96660063
58649.96717934 58649.97180897
58649.97238767 58649.98280434
58649.98396174 58649.98569786
58649.98627656 58649.99322100

B.3 X-ray low level periods

The photon arrival times were referred to the UTC standard

TSTART (MJD) TSTOP (MJD)

!!!2019/06/14
58648.93195863 58648.93253733
58648.93311604 58648.94411141
58648.98288456 58648.98346326
58648.98404196 58648.98462067

!!!2019/06/15
58649.64194786 58649.64252656
58649.64310526 58649.64426267
58649.64715619 58649.64773489
58649.64889230 58649.64947100
58649.65178582 58649.65236452
58649.65873026 58649.66104508
58649.68187841 58649.68477193
58649.68766545 58649.69287378
58649.70849878 58649.74553582
58649.76058211 58649.76289693
58649.77273489 58649.77331360
58649.77794323 58649.77852193
58649.78546637 58649.78662378
58649.78778119 58649.78835989
58649.79993397 58649.80051267

58649.82481823 58649.82713304
58649.83581360 58649.83697100
58649.84449415 58649.84507286
58649.84680897 58649.84738767
58649.87748026 58649.87805897
58649.88384600 58649.88558211
58649.88616082 58649.88789693
58649.89484137 58649.89599878
58649.89889230 58649.90004971
58649.90641545 58649.90988767
58649.91046637 58649.91104508
58649.95097563 58649.95155434
58649.95618397 58649.95849878
58649.96660063 58649.96717934
58649.98280434 58649.98396174
58649.99322100 58649.99379971

C 1.28 GHz lightcurves of J1109

C.1 1.28GHz lightcurve sampled at 10 minute exposure

#14Jun
#Peaks [Jy/beam],Noise [Jy/beam],Integration midpoint [mjd]
0.0002090535854222253,5.0962695240741596e-05,58648.65864583333
4.361586252343841e-05,4.052507574670017e-05,58648.66559027779
3.464292240096256e-05,2.3377582692774013e-05,58648.672534722224
-1.205180524266325e-05,4.9632111768005416e-05,58648.679479166676
9.966651850845665e-05,3.402555375942029e-05,58648.686423611114
0.00011193709360668436,3.7020367017248645e-05,58648.69336805557
8.330669515999034e-05,3.397376713110134e-05,58648.7003125
6.514161213999614e-05,3.1501454941462725e-05,58648.70725694446
0.0001182100095320493,4.903462831862271e-05,58648.7142013889
8.385472756344825e-05,2.978300108225085e-05,58648.72114583335
5.636466812575236e-05,4.167849328950979e-05,58648.72809027779
2.9644672395079397e-05,3.0418128517339937e-05,58648.73503472223
2.3101834813132882e-05,7.387992809526622e-05,58648.741979166676
5.837762000737712e-05,3.530828689690679e-05,58648.748923611136
7.985201955307275e-05,2.3182279619504698e-05,58648.75586805557
5.8163295761914924e-05,2.919091821240727e-05,58648.76281250003
1.7725706129567698e-06,2.6031590095954016e-05,58648.76975694446
5.0190265028504655e-05,2.3936992874951102e-05,58648.77670138891
3.5241650039097294e-05,2.930950176960323e-05,58648.78364583335
4.428037937032059e-05,2.3464248442905955e-05,58648.7905902778
7.989423465915024e-05,3.604468292905949e-05,58648.79753472223
3.2687123166397214e-05,2.2248334062169306e-05,58648.80447916669

5.023126504966058e-05,3.355802618898451e-05,58648.811423611136
6.255649350350723e-05,2.5443583581363782e-05,58648.81836805558
1.4364166418090463e-05,2.4977754947030917e-05,58648.82531250003
3.682374881464057e-05,3.785121225519106e-05,58648.832256944464
nan,nan,58648.83920138891
3.254599869251251e-05,2.8713784558931366e-05,58648.846145833355
5.409068398876116e-05,3.713379555847496e-05,58648.8530902778
3.9809765439713374e-05,2.560658504080493e-05,58648.86003472226
0.00010639600805006921,3.913035470759496e-05,58648.86697916669
6.587813550140709e-05,2.7874790248461068e-05,58648.87392361114
2.765928002190776e-05,3.5548418964026496e-05,58648.88086805558
0.0001169905299320817,3.6305402318248525e-05,58648.887812500034
5.613754547084682e-05,3.678916982607916e-05,58648.894756944464
2.7941781809204258e-05,5.3626514272764325e-05,58648.901701388924
3.389121047803201e-05,4.998537406208925e-05,58648.908645833355
#15Jun
#Peaks [Jy/beam],Noise [Jy/beam],Integration midpoint [mjd]
3.2609466870781034e-05,2.319078703294508e-05,58649.61766203704
4.2498599214013666e-05,2.6014215109171346e-05,58649.624606481484
8.821223309496418e-05,2.2736527171218768e-05,58649.63155092593
5.7543133152648807e-05,2.7519943614606746e-05,58649.63849537037
7.554821877420181e-06,2.3341757696471177e-05,58649.64543981481
6.184447556734085e-05,2.8692755222436972e-05,58649.65238425926
1.6994226825772785e-05,2.3858128770370968e-05,58649.65932870372
3.8290694647002965e-05,2.3407763364957646e-05,58649.66627314815
1.8599301256472245e-05,2.4214297809521668e-05,58649.6732175926
4.68161997559946e-05,2.2804235413786955e-05,58649.68016203704
0.00010234114597551525,3.5139964893460274e-05,58649.68710648149
5.593962123384699e-05,2.2269940018304624e-05,58649.69405092593
4.829308090847917e-05,2.6565652660792693e-05,58649.70099537038
7.186795119196177e-05,2.5826608180068433e-05,58649.70793981481
5.7014152844203636e-05,2.1646641471306793e-05,58649.71488425927
0.00013240269618108869,2.9345725124585442e-05,58649.72182870372
3.489968366920948e-05,2.1055933757452294e-05,58649.72877314816
7.350304804276675e-05,3.727477815118618e-05,58649.7357175926
0.00010287571785738692,4.235580490785651e-05,58649.742662037046
7.675691449549049e-05,1.925380820466671e-05,58649.74960648149
9.058944851858541e-05,2.680380202946253e-05,58649.75655092595
2.8098020266043022e-05,2.1581990949925967e-05,58649.76349537038
6.398174446076155e-05,2.4710137950023636e-05,58649.770439814834
5.3219908295432106e-05,2.3216603949549608e-05,58649.77738425927
0.00013159384252503514,2.396622221567668e-05,58649.784328703725
6.14174350630492e-05,2.4731238227104768e-05,58649.79127314816
4.6204255340853706e-05,2.160162512154784e-05,58649.798217592615
8.205452468246222e-05,2.3084272470441647e-05,58649.805162037046

7.49083046684973e-05,2.1879541236557998e-05,58649.812106481506
0.00011493504280224442,2.8859087251476012e-05,58649.81905092595
6.568225217051804e-05,2.2035716028767638e-05,58649.8259953704
nan,nan,58649.832939814834
0.00011562578583834693,2.6520967367105186e-05,58649.83988425928
7.80396512709558e-05,2.284984839207027e-05,58649.846828703725
6.508210935862735e-05,2.2308784537017345e-05,58649.853773148185
0.00012792350025847554,2.8349708372843452e-05,58649.860717592615
0.00011175517283845693,2.2190986783243716e-05,58649.867662037075
0.00012390433403197676,3.127050513285212e-05,58649.874606481506
0.00010390443640062585,2.052286254183855e-05,58649.88155092596
0.00012353333038493991,2.2542461010743864e-05,58649.8884953704
0.00011545751583762467,2.4253828087239526e-05,58649.89543981485
0.00026582719874568284,2.6604799131746404e-05,58649.90238425928
0.00011411618577549234,2.2222864572540857e-05,58649.90932870374
0.00011410936238244176,2.1561394532909617e-05,58649.916273148185
0.00011411805860698223,8.439031080342829e-05,58649.92321759263
5.4133390221977606e-05,2.4982518880278803e-05,58649.930162037075

C.2 1.28GHz lightcurve sampled at 30 minute exposure

#14Jun
#Peaks [Jy/beam],Noise [Jy/beam],Integration midpoint [mjd]
5.7663997722556815e-05,2.5224353521480225e-05,58648.66559027779
5.451973629533313e-05,2.2022941266186535e-05,58648.686423611114
5.236453944235109e-05,2.47592633968452e-05,58648.70725694446
3.702440153574571e-05,1.9120314391329885e-05,58648.72809027779
5.082243660581298e-05,1.9873359633493237e-05,58648.748923611136
4.0158265619538724e-06,1.7125787053373642e-05,58648.76975694446
3.925706914742477e-05,1.8453309166943654e-05,58648.7905902778
3.593047222238965e-05,1.522306956758257e-05,58648.811423611136
2.4190236217691563e-05,2.1852007193956524e-05,58648.832256944464
2.348197995161172e-05,1.6729354683775455e-05,58648.8530902778
3.93067421100568e-05,2.2284766600932926e-05,58648.87392361114
5.111348946229555e-05,2.881207001337316e-05,58648.894756944464
-8.801891453913413e-06,2.4511276933480985e-05,58648.915590277815
-1.770023663993925e-05,3.694091719808057e-05,58648.93642361114
6.12192670814693e-05,2.1234771338640712e-05,58648.95725694449
#15Jun
#Peaks [Jy/beam],Noise [Jy/beam],Integration midpoint [mjd]
3.938100780942477e-05,1.2127048648835625e-05,58649.624606481484
6.187287908687722e-06,1.5677385817980394e-05,58649.64543981481
1.3236916856840253e-05,1.4196424672263674e-05,58649.66627314815
5.887968291062862e-05,1.59021292347461e-05,58649.68710648149
3.6023739085067064e-05,1.4727273082826287e-05,58649.70793981481

4.737169001600705e-05,1.544112637930084e-05,58649.72877314816
4.8256384616252035e-05,1.3194689927331638e-05,58649.74960648149
3.8685589970555156e-05,1.2792345842171926e-05,58649.770439814834
7.7195574704092e-05,1.2831013009417802e-05,58649.79127314816
7.824039494153112e-05,1.430927022738615e-05,58649.812106481506
8.802201045909896e-05,1.5967409126460552e-05,58649.832939814834
8.054667705437168e-05,1.528285793028772e-05,58649.853773148185
0.00010617032239679247,1.4410235053219367e-05,58649.874606481506
0.00018137283041141927,1.3734284038946498e-05,58649.89543981485
0.000131925873574800 8,1.7351698261336423e-05,58649.916273148185

C.3 1.28GHz lightcurve sampled at 1hr exposure

#14Jun
#Peaks [Jy/beam],Noise [Jy/beam],Integration midpoint [mjd]
5.274524664855562e-05,1.538908327347599e-05,58648.67600694444
4.1014820453710854e-05,1.5091921341081616e-05,58648.717673611114
1.9471195628284477e-05,1.2331536709098145e-05,58648.759340277764
9.367048733111005e-06,1.0974636097671464e-05,58648.80100694444
2.0640083675971255e-05,1.4025887139723636e-05,58648.8426736111
3.5819703043671325e-05,1.5600771803292446e-05,58648.884340277764
-1.3173003935662564e-05,2.146394399460405e-05,58648.926006944435
#15Jun
#Peaks [Jy/beam],Noise [Jy/beam],Integration midpoint [mjd]
2.1272820958984084e-05,1.0991291674145032e-05,58649.63502314815
2.012128425121773e-05,1.1210040611331351e-05,58649.676689814805
3.782975909416564e-05,1.1375352187315002e-05,58649.718356481484
4.023595101898536e-05,1.0090971954923589e-05,58649.760023148134
6.280806701397523e-05,9.944327757693827e-06,58649.801689814805
8.040372631512582e-05,1.146818704000907e-05,58649.843356481455
0.00014237895084079355,9.511363714409526e-06,58649.885023148134

C.4 1.28GHz lightcurve sampled at 1hr30m exposure

#14Jun
#Peaks [Jy/beam],Noise [Jy/beam],Integration midpoint [mjd]
4.8826481361174956e-05,1.3789906006422825e-05,58648.686423611114
2.639358353917487e-05,1.1515607184264809e-05,58648.748923611114
-1.7775734022507095e-06,1.0200032193097286e-05,58648.811423611114
2.8038017262588255e-05,1.2514679838204756e-05,58648.873923611114
-4.903644367004745e-06,1.7697648218018003e-05,58648.936423611114
#15Jun
#Peaks [Jy/beam],Noise [Jy/beam],Integration midpoint [mjd]
1.0231832675344776e-05,8.590126526542008e-06,58649.64543981481
4.37263552157674e-05,9.281066013500094e-06,58649.70793981481
4.6576737076975405e-05,8.47496630740352e-06,58649.77043981481

7.76456217863597e-05,9.537649020785466e-06,58649.83293981481
0.00013630047033075243,8.337539838976227e-06,58649.89543981481

D Additional reduction information for planetary absolute angle calibration

D.1 MeerKAT data calibration procedure

We briefly highlight the main steps in the transfer calibration procedure in the flow diagram in Fig. 6. The calibration procedure mainly entails using CASA [104], WSCLEAN [112], TRICOLOUR [72], CRYSTALBALL DFT (`https://github.com/caracal-pipeline/crystalball`) software and miscellaneous scripts contained in, specific to this project: `https://github.com/bennahugo/LunaticPolarimetry`

The crux of the flow can be summarized in the following steps (and is applicable to any data reduction process):

- Correct handedness as defined by IAU convention for linear polarization, discussed in EVLA memo 219 [128]
- Apparent sky model prediction via the CRYSTALBALL package
- Calibration of the bandpass (B), delay (K), time-variable system amplitude (Ga), time-variable system phase (Gp). For each transfer field (polarization calibrator and secondary calibrator) the amplitude is fixed and only the phase is refined through self calibration. This is critical because for a linear feed system the diagonal of the coherency matrix (XX and YY component) measures the Stokes Q component of emission. Without an accurate model of source polarization (the goal of this work) unmodelled polarization will be absorbed into the solutions. `gaincal` in mode "T" can be used to solve for a constant amplitude matrix for both hands. This is only done for MeerKAT S band data.
- Calibration of relative leakages using an unpolarized source
- Calibration of HV delays (KX) and time-variable phases (Xf) using a polarized source (as explained knowing the angle is not strictly speaking necessary for the linear basis)
- Inspection and interval refinement is largely a manual process

It is worth noting that when self-calibrating the parallactic angle should not be applied to transfer (1GC) calibrated visibilities for the target field as it does not commute in the chain (with the exception of other rotation and constant matrices).

In the case of the Moon there is no power on the long spacings (the visibility function to a relatively flat disk (apparent) is a Bessil function of the first order which has most of its power in the short spacings). We only image transfer calibrated data. All measurements are based on dirty[6] images of the Moon. In the case of S-band tapers are applied to include only core spacings.

It is important to note that for the Lunar field databases parallactic angle derotation cannot be removed using standard CASA [104] routines as the ephemeris stored in the databases by the Karoo Array Telescope Visibility Format converter is stored with the incorrect ephemeris (the FK5 celestial coordinate of the first observed timestamp). A special utility function is included in the LUNATICPOLARIMETRY repository to apply derotation of the Lunar data from the feed-relative into sky-relative frame.

[6] We do not attempt to deconvolve the Lunar disk due to limitations of Multiscale Deconvolution as implemented in most imagers - the Lunar pillbox does not decompose well onto Gaussian bases. As we are actively tracking the Moon with the MeerKAT correlator system through its ephemeris background emission is largely washed out during the course of an observation.

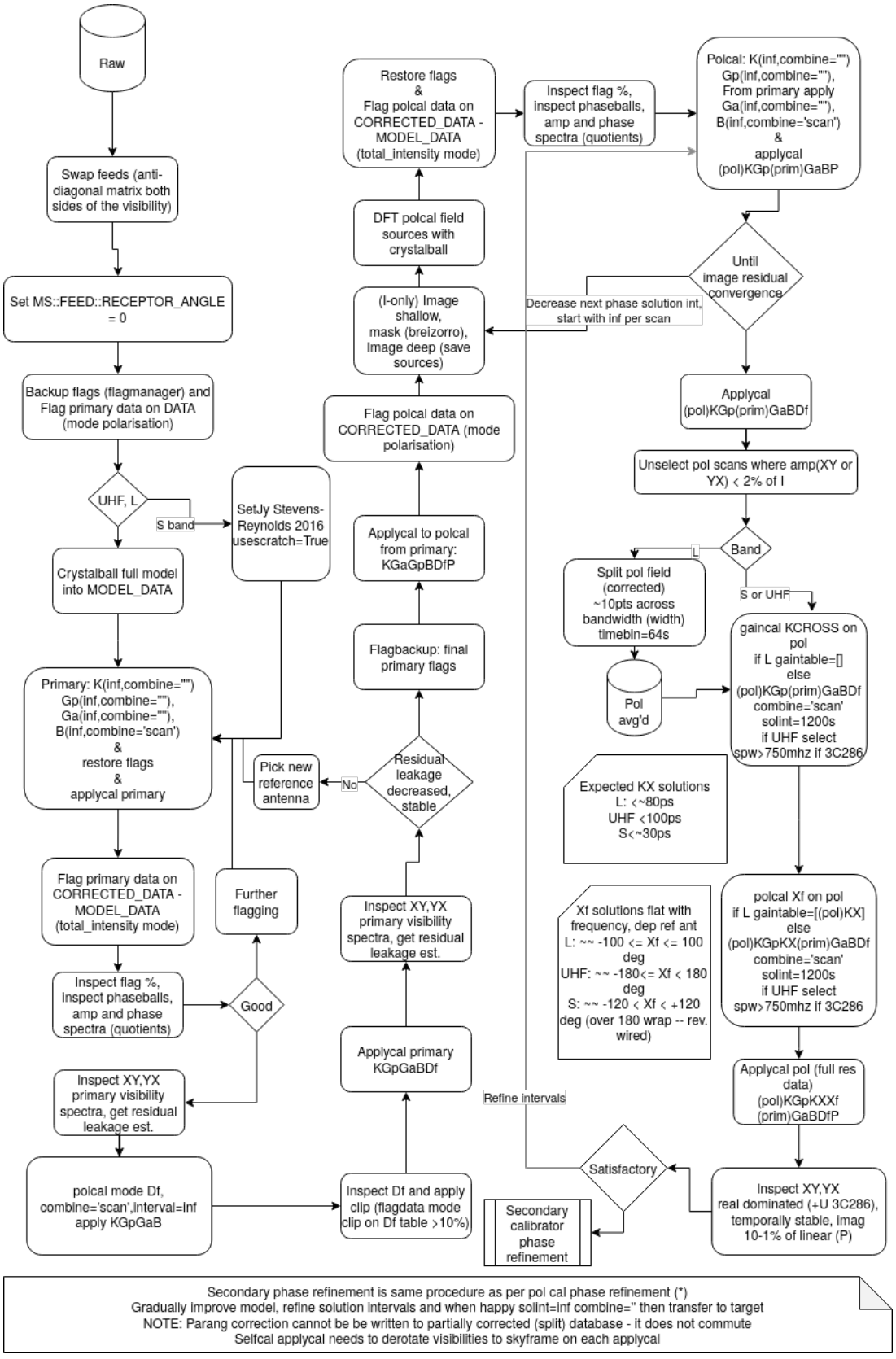

Figure 6: Calibration procedure of MeerKAT polarization data using CASA [104] and external utilities

Lastly due to a bug in the UVW calculations produced by the Karoo Array Telescope Visibility Format system[7] version 0.7 the UVW coordinates of the Lunar databases must be recomputed. This cannot be done using standard CASA [104] tasks for the same ephemeris reason the parallactic angle derotation routines cannot be used. A special "`fixvis`-like" script has been written using CASACORE measures to achieve this functionality with special body Ephemeris and is included in the LUNATICPOLARIMETRY repository. The results are shown in Fig. 7. Snapshot imaging and offset fitting with the routine discussed in Section 2.3 was instrumental in tracking down the issue and verifying corrective procedures.

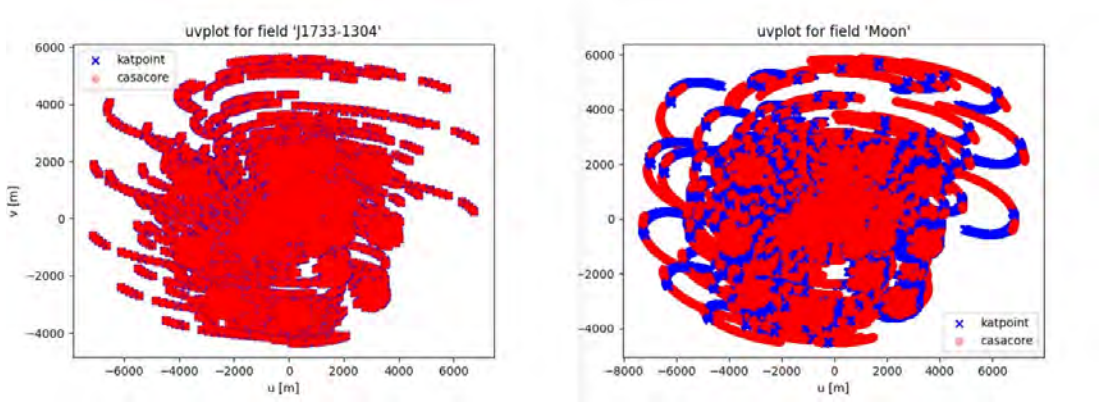

Figure 7: CASACORE measures generated vs. Karoo Array Telescope Visibility Format UVW coordinates for the extragalactic objects vs. nearby objects. For extragalactic objects the UVW coordinates are correct. The parallax error induced on the Moon position results in an apparent rotation in the UV-plane around the fringe stopping position at W. This results in (approximately) a rotation in image space which rotates the polarization vector and off-axis astrometry.

As a quick verification check one of us (Rick Perley) has independently reduced the raw Lunar and handedness datasets using AIPS [58]. The procedure applied is fully documented in EVLA memo 219 [128] with Lunar ephemeris tables generated by procedures provided by Bryan Butler and similar AIPS-based UVW corrections created, as those provided using CASACORE `measures`.

We briefly summarize the calibration procedure when using AIPS [58]:

- `FITLD`, to load the data into AIPS [58]. The polarization assignments are automatically adjusted.
- `MULTI`, subdivides the single MeerKAT spectral window into a 16-SPW database which simplifies subsequent steps.
- `UVFLG`, `CLIP`, etc., needed to remove RFI and other corrupted data.
- `FRING` and `CLCAL` to determine and apply parallel-hand delays. (SN1 and CL2 tables)
- `BPASS` to determine the bandpass functions (BP1)
- `CALIB` and `CLCAL` to determine and apply the parallel-hand gains (SN2 and CL3 tables)
- `RLDLY` to calibrate the reisudal cross-hand delay
- `PCAL` to determine the cross-hand leakages (PD1 table)
- `VHDIF` to find and remove cross-hand phase and delay (PP1, PD2, BP2 tables)

Note: use option "DOINVERS=1" when $|\rho| > 90$ — based on manual inspection of crosshand phases for `VHDIF`. `VHDIF` may fail on strongly sloped crosshand phases, although crosshand phase diode injection during MeerKAT array initialization by the Science Data Processor pipeline removes much of the initial crosshand delay, so this is not a substantial

[7] In treating coordinates in geocentric instead of topocentric frame, inducing an hour angle dependent rotation in the UV-plane with minimum at transit and a maximum of about 30 degrees at the horizon. Private comm. Ludwig Schwardt.

problem. RLDLY currently does work for strongly sloped EVPA sources or the MeerKAT linear feed systems. Caution needs to be applied when working at UHF frequencies with the depolarizing 3C286.

D.2 JVLA data reduction using AIPS

The main steps in the process to calibrate JVLA data are shown in Fig. 8.

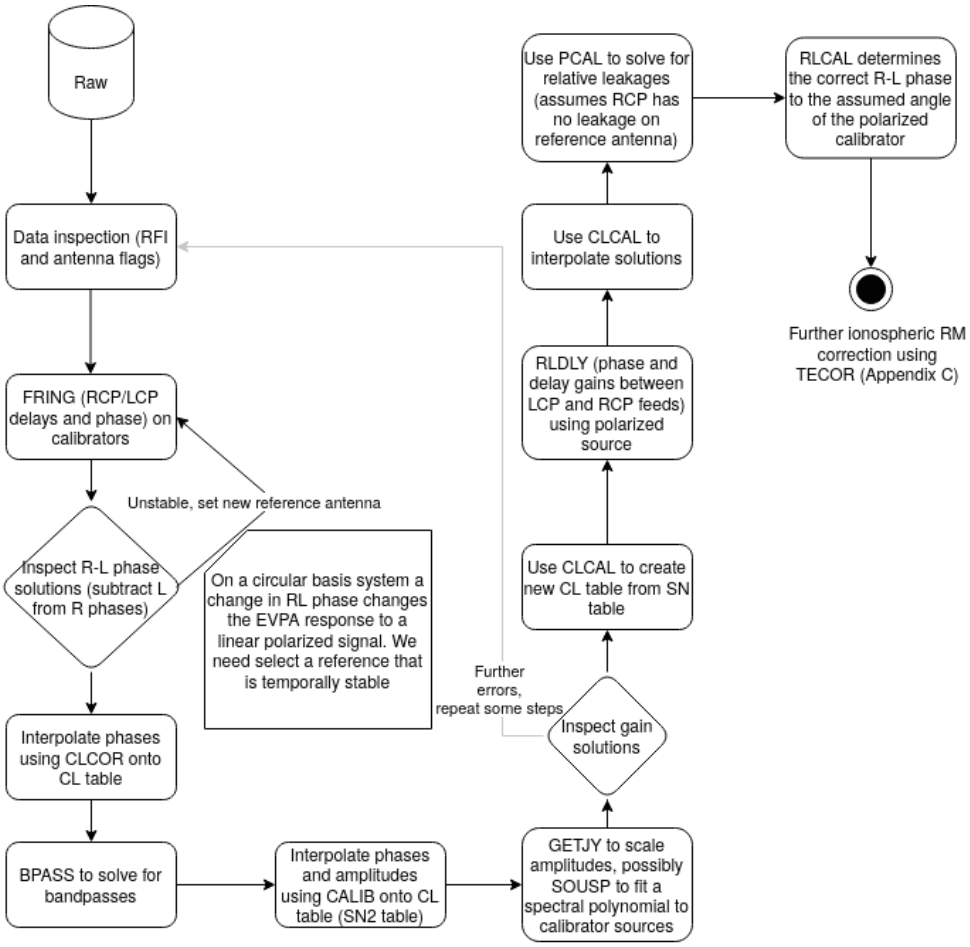

Figure 8: Main steps in AIPS [58] to do transfer polarization calibration (using 3C286 as initial guess for the angle, which is then corrected for offsets based on fit of the EVPA on the Moon, Mars or Venus depending on the band. Further corrections are made using AIPS [58] `TECOR` using the procedure outlined in Appendix D.3.

D.3 Ionospheric prediction using AIPS

Data loading and TEC correction computation using `TECOR` and helper routines is shown in Fig. 9. Here it is assumed the Measurement Set formatted data (in case of MeerKAT data) has been exported via the CASA [104] `exportuvfits` task. AIPS [58] `TECOR` requires antenna positions (minimum 4 recommended) and scan times from such a database. Users can use the multisource, field, spw, antenna and averaging parameters to effectively control the size of the output UVfits file inside of CASA [104].

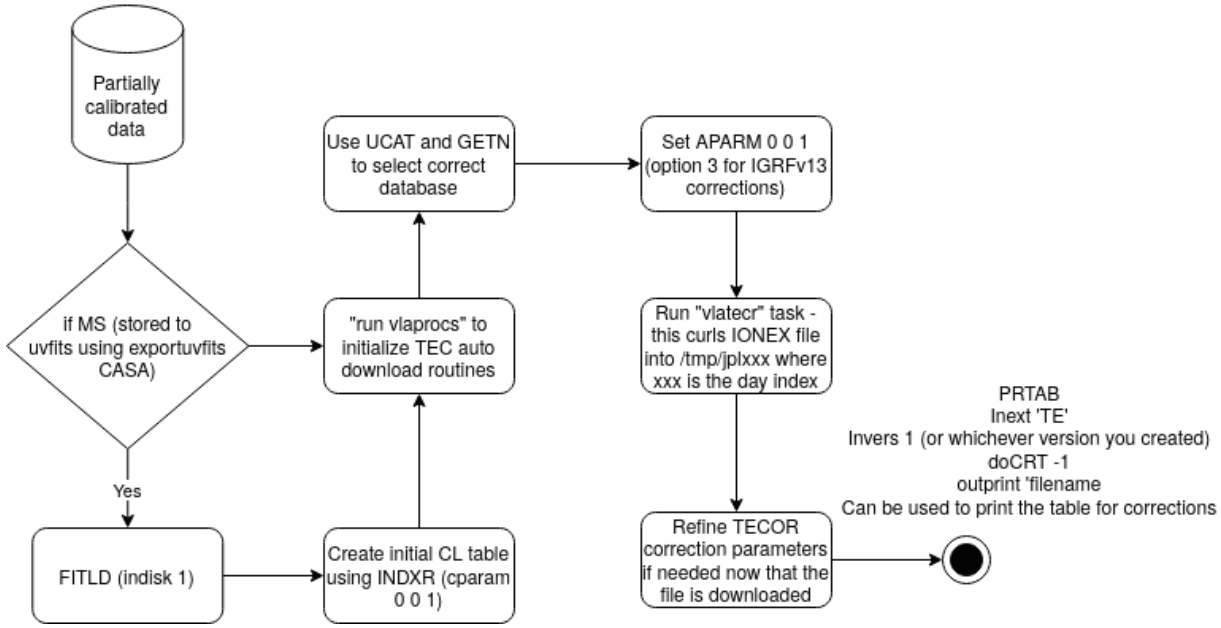

Figure 9: `TECOR` invocation flow for MeerKAT Measurement Set data. We do not rely on online corrections to make measurements in the case of MeerKAT. We simply read the computed slant TEC and RM values from a `PRTAB` printout of the TE table.

Bibliography

[1] M. Acuña, J. Connerney, P. Wasilewski, R. Lin, D. Mitchell, K. Anderson, C. Carlson, J. McFadden, H. Rème, C. Mazelle, et al. Magnetic field of Mars: Summary of results from the aerobraking and mapping orbits. *Journal of Geophysical Research: Planets*, 106(E10):23403–23417, 2001.

[2] I. Agudo, C. Thum, H. Wiesemeyer, S. N. Molina, C. Casadio, J. L. Gómez, and D. Emmanoulopoulos. 3C 286: a bright, compact, stable, and highly polarized calibrator for millimeter-wavelength observations. *Astronomy & Astrophysics*, 541:A111, 2012.

[3] P. Alken, E. Thébault, C. D. Beggan, H. Amit, J. Aubert, J. Baerenzung, T. Bondar, W. Brown, S. Califf, A. Chambodut, et al. International geomagnetic reference field: the thirteenth generation. *Earth, Planets and Space*, 73(1):1–25, 2021.

[4] M. Alpar, A. Cheng, M. Ruderman, and J. Shaham. A new class of radio pulsars. *Nature*, 300(5894):728–730, 1982.

[5] A. M. Archibald, S. Bogdanov, A. Patruno, J. W. Hessels, A. T. Deller, C. Bassa, G. H. Janssen, V. M. Kaspi, A. G. Lyne, B. W. Stappers, et al. Accretion-powered pulsations in an apparently quiescent neutron star binary. *The Astrophysical Journal*, 807(1):62, 2015.

[6] A. M. Archibald, V. M. Kaspi, J. W. Hessels, B. Stappers, G. Janssen, and A. Lyne. Long-Term Radio Timing Observations of the Transition Millisecond Pulsar PSR˜ j1023+ 0038. *arXiv preprint arXiv:1311.5161*, 2013.

[7] A. M. Archibald, I. H. Stairs, S. M. Ransom, V. M. Kaspi, V. I. Kondratiev, D. R. Lorimer, M. A. McLaughlin, J. Boyles, J. W. Hessels, R. Lynch, et al. A radio pulsar/X-ray binary link. *Science*, 324(5933):1411–1414, 2009.

[8] M. Atemkeng, S. Perkins, J. S. Kenyon, B. V. Hugo, and O. Smirnov. Xova: Baseline-Dependent Time and Channel Averaging for Radio Interferometry. 532:71, 2022.

[9] M. Atemkeng, S. Perkins, E. Seck, S. Makhathini, O. Smirnov, L. Bester, and B. Hugo. Lossy compression of large-scale radio interferometric data. *arXiv preprint arXiv:2304.07050*, 2023.

[10] M. Atemkeng, O. Smirnov, C. Tasse, G. Foster, A. Keimpema, Z. Paragi, and J. Jonas. Baseline-dependent sampling and windowing for radio interferometry: data compression, field-of-interest shaping, and outer field suppression. *Monthly Notices of the Royal Astronomical Society*, 477(4):4511–4523, 2018.

[11] M. T. Atemkeng. *Data Compression, Field of Interest Shaping and Fast Algorithms for Direction-dependent Deconvolution in Radio Interferometry*. PhD thesis, RHODES UNIVERSITY, 2016.

[12] C. Bailer-Jones, J. Rybizki, M. Fouesneau, M. Demleitner, and R. Andrae. Estimating distances from parallaxes. V. Geometric and photogeometric distances to 1.47 billion stars in Gaia Early Data Release 3. *The Astronomical Journal*, 161(3):147, 2021.

[13] C. Bailer-Jones, J. Rybizki, M. Fouesneau, G. Mantelet, and R. Andrae. Estimating distance from parallaxes. iv. distances to 1.33 billion stars in gaia data release 2. *The Astronomical Journal*, 156(2):58, 2018.

[14] C. A. Bailer-Jones. Estimating distances from parallaxes. *Publications of the Astronomical Society of the Pacific*, 127(956):994–1009, 2015.

[15] S. Berthier, M. Thomé, and P. Simonis. Circular polarization in nature: factual, theoretical and experimental summary. *Materials Today: Proceedings*, 1:145–154, 2014.

[16] R. Bignell and E. Seaquist. Observations of the linear polarization of radio sources at 2.8 and 4.5 CM. *Astronomical Journal, Vol. 78, p. 536 (1973)*, 78:536, 1973.

[17] D. Bilitza, D. Altadill, V. Truhlik, V. Shubin, I. Galkin, B. Reinisch, and X. Huang. International Reference Ionosphere 2016: From ionospheric climate to real-time weather predictions. *Space weather*, 15(2):418–429, 2017.

[18] G. J. Bishop, D. S. Coca, and C. Coker. Variations in ionospheric range error with GPS look direction. In *Proceedings of the 4th International Technical Meeting of the Satellite Division of The Institute of Navigation (ION GPS 1991)*, pages 1045–1054, 1991.

[19] R. Blandford and A. Königl. Relativistic jets as compact radio sources. *Astrophysical Journal, Part 1, vol. 232, Aug. 15, 1979, p. 34-48.*, 232:34–48, 1979.

[20] S. Bogdanov, A. T. Deller, J. C. Miller-Jones, A. M. Archibald, J. W. Hessels, A. Jaodand, A. Patruno, C. Bassa, and C. D'Angelo. Simultaneous Chandra and VLA observations of the transitional millisecond pulsar PSR J1023+ 0038: anti-correlated X-ray and radio variability. *The Astrophysical Journal*, 856(1):54, 2018.

[21] J. Bolton, F. Gardner, and M. Mackey. A radio source with a very unusual spectrum. *Nature*, 199(4894):682–683, 1963.

[22] H. E. Bond, R. L. White, R. H. Becker, and M. S. O'Brien. FIRST J102347. 6+ 003841: The First Radio-selected Cataclysmic Variable. *Publications of the Astronomical Society of the Pacific*, 114(802):1359, 2002.

[23] L. Brace and A. Kliore. The structure of the Venus ionosphere. *Space Science Reviews*, 55(1-4):81–163, 1991.

[24] M. A. Brentjens and A. De Bruyn. Faraday rotation measure synthesis. *Astronomy & Astrophysics*, 441(3):1217–1228, 2005.

[25] D. S. Briggs. High fidelity deconvolution of moderately resolved sources. *Ph. D. Thesis*, 1995.

[26] A. Brown, A. Vallenari, T. Prusti, J. De Bruijne, C. Babusiaux, C. Bailer-Jones, M. Biermann, D. W. Evans, L. Eyer, F. Jansen, et al. Gaia data release 2-summary of the contents and survey properties. *Astronomy & astrophysics*, 616:A1, 2018.

[27] A. G. Brown, A. Vallenari, T. Prusti, J. De Bruijne, C. Babusiaux, M. Biermann, O. Creevey, D. Evans, L. Eyer, A. Hutton, et al. Gaia early data release 3-summary of the contents and survey properties. *Astronomy & Astrophysics*, 649:A1, 2021.

[28] B. Burn. On the depolarization of discrete radio sources by Faraday dispersion. *Monthly Notices of the Royal Astronomical Society*, 133(1):67–83, 1966.

[29] D. N. Burrows, J. Hill, J. Nousek, J. Kennea, A. Wells, J. Osborne, A. Abbey, A. Beardmore, K. Mukerjee, A. Short, et al. The Swift X-ray telescope. *Space science reviews*, 120:165–195, 2005.

[30] S. Chapman. The absorption and dissociative or ionizing effect of monochromatic radiation in an atmosphere on a rotating earth. *Proceedings of the Physical Society*, 43(1):26, 1931.

[31] I. V. Cherniak, I. Zakharenkova, A. Krankowski, and I. Shagimuratov. Plasmaspheric electron content derived from GPS TEC and FORMOSAT-3/COSMIC measurements: Solar minimum condition. *Advances in space research*, 50(4):427–440, 2012.

[32] J. Condon. Cosmological evolution of radio sources. *The Astrophysical Journal*, 287:461–474, 1984.

[33] J. J. Condon and S. M. Ransom. *Essential radio astronomy*, volume 2. Princeton University Press, 2016.

[34] J. E. P. Connerney et al. The global magnetic field of Mars and implications for crustal evolution. *Geophysical Research Letters*, 28(21):4015–4018, 2001.

[35] T. Cornwell and R. Perley. Radio-interferometric imaging of very large fields-The problem of non-coplanar arrays. *Astronomy and Astrophysics*, 261:353–364, 1992.

[36] T. J. Cornwell, K. Golap, and S. Bhatnagar. The noncoplanar baselines effect in radio interferometry: The W-projection algorithm. *IEEE Journal of Selected Topics in Signal Processing*, 2(5):647–657, 2008.

[37] F. Coti Zelati, B. Hugo, D. F. Torres, D. d. Martino, A. Papitto, D. Buckley, T. Russell, S. Campana, R. v. Rooyen, E. Bozzo, et al. Simultaneous X-ray and radio observations of the transitional millisecond pulsar candidate CXOU J110926. 4-650224: The discovery of a variable radio counterpart. 2021.

[38] W. Cotton. Obit: A development environment for astronomical algorithms. *Publications of the Astronomical Society of the Pacific*, 120(866):439, 2008.

[39] W. Cotton. Obit development memorandum 72. *Obit memo series*, 2021.

[40] G. Cusumano, A. Segreto, V. La Parola, and A. Maselli. The 4th Palermo Swift-BAT catalogue: 100 months of survey of the hard X-ray sky. *Proceedings of Swift: 10 Years of Discovery (SWIFT 10*, page 132, 2014.

[41] R. Dach et al. Center for orbit determination in Europe (CODE). In *International GNSS service: technical report 2013 (AIUB)*, pages 21–34. IGS Central Bureau Pasadena, 2013.

[42] R. E. Daniell, L. Brown, D. Anderson, M. Fox, P. H. Doherty, D. Decker, J. J. Sojka, and R. W. Schunk. Parameterized ionospheric model: A global ionospheric parameterization based on first principles models. *Radio Science*, 30(5):1499–1510, 1995.

[43] K. Davies. *Ionospheric radio*. Number 31. IET, 1990.

[44] F. De Gasperin, M. Mevius, D. Rafferty, H. Intema, and R. Fallows. The effect of the ionosphere on ultra-low-frequency radio-interferometric observations. *Astronomy & Astrophysics*, 615:A179, 2018.

[45] D. De Martino, M. Falanga, J.-M. Bonnet-Bidaud, T. Belloni, M. Mouchet, N. Masetti, I. Andruchow, S. A. Cellone, K. Mukai, and G. Matt. The intriguing nature of the high-energy gamma ray source XSS J12270-4859. *Astronomy & Astrophysics*, 515:A25, 2010.

[46] M. S. de Villiers. MeerKAT Holography Measurements in the UHF, L, and S bands. *The Astronomical Journal*, 165(3):78, 2023.

[47] M. S. de Villiers and W. D. Cotton. MeerKAT Primary-beam Measurements in the L Band. *The Astronomical Journal*, 163(3):135, 2022.

[48] A. Deller, J. Moldon, J. Miller-Jones, A. Patruno, J. Hessels, A. Archibald, Z. Paragi, G. Heald, and N. Vilchez. Radio imaging observations of PSR J1023+ 0038 in an LMXB state. *The Astrophysical Journal*, 809(1):13, 2015.

[49] S. Elvidge, D. R. Themens, M. K. Brown, and E. Donegan-Lawley. What to do when the F10. 7 goes out? *Space Weather*, 21(4):e2022SW003392, 2023.

[50] R. Fender, R. Spencer, T. Tzioumis, K. Wu, M. van der Klis, J. van Paradijs, and H. Johnston. An asymmetric arcsecond radio jet from Circinus X-1. *The Astrophysical Journal*, 506(2):L121, 1998.

[51] K. Ferrière, J. West, and T. Jaffe. The correct sense of Faraday rotation. *Monthly Notices of the Royal Astronomical Society*, 507(4):4968–4982, 2021.

[52] G. Fjeldbo and V. Eshleman. Atmosphere of Venus as studied with the Mariner 5 dual radio-frequency occultation experiment. *Radio Science*, 4(10):879–897, 1969.

[53] G. Fjeldbo, B. Seiden, D. Sweetnam, and T. Howard. The Mariner 10 radio occultation measurements of the ionosphere of Venus. *Journal of Atmospheric Sciences*, 32(6):1232–1236, 1975.

[54] E. Gallo, N. Degenaar, and J. van den Eijnden. Hard state neutron star and black hole X-ray binaries in the radio: X-ray luminosity plane. *Monthly Notices of the Royal Astronomical Society: Letters*, 478(1):L132–L136, 2018.

[55] E. Gallo, J. Miller-Jones, D. Russell, P. Jonker, J. Homan, R. Plotkin, S. Markoff, B. Miller, S. Corbel, and R. Fender. The radio/X-ray domain of black hole X-ray binaries at the lowest radio luminosities. *Monthly Notices of the Royal Astronomical Society*, 445(1):290–300, 2014.

[56] D. Gannon and V. Sochat. Singularity: A container system for HPC applications, 2017.

[57] T. Gold. Rotating neutron stars as the origin of the pulsating radio sources. *Nature*, 218(5143):731–732, 1968.

[58] E. W. Greisen. The astronomical image processing system. *Acquisition, processing and archiving of astronomical images*, pages 125–142, 1990.

[59] J. Gubbay, A. Legg, D. Robertson, N. Craske, and G. Nicolson. The Structure of P 1934-63. *Astronomical Journal, Vol. 76, p. 965 (1971)*, 76:965, 1971.

[60] W. Gurtner and G. Mader. The RINEX format: current status, future developments. In *Proceedings of the Second International Symposium of Precise Positioning with the Global Positioning system, pp. 977ff, Ottawa*, 1990.

[61] J. Halekas, A. Poppe, Y. Harada, J. Bonnell, R. Ergun, and J. McFadden. A tenuous lunar ionosphere in the geomagnetic tail. *Geophysical research letters*, 45(18):9450–9459, 2018.

[62] C. A. Hales. Calibration Errors in Interferometric Radio Polarimetry. *The Astronomical Journal*, 154(2):54, 2017.

[63] J. Halpern, E. Gaidos, A. Sheffield, A. Price-Whelan, and S. Bogdanov. Optical observations of the binary MSP J1023+ 0038 in a new accreting state. *The Astronomer's Telegram*, 5514:1, 2013.

[64] J. Hamaker, J. Bregman, and R. Sault. Understanding radio polarimetry. I. Mathematical foundations. *Astronomy and Astrophysics Supplement Series*, 117(1):137–147, 1996.

[65] G. Helou, B. Madore, M. Schmitz, M. Bicay, X. Wu, and J. Bennett. The NASA/IPAC extragalactic database. In *Databases & On-Line Data in Astronomy*, pages 89–106. Springer, 1991.

[66] A. Hewish, S. Bell, J. Pilkington, P. Scott, and R. Collins. Observation of a rapidly pulsating radio source (reprinted from Nature, February 24, 1968). *Nature*, 224(5218):472, 1969.

[67] I. Heywood, E. Lenc, P. Serra, B. Hugo, K. W. Bannister, M. E. Bell, A. Chippendale, L. Harvey-Smith, J. Marvil, D. McConnell, et al. Field sources near the southern-sky calibrator PKS B1934-638: effect on spectral line observations with SKA-MID and its precursors. *Monthly Notices of the Royal Astronomical Society*, 494(4):5018–5028, 2020.

[68] A. Hill, A. Szostek, S. Corbel, F. Camilo, R. Corbet, R. Dubois, G. Dubus, P. Edwards, E. Ferrara, M. Kerr, et al. The bright unidentifiedγ-ray source 1FGL J1227. 9- 4852: can it be associated with a low-mass X-ray binary? *Monthly Notices of the Royal Astronomical Society*, 415(1):235–243, 2011.

[69] G. Hobbs, A. Faulkner, I. Stairs, F. Camilo, R. Manchester, A. Lyne, M. Kramer, N. D'Amico, V. Kaspi, A. Possenti, et al. The Parkes multibeam pulsar survey–IV. Discovery of 180 pulsars and parameters for 281 previously known pulsars. *Monthly Notices of the Royal Astronomical Society*, 352(4):1439–1472, 2004.

[70] B. Hoffman-Wellenhoff, H. Lichtenegger, and J. Collins. Global Positioning, 1994.

[71] B. Hugo, G. Bernardi, O. Smirnov, D. Dallacasa, T. Venturi, M. Murgia, and R. Pizzo. Radio multifrequency observations of Abell 781 with the WSRT. *Monthly Notices of the Royal Astronomical Society*, 526(4):5278–5291, 2023.

[72] B. V. Hugo, S. Perkins, B. Merry, T. Mauch, and O. M. Smirnov. Tricolour: an optimized SumThreshold flagger for MeerKAT. 532:541, 2022.

[73] C. L. Hull and R. L. Plambeck. The 1.3 mm full-stokes polarization system at CARMA. *Journal of Astronomical Instrumentation*, 4(01n02):1550005, 2015.

[74] A. Illarionov and R. Sunyaev. Why the number of galactic X-ray stars is so small? *Astronomy and Astrophysics*, 39:185, 1975.

[75] A. Jaodand, A. M. Archibald, J. W. Hessels, S. Bogdanov, C. R. D'Angelo, A. Patruno, C. Bassa, and A. T. Deller. Timing observations of PSR J1023+ 0038 during a low-mass X-ray binary state. *The Astrophysical Journal*, 830(2):122, 2016.

[76] A. D. Jaodand. Unravelling the nature of transitional millisecond pulsars. *Ph. D. Thesis*, 2019.

[77] D. L. Jauncey, G. L. White, M. J. Batty, and R. Preston. 1934-638 revisited. *Astronomical Journal (ISSN 0004-6256), vol. 92, Nov. 1986, p. 1036-1038. NASA-supported research.*, 92:1036–1038, 1986.

[78] J. A. Jawor and T. M. Tauris. Modelling spin evolution of magnetars. *Monthly Notices of the Royal Astronomical Society*, 509(1):634–657, 2022.

[79] S. Jin, C. Gao, L. Yuan, P. Guo, A. Calabia, H. Ruan, and P. Luo. Long-term variations of plasmaspheric total electron content from topside GPS observations on LEO satellites. *Remote Sensing*, 13(4):545, 2021.

[80] J. Jonas et al. The MeerKAT radio telescope. In *MeerKAT Science: On the Pathway to the SKA*, volume 277, page 001. SISSA Medialab, 2018.

[81] J. Jonas and M. Team. The MeerKAT radio telescope. *MeerKAT Science: On the Pathway to the SKA*, page 1, 2016.

[82] R. C. Jones. A new calculus for the treatment of optical systemsi. description and discussion of the calculus. *Josa*, 31(7):488–493, 1941.

[83] W. A. Joye and E. Mandel. New features of SAOImage DS9, 2003.

[84] G. Józsa, S. White, K. Thorat, O. Smirnov, P. Serra, M. Ramatsoku, A. Ramaila, S. Perkins, F. Maccagni, S. Makhathini, et al. Meerkathi-an end-to-end data reduction pipeline for meerkat and other radio telescopes. *Astronomical Data Analysis Software and Systems XXIX*, 527:635, 2020.

[85] K. Kellermann. The radio source 1934-63. *Australian Journal of Physics, vol. 19, p. 195*, 19:195, 1966.

[86] A. J. Kemball and W. M. H. MeasurementSet definition version 2.0. Technical report, NRAO CASA memo series number 229, 2000.

[87] J. Kenyon, O. Smirnov, T. Grobler, and S. Perkins. CUBICAL–fast radio interferometric calibration suite exploiting complex optimization. *Monthly Notices of the Royal Astronomical Society*, 478(2):2399–2415, 2018.

[88] J. S. Kenyon, S. Perkins, and O. Smirnov. QuartiCal-Embarrassingly Parallel Calibration of Radio Interferometer Data Using Numba and Dask. In *Astronomical Society of the Pacific Conference Series*, volume 532, page 349, 2022.

[89] E. King. Compact structure in southern peaked spectrum radio sources. *University of Tasmania*, 1994.

[90] L. Kogan and E. W. Greisen. Faceted imaging in AIPS. *AIPS memo*, 2009.

[91] M. Komesaroff, F. Gardner, D. Morris, J. Roberts, and J. Whiteoak. Observed limits to the circular polarization of nine quasars at radio frequencies. *Nature*, 218(5136):73–73, 1968.

[92] A. Komjathy. Global ionospheric total electron content mapping using the Global Positioning System. 1997.

[93] H. Kühr, A. Witzel, I. Pauliny-Toth, and U. Nauber. A catalogue of extragalactic radio sources having flux densities greater than 1 Jy at 5 GHz. *Astronomy and Astrophysics Supplement Series*, 45:367–430, 1981.

[94] A. Labiano, P. Barthel, C. O'Dea, W. de Vries, I. Pérez, and S. Baum. GPS radio sources: new optical observations and an updated master list. *Astronomy & Astrophysics*, 463(1):97–104, 2007.

[95] S. K. Lam, A. Pitrou, and S. Seibert. Numba: A llvm-based python jit compiler. In *Proceedings of the Second Workshop on the LLVM Compiler Infrastructure in HPC*, pages 1–6, 2015.

[96] A. Leick, L. Rapoport, and D. Tatarnikov. *GPS satellite surveying*. John Wiley & Sons, 2015.

[97] M.-Y. Lin and R. Ilie. A review of observations of molecular ions in the Earth's magnetosphere-ionosphere system. *Frontiers in Astronomy and Space Sciences*, 8:745357, 2022.

[98] L. Lindegren, S. Klioner, J. Hernández, A. Bombrun, M. Ramos-Lerate, H. Steidelmüller, U. Bastian, M. Biermann, A. de Torres, E. Gerlach, et al. Gaia early data release 3-the astrometric solution. *Astronomy & Astrophysics*, 649:A2, 2021.

[99] D. R. Lorimer and M. Kramer. *Handbook of pulsar astronomy*, volume 4. Cambridge university press, 2005.

[100] S. Makhathini. *Advanced radio interferometric simulation and data reduction techniques*. PhD thesis, Rhodes University, Drosty Rd, Grahamstown, 6139, Eastern Cape, South Africa, 4 2018. Available via `http://hdl.handle.net/10962/57348`.

[101] S. Makhathini. Advanced radio interferometric simulation and data reduction techniques. *Rhodes University*, 2018.

[102] J. B. Malins, S. White, G. Taylor, K. Stovall, and J. Dowell. Modeling the ionosphere with GPS and rotation measure observations. *Radio Science*, 53(6):724–738, 2018.

[103] K. Mason, A. Breeveld, R. Much, M. Carter, F. Cordova, M. Cropper, J. Fordham, H. Huckle, C. Ho, H. Kawakami, et al. The XMM-Newton optical/UV monitor telescope. *Astronomy & Astrophysics*, 365(1):L36–L44, 2001.

[104] J. P. McMullin, B. Waters, D. Schiebel, W. Young, and K. Golap. CASA architecture and applications. In *Astronomical data analysis software and systems XVI*, volume 376, page 127, 2007.

[105] D. Merkel et al. Docker: lightweight linux containers for consistent development and deployment. *Linux j*, 239(2):2, 2014.

[106] M. Mevius. RMextract: Ionospheric Faraday Rotation calculator. *Astrophysics Source Code Library*, pages ascl–1806, 2018.

[107] N. Mohan and D. Rafferty. Pybdsf: Python blob detection and source finder. *Astrophysics Source Code Library*, pages ascl–1502, 2015.

[108] C. E. Noll. The crustal dynamics data information system: A resource to support scientific analysis using space geodesy. *Advances in Space Research*, 45(12):1421–1440, 2010.

[109] J. E. Noordam and O. M. Smirnov. The MeqTrees software system and its use for third-generation calibration of radio interferometers. *Astronomy & Astrophysics*, 524:A61, 2010.

[110] C. P. O'Dea, S. Baum, and C. Stanghellini. What are the gigahertz peaked-spectrum radio sources? *The Astrophysical Journal*, 380:66–77, 1991.

[111] A. Offringa. Compression of interferometric radio-astronomical data. *Astronomy & Astrophysics*, 595:A99, 2016.

[112] A. Offringa, B. McKinley, N. Hurley-Walker, F. Briggs, R. Wayth, D. Kaplan, M. Bell, L. Feng, A. Neben, J. Hughes, et al. WSCLEAN: an implementation of a fast, generic wide-field imager for radio astronomy. *Monthly Notices of the Royal Astronomical Society*, 444(1):606–619, 2014.

[113] R. Ojha, A. L. Fey, K. J. Johnston, D. L. Jauncey, A. K. Tzioumis, and J. E. Reynolds. VLBI Observations of the Gigahertz-Peaked Spectrum Galaxy PKS 1934- 638. *The Astronomical Journal*, 127(4):1977, 2004.

[114] R. Orús et al. Improvement of global ionospheric VTEC maps by using kriging interpolation technique. *Journal of atmospheric and solar-terrestrial physics*, 67(16):1598–1609, 2005.

[115] F. Pacini. Rotating neutron stars, pulsars and supernova remnants. *Nature*, 219:145–146, 1968.

[116] A. Papitto, F. Ambrosino, L. Stella, D. Torres, F. C. Zelati, A. Ghedina, F. Meddi, A. Sanna, P. Casella, Y. Dallilar, et al. Pulsating in unison at optical and X-ray energies: simultaneous high time resolution observations of the transitional millisecond pulsar PSR J1023+ 0038. *The Astrophysical Journal*, 882(2):104, 2019.

[117] A. Papitto, D. de Martino, T. Belloni, M. Burgay, A. Pellizzoni, A. Possenti, and D. Torres. X-ray coherent pulsations during a sub-luminous accretion disc state of the transitional millisecond pulsar XSS J12270- 4859. *Monthly Notices of the Royal Astronomical Society: Letters*, 449(1):L26–L30, 2015.

[118] A. Papitto and D. d. Martino. Transitional Millisecond Pulsars. In *Millisecond Pulsars*, pages 157–200. Springer, 2021.

[119] A. Papitto and D. Torres. A propeller model for the sub-luminous state of the transitional millisecond pulsar PSR J1023+ 0038. *The Astrophysical Journal*, 807(1):33, 2015.

[120] A. Papitto, D. Torres, and J. Li. A propeller scenario for the gamma-ray emission of low-mass X-ray binaries: the case of XSS J12270- 4859. *Monthly Notices of the Royal Astronomical Society*, 438(3):2105–2116, 2014.

[121] V. Parekh, R. Kincaid, B. Hugo, A. Ramaila, and N. Oozeer. Third-Generation Calibrations for MeerKAT Observation. *Galaxies*, 9(4):90, 2021.

[122] B. Partridge, M. López-Caniego, R. Perley, J. Stevens, B. Butler, G. Rocha, B. Walter, and A. Zacchei. Absolute calibration of the radio astronomy flux density scale at 22 to 43 GHz using Planck. *The Astrophysical Journal*, 821(1):61, 2016.

[123] A. Patruno, A. Archibald, J. Hessels, S. Bogdanov, B. Stappers, C. Bassa, G. Janssen, V. Kaspi, S. Tendulkar, and A. Lyne. A new accretion disk around the missing link binary system PSR J1023+ 0038. *The Astrophysical Journal Letters*, 781(1):L3, 2013.

[124] M. Pätzold, B. Häusler, M. Bird, S. Tellmann, R. Mattei, S. Asmar, V. Dehant, W. Eidel, T. Imamura, R. Simpson, et al. The structure of Venus' middle atmosphere and ionosphere. *Nature*, 450(7170):657–660, 2007.

[125] M. Penston and R. Fosbury. Spectrophotometry of three radio galaxies. *Monthly Notices of the Royal Astronomical Society*, 183(3):479–490, 1978.

[126] R. Perley. Lunar Polarimetry at L-band. Technical report, NRAO EVLA memo series number 210, 2021.

[127] R. Perley and B. Butler. Integrated polarization properties of 3C48, 3C138, 3C147, and 3C286. *The Astrophysical Journal Supplement Series*, 206(2):16, 2013.

[128] R. Perley, E. Greisen, and B. Hugo. Enabling MeerKAT Polarimetric Imaging in AIPS. Technical report, NRAO EVLA memo series number 219, 2023.

[129] R. Perley, B. Wolfe, and E. Greisen. Testing the Efficacy of the AIPS program 'TECOR'. Technical report, NRAO EVLA memo series number 226, 2023.

[130] R. A. Perley and B. J. Butler. An accurate flux density scale from 50 MHz to 50 GHz. *The Astrophysical Journal Supplement Series*, 230(1):7, 2017.

[131] A. Plavin, W. Cotton, and T. Mauch. Obit development memorandum 62. *Obit memo series*, 2021.

[132] N. Porayko, A. Noutsos, C. Tiburzi, J. Verbiest, A. Horneffer, J. Künsemöller, S. Osłowski, M. Kramer, D. Schnitzeler, J. Anderson, et al. Testing the accuracy of the ionospheric Faraday rotation corrections through LOFAR observations of bright northern pulsars. *Monthly Notices of the Royal Astronomical Society*, 483(3):4100–4113, 2019.

[133] V. Radhakrishnan and G. Srinivasan. On the origin of the recently discovered ultra-rapid pulsar. *Current Science*, pages 1096–1099, 1982.

[134] J. Reynolds. A revised flux scale for the AT Compact Array. *ATCA memo series*, 39.3/040, 1994.

[135] J. Reynolds. A revised flux scale for the AT Compact Array. Technical report, AT Memo 39.3/040, 1994.

[136] T. P. Robitaille, E. J. Tollerud, P. Greenfield, M. Droettboom, E. Bray, T. Aldcroft, M. Davis, A. Ginsburg, A. M. Price-Whelan, W. E. Kerzendorf, et al. Astropy: A community Python package for astronomy. *Astronomy & Astrophysics*, 558:A33, 2013.

[137] M. Rocklin et al. Dask: Parallel computation with blocked algorithms and task scheduling. In *Proceedings of the 14th python in science conference*, volume 130, page 136. SciPy Austin, TX, 2015.

[138] S. Sanidas, M. Caleb, L. Driessen, V. Morello, K. Rajwade, and B. W. Stappers. MeerTRAP: A pulsar and fast transients survey with MeerKAT. *Proceedings of the International Astronomical Union*, 13(S337):406–407, 2017.

[139] R. Sault. ATCA flux density scale at 12mm. *ATCA memo series*, 39.3/124, 2003.

[140] R. J. Sault and R. A. Perley. Determining full EVLA polarization leakage terms at C and X bands. Technical report, NRAO EVLA memo series number 170, 2013.

[141] F. R. Schwab. Adaptive calibration of radio interferometer data. In *1980 Intl Optical Computing Conf I*, volume 231, pages 18–25. SPIE, 1980.

[142] G. Seeber. *Satellite geodesy*. Walter de gruyter, 2003.

[143] M. Serylak, S. Johnston, M. Kramer, S. Buchner, A. Karastergiou, M. Keith, A. Parthasarathy, P. Weltevrede, M. Bailes, E. Barr, et al. The thousand-pulsar-array programme on MeerKAT IV: Polarization properties of young, energetic pulsars. *Monthly Notices of the Royal Astronomical Society*, 505(3):4483–4495, 2021.

[144] H. Shinagawa. The ionospheres of Venus and Mars. *Advances in Space Research*, 33(11):1924–1931, 2004.

[145] L. L. Smarr and R. Blandford. The binary pulsar-Physical processes, possible companions, and evolutionary histories. *Astrophysical Journal, vol. 207, July 15, 1976, pt. 1, p. 574-588.*, 207:574–588, 1976.

[146] O. M. Smirnov. Revisiting the radio interferometer measurement equation. I. A full-sky Jones formalism. *Astronomy & Astrophysics*, 527:A106, 2011.

[147] D. H. Staelin and E. C. Reifenstein III. Pulsating radio sources near the Crab Nebula. *Science*, 162(3861):1481–1483, 1968.

[148] B. Stappers, A. Archibald, J. Hessels, C. Bassa, S. Bogdanov, G. Janssen, V. Kaspi, A. Lyne, A. Patruno, S. Tendulkar, et al. A state change in the missing link binary pulsar system PSR J1023+ 0038. *The Astrophysical Journal*, 790(1):39, 2014.

[149] L. Strüder, U. Briel, K. Dennerl, R. Hartmann, E. Kendziorra, N. Meidinger, E. Pfeffermann, C. Reppin, B. Aschenbach, W. Bornemann, et al. The European photon imaging camera on XMM-Newton: the pn-CCD camera. *Astronomy & Astrophysics*, 365(1):L18–L26, 2001.

[150] P. Szkody, O. Fraser, N. Silvestri, A. Henden, S. F. Anderson, J. Frith, B. Lawton, E. Owens, S. Raymond, G. Schmidt, et al. Cataclysmic variables from the sloan digital sky survey. II. The second year. *The Astronomical Journal*, 126(3):1499, 2003.

[151] J. Takata, K. Li, G. C. Leung, A. Kong, P. Tam, C. Hui, E. Wu, Y. Xing, Y. Cao, S. Tang, et al. Multi-wavelength emissions from the millisecond pulsar binary PSR J1023+ 0038 during an accretion active state. *The Astrophysical Journal*, 785(2):131, 2014.

[152] C. Tasse, B. Hugo, M. Mirmont, O. Smirnov, M. Atemkeng, L. Bester, M. Hardcastle, R. Lakhoo, S. Perkins, and T. Shimwell. Faceting for direction-dependent spectral deconvolution. *Astronomy & Astrophysics*, 611:A87, 2018.

[153] G. B. Taylor, C. L. Carilli, and R. A. Perley. Synthesis imaging in radio astronomy II. *Synthesis Imaging in Radio Astronomy II*, 180, 1999.

[154] A. R. Thompson, J. M. Moran, and G. W. Swenson. *Interferometry and synthesis in radio astronomy*. Springer Nature, 2017.

[155] J. R. Thorstensen and E. Armstrong. Is FIRST J102347. 6+ 003841 Really a Cataclysmic Binary? *The Astronomical Journal*, 130(2):759, 2005.

[156] J. A. Tomsick, S. Chaty, J. Rodriguez, R. Walter, and P. Kaaret. Chandra localizations and spectra of integral sources in the galactic plane: the cycle 9 sample. *The Astrophysical Journal*, 701(1):811, 2009.

[157] M. J. Turner, A. Abbey, M. Arnaud, M. Balasini, M. Barbera, E. Belsole, P. Bennie, J. Bernard, G. Bignami, M. Boer, et al. The European photon imaging camera on XMM-Newton: the MOS cameras. *Astronomy & Astrophysics*, 365(1):L27–L35, 2001.

[158] A. Tzioumis, E. King, R. Morganti, D. Dallacasa, C. Tadhunter, C. Fanti, J. Reynolds, D. Jauncey, R. Preston, P. McCulloch, et al. A sample of southern Compact Steep Spectrum radio sources: The VLBI observations. *Astronomy & Astrophysics*, 392(3):841–850, 2002.

[159] A. Tzioumis, E. King, J. Reynolds, D. Jauncey, R. Gough, R. Preston, D. Murphy, S. Tingay, D. Meier, D. Jones, et al. Multi-Frequency VLBI Observations of the GPS Source 1934–638. In *International Astronomical Union Colloquium*, volume 164, pages 179–180. Cambridge University Press, 1998.

[160] A. Tzioumis, S. Tingay, B. Stansby, J. Reynolds, C. Phillips, S. Amy, P. Edwards, M. Bowen, M. Leach, M. Kesteven, et al. Evolution of the Parsec-Scale Structure of PKS 1934- 638 Revisited: First Science with the ASKAP and New Zealand Telescopes. *The Astronomical Journal*, 140(5):1506, 2010.

[161] S. Van Der Walt, S. C. Colbert, and G. Varoquaux. The NumPy array: a structure for efficient numerical computation. *Computing in science & engineering*, 13(2):22–30, 2011.

[162] G. Van Rossum and F. L. Drake. *Python 3 Reference Manual*. CreateSpace, Scotts Valley, CA, 2009.

[163] X. Wang, Z. Wang, and N. Morrell. Infrared observations of the millisecond pulsar binary J1023+ 0038: evidence for the short-term nature of its interacting phase in 2000–2001. *The Astrophysical Journal*, 764(2):144, 2013.

[164] Z. Wang, A. M. Archibald, J. R. Thorstensen, V. M. Kaspi, D. R. Lorimer, I. Stairs, and S. M. Ransom. SDSS J102347. 6+ 003841: A millisecond radio pulsar binary that had a hot disk during 2000–2001. *The Astrophysical Journal*, 703(2):2017, 2009.

[165] P. A. Woudt, B. Warner, and M. L. Pretorius. High-speed photometry of faint cataclysmic variables-IV. V356 Aql, Aqr1, FIRST J1023+ 0038, Ha 0242-2802, GI Mon, AO Oct, V972 Oph, SDSS 0155+ 00, SDSS 0233+ 00, SDSS 1240-01, SDSS 1556-00, SDSS 2050-05, FH Ser. *Monthly Notices of the Royal Astronomical Society*, 351(3):1015–1025, 2004.

[166] E. Yizengaw, M. Moldwin, D. Galvan, B. Iijima, A. Komjathy, and A. Mannucci. Global plasmaspheric TEC and its relative contribution to GPS TEC. *Journal of Atmospheric and Solar-Terrestrial Physics*, 70(11-12):1541–1548, 2008.

[167] F. C. Zelati, A. Papitto, D. De Martino, D. A. Buckley, A. Odendaal, J. Li, T. D. Russell, D. F. Torres, S. M. Mazzola, E. Bozzo, et al. Prolonged sub-luminous state of the new transitional pulsar candidate CXOU J110926. 4- 650224. *Astronomy & Astrophysics*, 622:A211, 2019.

[168] T. Zhang, W. Baumjohann, C. Russell, J. Luhmann, and S. Xiao. Weak, quiet magnetic fields seen in the Venus atmosphere. *Scientific reports*, 6(1):23537, 2016.

[169] X.-Z. Zhang, A. Gray, Y. Su, J.-D. Li, T. Landecker, H.-B. Zhang, and C.-L. Li. New radio observations of the Moon at L band. *Research in Astronomy and Astrophysics*, 12(9):1297, 2012.